Buffer-Gas Cooling of Diatomic Molecules

A thesis presented

by

Dimitri Michael Egorov

to

The Department of Physics

in partial fulfillment of the requirements

for the degree of

Doctor of Philosophy

in the subject of

Physics

Harvard University

Cambridge, Massachusetts

August 2004

To my parents

Thesis advisor

John Morrissey Doyle

Author

Dimitri Michael Egorov

Buffer-Gas Cooling of Diatomic Molecules

Abstract

Development of novel methods of molecular cooling and progress towards a general technique for molecular trapping are reported. Buffer-gas cooling of laser-ablated molecules is used to produce 10^{12} molecules of lead monoxide PbO in the ground $X^1\Sigma(v''=0)$ state at 4 K, opening a possibility for improved sensitivity of searches for the electric dipole moment of the electron. A new method of loading atoms and molecules into a buffer gas cell is developed, and is used to produce 10^{12} Rb atoms at 4.5 K and 10^{12} molecules of imidogen NH $X^3\Sigma^-(v''=0)$ at <6 K. A next-generation trapping apparatus combining a molecular-beam loaded buffer gas cell with an in-vacuum 4.5-Tesla magnetic trap is developed. A critical parameter in buffer-gas-based magnetic trapping, the Zeeman relaxation rate in molecule-helium collisions, is measured for collisions of calcium monofluoride CaF with He. Up to 5×10^{13} CaF $X^2\Sigma^+(v''=0)$ molecules are produced via laser ablation at temperature of 2 K in helium buffer gas; the Zeeman relaxation rate is found to be 7.7×10^{-15} cm^3s^{-1}. The result is consistent with a recent theoretical prediction, which indicates that the theory may be successfully used to predict suitability of molecular candidates for buffer-gas based trapping experiments and supports the continued use of new theoretical approaches to the calculation of molecular collisional processes.

Table of contents

List of Figures

List of Tables

Citations to Previously Published Work

Portions of this thesis have appeared previously in the following papers:

D. Egorov, J. D. Weinstein, D. Patterson, B. Friedrich and J. M. Doyle. "Spectroscopy of laser-ablated buffer-gas-cooled PbO at 4 K and the prospects for measuring the electric dipole moment of the electron." Physical Review A 63, 030501(R) (2001).

D. Egorov, T. Lahaye, W. Schöllkopf, B. Friedrich and J. M. Doyle. "Buffer-gas cooling of atomic and molecular beams." Physical Review A 66, 043401 (2002).

J. G. E. Harris, R. A. Michniak, S. V. Nguyen, W. C. Campbell, D. Egorov, S. E. Maxwell, L. D. v. Buuren and J. M. Doyle. "Deep superconducting magnetic traps for neutral atoms and molecules." Review of Scientific Instruments 75, 17 (2004).

Acknowledgements

I would first like to thank my advisor, John Doyle, for supporting this work and for teaching me the numerous skills that will help me to succeed in my future career path.

I would like to gratefully acknowledge people who contributed to the experiments described in this thesis: Dave Patterson for the PbO project; Thierry Lahaye and Wieland Schoellkopf for the Rb beam experiment; Bum Suk Zhao for NH production tests; Laurens van Buuren and Edem Tsikata for the current NH trapping effort; Charlie Doret, Matt Hummon, Joel Helton, Kenneth Maussang, and Roman Krems for CaF Zeeman relaxation measurement; and everybody else in the group who made the lab such a stimulating and productive environment.

My special thanks go to Jonathan Weinstein and Rob deCarvalho for helping a young clueless grad student get his bearing in the lab, and to Bretislav Friedrich for teaching me everything I know about molecules.

Very special thanks go to Steve Maxwell, Scott Nguyen, and Wes Campbell, who contributed to the experiments described in this work, and whose friendship helped me survive the long long years of graduate school.

Finally, without listing everybody, I thank all my friends for making my time at Harvard enjoyable.

1 Introduction

1.1 Applications of cold trapped molecules

There is significant current interest in producing cold and trapped molecules. One reason for this interest is dramatic advances in atomic physics generated by the ability to produce cold and trapped atoms. Bose-Einstein condensation [1], Fermi degeneracy [2], superfluidity in a gas [3], atom lasers [4] all became possible once techniques to cool and trap atoms were available. Molecules offer a vast range of properties not available in atoms, so experiments with cold trapped molecules promise to generate more dramatic advances.

Several key differences make molecules particularly promising. First, molecules have multiple internal degrees of freedom (rotational, vibrational) that are not present in

atoms. Second, molecules, unlike atoms, are not necessarily spherical; in addition to a magnetic dipole moment they can possess a non-zero electric dipole moment and anisotropic short- and long-range electrostatic interaction. Finally, there are many more different sets of properties available among known diatomic molecules than among atoms in the periodic table; if one is searching for a system that possesses certain properties, there may be a better chance to find an appropriate candidate among molecules.

Experiments with cold trapped molecules may contribute significantly to various areas of physics. Precision spectroscopy may benefit from reduced linewidths and long interaction times of cooled and trapped samples. External-field manipulation, e.g focusing [5] and guiding, can take advantage of low translational energy of cooled molecules. Quantum computing with trapped polar molecules has been proposed [6]. Quantum-degenerate gases of molecules are predicted to exhibit novel phenomena, due to strong and anisotropic electric dipole interactions between molecules [79]. Sensitivity of certain precision measurements may be greatly increased by the ability to produce large numbers of molecules in a given internal state, as described in Chapter 2.

Collisional properties of molecules in cold and ultracold regime are of significant interest, since they largely determine directions in which experiments with cold molecules may proceed. Presence of internal degrees of freedom, electric and magnetic dipole moments, reactive channels, and various internal coupling mechanisms make molecular collisions a very exciting area [10-27]

1.1.1 Spectroscopy

Consider a spectroscopic measurement where precision is limited by photon-counting statistics. Spectroscopic measurements on molecules are typically done in either a vapor cell or in a molecular beam, and usually involve a single ro-vibrational state. In a vapor cell, the total number density of molecules is set by the saturated vapor pressure curve, and the population of individual rotational states is set by the Boltzmann distribution. Attempts to increase the photon counting rate by increasing cell temperature are counteracted by the spread of the population over a larger number of rotational states and by the increase in Doppler width. In a molecular beam, the molecules are typically cold, both internally and translationally, in a moving frame; typical temperatures are a few Kelvin. However, the beam velocity in the lab frame is very high, and photon statistics becomes limited by the maximum measurement time set by the time it takes the molecular pulse to traverse the apparatus.

Cooling of molecules results in reduction of Doppler linewidth and increase of low rotational level populations. It also allows long interaction times, since the molecules are moving slowly in the laboratory frame. In addition, cooling of molecules using the buffer gas technique described in Section 1.4 increases the measurement time even further by replacing ballistic travel with slow diffusion through buffer gas. The gain may be offset by collision-induced decoherence, which may limit the measurement time to mean time between collisions with helium. However, for many types of measurements collisions with helium are known to not result in state decoherence [28].

1.1.2 Tests of fundamental symmetries

A particularly exciting application of precision spectroscopy, one that has implications for fields far beyond atomic physics, is tests of fundamental symmetries [29]. Certain molecules appear to be very promising candidates for searches of time symmetry violation (T-violation). Searches for T-violation in atoms and molecules are essentially attempts to measure a non-zero value of the electric dipole moment of the electron (EDM). In contrast with measurements on heavy particles in accelerators, measurements on atoms and molecules suffer from few major model-related uncertainties. Molecules, despite the complexity associated with using them, have advantages over atoms. The EDM measurement requires subjecting an electron to the highest electric field possible; internal fields in molecules can be orders of magnitude stronger than those in atoms. Presence of internal molecular structure can allow a substantial reduction of many systematic errors. Cooling of molecules increases the measurement's statistical sensitivity by increasing the population of the ground rotational state and by allowing long measurement times.

1.1.3 Cold collisions and ultracold chemistry

Collisions of molecules in the past have been studied in molecular beams at collision energies of many cm^{-1}. Cold collisions, those with collision energies below ~1 cm^{-1}, are quite challenging to study using conventional methods. A number of collisional phenomena, such as elastic scattering, rotational and vibrational state changes, spin depolarization, and reactive collisions can occur in the cold regime, and their

cross-sections are expected to be modified substantially compared to high-energy collisions due to pronounced quantum-mechanical effects. Understanding of cold collisions in molecules, interesting in itself, is also critical for determining future directions in which molecular cooling and trapping experiments can advance. A significant amount of theoretical work exists [10-27], predicting various rates for cold collisions of molecules with molecules and of molecules with atoms, but the experimental data has been scarce and so far been insufficient to verify validity of these theories.

Another regime of molecular collisions, ultracold collisions, has not been accessible so far to experimental studies. The term "ultracold regime" implies dominance of only one partial wave in the collision, which requires molecules to be at sub-milliKelvin temperatures. Ultracold collisions of atoms have been studied in numerous experiments; molecules, and especially polar molecules, are expected to exhibit collisional phenomena not possible in atoms. For atoms without a magnetic moment, the dominant atom-atom interaction term is a van-der-Waals potential of the form

$$U_{VdW} = -\frac{C_6}{R^6} \tag{1}$$

Polar molecules, in addition to the van-der-Waals interaction, have electric dipole-dipole interaction of the form

$$U_{dd} = \frac{\vec{d}_1 \cdot \vec{d}_2 - 3(\vec{d}_1 \cdot \hat{r})(\vec{d}_2 \cdot \hat{r})}{R^3} \tag{2}$$

which, unlike (1), is long-range and anisotropic. Atoms with a magnetic moment also interact via a long-range anisotropic potential of the form (2), were electric dipole moment $\vec{d}$ is replaced with the magnetic dipole moment $\vec{\mu}$. However, for typical values

of $\vec{d}$ and $\vec{\mu}$, the magnetic interaction is thousands of times ($\sim\alpha^2$) weaker than electric. This strong anisotropic long-range interaction between polar molecules is expected to determine their collisional properties in the ultracold regime, and one may expect novel phenomena to be observed [7-9].

1.2 Getting molecules cold

Experiments with ultracold atoms rely on the following three steps to achieve ultra-low temperatures. First, atoms from a hot source are cooled to a temperature in the Kelvin to milli-Kelvin range. The most common technique for this step is laser cooling. Once the temperature is low enough for trapping to be possible, atoms are placed into a trap. Finally, evaporative cooling is used to bring atoms into the ultracold regime.

With exception of photoassociation and Feshbach resonance, all currently-proposed methods for creation of ultracold molecules rely on the same three steps. The challenge with molecules lies in the fact that laser cooling, a technique that works well for certain atoms, is extremely difficult to implement for molecules. An alternative cooling technique is necessary; a range of such techniques is currently being developed, as described in the following sections.

1.2.1 Laser cooling

Laser cooling relies on molecules absorbing photons from a laser beam that propagate anti-parallel to the molecules; absorbed photon's momentum reduces the molecule's velocity. In order to slow molecules down from room-temperature velocities, a transition between ground and excited states must occur thousands of times. For laser cooling to function, either the ground-to-excited state transition must be closed-cycle to within a part in a thousand, or lasers must be added to re-pump back into the ground state

the molecules that decayed into a non-ground state. Difficulty in laser cooling molecules comes from the complex ro-vibrational structure of energy levels [30]. Branching ratios between different rotational de-excitation paths are order unity [31], so closed-cycle transitions are not possible in molecules. Rotational states can potentially be re-pumped, but vibrational state leakage for most molecules is also significant, making the number of required repump lasers prohibitively large. Proposals exist for laser-cooling of certain molecules which have near-diagonal vibrational state coupling matrices[32], and work is being done on non-traditional versions of laser cooling that may be applicable to molecules [33]. However, it is unlikely for a general laser cooling method of molecules at high flux to become available in the near future.

1.2.2 Photoassociation

Photoassociation [34-37] is a way to take advantage of the success of laser cooling in atoms: ultracold molecules are formed directly from ultracold atoms. Resulting molecules are translationally at ultracold temperatures; cooling, trapping, and evaporative cooling of molecules, and challenges associated with each of the steps, are completely circumvented. This aspect gives photoassociation a significant advantage for some types of experiments, especially since very little is known about evaporative cooling properties of molecules. However, the method has significant limitations on the range of species that it can produce: at this time, photoassociation is limited to alkali diatoms only [38-44].

1.2.3 Feshbach resonance method

Another method of creating ultracold molecules directly out of ultracold atoms, referred to here as the Feshbach resonance method, has been realized recently [45-48]. The method relies on adiabatic passage through a magnetically-tunable scattering resonance between two atoms and a molecular state, or a Feshbach resonance. The molecules are produced in highly excited vibrational states, e.g. $^6Li_2$ $X^1\Sigma_g^+(v''=38)$ in [48], but have surprisingly long lifetimes of up to 1 sec*, which allows formation of molecular BEC [49], molecular superfluid [50], etc. The method produces comparatively large numbers of ultracold molecules, but is limited to alkali dimers, and production of vibrationally cold molecules is yet to be demonstrated.

1.2.4 Stark deceleration

Stark deceleration [51; 52] is a general method to slow down polar molecules from a room-temperature supersonic molecular beam. The experimental setup is essentially a linear accelerator running in reverse: a molecular beam pulse propagates along variable-voltage electrodes; each electrode stage removes a small amount of kinetic energy from the molecules until they are slowed. It is important to note that Stark deceleration is not really a cooling technique: cooling of internal degrees of freedom and narrowing of the velocity distribution (referred to as "cooling in a moving frame") is accomplished by the supersonic expansion, not deceleration. The decelerator merely

* for Fermi-degenerate atomic systems, like ^6Li, ^{40}K, etc.; the long lifetime is due to suppression of *s*-wave interactions between fermions

slows down an already-cold pulse; as a consequence, the number of cold molecules that can be produced using Stark deceleration is rather limited. The technique thus excels as a simple and general way to produce small samples of milli-Kelvin-range cold polar molecules.

1.2.5 Velocity selection

Like Stark deceleration, velocity selection [53; 54] is not really a cooling technique, i.e. it does not involve energy dissipation. The method relies on the fact that at room temperature some molecules in the Maxwell-Boltzmann distribution have translational energies in the sub-Kelvin range. It is possible to select only these molecules, e.g. by sending a molecular pulse into a curved magnetic guide that deflects only molecules with sub-Kelvin translational energies. The method can be simple to implement, but suffers from rapidly decreasing numbers of molecules as the desired temperature is lowered.

1.2.6 Other approaches

Other methods of production of cold molecules, e.g. counter-rotating nozzle [55], laser scoop [56], and billiard-like collisions [57], have been proposed in the recent years. A common feature of all of these methods is their reliance on a supersonic expansion to cool molecules in the moving frame. This typically places severe restrictions on the ability to produce substantial numbers of cold molecules.

1.2.7 Buffer-gas cooling

Buffer-gas cooling [58; 59], further described in Section 1.4, stands apart from all other techniques described in this chapter. It is completely general, i.e. it does not rely on the molecule possessing an electric dipole or a specific optical transition. The method can be applied to virtually any molecule, regardless of atomic composition or the possibility of high-performance supersonic cooling; the only requirement for the molecule is that it survives multiple collisions with low-energy helium atoms, which most molecules do[†]. More importantly, buffer gas cooling is a true cooling method. It takes at its input the entire Maxwell-Boltzmann distribution of molecules and provides cooling of translational and rotational degrees of freedom in a lab frame. This allows to produce cold molecules in numbers far exceeding those possible with any other technique. The main disadvantage of the method is the technical complexity of the apparatus, which grows rapidly as the temperature is decreased.

1.2.8 State of the art

Table 1 provides information on present accomplishments of each of the major techniques described above. It is important to note that, at this time, there is no clear means of comparing methods that produce high numbers of cold molecules with those that produce low numbers but at lower temperatures, as little is known about losses of molecules during evaporative cooling to ultracold temperatures.

[†] Survival of metastable molecules, e.g. NH $a^1\Delta$, in collisions with helium gas is an intriguing question that may have to be answered in the near future, as described in section 4.2.3.

Method	Number	Temperature	Species	References
Stark deceleration	10^8	30 mK	ND_3	[60]
	-	-	CO, YbF (high-field seekers)	[61; 62]
Photoassociation	10^6	~ μK	Li_2	[63]
	-	100 μK	RbCs (polar)	[64]
Feshbach resonance	3×10^5	150 nK	$^{40}K_2$	[65]
Buffer gas cooling	10^8	400 mK	CaH	[66]
	10^{12}	**4 K**	**PbO, NH**	**[67], this work**
	5×10^{13}	**1.5 K**	**CaF**	**this work**
Other approaches	-	10 K	O_2	[55]
	-	400 mK	NO	[57]
	-	few K	H_2CO, etc.	[53; 54]

Table 1: Advances in molecular cooling and trapping.

Dash indicates that the value is not explicitly quoted in the reference.

1.3 Trapping and evaporative cooling

Several trapping techniques have been developed for neutral particles [68]. All of them are potentially applicable to molecules; at this moment it is not clear which ones can provide an environment where long hold times and evaporative cooling can be accomplished. This section provides a brief overview of the common trapping techniques.

1.3.1 Magnetic traps

Magnetic trapping relies on interaction of the molecule's magnetic dipole with a non-uniform external field ("trapping field"). Magnetic trapping is applicable to virtually any paramagnetic molecule[*]. The energy of interaction of a paramagnetic molecule with the field can be written as

$$E = -\mu B \tag{3}$$

where μ is the magnetic dipole moment of the molecule and B is the field magnitude.

The typical scale for μ of paramagnetic molecules is 1 μ_B = 0.6717 Kelvin/Tesla. A high-performance trapping magnet can achieve trapping fields of up to 4.5 Tesla; this sets a typical temperature scale for the molecules to be trapped of ~3 Kelvin[†], which indicates

[*] The majority of diatomic molecules are in fact paramagnetic [69]; some limits on applicability of magnetic trapping will be discussed in further chapters.

[†] In this chapter we calculate trapping threshold temperature assuming trapping can occur at η=1, i.e. we assume $T_{trapping} = E_{trap} / k_B$. See [70] and [71] for deeper discussions of trapping thresholds and trap losses.

that all techniques described in section 1.2 may be used to load a magnetic trap. Table 2 provides examples of temperatures required to trap certain molecules of interest.

Molecules	Ground state	Magnetic moment	Temperature corresponding to 4.5 T
Many monohydrides and halides, esp. group II based (CaH, CaF, CaCl, MgH, MgF, …)	$^2\Sigma$	1 μ_B	3 K
Several stable diatomics (SO, O_2, S_2)	$^3\Sigma$	2 μ_B	6 K
Many monohydrides and halides, esp. group V based (NH, NF, NCl, NI, PH, PF, …)	$^3\Sigma$	2 μ_B	6 K
Exotic species (BCl, FeO, MnH, …)	$^5\Sigma$	4 μ_B	12 K
	$^6\Sigma$	5 μ_B	15 K
	$^7\Sigma$	6 μ_B	18 K

Table 2: Temperatures required for trapping of selected Σ-state diatomic molecules.

A detailed description of various loss mechanisms that occur in magnetic traps can be found in [72]. Quantitative theoretical understanding of collision-induced loss rates in magnetically trapped molecular samples is currently limited. One may expect the molecule-molecule inelastic collisional cross-sections to be comparatively small due to weakness of magnetic dipole-dipole interactions; if this is true, magnetic traps are a top candidate for an attempt at evaporative cooling of molecules into the ultracold regime.

1.3.2 Electrostatic traps

Electrostatic traps [73] rely on a first-order Stark interaction of the molecule's electric dipole moment with a trapping electrostatic field:

$$E = -d\mathscr{E} \tag{4}$$

For a typical 1-Debye dipole moment and a 10 kV/cm trapping field, the trapping threshold temperature is 240 mK. Electrostatic traps suffer from two limitations. First, the molecule of interest has to exhibit a first-order Stark effect (i.e. be easily polarizable) for the field strengths that can be attained in a given apparatus[‡]. More importantly, the interaction between two 1-Debye electric dipoles is ~900 times stronger than interaction between two 1-μ_B magnetic dipoles; this immediately points to potential difficulties in attainment of long trap hold times or in attempts at evaporative cooling.

1.3.3 Optical traps

Far off-resonance optical trap [74] (FORT) is perhaps the "perfect" trap: it is applicable to any atom or molecule, and does not suffer from many of the loss mechanisms present in magnetic or electrostatic traps. However, trap depths that are possible with existing laser technology are in the sub-milli-Kelvin range. As described in section 1.2, producing substantial numbers of molecules at milli-Kelvin temperatures remains beyond the reach of existing cooling techniques.

[‡] and, as described in further chapters, the maximum electric field strength can be greatly reduced by presence of a background gas.

1.4 Buffer gas cooling and magnetic trapping

Among the cooling and trapping techniques discussed in previous sections, the combination of buffer gas cooling and magnetic trapping is the combination offering both large numbers of trapped molecules and significant chances of successful evaporative cooling to ultracold temperatures. A critical question that determines whether buffer-gas cooling plus magnetic trapping is successful for a given molecule is the question of how quickly inelastic spin-depolarizing collisions of the trapped molecules with helium atoms of the buffer gas depopulate the (trappable) low-field-seeking state population. In a magnetic field, the low-field seeking state is at a higher energy than the high-field seeking state, so being trapped is thermodynamically unfavorable for molecules. Transitions between two states can not occur spontaneously [24], but collisions with other atoms and molecules can induce them. Given low densities of molecules compared to high densities of helium, with a typical difference of 5 orders of magnitude, only molecule-helium collisions have to be considered. For buffer-gas based trapping to succeed, the transition rate ("Zeeman loss rate") has to be slow enough so that buffer gas can be removed before the trapped state is completely depopulated.

Zeeman loss rate has been measured at Kelvin-range temperatures for a number of atoms, and general trends have been observed that may allow predictions of Zeeman loss rates for other atoms. For molecules, however, rate information is scarce, as can be seen from Table 3; theoretical work, further described in chapter 7, has had limited experimental verification. One of the goals of this work was to expand our understanding

of Zeeman-relaxation collisions of molecules with helium, which may allow the theory to guide future buffer-gas trapping experiments.

Species	Cooled in magnetic field	Measured Zeeman rates	Trapped in buffer gas	Removed buffer gas	Reference
Eu, Cr, Mn, Mo	yes	yes	yes	yes	[72; 75; 76]
Ho, Dy (non-S state)					
Er, Tb, etc.	yes	yes	yes	no	[76]
Ti, Sc	yes	yes	no	no	[77]
CaH	yes	yes	yes	no	[66]
VO	yes	no	no	no	[78]

Table 3: Magnetic trapping of atoms and molecules using buffer gas method.

1.5 Choosing a molecule to trap

While buffer gas cooling and magnetic trapping are general techniques applicable to any paramagnetic molecule, it was necessary to carefully evaluate which molecule to start with for our new-generation experiment. This section outlines a number of factors that were considered in this evaluation.

1.5.1 Interesting physics

Potential impact of physics that can be done with the molecules was perhaps the most important factor considered. This favors two categories of molecules: on one side there are weakly-interacting, simple, well-studied molecules for which one expects a fair chance of reaching quantum degeneracy; on the other side, there are strongly-interacting polar molecules, which are of particular interest for investigations of ultracold collisions, novel phenomena in quantum gases, and quantum computing.

1.5.2 Molecular structure

Only diatomic molecules were considered at this stage of the project. Polyatomic molecules have many more degrees of freedom into which collision energy can be channeled, and therefore polyatomics are likely to possess highly unfavorable collisional properties. Diatomic molecules also have simpler spectra and many have substantial

amounts of spectroscopic data readily available. Finally, any theoretical calculations of collisional properties of polyatomic molecules would be extremely challenging.

The molecules considered were in a Σ ground state, i.e. had zero orbital angular momentum about the molecular axis Λ. Theoretical studies predict that non-zero orbital angular momentum atoms typically have unfavorable Zeeman relaxation rates compared to S-state atoms, and one may expect molecules with non-zero angular momentum to have high Zeeman loss rates as well. Once better understanding of collisional properties of Σ-state molecules is developed, it would be interesting to investigate molecules with non-zero orbital angular momentum, e.g. Π-state molecules. In fact, certain non-S state atoms* are known to have S-state like collisional properties [77], and it is possible that similar behavior exists in non-Σ state molecules.

1.5.3 Technical issues

Technical aspects of our experimental setup result in significant limitations on the types of molecules that can be used. While the limitations are not fundamental, circumventing them may require substantial changes in the design of our apparatus. One limitation is set by the maximum trap depth that can be produced using our superconducting magnet technology; it constrains the magnetic moment of molecules considered to a minimum of 2 μ_B [71], at least if the added complexity of a dilution refrigerator is to be avoided.

* see also Table 3

When discussing the molecule's magnetic moment, we refer to the ratio of the Zeeman energy of the trapped state to the applied magnetic field. Field magnitudes present in our trap may be sufficient to couple different rotational states of the molecule, so the slope of the Zeeman energy shift with applied field for these high fields may decrease or even become negative, depending on the exact values of molecular constants. Therefore an additional requirement set by the technical aspects of the experimental setup is that the slope of Zeeman energy remains nearly constant for fields between zero and 4.5 Tesla[†].

Numerous techniques exist to detect atoms and molecules and investigate their translational and internal energy distributions [79; 80][‡]. The technique that is easiest to combine with a cryogenic apparatus is laser induced fluorescence (LIF) in near-UV to near-IR spectrum range; all current buffer-gas cooling experiments use either LIF or laser absorption for detection. Consequently, a molecule is required to have a well-studied strong optical transition from the ground state. This requirement is rather restrictive, especially when one considers the requirement on transition strength set by sensitivity of our fluorescence detectors. The constraint is, however, by no means fundamental; other methods of detection of molecules in buffer gas may be attempted in the future.

1.5.4 Comparison of O_2 and NH

[†] this requirement is referred to as "molecule having a low-field-seeking ground state"

[‡] I highly recommend this book to new graduate students

In this section we compare two primary candidates that we considered for the next-generation molecular trapping experiment in this work: oxygen (O_2) and imidogen (NH). Their relevant properties are outlined in Table 4. Both molecules were great candidates for trapping in our apparatus; technical hurdles [81] associated with spectroscopic detection of O_2 were much greater than those associated with production of NH beam, so NH was ultimately chosen.

	O_2	NH
Structure	$^3\Sigma^-$	$^3\Sigma^-$
Magnetic moment	2 μ_B	2 μ_B
Low-field seeking	yes, for $^{17}O^{17}O$	yes
Fluorescence: wavelength	760 nm	336 nm
Radiative lifetime	12 s	450 ns
Physics	non-polar	polar: 1.39 Debye
Statistics	boson	boson : ND, ^{15}NH fermion: NH, ^{15}ND

Table 4: Properties of O_2 and NH.

1.6 Loading of buffer gas cell

Buffer gas cooling is a general technique that can produce large numbers of cold molecules of virtually any species. In order to cool a large number of molecules, the molecules themselves have to be produced in large numbers and introduced into the buffer gas. Several methods of accomplishing this task have been demonstrated, each of them having its unique strengths.

1.6.1 Laser ablation

In laser ablation, shown schematically in Figure 1(a), an intense laser pulse illuminates a solid target of a precursor (e.g. CaF_2) and heats up the surface to very high temperatures. Ablation products, such as precursor molecules (CaF_2), their fractions (CaF, Ca, F), molecular and atomic ions, clusters, etc., are ejected from the surface into the buffer gas. The particles of interest (CaF in this example) are cooled in collisions with helium buffer gas; other ablation byproducts may also be cooled. If the ratio of density of buffer gas to density of ablation byproducts is sufficiently high, the unwanted byproducts are effectively separated from the molecules of interest by the buffer gas, which prevents rapid recombination and loss of molecules of interest. Spectroscopic measurements can then be done, as long as spectral lines of unwanted byproducts do not interfere with the measurement. If the molecule of interest is the most magnetic of all ablation byproducts, it is retained by the magnetic trap while other byproducts diffuse to the wall where they

are absorbed. Eventually one obtains a trapped sample of the molecule of interest surrounded by buffer gas free of interfering impurities.

Laser ablation works quite well for certain molecules. Stable diatomics that have a solid phase at room temperature (e.g. PbO) are easily produced with laser ablation, with yields of as much as 10^{12} molecules per ablation pulse. For certain radicals (e.g. CaH, CaF), a convenient solid precursor (e.g. CaH_2, CaF_2) may give significant yield as well, $\sim 10^{11} - 10^{13}$ molecules per ablation pulse. Laser ablation is very easy to implement in a cryogenic buffer gas environment. An additional benefit is a nearly-uniform initial spatial distribution of the molecules in the buffer gas cell, see Appendix B.

Laser ablation suffers from some important disadvantages. The most important drawback of the method is unpredictability of its yield. It is essentially impossible to estimate *a priori* the yield of a given byproduct from a given precursor. For many molecules (e.g. O_2), a convenient solid precursor is not available at all. Even when a solid precursor exists and provides significant yields of molecules of interest, presence of unwanted ablation byproducts may result in detrimental effects of varied degree of severity. Many precursors generate dust that covers cell windows, impairing optical access. Clusters, which are often paramagnetic, may act as condensation centers for trapped molecules. Other ablation byproducts may recombine with the molecules of interest, resulting in rapid losses, as discussed further in section 7.4.

1.6.2 Capillary filling

Capillary filling is a technique that is well-suited for stable molecules that remain gaseous at low temperatures, e.g. O_2 or CO [59; 82; 83]. In this method a thin capillary

connects the low-temperature buffer gas cell with a room-temperature gas supply, as shown in Figure 1(b). Molecules are driven into the cell by the supply pressure. The method is simple, but has limited applicability, as only stable molecules with high vapor pressures can survive the trip along a thin cold channel without condensing or recombining. The maximum number of molecules that can be loaded using the method is limited by the requirement to keep flux through the capillary low to prevent clogging.

1.6.3 Beam loading

In order to circumvent the limitations of laser ablation and capillary filling, we have undertaken a development of a novel loading technique, molecular beam loading. In this method, a molecular beam from a room-temperature source is injected into a cryogenic buffer gas cell. The method is very general, as decades of molecular beam research have resulted in an ability to produce molecular beams of virtually any species, including, e.g., unstable molecules. It is possible to "clean up" the beam of any unwanted byproducts by introducing standard electrostatic or magnetic filters. Number of molecules that can be loaded using this method is expected to be quite high; potential limitations are discussed in further chapters.

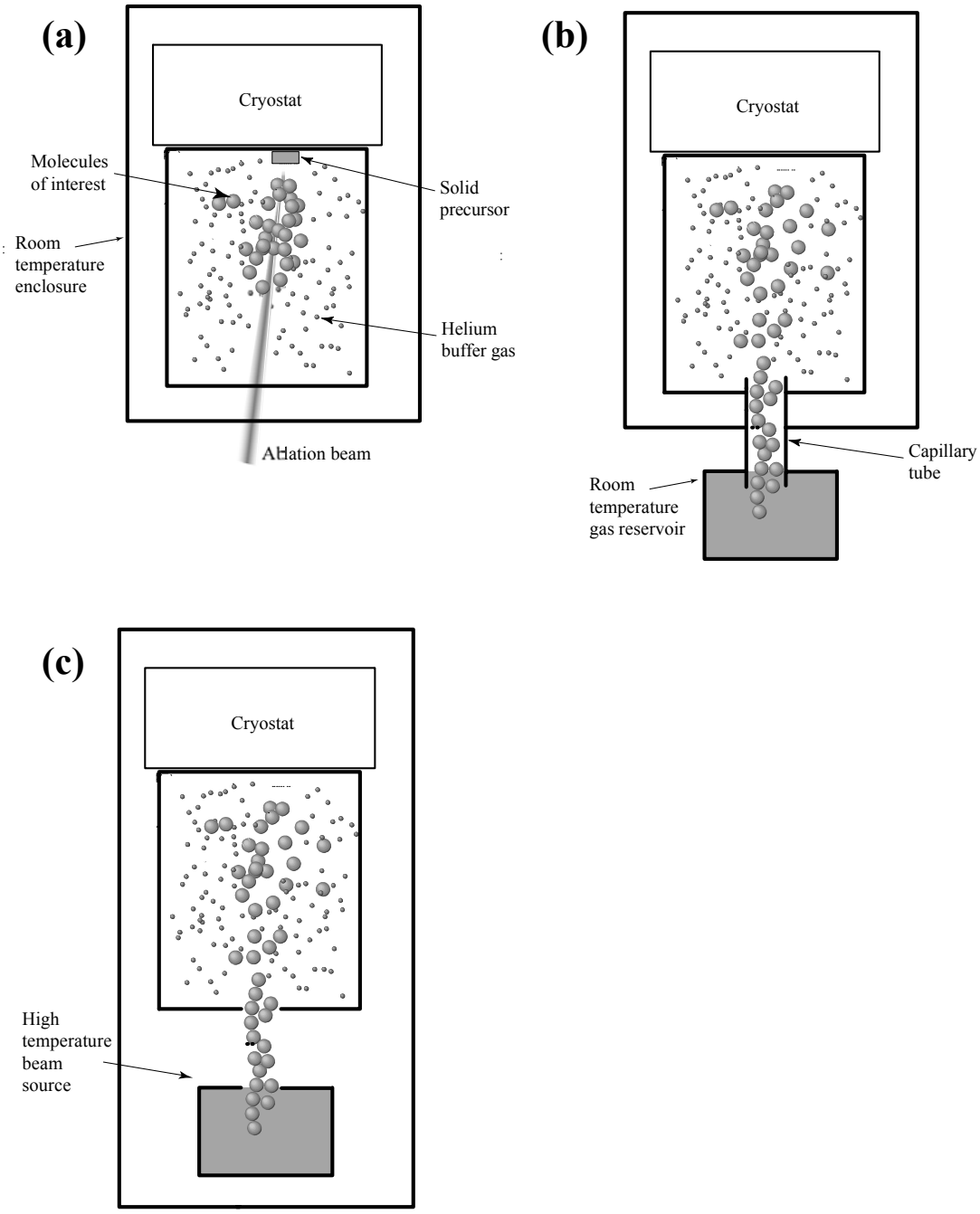

Figure 1: Methods of loading molecules into cryogenic buffer gas cell. (a) laser ablation; (b) capillary filling; (c) beam loading.

2 Buffer-gas cooling of PbO

This chapter describes an experiment on buffer-gas cooling of lead monoxide (PbO) molecules. PbO is an important candidate for the search for the electric dipole moment of the electron, and buffer-gas cooling of PbO offers a possibility to increase the sensitivity of the search by several orders of magnitude.

2.1 Connection between PbO and EDM

Search for the electric dipole moment of the electron (EDM) is one of the most promising approaches to testing of time reversal symmetry, which could uncover the explanation for baryon asymmetry of the universe [29] and evidence of physics beyond

the Standard Model. The current experimental upper bound* on the value of the electron EDM is 4×10^{-27} e·cm (i.e., 1.6×10^{-18} Debye) [85], which, as seen in Figure 2, is already sufficient to narrow the range of theoretical contenders for particle physics beyond the Standard Model. Further improvement in measurement sensitivity has potential for dramatic impact on our understanding of fundamental physics.

* A newer measurement has been published [84] since this chapter was written; the current limit for electron EDM is $1.6\text{x}10^{-27}$ e·cm. Conclusions of this chapter are not affected by this change.

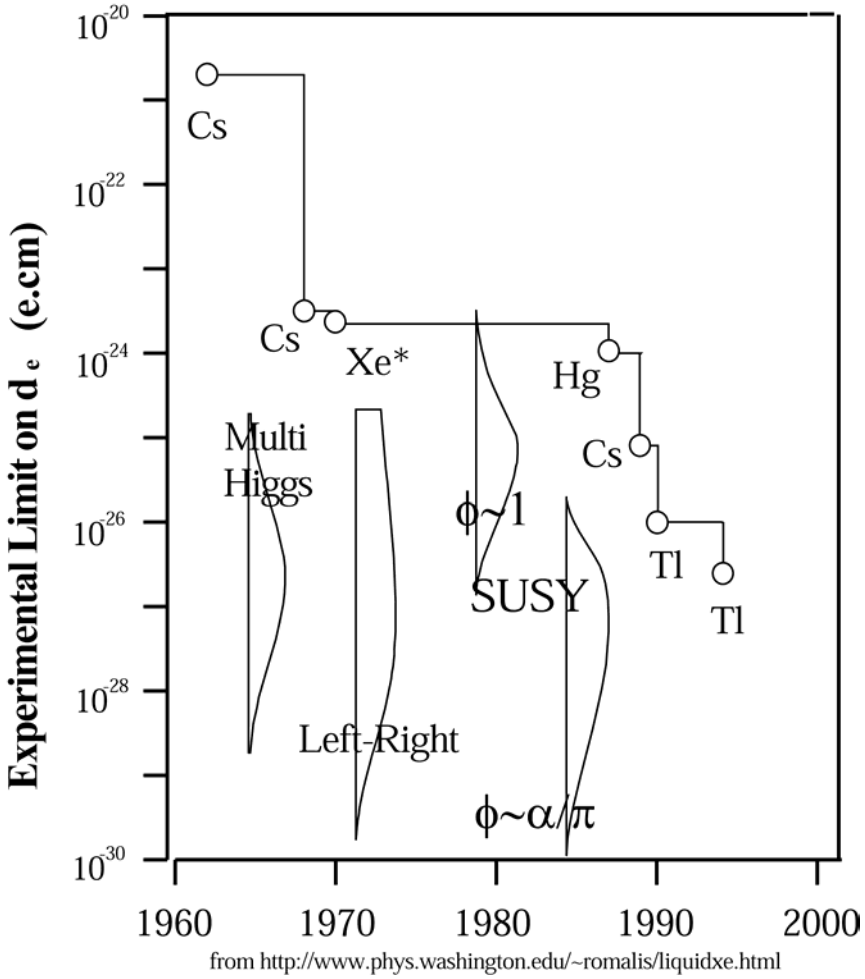

Figure 2: Measurement of electron EDM and physics beyond the Standard Model. Circles indicate measurements with various atomic systems done in corresponding years; shaded areas indicate theoretical predictions from corresponding theories. Note that the experimental limit already approaches the range predicted by the popular supersymmetry (SUSY) theories.

Past EDM experiments have focused on atomic systems (see Figure 2); however, at this point any further improvement of sensitivity in atomic experiments is associated with significant difficulties. Most promising current experimental approaches employ molecules instead of atoms [86; 87].

Inside a molecule containing a high-Z atom, such as YbF [88] or PbO [89], an unpaired electron is subject to a huge effective internal electric field, of the order 10 GV/cm [90; 91] when modest (~10 V/cm) external fields are applied. The internal field can be oriented in the laboratory frame by orienting the molecular axis; the electron spin can be oriented with an external magnetic field. An interferometric technique can then be used to search for tiny frequency shifts associated with reversing the field direction, which would be an indication of a non-zero EDM [87].

The orientation of the molecular axis is characterized by $\langle\cos\theta\rangle$, the expectation value of the cosine of the polar angle θ between the molecular axis and the external electric field. In the EDM search it is desirable to have the largest feasible magnitude for $\langle\cos\theta\rangle$. This can be attained either by making the molecules pendular in a strong field (typically of about 10 kV/cm), or, in the case of symmetric top molecules or equivalent, by exploiting the first-order Stark effect (the requisite field strength can be as low as 1 V/cm). Attainable values of $\langle\cos\theta\rangle$ are particularly large for the low rotational levels. However, in the molecular beam [88] or vapor cell [89] techniques so far used in EDM experiments, the low rotational levels are sparsely populated. Large thermal velocities of the molecules also limit the time available to produce observable interferometric phase shifts. Cooling the molecules could thus greatly enhance the EDM experiment by populating low rotational levels and decreasing thermal velocities.

Production of electric fields inside a buffer gas cell may seem a major challenge. Both in a PbO vapor cell and in helium buffer gas, only low electric fields (of up to about

30 V/cm[†]) can be applied without causing an electric discharge [92]. However, in molecules like PbO, the external electric field required to fully orient the molecule is ~10 V/cm, so the EDM experiment can be, in principle, performed in the buffer gas environment.

In this chapter we present an analysis indicating that the EDM search could be done in the cryogenic cell with either the $a^3\Sigma^+$ or $B^3\Pi_1$ state of PbO. Use of $B^3\Pi_1$ state is connected with fewer uncertainties, but use of the $a^3\Sigma^+$ state would shorten the integration time by between 2 and 3 orders of magnitude compared with the B-state. Nevertheless, reducing the upper bound on the electron's EDM to 10^{-29} $e \cdot cm$ (neglecting systematic considerations) seems within reach even with the B-state[‡].

2.2 Experiment

The experimental setup consists of four main parts: a cryogenic cell with optical access, a liquid helium cryostat to which the cell is anchored, an ablation laser, and a probe laser system. Figure 3 shows the cell along with the ablation and probe laser paths.

[†] amusingly, $T = 4$ K and $n = 10^{16}$ cm^{-3} correspond to the minimum of Paschen law curve for helium; see also section 4.2.1

[‡] assuming cell temperature of 0.5 K, achievable with a ^{3}He refrigerator.

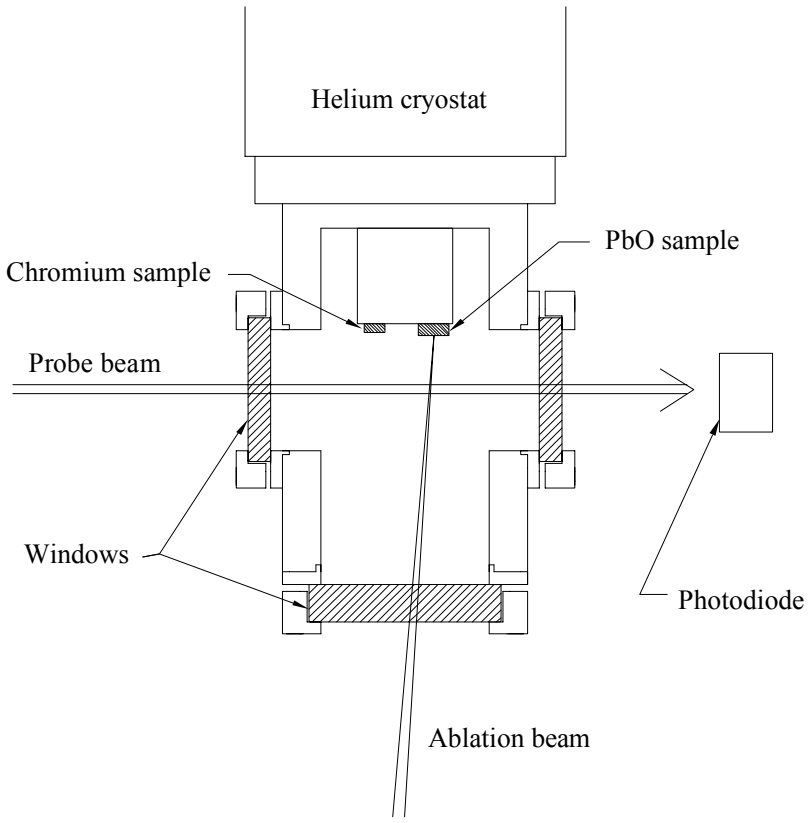

Figure 3: PbO apparatus, schematic view.
Photomultiplier optical access (not shown) is along axis perpendicular to paper plane. Liquid nitrogen vessel and shield not shown.

The cell, made out of brass, is of cylindrical shape with an outer diameter of 6 cm and 10 cm long. It has a five-way optical access through windows made out of BK7. The cell is filled with ^{4}He buffer gas and holds a PbO target (see description of target below). The cell is attached to a liquid helium cryostat that maintains it at 4.2 K. An aluminum shield, equipped with BK7 windows, is connected to a liquid-nitrogen dewar and protects the cryostat and the cell from room-temperature thermal radiation. A stainless steel tube of 2 mm diameter connects the cell with a gas handling system. The number density of

the He buffer gas was maintained in the range between 2-3×10^{16} cm^{-3} by periodically adding gas to the cell's volume (of about 150 cm^3)[§].

The target is ablated with a frequency-doubled Nd:YAG pulsed laser, with a pulse duration of 5 ns and a typical energy of 25 mJ per pulse focused to a waist of about 100 μm, yielding an intensity of about 10^{10} W/cm². The repetition rate of 2.5 Hz was set by performance limits of photomultiplier shutter.

The PbO target is a vacuum hot-pressed disk, about 1 cm in diameter and 3 mm high with the lead and oxygen isotopes present presumably in their natural abundances (see Table 5). Initially, we attempted preparing targets by compressing PbO powder[**] into a brass holder using a manual press at room temperature. Such targets released large amount of dust when ablated, rapidly impairing optical access and necessitating re-aiming at a new spot every ~1000 pulses in order to ensure a steady yield of gaseous PbO. Commercially produced vacuum-hot-pressed targets[††], in contrast, released no visible dust and the ablation yield remained steady over about 10^5-10^6 ablation pulses aimed at the same spot. The yield also remains consistent from spot to spot when the laser was re-aimed.

[§] Helium was "lost" on a timescale of many hours. Based on changes of loss rate with time and pressure changes during ablation we attribute this loss to adsorption by the ablation targets. The helium was released after the cell was warmed up.

[**] Sigma-Aldrich Co.

[††] Sophisticated Alloys Inc., Butler, PA

$X^1\Sigma$ (v"=0)	$^{206}Pb^{16}O$	$^{207}Pb^{16}O$	$^{208}Pb^{16}O$
ω_e	721.2079	721.8023	720.9580
$\omega_e x_e$	3.5185	3.5173	3.5161
B_e	0.30657	0.30646	0.30636
$B^3\Pi_1$ (v'=1)			
ω_e	498.4607	498.37396	498.2880
$\omega_e x_e$	2.1695	2.16875	2.1680
B_e	0.26105	0.26096	0.26087

Table 5: Constants of $^{X}Pb^{16}O$ (in cm^{-1}).

Values for $^{208}Pb^{16}O$ taken from Ref. [93]; values for other isotopic variants of PbO obtained henceforth by mass scaling. The natural abundances of the Pb-isotopes are 23.6%, 22.6%, and 52.3% for ^{206}Pb, ^{207}Pb, and ^{208}Pb, respectively [94].

The ablation pulse creates a plasma cloud in the cell that emits bright broadband[‡‡] glow for tens of milliseconds. The fluorescence detector had to be shielded from this glow (see below). It was noticed with the vacuum hot-pressed sample that when the ablation laser was aimed at a fresh spot the plasma glow was initially very high, but over several thousand pulses it decreased to about 10% of its maximal level and remained steady afterwards. Sometimes, during a measurement, an order of magnitude increase in plasma glow level occurred and disappeared again after several thousand pulses. We

[‡‡] or at least multi-wavelength, as interference filters are not effective at filtering it out

attribute this effect to changes in the surface properties of the sample due to the ablation. The glow intensity also showed some pulse-to-pulse fluctuations. However, the number of PbO molecules detected after each pulse remained steady, with no apparent relation to the level of the glow.

The molecules released into the gas phase by the ablation pulse were probed by laser induced fluorescence excited in the X(v"=0)→B(v') bands at either 441 nm (v'=1) or 432 nm (v'=2) and detected in the B(v')→X(v") bands, either with v'=2, v"=3 at 475 nm or with v'=1, v"=6 at 541 nm.

The probe beam was produced by frequency-doubling the output of an actively stabilized Ti:Sapphire ring laser[§§] in a lithium triborate crystal cavity[***]. The resulting beam with a typical power of 10 mW was acousto-optically amplitude-modulated at 15 kHz, passed horizontally through the central region of the cell, and monitored by a silicon photodiode. A photomultiplier tube (PMT), placed perpendicular to both the ablation and probe beams, was protected from high light levels arising from the ablation pulse and the early plasma glow by a mechanical shutter[†††] and by gating of the PMT base[‡‡‡]. The PMT was exposed to light only during times between 30 ms and 150 ms after the ablation pulse. Since the plasma glow intensity goes down much faster then the density of PbO molecules, opening the gate with the 30 ms delay allowed us to cut down significantly the noise from the background light. Band-pass interference filters in front of the PMT

[§§] Coherent 899-21, pumped with Coherent Innova Ar^+ laser

[***] LAS GmbH., not Delta concept

[†††] JML Optical Industries Inc., SES16490/900 45 mm shutter

[‡‡‡] Products For Research Inc., Danvers, MA

further reduced the background from the glow as well as from the scattered probe beam. The photomultiplier was used in the current mode; its output was fed into a lock-in amplifier. The resulting signal was normalized by the laser power as indicated by the photodiode. Laser-induced fluorescence spectra were measured over a range of 7 cm^{-1} in stretches of 0.3 cm^{-1}. Within each stretch, the laser was scanned in steps of 20 MHz. In order to determine the line-broadening profile, the step size was reduced to 10 MHz. The probe-laser frequency was measured with a wavemeter[§§§]. As absorption of PbO was below the detectable limit, PbO fluorescence collection was calibrated using chromium atoms as a standard[****]. A chromium sample, also placed in the cell, was ablated and the signal from $^7S_3 \rightarrow {}^7P_3$ transition at 427 nm was observed in both absorption and fluorescence [75]. Light collection efficiency was then extracted, adjusted for filter transmission and PMT sensitivity variations, and used to convert PbO fluorescence signal into absolute numbers of molecules.

[§§§] Burleigh W-20

[****] Chromium is a convenient standard because the transition is strong, ablation yields are large, and wavelength of the transition is close to that of PbO.

2.3 Results

Figure 4 shows the fluorescence spectra excited in the X(v"=0)→B(v'=1) band at 441 nm and detected in the B(v'=1)→ X(v"=6) band at 541 nm. The shaded bars show the measured spectrum. The width of the bars represents the error in determining the transition frequency (about ±1 GHz); The error in determining the relative line intensity was about ±30%. The dark-shaded bars correspond to data obtained under different experimental conditions than the rest. The inaccuracies arise predominantly from the manual scan of the probe laser and the corresponding lack of control of its frequency. The accuracy of our spectroscopic measurements could be dramatically improved by scanning the laser continuously, as was done in our earlier work [58]. Also shown is a simulated spectrum based on molecular constants of Ref. [93], summarized in Table 5. The lines in the calculated spectrum are represented by Gaussians whose positions and heights correspond to the energies,

$$(E'-E'')/hc\,,$$

and intensities,

$$I_{J''} = w_{J''} S_{J''\to J'},$$

with $S_{J''\to J'}$ the line strengths [31] and

$$w_{J''} = (2J''+1)\exp(-J''(J''+1)B_e''/kT)/Q$$

the Boltzmann factors; here Q is the rotational partition function, k the Boltzmann constant, and T the temperature.

The width of the lines (FWHM) was measured to be 80±20 MHz, which is consistent with a Doppler broadening at a translational temperature of 4±1 K. From the intensity distribution of the lines the rotational temperature was determined to be likewise 4±1 K. The molecules were found to thermalize with the buffer gas on a time scale of less than 30 ms. Adding buffer gas into the cell was found to extend the lifetime of the PbO molecules, indicating a diffusion-limited loss process [78].

The simulated spectrum agrees well with the measured one and provides an assignment of the observed transitions. The $^{207}Pb^{16}O$ isotope possesses a hyperfine structure due to the magnetic dipole moment of the ^{207}Pb nucleus [94]. This was not resolved in the spectrum and was omitted from the simulation. As can be seen in Figure 4, the bandhead region of the spectrum is solely due to an R-branch, which is followed by a sparse Q-branch toward longer wavelengths. Also several P-branch transitions were detected. The most populated rotational state is the one with $J''=2$. All the transitions occur in "triplets," due to the presence of the three isotopic variants of PbO; it is the different vibrational frequencies that are mainly responsible for the observed frequency shifts within a given "triplet." The assignment of the lines in the spectrum according to the isotopic variant of PbO is also indicated. In the spectral range covered (7 cm^{-1}) all transitions were found to be due to the B-X band of the PbO molecule only. With the aid of a calibration based on the absorption and fluorescence of laser-ablated Cr atoms, we determined the number of the thermalized PbO molecules following a single ablation pulse to be $N = 10^{12}$.

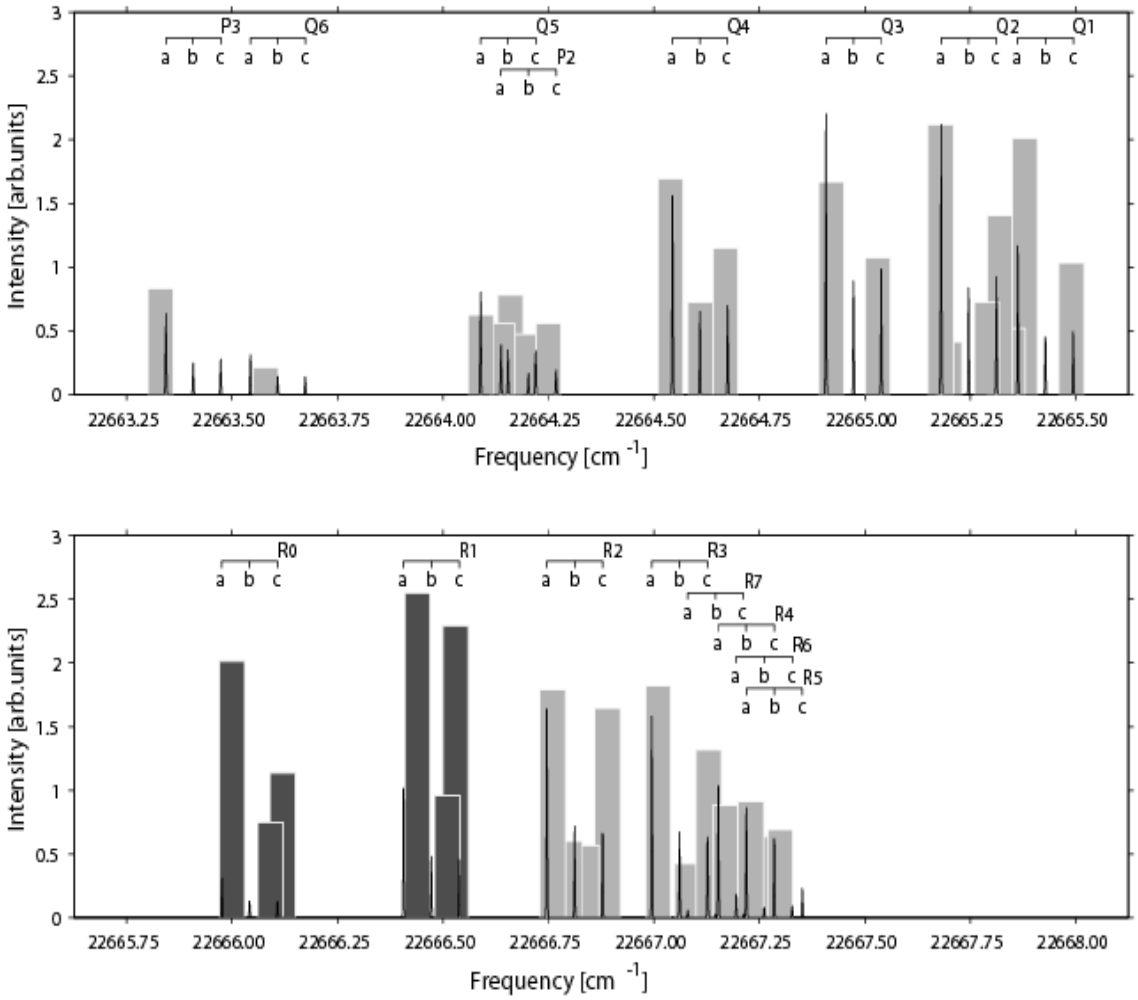

Figure 4: Measured PbO spectrum.

The fluorescence spectrum excited in the X(v''=0)→ B(v'=1) band at 441 nm and detected in the B(v'=1) →X(v''=6) band at 541 nm. Shaded bars show the measured spectrum, the Gaussians the simulation. Transitions due to $^{208}Pb^{16}O$, $^{207}Pb^{16}O$, and $^{206}Pb^{16}O$, are labeled as "a", "b", and "c", respectively. Laser frequency scale is the wavemeter reading.

2.4 Discussion

Based on these results, the prospects of using buffer-gas cooled PbO in the EDM search are promising. From the measured diffusion lifetime of the molecules in the cell, we estimate the mean time between collisions with helium in the buffer gas (at helium number density $n \approx 10^{16}$ cm^{-3} and temperature $T \approx 4$ K) to be ~ 1 μs. If collisions with the He atoms in fact limit the coherence time of the EDM measurement to a microsecond timescale, then there may be no appreciable disadvantage to using the B-state of PbO whose radiative lifetime has been measured to be $\tau_B = 3$ μs [89]. For the actual EDM experiment it should be possible to set up the necessary coherent superposition of molecular spin states in less than a microsecond using pulsed excitation [87]. However, since spin decoherence may require many collisions, it is possible that the $a^3\Sigma^+$-state (with a natural lifetime $\tau_a = 80$ μs [89]), singled out for the vapor cell experiment by DeMille et al. [89], may also be usable in the buffer-gas cell. The B-state is a $^3\Pi_1$ state with a small Ω doubling [93]; its symmetric top states with J, M, and Ω all nonzero can be oriented by an electric field of a few V/cm [95]. The internal electric field within the PbO $B^3\Pi_1$ molecule can be expected to be similar to the one in PbO $a^3\Sigma^+$, calculated to be ~6 GV/cm[89]. The electric breakdown in the buffer gas cell is likely to occur at an electric field of about 30 V/cm [92], much greater than what's needed for field orientation.

We now evaluate the statistical sensitivity of the EDM measurement. We follow the analysis (and use most of the notation) of DeMille et al. [89]. For either the a- or B-

state, we assume R(J"=0) to be the probed rotational transition. We begin by considering the photon count rate for the experiment. Once a PbO molecule is excited, it will likely decay to a different vibrational level, and cross-sections for vibrational relaxation at ≈1 K are typically extremely small [66; 78]. Because of this, we assume that each PbO molecule can only be excited once in the proposed experiment. Our photon count rate R is thus limited to

$$R = \varepsilon_e \varepsilon_d \dot{N}_0 \tag{5}$$

where ε_e and ε_d are excitation and detection efficiencies and $\dot{N}_0$ is the rate at which ground state molecules are produced. The ground-state production rate is given by

$$\dot{N}_0 = w_0 \dot{N} \tag{6}$$

where $\dot{N}$ is the total production rate of the molecules and w_0 the population of the ground rotational state. Since

$$w_0 = Q^{-1} \approx B_e'' / kT \tag{7}$$

which is a good approximation down to $kT \approx B_e''$, we have

$$R = \varepsilon_e \, \varepsilon_d \, \dot{N} \, B_e'' / kT \tag{8}$$

Due to the large oscillator strength of the B↔X transition, it should be straightforward to achieve $\varepsilon_e \approx 1$ with standard pulsed laser systems. Assuming $\varepsilon_d \approx 0.1$ and $\dot{N} \approx 10^{15}\,\mathrm{Hz}$, we finally have $R \approx 10^{14}\,\mathrm{Hz}$ at 0.5 K. The photon count rate for the a-state may be somewhat lower, due to the reduced oscillator strength of the a↔X transition. However, for the same photon scattering rate, the attainable energy resolution, $\delta(\Delta E)$, should be higher for the a-state since

$$\delta(\Delta E) = \frac{\hbar}{\tau\sqrt{t\,R}} \tag{9}$$

where t is the integration time (i.e., time of the measurement). The nomogram of Figure 5 shows the values of the integration time and of the product $\tau^2 R$ that are required in order to attain a given statistical sensitivity for a given upper bound on d_e, the electron's EDM. Here we assume

$$\Delta E = \left| d_e\, \varepsilon_{eff} \right| \tag{10}$$

with ε_{eff} = 6 GV/cm, the effective electric field strength inside the molecule, and take $R \approx 10^{14}$ Hz.

The arrows on the upper abscissa indicate the values of the $\tau^2 R$ product for the a- and B-states of PbO at a cell temperature of 0.5 K. Although the integration times are about 2-3 orders of magnitude greater for the measurements with the B-state compared with the a-state, reaching $\delta(d_e)$ of 10^{-29} e·cm with the B state could be feasible for one day of integration, yielding a hundred-fold improvement over the current value of statistical sensitivity of the EDM measurement.

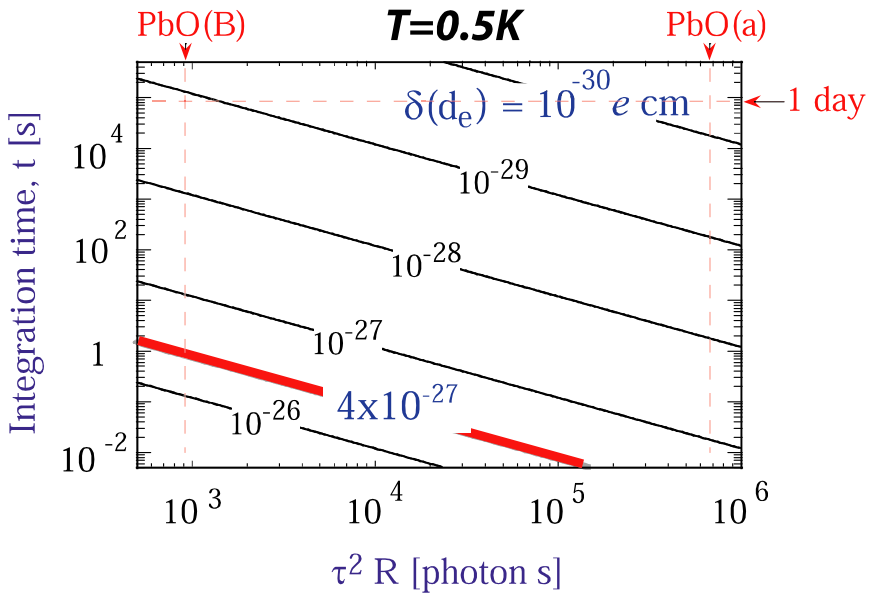

Figure 5: Nomogram for values of integration time required to attain a given statistical sensitivity $\delta(d_e)$ for a given upper bound on electron EDM.

The arrows on the upper abscissa indicate the values of the $\tau^2 R$ product for the $a^3\Sigma^+$ and $B^3\Pi_1$ states of PbO at a cell temperature of 0.5 K. Also indicated with a gray line is the value of the upper limit on d_e from Ref. [85].

3 Beam loading of buffer gas: the Rb experiment

This chapter describes a proof-of-principle experiment that demonstrates loading of a cryogenic buffer-gas cell at 4.2 K with a beam of rubidium atoms and thermalization of the atoms with the buffer-gas. The beam loading method offers a number of advantages over laser ablation or capillary filling:

(1) It is versatile - atomic and molecular beam sources for a variety of atoms and molecules, including radicals, metastable species and room-temperature solids, are available [96],[97];

(2) Fluxes as large as 10^{15} s^{-1} entering the cell can be expected from high-intensity beam sources, potentially leading to trapping of $>10^{14}$ molecules (or atoms) using buffer-gas trapping techniques [58];

(3) Beam sources make it possible to eliminate or control the formation of clusters or other unwanted species;

(4) For many gases and low-melting point solids, sources are simple in design and inexpensive;

(5) Multiple sources can be operated so as to introduce a combination of species into the buffer gas.

3.1 Experimental setup

The apparatus, shown in Figure 6, consists of two main parts, one cryogenic and one at high temperature. These are interfaced via a gate valve. The cryogenic part is based on a small liquid helium cryostat with a 1.2 liter helium bath[*]. A cylindrical brass cryocell[†] is thermally anchored to the liquid helium bath. The cryocell is 10 cm long, and has an outer diameter of 6 cm and an internal volume $V = 150$ cm³. The side of the cell facing the interface gate valve has a thin replaceable front cover, made of copper, mounted on an indium seal. The front cover has a circular orifice (cell orifice) the diameter of which can be varied from 0 up to 3 mm[‡]. A molecular beam[§] enters the cell through this orifice. At the same time, helium buffer gas streams out through the cell orifice. A heat exchanger, made out of copper tubing 1.7 mm inner diameter, 50 cm long is mounted on the cryostat cold plate. The outlet of the heat exchanger is connected to the cell; the inlet (at room temperature) to an external gas handling system via a 1.1 mm

[*] HDL-5, Infrared Laboratories, Tucson, AZ

[†] Nearly identical to the cell described in Chapter 2.

[‡] By replacing the entire front cover with a different one, of course. So far we weren't able to come up with a design where orifice diameter can be changed without taking the apparatus apart.

[§] Following physical chemistry convention, we refer to beams of both atoms and molecules as "molecular beams".

inner diameter stainless steel tube. The gas handling system supplies helium gas[**] at an adjustable steady rate such that the helium pressure in the cell remains constant, balanced by the helium leaving through the cell orifice[††]. The heat exchanger ensures that helium gas entering the cell has the temperature of the liquid helium bath. The cryocell is equipped with a pair of windows which enable optical access to a cell region. The temperature of the cell is monitored by silicon diode thermometers[‡‡].

The pressure in the cell is monitored by a Pirani gauge[§§] connected to the cell via a straight stainless steel tube, 45 cm long and of a 1.9 mm inner diameter. The gauge is at room temperature, so a difference between the pressure reading and the actual pressure in the cryogenic cell can exist. This difference, known as transpiration or thermo-molecular effect, has been studied for certain types of tubes, e.g. see Ref. [98]; the exact ratio depends on both the geometry and surface condition of the tubing used, and it is difficult to predict its value accurately for a realistic experimental setup. In addition, helium gas flow may affect the pressure reading. In order to remove any uncertainties, we performed a number of measurements, such as drop of pressure in known-volume gas supply vessel and pressure measurements for different orifice openings with a ruthenium oxide

[**] Matheson Tri-Gas Inc., 99.999% purity

[††] see section 5.3.2 for more discussion

[‡‡] Uncalibrated DT-470-SD-13 and calibrated DT-470-CU-1.4B; Lakeshore Cryotronics Inc., Columbus, OH

[§§] Grainville-Phillips Convectron 250, Helix Technology Corp., Longmont, CO

sensor[***] suspended inside the cell, we established that these effects fall within the absolute calibration uncertainty of the pressure gauge, and have no effect on its relative accuracy.

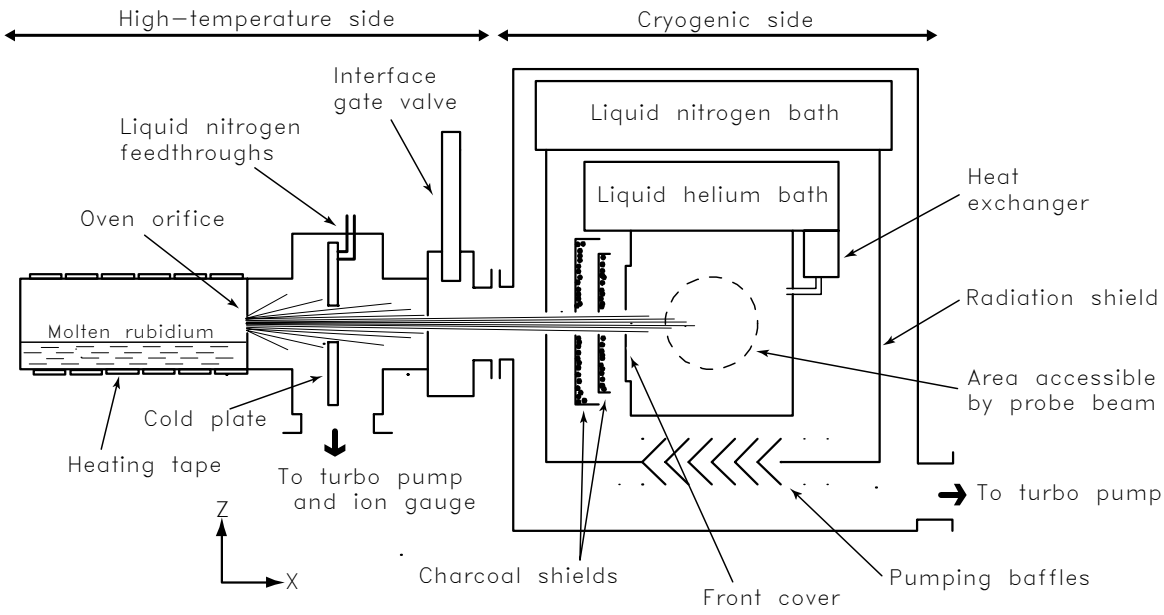

Figure 6: Rb apparatus, schematic view.
Diameter of the oven orifice is 3.9 mm; diameter of the orifice in the cell front cover was varied between 0 and 3 mm; distance between oven orifice and cell orifice is 25 cm.

The liquid helium bath and the cell are surrounded by a stainless steel radiation shield connected to a liquid nitrogen bath. Two "charcoal shields", thin copper cups with 20/40 mesh coconut[†††] activated charcoal[‡‡‡] attached to copper by epoxy[§§§], are placed

[***] Bare-chip RX-102A-BR from Lakeshore Cryotronics excited by current between 10 μA and 1 mA; at high currents the indicated resistance is pressure-dependent due to heat dissipation into buffer gas.

[†††] an important detail, see [99; 100]

between the cell orifice and the liquid nitrogen shield to pump the He which leaks out from the cell orifice. The inner charcoal shield is thermally linked to the cell, and the outer charcoal shield is thermally to the liquid helium bath. Most of the helium atoms leaving the cell are pumped by the inner shield and thus cannot reach the liquid-nitrogen radiation shield. Those that do are likely to hit the outer charcoal shield after they bounce back from the liquid nitrogen shield. The heat imparted to the He atoms by the liquid-nitrogen shield is then deposited in the liquid helium bath and does not increase the temperature of the cryocell. Charcoal saturation can be a problem for very high helium flow rates, so resistive heaters are placed on the shields to "regenerate" the charcoal if necessary. Under typical operating conditions, saturation does not occur for many hours, as expected from published data on charcoal cryopumping properties [99]. When saturation occurs, the shields quickly overheat and self-regenerate, so the system is back in operation within minutes.

While charcoal cryopumping is effective in preventing heating of the cryocell, the probability of a helium atom sticking to charcoal in a single collision is less than unity[****]. Therefore, some atoms will bounce off the shields multiple times and eventually reach regions of the cell that are not protected by the charcoal shields, where they will cause rapid heating. Due to design constraints, it was not practical to increase the charcoal coverage area. Instead, we enhanced the system's pumping speed with a

---

[‡‡‡] Supelco #10275, Sigma-Aldrich Corp., St. Louis, MO

[§§§] Stycast 2850FT, Emerson & Cuming, Billerica, MA; attempts to use Stycast 1266 failed miserably.

[****] Ref. [101] quotes the value of 25%

turbomolecular pump. The bottom of the radiation shield is fitted with optically opaque chevron baffles[††††], which allow helium gas to pass through but block room-temperature radiation[‡‡‡‡]. The total estimated pumping speed from the turbopump-based part of the system is 100 L/s. We found that, even with no optimization of the charcoal shield or baffle designs, the thermal load due to a typical buffer gas flow was constrained to under 2 mW, which is acceptable for a 4.2 K setup. Our simple design is not limited to liquid helium temperatures, however: in a pumped ^{4}He or ^{3}He system, the cryocell could be protected with an additional radiation shield kept at 4.2 K. Since helium atoms would bounce back from a lower-temperature surface, heat loads would be dramatically reduced, allowing very low temperature operation.

The high-temperature part of the apparatus consists of an oven and a collimation chamber. The front wall of the oven has a 3.9 mm diameter orifice. The distance between the orifice and the front of the cryocell is 25 cm. The oven is loaded with rubidium[§§§§], and heated up to about 350°C (measured by thermocouples) with high-temperature heating tape[*****]. Despite our efforts to ensure uniform tape coverage and aluminum foil

---

[††††] See [102] for design considerations and pumping speed calculations

[‡‡‡‡] To reduce radiative heat load onto the 4 K cell from both room temperature and 77 K shield, the surfaces facing room temperature are painted black with Krylon #1601 ultra-flat black paint, and surfaces facing the cryocell are covered with aluminum foil tape. For Krylon paint IR reflectivity data, see [103] or [104]. Krylon Brown primer should be used on copper to achieve adhesion that can withstand temperature cycles to 77 K; Krylon Gray primer or no primer will cause the paint to peel off.

[§§§§] 99.75% metals basis, Alfa Aesar, Ward Hill, MA

[*****] Omega Engineering Co.

wrapping, the temperature of the oven is non-uniform, with measured temperature differentials between different surface points of up to 30°C. We used the reading of the thermocouple closest to the oven orifice as the nominal oven temperature. The typical load of Rb is 5 gram per run; we note that since we use less than 10^{-3} sr of the beam, a recirculating source [105] might have been a better choice for long-term operation.

The collimation chamber, located between the oven and the interface gate valve, is fitted with a connection to a turbo pump and a liquid-nitrogen cooled (to ~160 K) condenser plate placed about 6 cm downstream from oven orifice. The plate has an 8 mm diameter aperture to collimate the beam. As the flux of the atoms out of the oven increases with increasing temperature, the pressure in the chamber rises above 10^{-4} mbar[†††††]. We did not observe any reduction of the beam flux into the cryocell due to high background pressure in the chamber. The condenser plate in the collimation chamber was implemented because rubidium reacts violently with water, and thus it is necessary for practical reasons to minimize rubidium accumulation inside the cryostat. For other species the condenser plate would not be necessary

We note that in the case of a 650 K oven coupled to a 4 K cryostat, thermal radiation propagating from the oven along the beam path does not represent a significant source of heating. However, if a lower loading temperature is desired and a ^{3}He cryostat or a dilution refrigerator has to be used, or in the case of significantly higher oven temperatures, heating by thermal radiation can no longer be neglected. A solution would be to use a pair of cooled "chopper" disks with non-overlapping slits that allow the

[†††††] the upper limit of our ion gauge

molecular beam pulses to pass through, but completely block the co-propagating thermal radiation.

We measured the temperature and density of the Rb atoms in the cell using $5^2S_{1/2}(F=2) \rightarrow 5^2P_{3/2}(F'=1,2,3)$ hyperfine transitions of the strong D_2 absorption line of ^{87}Rb (natural abundance of 27%) at 780 nm. The separations of these lines are the largest among the four D_2 hyperfine triplets of both Rb isotopes [106], thus the overlap of Doppler-broadened lines at 4.2 K is avoided. The natural linewidth of the transitions of about 6 MHz is about a factor of 10 smaller than the 4.2 K Doppler broadening; translational temperature of the Rb atoms can be accurately determined from fitting the measured line profiles to Voigt line shapes. Our laser source has a typical linewidth of 1 MHz and a Gaussian intensity profile with a 0.9 mm e^{-2} width. The laser beam is split between a single-mode fiber transmitting several micro-Watt to the cryocell, a wavemeter, and a saturation absorption setup used for calibrating both the wavelength and the optical density [107]. The cryostat is fitted with a platform which consists of a fiber out-coupler and a photodiode mounted on an X-Z translation stage (X is the direction of the Rb beam, Y the direction of the probe laser beam). This allows the probe beam to address points inside the cell anywhere within the 30 mm diameter cell window. The laser frequency can be scanned over 1 GHz using external voltage control. The photodiode signal was averaged typically over 30 scans per data point. Baseline subtraction was accomplished by blocking the Rb beam. The sensitivity of the absorption measurement was better than 10^{-3}.

3.2 Results

In order to test and characterize the beam loading technique, we carried out a series of experiments in which we determined the effects of buffer-gas density and oven temperature (molecular beam flux) on the Rb number density. We also measured the spatial density distribution of Rb throughout the cryocell and determined the temperature of the Rb atoms within the cell. The results of these experiments are described and discussed below.

3.2.1 Effect of buffer-gas density

The loading process is sensitive to the density of the buffer gas. If the density is too low, the molecular beam will not be thermalized. If the density is too high, the molecules[‡‡‡‡‡] will thermalize too close to the cell entrance and a significant fraction of them will hit the inside of the cell front cover, stick to it, and be lost. Also, the buffer gas emerging from the cell will scatter the incoming molecules and thus decrease their flow into the cell. *A priori* it was not clear whether an optimum balance (when the majority of Rb atoms within the solid angle of the entrance orifice enter the cell) could be achieved. Therefore, we first established the dependence of the number density of the Rb atoms loaded into the buffer-gas cell on the buffer gas density. The results are presented in Figure 7. Absorption signal, proportional to the Rb number density, was measured at the

[‡‡‡‡‡] we use "molecules" when referring to particles in the molecular beam, even when the particles are mono-atomic

center of the cell. At very low buffer gas densities (or with no buffer gas), the absorption signal is strong, due to the collimated and unattenuated Rb-beam inside the cell; the signal drops rapidly as the probe beam is moved away from the cell center along the Z direction. Data points corresponding to such low buffer-gas densities are excluded from Figure 7, since in that case no thermalization with the buffer gas takes place. All the data points shown correspond to full thermalization of the Rb atoms (see below). As seen in Figure 7, the Rb density first sharply increases, reaches a maximum at about $n_{He} \approx 1.2\times10^{16}$ cm^{-3}, and levels off with increasing n_{He}. This distinctive behavior can be accounted for by a simple gas-kinetic model, used to fit the data in Figure 7.

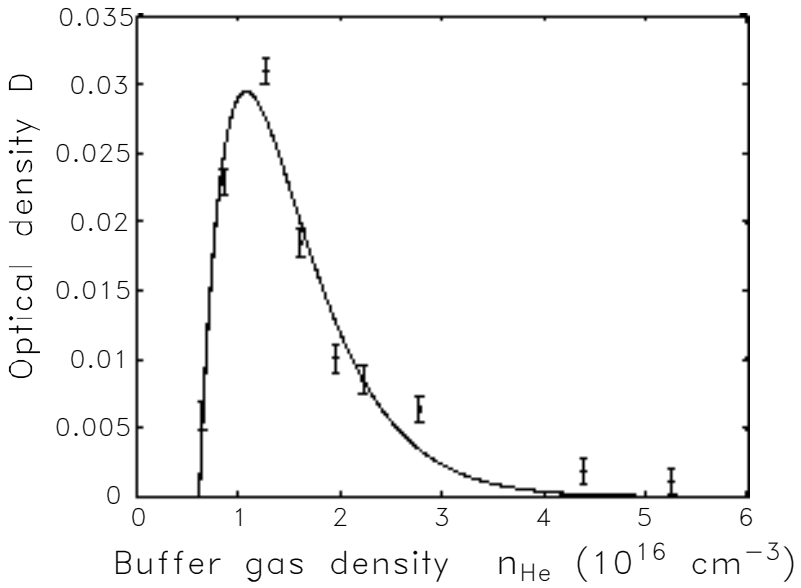

Figure 7: Effect of buffer gas density on Rb beam loading.
Observed optical density of Rb atoms at the center of the cell held at a temperature of 4.3±0.1 K as a function of buffer-gas density. All data points correspond to a complete thermalization. From the best fit of Eq. (17) (line) the optimal buffer-gas density for our cell configuration is 1.2×10^{16} cm^{-3}, with an uncertainty of about 30%. The maximum total number of cold Rb atoms achieved was 1×10^{12}.

For an effusive flow from a uniformly heated oven at a temperature T_0, the flux is

$$\Phi_0 = \frac{1}{4} n_0 v_0 A_0 \tag{11}$$

with n_0 the Rb number density in the oven, $v_0 = \sqrt{8k_B T_0 / (\pi M)}$ the average Rb velocity, M the Rb mass, and A_0 the oven orifice surface area. Most of the flux is cryopumped away, except for a fraction that passes through the condenser plate aperture to form a Rb-beam directed toward the cryocell. In the absence of the buffer gas, the Rb-beam intensity, I_0, intercepted by the cell's entrance aperture is

$$I_0 \approx \frac{\Phi_0}{2\pi L^2} \tag{12}$$

where L is the distance between the oven orifice and the cell aperture. In the presence of the He-buffer gas, there is a steady flow of He out of the cell towards the collimation chamber. This flow results in an average He-number density, $\overline{n}_{He}$, inside the region shielded by the charcoal cups (and possibly beyond) which attenuates the Rb beam by a factor $\exp[-\overline{n}_{He}\Lambda\sigma]$, with Λ the effective length over which scattering occurs, and σ the Rb-He scattering cross section. As a result, the Rb- beam intensity that reaches the cell is reduced to

$$I_c = I_0 \exp[-\overline{n}_{He}\Lambda\sigma] \tag{13}$$

yielding a number density $n_c = I_c / v_0$ at the cell entrance. The values of $\overline{n}_{He}$ and Λ depend on the He flow, the pumping speed, and the geometry of the cell. In general, we assume that Λ is constant, and that $\overline{n}_{He} = B\, n_{He}$, with B a proportionality constant.

The number of thermalized Rb atoms inside the cryogenic cell, N_{Rb}, is given by the flux of the Rb atoms into the cell, $\dot{N}_{in} = I_c A_c$ (with A_c the cell aperture surface area) and the diffusion time τ to the cell walls,

$$N_{Rb} = \dot{N}_{in}\,\tau \tag{14}$$

Using the expression for the diffusion time

$$\tau \approx \frac{3V^{2/3}\sigma\, n_{He}}{v_0} \tag{15}$$

where V is the volume if the cell, the Rb number inside the cell becomes

$$N_{Rb} = A\, n_{He} \exp[-B\, n_{He}\Lambda\sigma] \tag{16}$$

with $A \equiv 3A_c\, I_0\, V^{2/3}\sigma / v_0$. The functional form of Eq. (16) was fitted to the measured optical density, $D \propto \bar{n}_{Rb} \propto N_{Rb}/V$. The actual functional form used was

$$D = a\,(n_{He} - c)\,\exp[-b\,(n_{He} - c)] \tag{17}$$

The solid line in Figure 7 corresponds to the fitting parameters a=0.174, b=2.17, c=0.61, with n_{He} in units of 10^{16} cm^{-3}. Despite the simplifications of the model the best fit reproduces the main features of the observed data well. It reaches a maximum at $n_{He}^{\max} = b^{-1} + c$ corresponding to $n_{He}^{\max} = 1.2\times10^{16}$ cm^{-3}. The value for c is larger than could be explained by an offset in the absolute reading of the pressure gauge; however, the model does not attempt to accurately describe the low buffer-gas density, long mean free path regime. The value of b corresponds to $n_{He}/\bar{n}_{He}$, assuming Λ = 1 cm and σ = 100 Å^2, which is consistent with estimates for pumping speed for He within the region shielded by the charcoal cups.

3.2.2 Effect of oven temperature

We also established the dependence of the number density of the Rb atoms loaded into the buffer gas on the oven temperature. The results are presented in Figure 8 for a buffer gas number density of 1.5×10^{16} cm^{-3} and a cell temperature of 4.2 K.

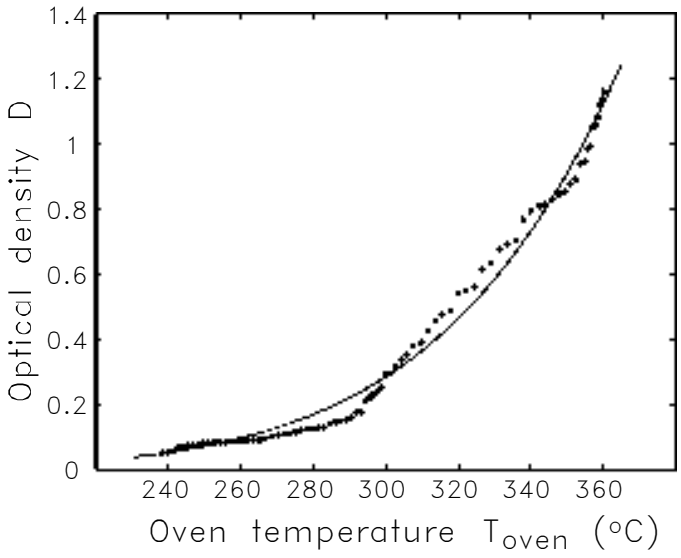

Figure 8: Rb signal dependence on oven temperature.
Optical density of Rb atoms at the center of the cryogenic cell as a function of oven temperature. The cell temperature was 4.5±0.5 K, buffer gas density 1.5×10^{16} cm^{-3}. The data was taken while the oven was slowly cooling down at a rate of about 0.1°C/s, to reduce any effects due to non-uniform temperature distribution.

The beam is not purely effusive[§§§§§] at the higher end of the temperature range used; e.g., at 368°C, the saturated vapor pressure of Rb is 10 mbar [108], which is too high for an effusive source with a mm-scale orifice diameter. However, the measured

[§§§§§] i.e. partially hydrodynamic; see [97] and [96] for a detailed discussion

optical density $D \propto n_{Rb}$, which is proportional to the incoming flux, Eq. (14), can still be well fitted by

$$D(T_0) = \alpha \frac{P_{T_0+T'}}{\sqrt{T_0 + T'}} \tag{18}$$

where $P_{T_0+T'}$ is the Rb vapor pressure inside the oven as a function of the effective oven temperature $T_0 + T'$, with the coefficient of proportionality $\alpha = 2.5\sqrt{\text{K}}/\text{torr}$. The value of the fitting parameter T' = 26 K suggests that the effective oven temperature is 26 K larger than the temperature indicated by the thermocouple. Initially, we expected to reach temperatures at which the flux in the forward direction stops increasing with increasing temperature, due to broadening of the angular distribution of the beam and due to cluster formation. However, we do not observe this effect up to the maximum oven temperature of 360°C. This indicates that the Rb atom flux could be further increased by increasing the oven temperature. We also did not observe any effects of the oven temperature or of the atom flux on the loading or thermalization efficiency.

3.2.3 Thermalization

Rubidium thermalization was determined from the measured absorption lineshapes. Figure 9 shows sample spectra of rubidium in the cell with and without buffer gas. Several effects contribute to the total linewidth, such as pressure, intensity, and Doppler broadening.

The relation between the Doppler broadening and the Rb temperature is dramatically different for atoms in the beam and in the buffer gas. In the case of the beam

atoms, the observed broadening is a measure of the transverse velocity, which can be smaller than the longitudinal velocity by a factor of several hundred, due to beam collimation. On the other hand, for the Rb atoms in the buffer-gas cell, the Doppler broadening is in fact an accurate measure of the atoms' temperature, since the directions of their velocity vectors are randomized. As shown in Figure 9, without the buffer gas, the Rb beam, collimated to about 30 mrad, yields a nearly natural linewidth, corresponding to a sub-Kelvin transverse energy spread. As the buffer gas density is increased, the beam becomes spatially dispersed, the (still fast) atoms no longer move in the same direction and so the observed linewidth rapidly increases. At the same time, the absorption signal drops, due to a decrease of Rb number density in the probe region. As the buffer gas density is further increased, the absorption signal begins to reappear, due to an increase of the diffusion time of Rb in the buffer gas. The linewidth narrows, reflecting the onset of thermalization. The linewidth approaches the value corresponding to the cell temperature at a buffer gas number density of about 10^{16} cm^{-3}, and maintains this value at larger densities.

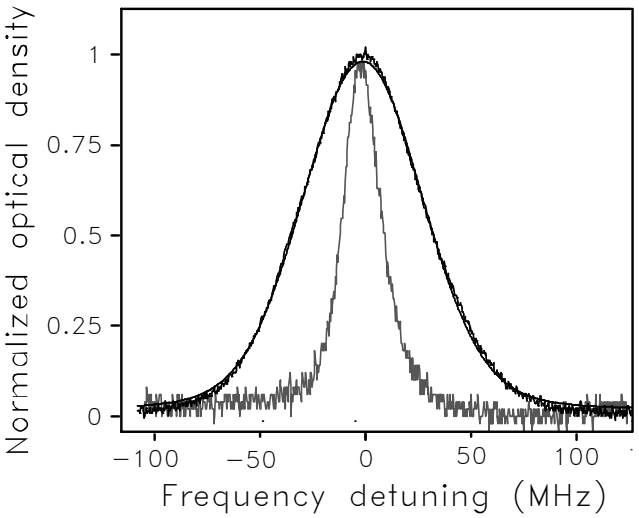

Figure 9: Rb spectrum and translational temperature fit.
Absorption line profile of rubidium inside the cell with (dark trace) and without (light trace) buffer gas. From the best fit of Voigt profile (thin line) the Rb temperature was determined to be 4.5±0.3 K. The cell temperature was 4.3±0.1 K, buffer gas density 1.5×10^{16} cm^{-3}, oven temperature 270±10 °C

In fitting the measured lineshapes to Voigt profiles, we fixed the contributions from homogeneous broadening sources. This allowed us to extract the Doppler width and the temperature with a better accuracy. The pressure broadening was taken from the data in Ref. [109], the natural linewidth was taken from Ref. [107]. Moreover, since only a narrow range of buffer gas densities, between 7×10^{15} cm^{-3} and 3×10^{16} cm^{-3}, leads to absorption signals large enough to make accurate fits, we did not observe any increase in pressure broadening over this range. The Rb temperature obtained from the fit of the data of Figure 9 is 4.5±0.3 K, close to the measured cell temperature of 4.3±0.1 K. This data was taken at a buffer-gas density of 1.5×10^{16} cm^{-3}, and oven temperature of 270±10 °C. The Rb temperature across the field of view was uniform, consistent with conclusions from our Monte Carlo simulations and the model below.

The thermalization process can be modelled by assuming elastic collisions between two point masses, m (^{4}He buffer-gas atom) and M (species-to-be-cooled, i.e. ^{87}Rb in our case) [58]. From energy and momentum conservation in a hard-sphere model, after thermal averaging the difference ΔT in temperature of the Rb atom before and after a collision with the He atom is given by ΔT=-(T_i-T)/κ, with T the temperature of the buffer gas, T_i the kinetic energy of the Rb atom before the collision divided by Boltzmann constant, and $\kappa \equiv (M+m)^2/(2Mm) \approx 12$. The temperature T_N corresponding to Rb atoms, which had been at initial temperature T_0 and underwent N collisions each with the buffer gas atoms, is

$$T_N \approx (T_0 - T)\exp[-N/\kappa] + T_0 \tag{19}$$

From (19) we see that in order for T_N to fall within 5% of $T \approx 4$ K, the Rb atoms have to undergo $N \approx 100$ collisions. In the course of the thermalization, the Rb atom will move over a distance

$$L_N \approx \frac{\sqrt{N}}{n_{He}\sigma} \tag{20}$$

Assuming a Rb-He elastic cross section $\sigma \approx 50$ Å^2, we have $L_{N=100} \approx 0.2$ cm at $n_{He} \approx 10^{16}$ cm^{-3}. This is consistent with our observations: we find the Rb atoms thermalized in the probed region which is about 10 mm downstream from the cell entrance.

3.2.4 Density distribution over the cryogenic cell

If all rubidium atoms are thermalized, the absorption signal is proportional to the integral of rubidium number density along the laser beam, i.e. along the Y-axis. To

convert the signal into local rubidium densities or into the total number of atoms loaded into the cell, it is necessary to adopt a model of rubidium density distribution[******]. A Monte-Carlo simulation [71] of elastic collisions gives a very accurate description of the loading process, however, due to significant computing time requirements it was used to process only a small fraction of the data. From our Monte-Carlo simulations we found that the range of input parameters that describes the optimal buffer-gas density corresponds to atoms entering the cell and thermalizing within several millimeters from the opening, and then diffusing across the cell into the probed volume. This behavior can be approximated by a diffusion equation with boundary conditions corresponding to absorption of particles at the walls, which is then used to convert the absorption data into number densities.

[******] see also Appendix B

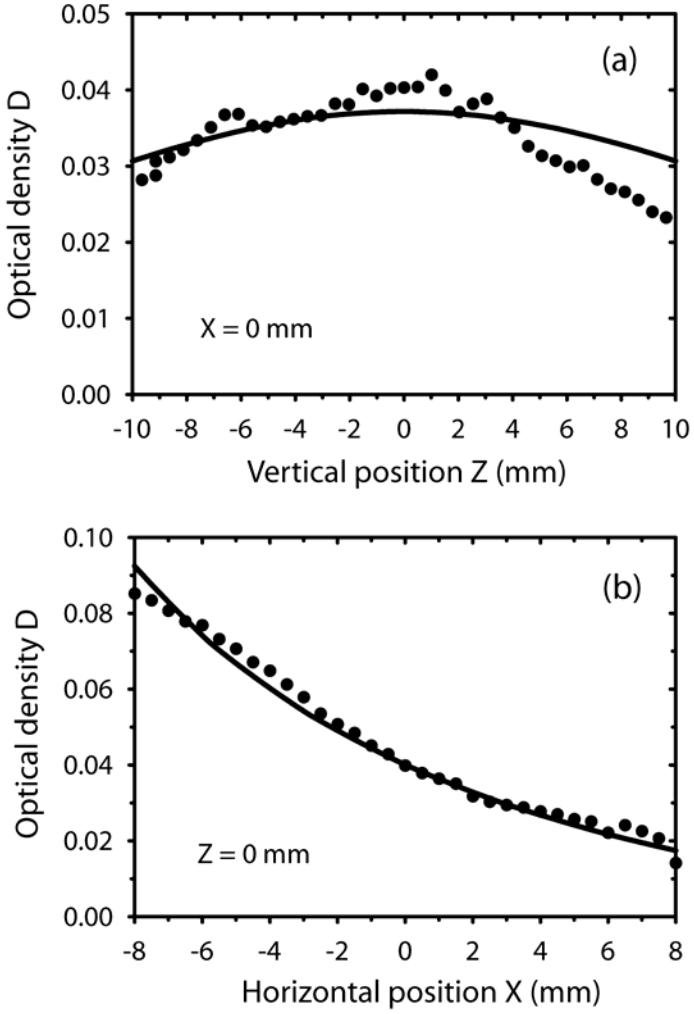

Figure 10: Spatial distribution of Rb atoms in the cell

Optical density of Rb atoms in the cell as a function of the probe beam position. Circles are experimental data, lines are simulations based on the diffusion model. Cell center defines the origin of the coordinate system. Cell temperature was 4.3±0.1 K, buffer gas density 1.5×10^{16} cm^{-3}.

(a) Probe beam is scanned vertically along Z-axis at X=0 mm; (b) Probe beam is scanned horizontally along X-axis at Z=0 mm.

Figure 5 shows comparisons of absorption signals at different locations in the cell with the predictions of the diffusion model. At the (near-optimal) buffer-gas density of $n_{He} = 1.5\times10^{16}$ cm^{-3}, Rb density of

$$n_{Rb} = (8\pm4)\times10^{9} \text{ cm}^{-3}$$

at the center of the cell is observed, indicating a total number of thermalized Rb atoms loaded into the cell of

$$N_{Rb} = (1\pm0.5)\times10^{12}.$$

To determine F_c, the flux of Rb atoms entering the cell with no buffer gas present, we scanned the probe beam across the atomic beam inside the cell, and converted the absorption signal into F_c. In doing so, we took into account the Gaussian intensity profile of the laser beam and cylindrical symmetry of the atomic beam. We then introduced buffer gas into the cell, and measured the corresponding N_{Rb}. Due to technical limitations, we were able to perform this measurement only at low fluxes, up to the level $F_c = 5\times10^{11}$ s^{-1}, for which $N_{Rb} = 1.5\times10^{10}$. We assume, based on Eq. (14) above, that with increasing flux of Rb atoms N_{Rb} should not increase more rapidly than F_c. We therefore estimate the highest flux achieved in our experiment to be at least

$$F_c = (3\pm1.5)\times10^{11} \text{ s}^{-1}.$$

Based on the value for Rb-He diffusion coefficient in Ref. [28] we estimate the scattering cross-section, σ, at 4.2 K to be 50 Å^2, which gives the diffusion time $\tau \approx 100$ ms . For $\tau = 100$ ms and $N_{Rb} = 1.5\times10^{10}$ we calculate, using Eq. (14), the number of Rb atoms entering the cell with the buffer gas present as $\dot{N}_{in} = 1.5\times10^{11}$ s^{-1}. This number is approximately 3 times smaller than the measured number of atoms entering the cell with

no buffer gas. This indicates that a significant fraction of Rb atoms coming towards the cell orifice are loaded into the buffer gas.

3.3 Discussion

Direct loading of a molecular beam into a cryogenic buffer-gas cell is a simple and efficient technique of cooling gaseous species. The apparatus described can be used to carry out a variety of spectroscopic measurements on atoms, molecules, radicals, and metastable species at cryogenic temperatures. The apparatus can be extended by adding another molecular beam, to study cold collisions and chemical reactions.

An exceptionally wide variety of atomic and molecular species can be produced in a molecular beam [96; 97; 110]. Since the technique makes no use of cooling due to the beam expansion, the only parameter of interest is the beam flux in the forward direction. As a result, a simple effusive source with modest pumping requirements may suffice; the stagnation pressure can, of course, be significantly increased if greater flux is required. Since the beam temperature is insignificant in our scheme, the source can be operated at as high a temperature as necessary for raising the vapor pressure or for enabling the generation of the species of interest. As a result, any species that can form a molecular beam can be loaded into the cryogenic cell, including reactive species such as radicals.

4 NH experiment:

Introduction

4.1 Meet the molecule

Basic considerations that led us to choose NH as a primary candidate for a next-generation buffer gas cooling experiment were outlined in section 1.5. This chapter presents further helpful details on the molecule.

4.1.1 Molecular structure

The NH radical is a fairly well-studied molecule, studied in part due to its importance in astrophysics [111]. Four isotopic versions exist, two bosons and two fermions, as shown in Table 6. The natural isotope mixture is strongly dominated by $^{14}N^{1}H$ version, which simplifies rotational spectrum interpretation*. Certain experiments in the ultracold regime may benefit from the ability to switch to a boson version of the same species; switching to $^{14}N^{2}D$ simply involves replacing ammonia ($^{14}N^{1}H_3$) in the process gas (see section 5.3.1) with easily available deuterated ammonia ($^{14}N^{2}D_3$)†. For production of two other isotopic versions, $^{15}N^{1}H_3$ and $^{15}N^{2}D_3$ gases are also available‡, although at substantial cost. In the remainder of this work we will be discussing only the $^{14}N^{1}H$ isotopic version of NH.

Table 7 gives information on electronic energy levels of NH. Two states of particular interest to us are the ground state $X^3\Sigma^-$ and the lowest excited state with an

* compared, for example, with PbO, as described in section 2.3

† Spectra Gases Inc., Branchburg, NJ

‡ Cambridge Isotope Laboratories Inc., Andover, MA

allowed optical transition $A^3\Pi_i$. The goal of the experiment is to cool and trap NH in its ground ($X^3\Sigma^-$) state, and to probe its properties on an X↔A transition. Another state that may play a significant role at future stages of the experiment is the metastable $a^1\Delta$; its importance is discussed in section 4.2.3.

	$^{14}N^{1}H$	$^{14}N^{2}D$	$^{15}N^{1}H$	$^{15}N^{2}D$
Mass, A.U.	15	16	16	17
Statistics	fermion	boson	boson	fermion
Abundance	99.615 %	0.015 %	0.370 %	0.000055 %

Table 6: Isotopes of NH.

State	$\mathbf{T_e}$	$\boldsymbol{\omega_e}$	$\boldsymbol{\omega_e x_e}$	$\mathbf{B_e}$	$\boldsymbol{\alpha_e}$	$\mathbf{D_e}$	**Transition**	$\boldsymbol{\nu_{00}}$
$d\ ^1\Sigma^+$	83160	2672.6	71.2	14.390	0.621	16.0E-4	d→c; τ=18 ns	39512.26
$c\ ^1\Pi$	(43744)	[2122.6]		14.537	0.593	[22.0E-4]	d→b	61619.60
							c→b; τ=460 ns	22106.62
							c→a; τ=460 ns	30755.54
$A\ ^3\Pi_i$	29807.4	3231.2	98.6	16.674	0.745	[17.8E-4]	A↔X; τ=404 ns	29776.76
$b\ ^1\Sigma^+$	21202	3352.4	74.24	16.705	0.591	16.0E-4	b→X; τ=18 ms	21238
$a\ ^1\Delta$	(12566)	[3188]	(68)	[16.43]	0.66	[16.2E-4]	a→X; τ=2 s	12589
$X\ ^3\Sigma^-$	0	3282.27	78.35	16.699	0.649	[17.1E-4]		

Table 7: Energy levels of NH.

All numbers are cm^{-1}; radiative lifetimes for v=0 levels[§].

From [112].

[§] As a reminder:

$$G(v) = \omega_e(v+1/2) - \omega_e x_e\ (v+1/2)^2$$

$$F(v,J) = [B_e - \alpha_e(v+1/2)]\ J\ (J+1) - D_e\ [J(J+1)]^2$$

$$B_v = B_e - \alpha_e(v+1/2)$$

4.1.2 Spectroscopic info

In our experiment NH detection and thermalization diagnostics is performed using laser-induced fluorescence and laser absorption spectroscopy on the $X^3\Sigma^-(v''=0) \leftrightarrow A^3\Pi_i(v'=0)$ transition. The wavelength of the transition is 336nm, the Franck-Condon factor is 0.9998, and Einstein's A coefficient 2.52×10^6 s^{-1} [113] - a reasonably strong transition easily accessible with a doubled dye laser.

The coupling case of the ground state, as for most $^3\Sigma$ states, is Hund's case (b)[**]: N, J, $\Lambda, \Sigma, S, \Omega$ are all good quantum numbers, and the rotational energy is $E = B_v N(N+1)$. The excited $A^2\Pi_i$ state is coupling case (a)[††] for low rotational number values (J<3): J, Λ, Σ, S, Ω are good quantum numbers, and rotational energy is given by $E = B_v J(J+1)$. The coupling turns into case (b) for high rotational numbers [114].

Figure 11 provides an illustration of available low-lying rotational lines. All low-lying lines have comparable intensities, as $A^3\Pi_i$ is Hund's case (a) for J'≤3. Please note that energy level spacing is not shown to scale.

Since the rotational constant for the ground $X^3\Sigma^-$ state is B_e = 16.7 cm^{-1}, we expect that after thermalization with buffer gas all NH molecules are in the ground ro-vibrational state $X^3\Sigma^-(v''=0,N''=0)$. This state contains 5 hyperfine levels [115]

[**] Small spin-orbit coupling, small Σ–multiplet splitting

[††] Small spin-orbit coupling, large Σ–multiplet splitting

spanning ~120 MHz, which for typical cryocell temperatures are not resolved due to Doppler broadening. The hyperfine structure introduces a rather unfortunate complication into the analysis of the experimental spectra, as further described in section 6.2.3: the present knowledge of the hyperfine structure is insufficient to determine the translational temperature of the molecules as accurately as we would normally desire. However, as the apparatus reaches lower temperatures in the future stages of the experiment, we should be able to resolve the hyperfine structure, accurately measure the hyperfine constants, and dramatically improve the accuracy of our translational temperature measurements.

The ideal transition for molecular detection would be a closed-cycling transition as the signal-to-noise ratio of measurement can be improved by using high laser intensities without worrying about spectral hole burning. Franck-Condon factor matrix of NH is near-diagonal, so one would hope that a closed-cycling transition is available. However, since the $A^3\Pi_i$ state is Hund's case (a) for $J'<3$, the closed-cycling transitions do not exist, and rotational leakage is always on the order of 75%[‡‡]. We perform most of our detection on:

$R_{11}(0)$: $X^3\Sigma^-(v''=0,N''=0,J''=1) \rightarrow A^3\Pi_0(v'=0,J'=2)$

The excited molecules then decay on:

$R_{11}(0)$: $X^3\Sigma^-(v''=0,N''=0,J''=1) \leftarrow A^3\Pi_0(v'=0,J'=2)$,

$R_{13}(2)$: $X^3\Sigma^-(v''=0,N''=2,J''=1) \leftarrow A^3\Pi_0(v'=0,J'=2)$,

$Q_{13}(2)$: $X^3\Sigma^-(v''=0,N''=2,J''=2) \leftarrow A^3\Pi_0(v'=0,J'=2)$

$P_{11}(2)$: $X^3\Sigma^-(v''=0,N''=2,J''=3) \leftarrow A^3\Pi_0(v'=0,J'=2)$

transitions in ratios according to the corresponding Honl-London factors [116].

[‡‡] which means that laser cooling of NH would require a minimum of 3 re-pump lasers

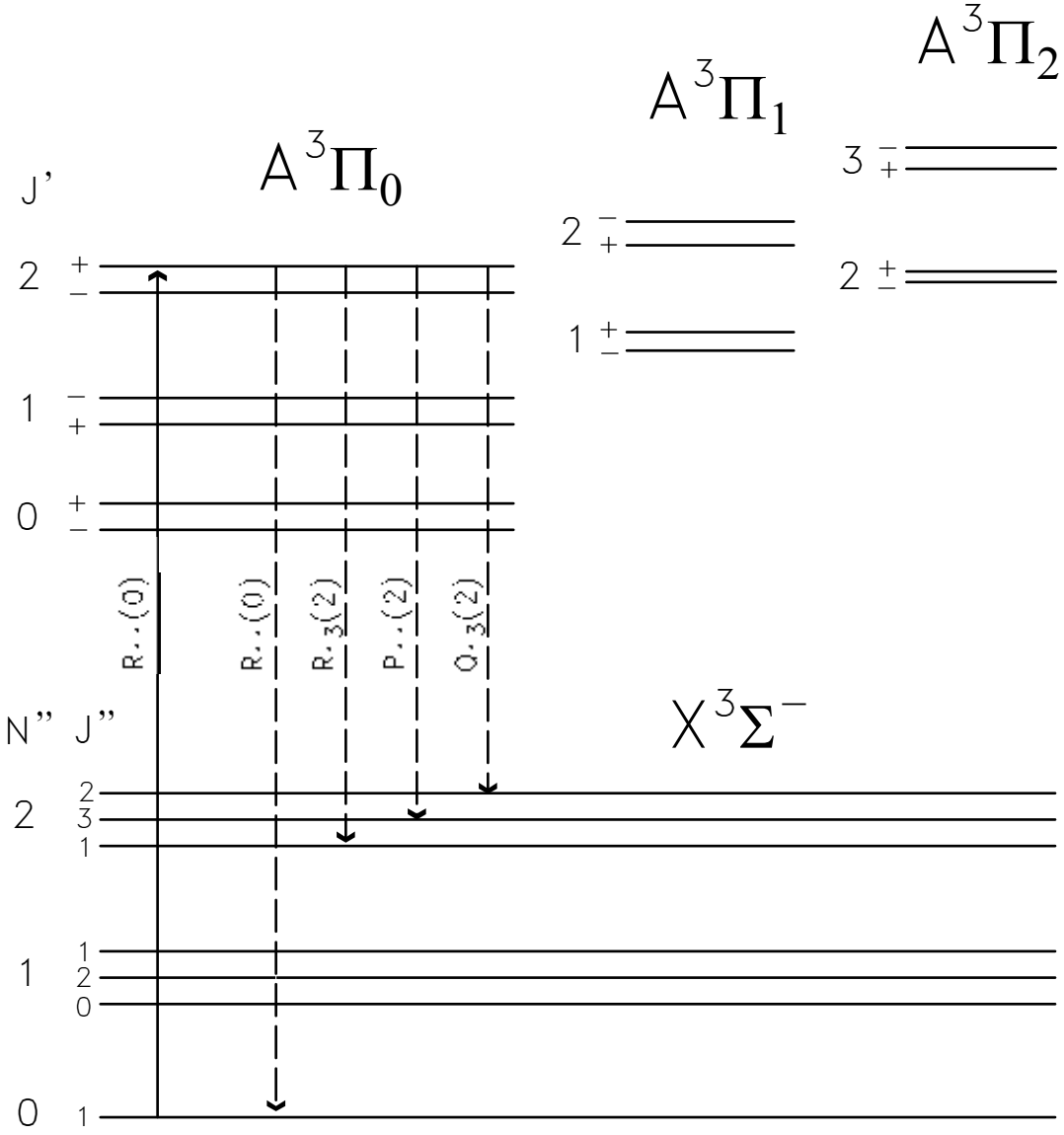

Figure 11: Rotational lines of NH used for optical detection.

In order to determine the degree to which vibrational states of the ground electronic state are out of thermal equilibrium, it is necessary to probe transitions from higher vibrational states $X^3\Sigma^-(v''>0)$. Also, exciting non-diagonal transitions $X^3\Sigma^-(v''=0) \rightarrow A^3\Pi_i(v'>0)$ may improve suppression of background scatter that limits the sensitivity of our laser-induced fluorescence setup. Table 8 gives the

wavelengths and Frank-Condon factors[§§] for these transitions. From the table it follows that a CW doubled dye laser can be used to probe diagonal transitions $X^3\Sigma^-(v''=n)\rightarrow A^3\Pi_i(v'=n)$, while a pulsed dye laser would be necessary to excite rather weak off-diagonal $X^3\Sigma^-(v''=0)\rightarrow A^3\Pi_i(v'=n>0)$ transitions.

[§§] our experience with CaF spectroscopy [117] indicates that sometimes published values of off-diagonal Franck-Condon factors may contain order-of-magnitude scale errors, so values in Table 8 should be used as a rough guide only

$X^3\Sigma^-(v'')\leftrightarrow A^3\Pi_i(v')$ transitions			
v' \ v''	0	1	2
0	335.8 nm 0.9998	375.2 nm 0.204e-3	422.3 nm 0.202e-4
1	304.7 nm 0.198e-3	336.9 nm 0.997	374.3 nm 0.258e-2
2	280.5 nm 0.284e-4	307.5 nm 0.250e-2	338.4 nm 0.987

Table 8: Off-diagonal X-A transitions in NH.

Top: bandhead position calculated from Table 7.

Bottom: Franck-Condon factors from [113].

Einstein A coefficient is 2.20×10^6 s^{-1} for (v'=n, v''=n), n=0,1,2 [113].

4.1.3 Magnetic trapping

The success of magnetic trapping critically depends on the linearity of Zeeman shift for magnetic fields of up to 4.5 Tesla, and on spin-depolarization (Zeeman relaxation) rates in collisions with cold helium atoms. Little is known at this point about spin-depolarization rates, although theoretical predictions indicate a rate that is favorable for magnetic trapping [22]. The Zeeman shift, on the other hand, is fairly well understood. Figure 12 shows results of diagonalization of molecular Zeeman Hamiltonian at fields up to 5 Tesla for the low-lying rotational states of $X^3\Sigma^-(v''=0)$ [118]. In this

range of fields the slope of Zeeman shift of the lowest rotational state remains linear at ~2 μ_B. This calculation is supported by a direct Stern-Gerlach-type measurement [119].

In order to be able to interpret observed Zeeman spectra it is critical to be able to predict the magnetic broadening of the transition. Theoretical predictions, based on diagonalization of molecular Hamiltonian with known molecular constants, exist [118] and predict a linear shift of 6.92 GHz/Tesla for our range of fields. This is not surprising: the spacing between rotational levels is high compared to Zeeman energies, so the effect of nearby rotational levels comes only a small perturbation.

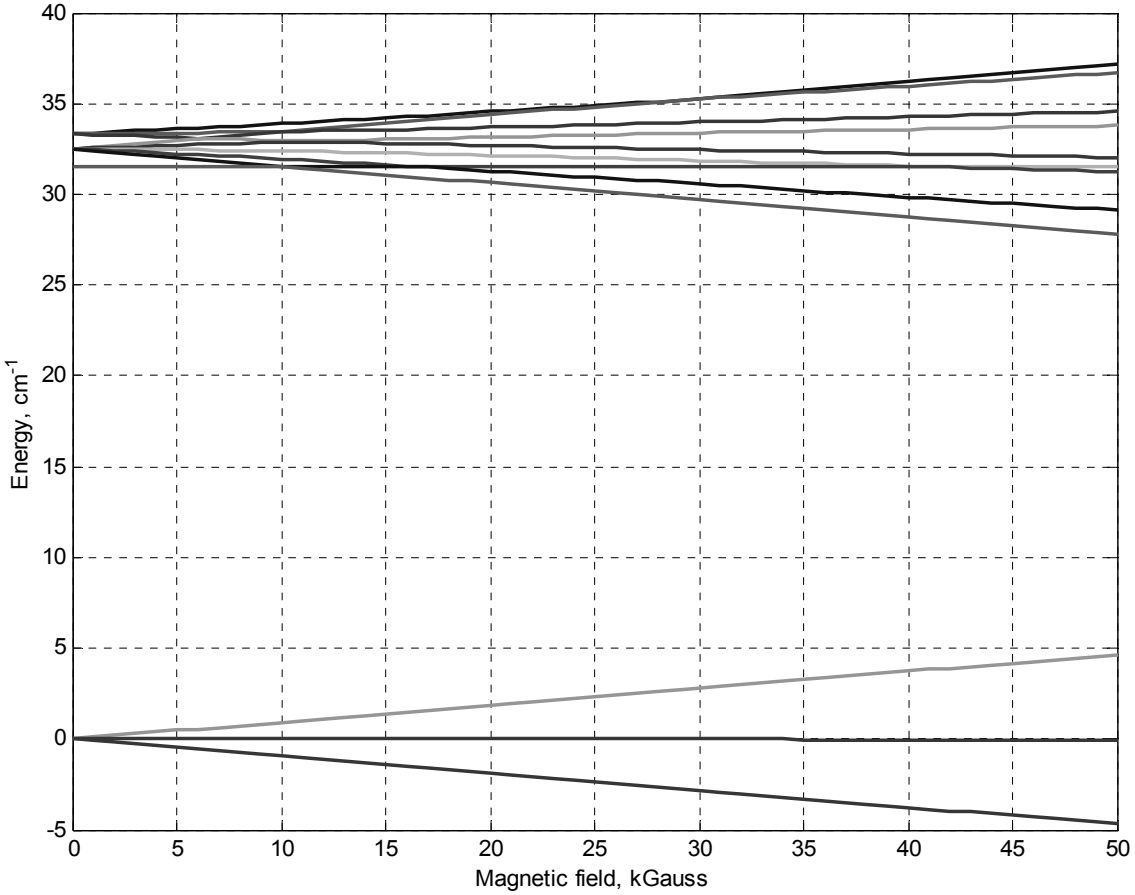

Figure 12: Zeeman effect in NH $X^3\Sigma^-$(v"=0, J"=0) and $X^3\Sigma^-$(v"=0, J"=1). Based on [118].

4.2 Production of NH

A number of radical production techniques are described in the literature, and a number of them have been applied to NH production. These include:

- pyrolysis of NH_3 (ammonia) [120]
- excimer laser photolysis of NH_3 or N_3H (hydrozoic acid) [121-127]
- Nd:YAG laser photolysis of N_3H [123]
- RF/microwave discharge in NH_3 [115; 128]
- glow and corona discharge in NH_3 [129-131]

and others.

The most popular high-yield NH production technique is photolysis, either of NH_3 or N_3H. Photolysis of ammonia NH_3 requires rather complex equipment, namely a VUV excimer laser[***]. Photolysis of hydrozoic acid N_3H does not require lasers as complex, it can be done with a quadrupled Nd:YAG or with a UV excimer, and offers both order-

[***] In photolysis, an excimer laser beam overlaps with a molecular beam of ammonia (excimer pulses are typically ~10 ns in length, so beam co-propagation is the ideal geometry). Ammonia molecules absorb laser photons and decompose into NH, NH_2, H, and H_2, with yields strongly dependent on photon wavelength. (cont'd on next page)

Reaction $NH_3+h\nu \rightarrow NH(X^3\Sigma^-)+H_2$ is spin-forbidden and no $NH(X^3\Sigma^-)$ is observed for wavelengths above 160 nm [132]. A possible NH production channel is two-photon photolysis $NH_3+2h\nu$ (193nm,ArF laser)$\rightarrow NH(A^3\Pi)+2H$ with a 5×10^{-4} quantum yield [125]. $NH(A^3\Pi)$ radiatively decays into $NH(X^3\Sigma^-)$ in 450 ns. A longer-wavelength single-photon channel $NH_3+h\nu$ ($\lambda<219$nm)$\rightarrow NH(a^1\Delta)+H_2$ is also possible, but requires pumping down or quenching the metastable $NH(a^1\Delta)$, see section 4.2.3.

unity quantum yield and state-selective production. We chose to avoid technical difficulties related to handling of hydrozoic acid, and did not pursue any of the photolysis approaches. At a later time, however, the benefits of a yield increase up to ×1000 and state selectivity associated with photolysis of hydrozoic acid may outweigh the technical difficulties of handling a toxic and highly explosive compound, and we may reconsider this option.

Another significant consideration for choice of production method in our experiment was its flexibility in which radicals can be produced by it. This consideration favors discharge methods, as switching to a different radical may be as simple as replacing the process gas. Sections below provide overview of different discharge methods, and discuss certain options that we may be able to implement in the near future.

4.2.1 Gas discharge physics

Ref. [133] provides an excellent treatment of all aspects of gas discharge physics. Gas discharges can be classified into two principal groups, DC and RF/microwave. DC discharges include arc, glow, corona, and spark discharge. Table 9 highlights the principal difference between them.

The Townsend model of avalanche and Paschen law of breakdown, fully described in Ref. [133], are two important models for basic understanding of gas discharges. In summary, Paschen law states that the discharge ignition voltage V_i for a

given gas is a function only of parameter $p \cdot d$, where p is gas pressure and d is electrode separation[†††]:

$$V_i = c_1 \frac{p \cdot d}{c_2 + \ln(p \cdot d)} \tag{21}$$

where c_1 and c_2 are gas-dependent constants. V_i increases for $p \cdot d \to \infty$ and $p \cdot d \to 0$, and passes through a single minimum V_i^{min} at $(p \cdot d)^{min}$; e.g. for He at 300 K V_i^{min} = 156 V and $(p \cdot d)^{min}$ = 4.0 torr·cm.

Townsend model describes avalanche formation when the breakdown occurs. Consider a gas of neutral atoms filling a gap between two electrodes. The initial electrons (from cosmic rays, ionizing radiation, thermionic emission of cathode, etc.) are accelerated by the applied voltage. The average energy the electrons acquire between energy-dissipating collisions with neutral atoms is only ~1-10 eV, but electron-electron collisions create a Maxwell distribution, and the "tail" of the distribution has sufficient energy (~100 eV) to ionize atoms on impact. The ionization produces secondary electrons, and the avalanche grows; typical timescales of avalanche formation are 1 μs to 1 ms. Electrons in the avalanche are lost due to recombination, wall collisions, and attachment to electronegative atoms; the discharge can only be sustained if the rate of production of secondary electrons exceeds their loss rate. Different gases have very different elastic and ionization cross-sections, as shown in Table 10; the sustainability of the avalanche for a given parameter set, therefore, critically depends on the exact gas mixture used. We will not attempt to predict which gas mixture is an optimal one for the

[†††] the law is usually written for temperature of 300 K; for other temperatures, the parameter should be written as $n \cdot d$, where n is gas number density

experiment, but we point that Ne is a clear favorite for high multiplication, high electron energy, low ignition voltage discharge, and that Ar offers better cryopumping properties and smaller forward beam velocities with a trade-off of lower discharge performance.

	Arc	Glow	Corona	Spark
Cathode emission	Thermionic (temperature of cathode is sufficient to produce above-barrier electrons)	Secondary (incoming ion's field lowers energy barrier, electrons tunnel out to neutralize the ion, the ionization energy released, knocks out more electrons)	Glow discharge in strongly non-uniform field that is insufficient to produce breakdown in entire region	Non-self-sustaining discharge in long narrow plasma channel; typical for high pressures, large electrode separations, very high voltages
Cathode temperature	~ 10^3 K	Room temperature (300 K)		
Electron temperature	~10^4 K	~10^4 K		
Ion and neutral atom temperature	In equilibrium with electrons (~10^4 K)	Room temperature (300 K)		
Typical ionization	10^{-3} … 10^{-1}	10^{-8} … 10^{-6}		

Table 9: Classification of DC discharges.

	He	Ne	Ar	Kr	Xe	N_2	H_2
Electron MFP[‡‡‡], mTorr·cm	60	120	30			30	20
Ionization coefficient[§§§], cm^{-1}	50	50	5				
Secondary emission yield[****]	0.21	0.30	0.09		0.02	0.005	0.003
Breakdown voltage at $p \cdot d$ = 100 torr·cm, kV	1.5	0.8	1.5			6.3	4
Molar mass, g/mol	4.0	20.2	39.9	83.8	131.3	28.0	2.0
Boiling point, K	4	27	87	120	165	77	20

Table 10: Comparison of glow discharge properties for various carrier gases.

4.2.2 Glow discharge

While beams of radicals have been produced using glow, arc, corona, RF, and microwave discharges, we chose a DC glow discharge in a slit geometry for production of NH: the setup is very simple and provides a large number of parameters that can be tweaked to optimize radical production.

Our setup is largely modeled on the one described in Ref. [134]. As shown in Figure 13, the discharge occurs between electrodes positioned immediately outside the

[‡‡‡] typical, for 1-10 eV electrons; see p.11 in [133]

[§§§] approximate value for 1 kV potential difference, 0.1 cm electrode separation, 1000 torr pressure, (i.e. E/p = 10 V/cm·torr); p.55 in [133]

[****] number of electrons emitted from a tungsten/platinum cathode per incident ion; p.71 in [133]

beam source. Electrons and ions in the discharge collide with precursor molecules and form radicals of interest. The carrier gas in the mixture sustains the discharge by providing avalanche electron multiplication, and shields radicals from each other and the walls to prevent recombination. The density of gas drops rapidly outside the discharge region, limiting recombinative processes to the discharge region only. By varying mixture composition, electrode separation, production channel length, stagnation pressure, and discharge voltage, we optimize the production of molecules of interest[††††].

As the parameters are varied, special care needs to be taken to prevent a transition from glow into arc discharge. The kinetics of an arc discharge is dramatically different from that of glow, and direct comparison between the yields of the two is not possible. Arc discharge has a significant disadvantage of rapid cathode erosion, which introduces uncontrollable time dependence of the discharge parameters into the study. Section 5.2.2 describes the issue in more detail.

[††††] NH_3 can decompose either into NH_2+H, or into NH+2H; the former is energetically favorable. NH_2 can subsequently decompose into NH+H, or react with other particles in the beam to form other molecules; NH can also recombine $2NH \rightarrow N_2H_2$, $NH+H \rightarrow NH_2$, etc. Overall yield of NH will depend on the kinetics of the process; a large number of easily variable parameters in our discharge setup allows us to find a high-yield setting without having to understand the kinetics in detail.

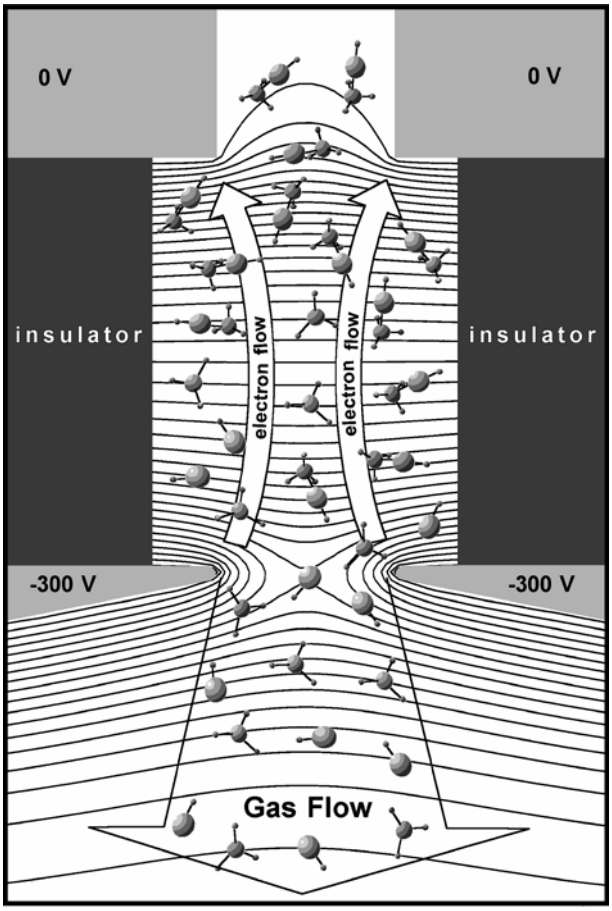

Figure 13: Radical production in slit glow discharge.
From Ref. [134].

4.2.3 Byproducts of glow discharge

Glow discharge, like laser ablation, may generate a range of unwanted byproducts that may interfere with the molecules of interest. The byproducts may cause NH to recombine and be lost. Paramagnetic byproducts, most notably nitrogen $N(^4S_{3/2})$ which has a magnetic moment $\mu = 3\ \mu_B$, will be retained by the magnetic trap and may cause NH to undergo collision-induced Zeeman relaxation. Although up to now we never

observed any unwelcome effects due to discharge byproducts, it is important to discuss this possibility.

The density of molecules in the molecular beam away from the discharge region is so low that virtually no collisions occur within the beam; the byproducts only become a potential issue once inside the buffer gas cell. This immediately points to a way of preventing any unwanted interference from the byproducts that is not available for laser ablation: introduce a filtering stage between the discharge region and the cell entrance to filter out all byproducts but let the molecules of interest pass. To filter out most byproducts of NH production, such as N, H, NH_2, NH_3, N_2, H_2, noble gas atoms, ions, and various complexes, a rather straightforward method of Stern-Gerlach filtering can be introduced, as described in section 8.2.

For the particular case of NH there exists a discharge byproduct that is a potential threat to the trap population and can not be filtered using Stern-Gerlach filtering. It is a metastable state NH $a^1\Delta$, which has a radiative lifetime of 2 seconds, significantly longer than other relevant timescales in the experiment (e.g. diffusion time), and magnetic moment of $2\mu_B$, identical to that of NH $X^3\Sigma^-$. We may expect a significant fraction of NH to be produced in the $a^1\Delta$ state: angular momentum conservation dictates a preferred channel of NH_3 fragmentation to be [124; 135] $NH_3 \rightarrow NH\ a^1\Delta + H_2$.

Multiple-body collisions in a high-density region of the discharge may significantly affect the angular momentum considerations above, so an experimental verification would be necessary if adverse effects due to presence of NH $a^1\Delta$ are suspected. Fortunately, NH $a^1\Delta$ is easily detected on $a^1\Delta(v''=0) \leftrightarrow c^1\Pi(v''=0)$ transition at 335 nm. The Franck-Condon factor for this transition is 0.756 and the Einstein A

coefficient is 1.40 MHz, i.e. the transition is similar in strength to $X^3\Sigma^- \leftrightarrow A^3\Pi_i$ used to detect ground-state NH in our experiment. We also have to address potential solutions to the adverse effects of the presence of NH $a^1\Delta$. Waiting for a few seconds for the state to decay radiatively is not an option in our setup. Pumping the state down with a pulsed laser is a possibility [136], although high laser energies will be required. The most promising approach seems to be relying on collisional quenching of the metastable state. Studies indicate that gases such as N_2 [137] and Xe [138; 139] efficiently quench excited electronic states. It may be possible to modify the process gas mixture and discharge region geometry to reduce the population of NH $a^1\Delta$ without depleting the population of NH $X^3\Sigma^-$.

5 NH Experiment:

Experimental setup

Several generations of the apparatus were used for different stages of the experiment described in this work. In this chapter we describe the most complete version of the apparatus; any significant deviations from this description will be listed in the corresponding sections. The apparatus is schematically shown in Figure 14. The main elements of the system are as follows.

- Molecular beam production system, where the process gas mixture is prepared, supplied to the discharge region, and converted into a radical-carrying beam in a high voltage discharge. It consists of a gas handling system (section 5.3), beam source (section 5.1), and high voltage system (section 5.2).
- Cooling and trapping system, which provides cold helium gas in a cryogenic cell and which creates required magnetic fields. It consists of a buffer gas supply (section

5.3.2), helium containment (section 5.6), cryogenic equipment (section 5.5), and superconducting magnet (section 5.7).

- The detection system consists of an excitation laser, laser wavelength monitors, absorption detectors, and fluorescence detectors (section 5.8).
- Vacuum chamber and associated vacuum pumps provide vacuum required for successful operation of the beam source and the cryogenic equipment (section 5.4).
- The data acquisition system provides status information on various parts of the system and ensures fail-safe operation of the apparatus.

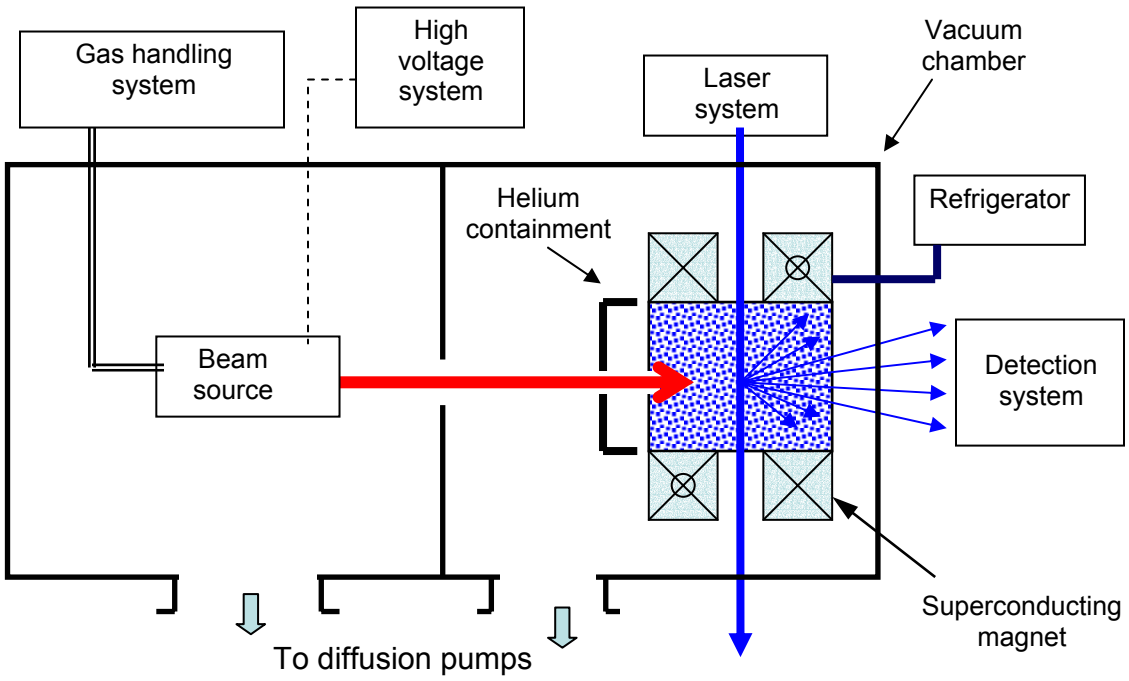

Figure 14: Schematic of NH trapping apparatus.

5.1 Beam source

The key parts of the radical beam source are depicted in Figure 15.

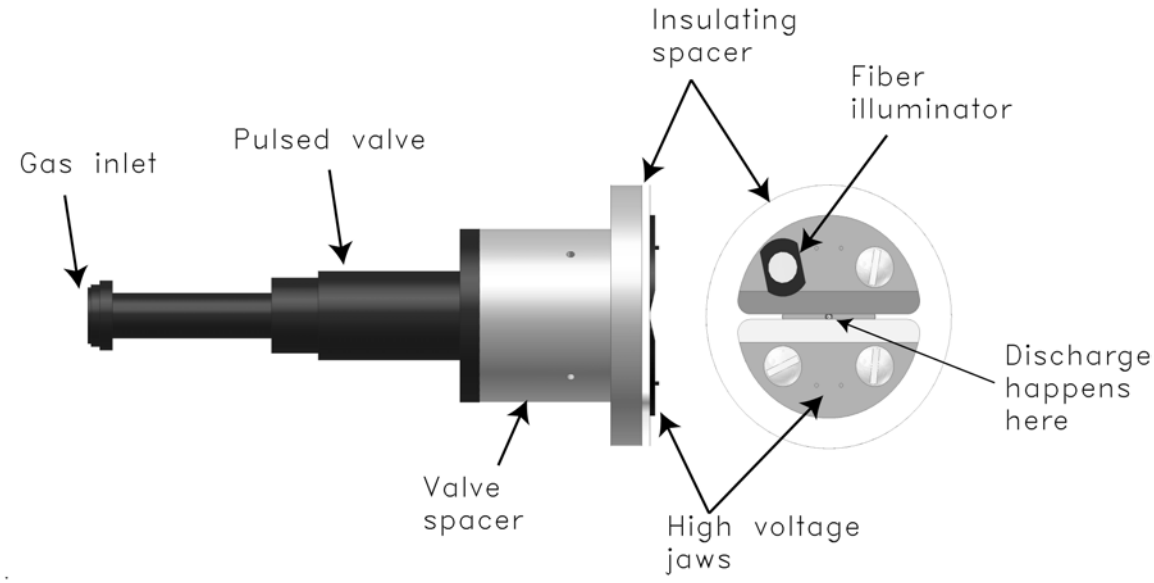

Figure 15: Pulsed valve and discharge region, scale drawing.

5.1.1 Discharge region

The discharge region consists of metal jaws held at negative high voltage, a metal valve spacer held at ground potential of the high voltage circuit, and an insulating spacer separating them. The assembly is held together with insulating screws; one of the screws is fitted with a fiber-optic illuminator for alignment purposes.

NH radicals may recombine when they collide with each other and with other by-products of the discharge; it is unlikely that they can guided by any sort of physical

channel. Radical production must therefore occur in a wall-free environment of a molecular beam. We rely on electrons and ions in the discharge to break apart ammonia molecules; it is important to maintain a high density of process gas in the discharge region. This dictates placement of high voltage jaws immediately outside the valve nozzle. We found that heat generated in the discharge adversely affects the valve poppet in such an arrangement. To prevent poppet damage, we introduced the valve spacer, an aluminum cylinder 32 mm long with a 1.6 mm diameter axial channel. The valve spacer carries process gas from the pulsed valve nozzle to the discharge jaws and diverts the heat of the discharge away from the valve.

The insulating spacer is a 1.52 mm thick 50 mm diameter disk with a 1.60 mm wide 18 mm long slit in it. The material is HBC grade hot-pressed boron nitride[*], chosen for its exceptional thermal conductivity (29 W/m·K, or 10% that of copper), heat and chemical resistance, and dielectric strength (>10^5 V/mm). The insulating spacer serves several functions: it provides physical and electrical separation between the jaws and the valve spacer, conducts discharge heat away from the jaws, and shapes gas flow from circular into near-rectangular shape.

The high voltage jaws are 1 mm thick custom-made stainless steel blades positioned 1.1 mm apart. The jaws are connected to the high voltage circuit via stainless steel 304 3x7 wire rope or 1/32" nominal diameter[†] welded onto them; same type of current leads is used to connect the valve spacer to high voltage ground. The jaws are held in place with nylon screws. Nylon represents a compromise between dielectric

[*] GE Advanced Ceramics, Cleveland, OH

[†] 0.1 Ohm/cm resistivity

strength, tensile strength, and chemical and temperature resistance. Earlier versions of screws were made of fluorinated plastics (ETFE, PTFE), which offered better chemical and thermal resistance, but did not have sufficient strength to withstand multiple tightening cycles. We observe gradual deterioration of the stainless steel jaws, presumably due to cathode evaporation in occasional arcing. At this point, low cost and ease of replacement dictated the choice of stainless steel as jaw material, but it would be ideal to prevent the gradual change in the discharge geometry and any beam contamination by utilizing tungsten, which offers much better heat resistance and is known to be the best-performing cathode material.

It is important to explain our reasons for choosing the slit discharge geometry, as they are different from those of physical chemists. In physical chemistry, the typical application of slit beam geometry is in absorption spectroscopy done immediately outside the nozzle; slit geometry maximizes the optical depth of the beam for a given total beam flux. Our choice was due to a desire to be able to quickly modify the shape of gas expansion, which may have a dramatic effect on the yield of NH radicals; in a slit geometry the modification is accomplished by simply moving the jaws in and out, and there is no need to machine new parts.

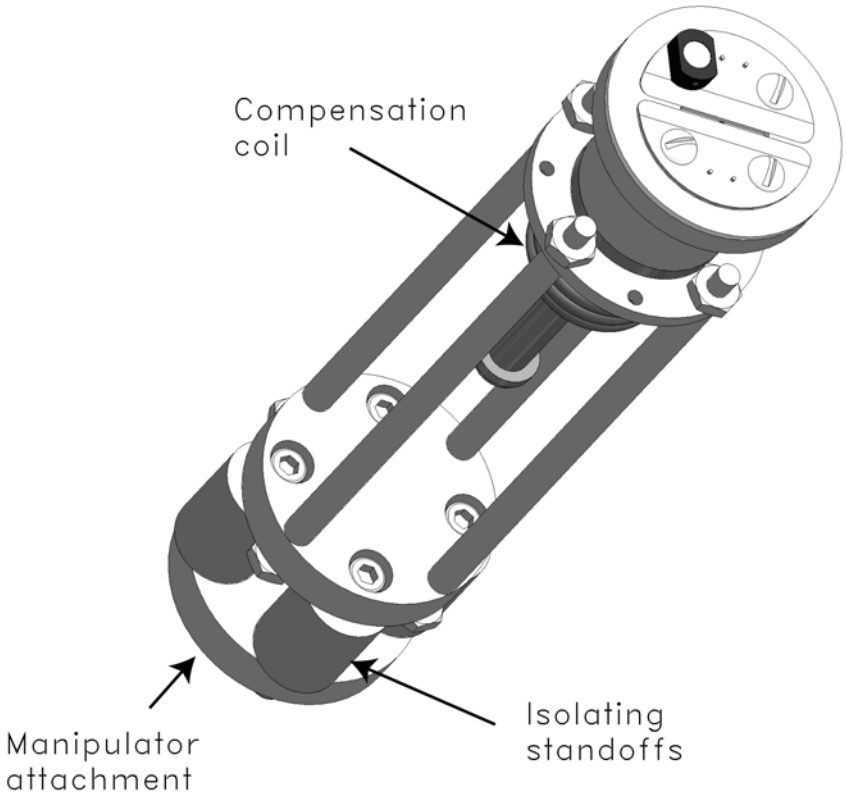

Figure 16: Valve assembly, scale drawing.

5.1.2 Pulsed valve assembly

The pulsed valve assembly is shown in Figure 16. The assembly consists of a solenoid valve[‡] with 0.030" nominal nozzle diameter, the discharge region described above, a compensation/cooling coil, and a valve holder. The valve actuation coil, which is electrically isolated from the valve body or system ground, is connected to an external

[‡] General Valve Series 9 p/n 009-0378-900, Parker Hannifin Corp., Chicago, IL

valve driver[§]. The holder, made of aluminum, mechanically attaches the valve to an XYZ manipulator used to position the valve with respect to the cryogenic cell. In order to ensure that the discharge current, which flows from the discharge jaws into the valve spacer, is returned into the high voltage circuit via a return lead attached to the valve spacer, we electrically isolate the valve assembly from the chamber. The holder is mounted on ceramic standoffs, and the process gas supply line (not shown in Figure 16) is fitted with a ceramic break.

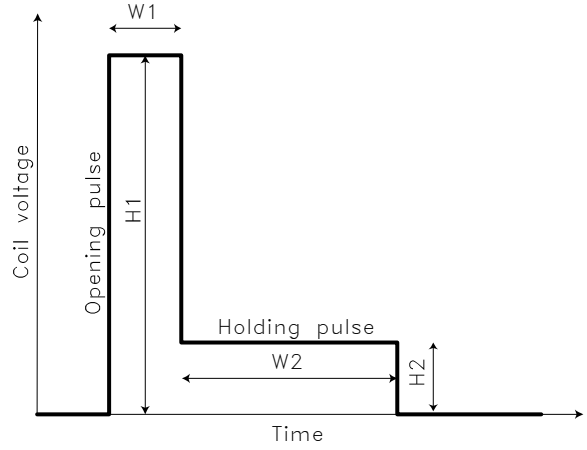

Figure 17: Iota One output diagram.

The valve driver outputs a voltage pulse schematically shown in Figure 17. The operator can vary opening pulse width W1 in the range from 0 to 320 μs, holding pulse width W2 from 500 μs up[**], holding pulse height H2[††], and repetition rate from 0.1 Hz

[§] Iota One single-channel driver, Parker Hannifin Corp., Chicago, IL

[**] The nominal setting range is 5 μs to 9999 minutes, however, settings below 500 μs do not produce shorter valve opening times

up[‡‡]; opening pulse height H1 is fixed at ~240 V. We found that small changes in these have dramatic effects on the gas flow profile. The profiles fall into two categories: the no-hold mode, where the valve is driven open by the opening pulse but not held open by the holding pulse, and the full-open mode, where the valve is held open for extended periods of time. Figure 18 shows a comparison of these two modes. We suspect that radical production is extremely sensitive to the gas flow profile, however, we lack sufficient data to make any conclusions. Studies are currently underway to further understand the influence of driver settings on radical yield.

[††] The nominal settings are 12 V, 20 V, 24 V, and 28 V. There is no simple conversion between the nominal setting and the actual output, and higher nominal settings actually produce lower output. To avoid confusion, we always refer to the nominal H2 setting.

[‡‡] Repetition rates above 50 Hz may result in poppet damage and are avoided

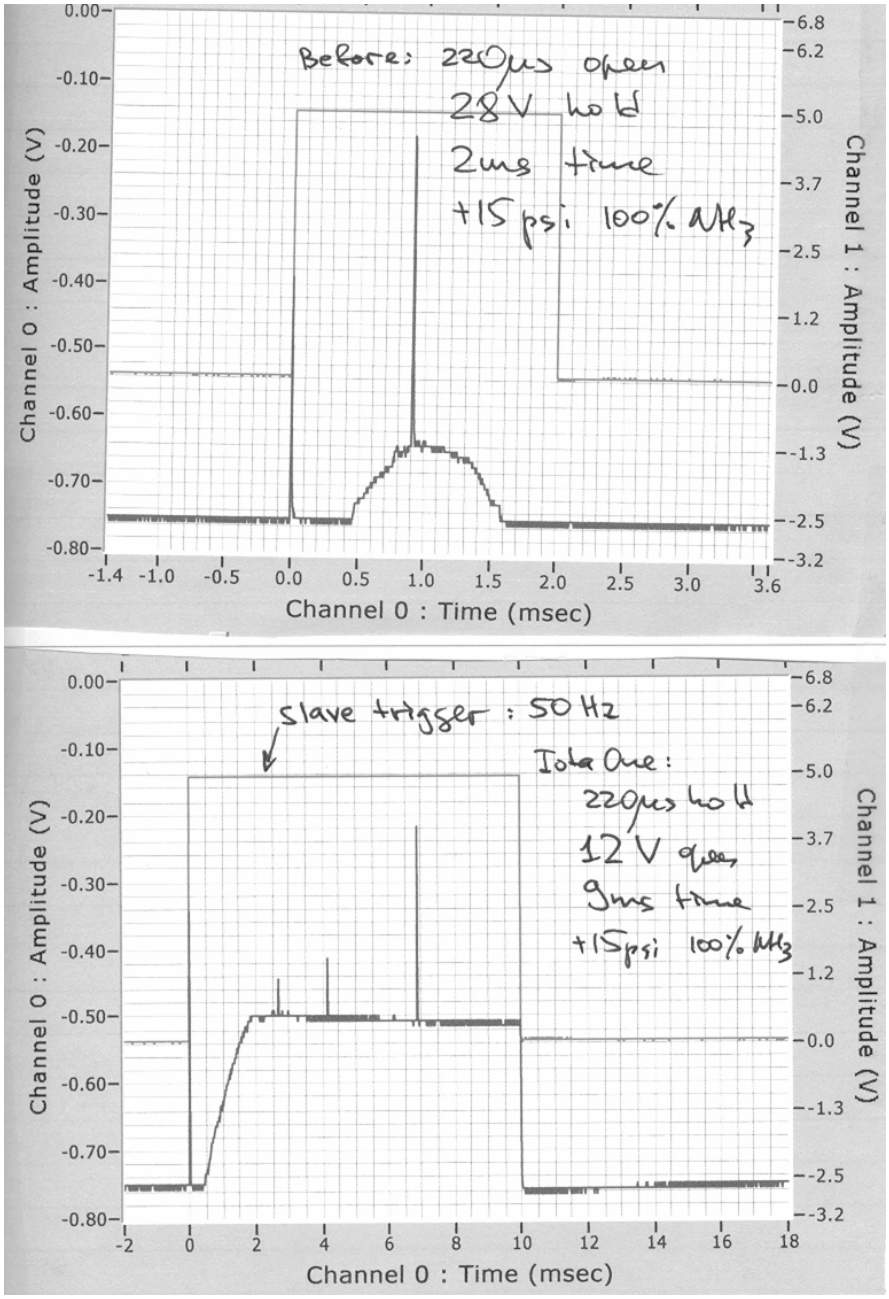

Figure 18: Discharge current profile at different valve driver settings.

Channel 0 is jaw voltage monitor (via 2000:1 divider); change in jaw voltage monitor output indicates discharge current at 0.5 Amp/Volt conversion.

Channel 1 is TTL signal from master/slave trigger circuit which controls the high voltage switch; 5 V sets high voltage on.

Process gas here is 100% NH_3 at +15 psig (i.e. 2 atm stagnation pressure).

5.1.3 Valve positioning and beam dynamics

Beam dynamics phenomena in supersonic beams can be extremely complex [110] and their effects on numbers of molecules that can pass through a small opening, like that in our cryocell, can be rather counter-intuitive [96]. Shock waves generated at walls and edges can alter the expansion and greatly reduce cell loading numbers, forward flux of the beam may have a strongly non-linear dependence on the stagnation pressure of the expansion, etc. It is critical to verify whether for the specific range of parameters employed in our setup the expansion fits the intuitive, linear free-flight model.

To verify the above, we connected a mass-spectrometer to the cryocell, and measured the dependence of its signal on various system parameters. In order to separate the effects of beam dynamics from any chemistry-related radical loss effects, we performed the test with a pure He beam. Figure 19(a) shows the dependence of atom flux into the cryocell on valve Z[§§] position. We observe a quadratic dependence of flux on Z position, which points to a free-flight nature of the beam expansion. Figure 19(b) shows the dependence of atom flux into the cryocell on valve Y position; here the dependence is also consistent with a symmetric forward-peaked expansion. The width of the curve indicates that valve positioning can be done to a few-mm precision without substantial change in the signal, which is comforting for operating an apparatus where displacement of features due to thermal contraction can be up to 5 mm. Finally, the dependence of

[§§] Z axis points along the beam propagation direction; Y axis is perpendicular to both Z axis and the long axis of the discharge region slit. All distances are relative.

atom flux on stagnation pressure, shown in Figure 19(c), also fits a linear expansion model. This test confirms that, at least for the range of parameters where we operate, the behavior of the expansion is intuitive; any counter-intuitive losses in signal that we may observe as parameters are varied are likely due to radical under-production or recombination rather than beam dynamics phenomena.

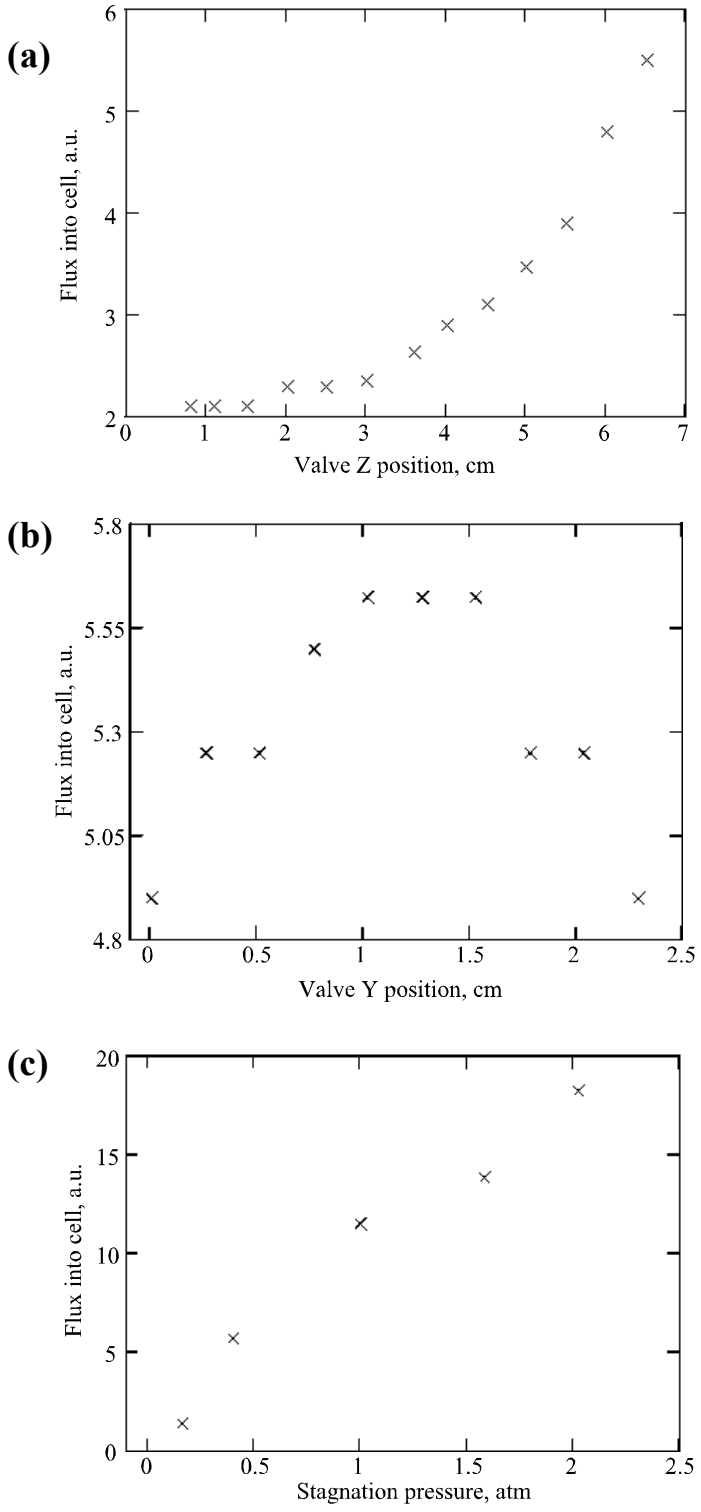

Figure 19: Dependence of beam flux entering the cryocell on: (a) valve-to-cell distance; (b) vertical alignment; (c) stagnation pressure.

Z axis is directed from the valve to the cell; positions are relative.

5.1.4 Compensation coil

In an effort to maximize molecule flux entering the cryocell we try bringing the beam source as close to the cell entrance as possible, which means that the pulsed valve may be subjected to high magnetic fields generated by the trapping magnet. Operation of the valve actuator, a solenoid coil moving a spring-loaded soft-iron armature, is adversely affected by external magnetic field. Figure 20 shows calculated field profiles along Z axis for typical magnet operating conditions; using a test solenoid magnet to simulate similar magnetic fields and field gradients, we found that:

- valve poppet spontaneously stops sealing as field magnitude is increased past ~400 G;
- poppet seal leak rate remains $<10^{-7}$ mbar·l/s for fields up to ~300 G;
- valve performance, defined as the amount of gas released per pulse, is degraded at a linear rate of 0.5% of total capacity per Gauss of external field;
- for a Teflon poppet, valve performance is permanently degraded after exposure to magnetic field of ~400 G; the degradation of valve performance is ~20% at zero applied field;
- for Kel-F poppet, no observable permanent degradation occurs;
- field polarity or field gradients have no effect on the above .

To compensate the external magnetic field we installed a compensation coil around the valve actuator. The coil is made of 18 windings of 1/8" nominal diameter alloy 122 copper tubing; it is connected to an external current source whose output tracks that of the magnet power supply. The coil produces peak field of 4.9 Gauss per Ampere of current. Cooling water flowing through the tubing allows the coil can operate at up to

100 Amp in a continuous mode; higher currents would be possible with minor modifications to current supply leads.

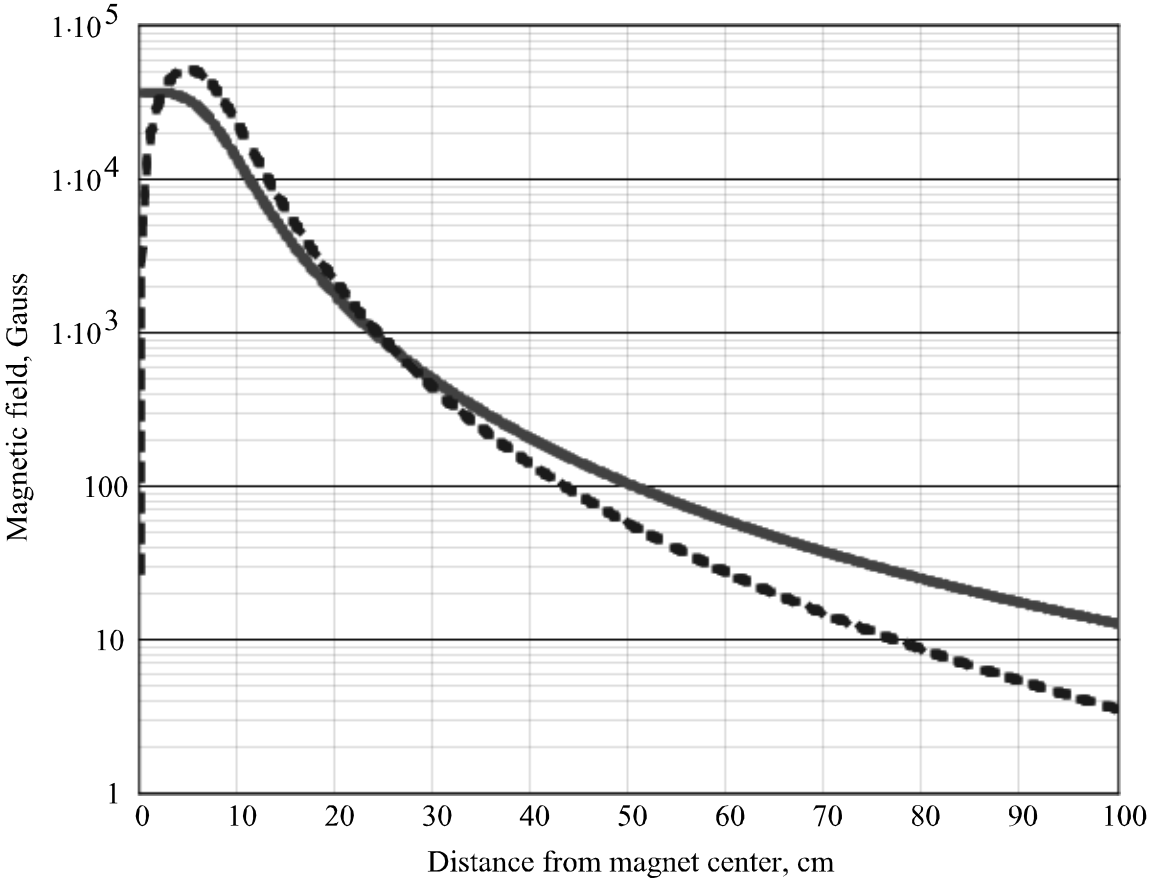

Figure 20: Magnetic field along magnet axis
Solid curve: Helmholtz configuration, dashed curve: anti- Helmholtz configuration.
Both curves are for corresponding operating currents, see Table 11.

In addition to the compensation-coil resistive heating and water cooling, the valve is subjected to the following heating and cooling sources: discharge heating (particularly strong during glow-to-arc transitions), poppet actuator heating (especially for high repetition rates), and radiative heat transfer to the 77-K shield that surrounds the valve

assembly. Overheating of the valve may result in damage to the poppet; overcooling may result in ammonia condensation (see Figure 21) and in unpredictable opening performance. Cooling water flowing through the compensation coil acts as a stabilizer, maintaining the valve body within 20°C of room temperature. Temperatures of valve assembly are monitored with K-type thermocouples at the front of the valve spacer, in the middle of the valve body, and on a current lead of the compensation coil.

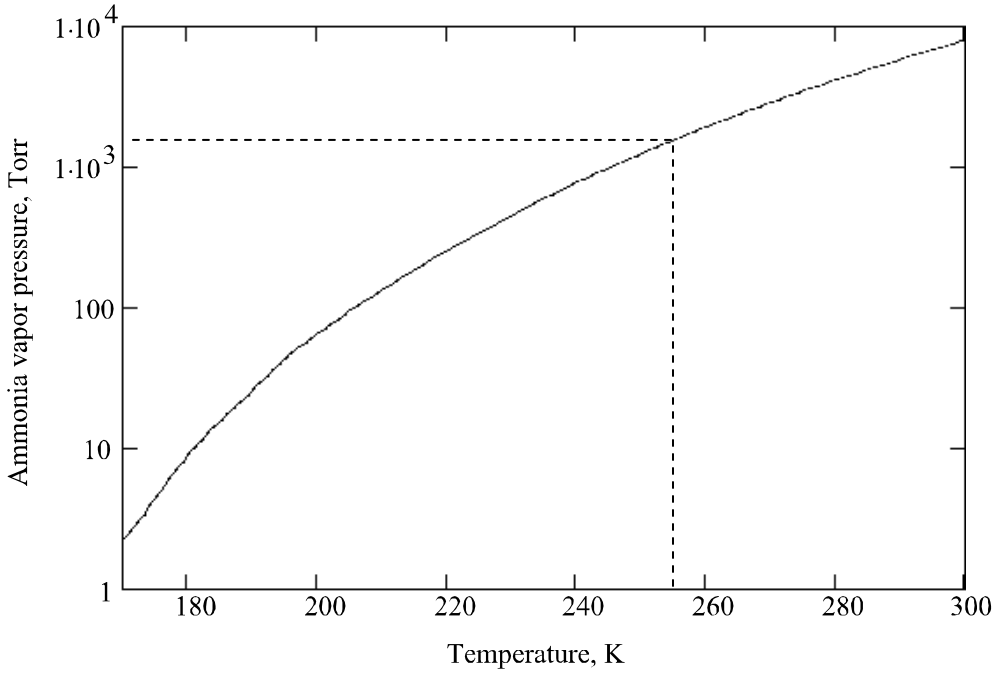

Figure 21: Saturated vapor pressure of ammonia.
Valve operation below -20°C for +15 psig stagnation pressure is highly undesirable due to ammonia condensation. Based on data from [108].

5.2 High voltage circuit

The high voltage circuit is responsible for providing a high-voltage discharge pulse, for stabilizing the discharge against arcs, and for monitoring of the discharge performance. The schematic is provided in Figure 22; the sections below describe individual components of the circuit. Note that the only low-impedance grounding point in the entire circuit is the return terminal of the high voltage power supply; this allows us to detect ground shorts and unintended discharge paths.

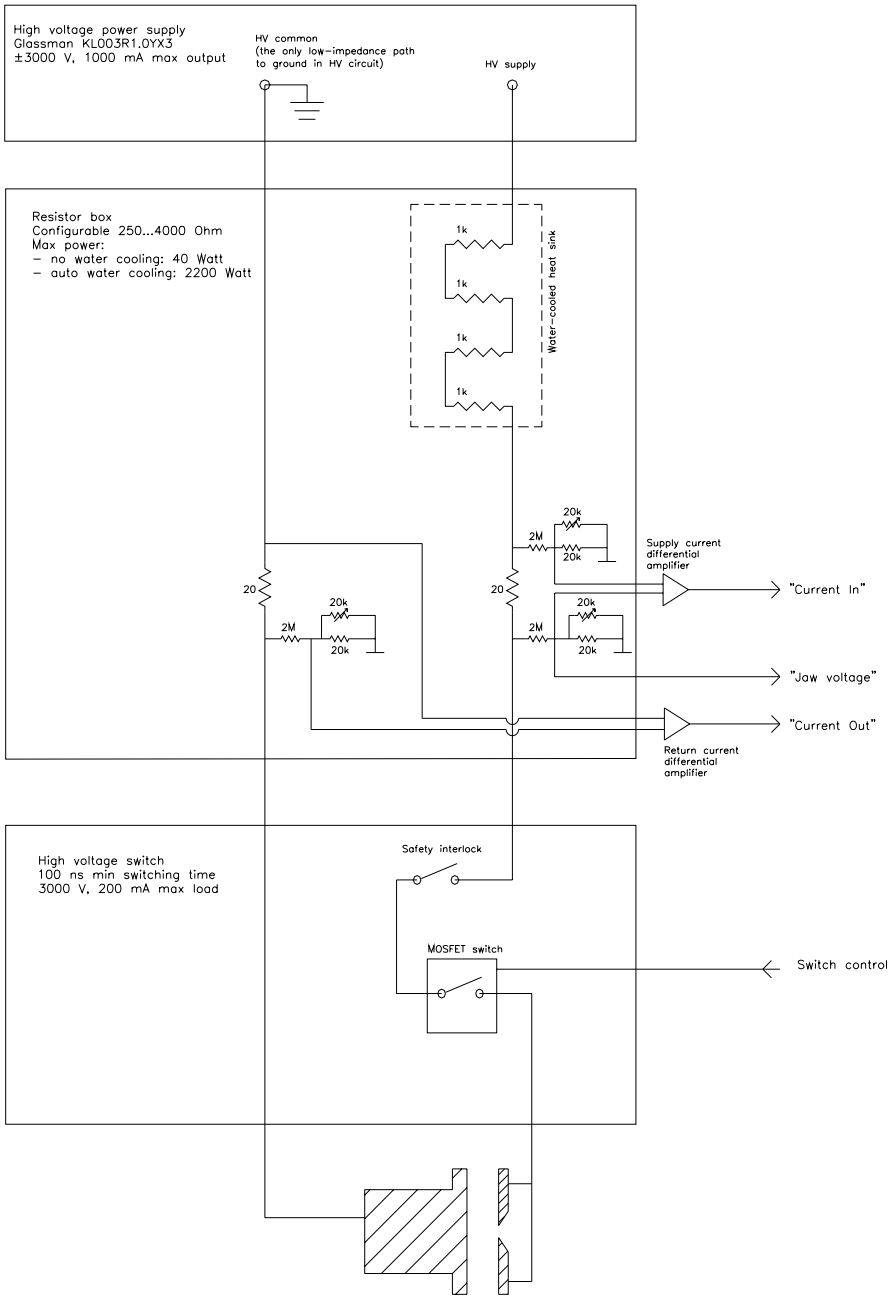

Figure 22: High voltage circuit.

5.2.1 Resistor box

Figure 23 shows a schematic gas discharge *I-V* curve. The ideal operating point is the maximum current point of normal glow discharge, indicated with a double arrow. Above this point, the required voltage grows with little increase in current (the abnormal glow region) until a rapid transition into a highly undesirable arc mode occurs.

Upon inspection of Figure 23 it becomes clear that discharge operation with only a power supply is not possible. Consider the gas with no voltage applied. As the voltage is increased, the conditions are not sufficient for the avalanche to sustain itself, so only primary electrons contribute to the current. Once the voltage reaches the ignition voltage $V_{i,}$ the avalanche becomes sustainable. Further increase in discharge current is accompanied by a decrease in voltage drop: the unstable region in Figure 23 has a negative differential resistance $R_{diff} = dV/dI$. This means that if after ignition the glow discharge is simply provided with a constant source of high voltage, the circuit will not remain stable but will oscillate between no-avalanche and unstable regions, as indicated in Figure 23 with a two-ended arrow – a well-known neon lamp oscillator circuit is a good example of this behavior. In order to stabilize the discharge and bring operating current and voltage to the desired normal-glow point, the overall circuit must have a positive differential resistance. This can be achieved by adding a sufficiently large resistor in series with the discharge; the resistor *I-V* curve is schematically shown with a dashed line. The discharge voltage and current are then set by the intersection of the discharge *I-V* curve and the circuit load line, shown by a dash-dot line in Figure 23; V_0 is the power supply voltage and R_0 is the resistor value.

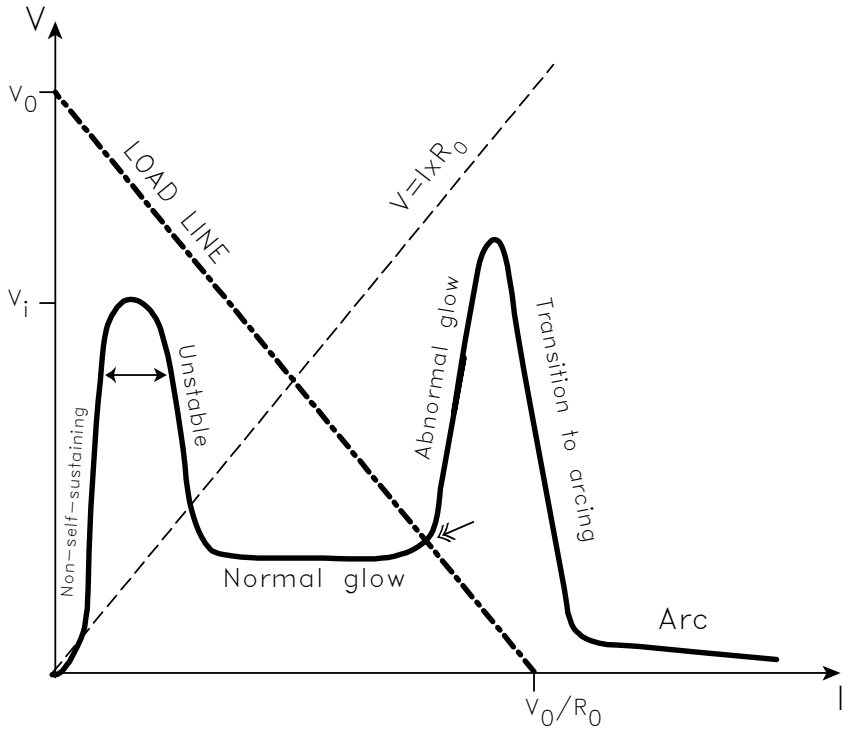

Figure 23: Typical discharge *I-V* curve.

In our apparatus the stabilizing resistance is provided by four 1000-Ohm 600-Watt resistors[*]; the resistors are mounted on a water-cooled heat sink to permit high duty cycle operation. To prevent moisture condensation on high-voltage components, cooling water is automatically turned on only when the heat sink temperature is above 70°C, which occurs at ~40 Watt average power dissipation.

We attempt to operate the discharge in a normal-glow regime and to make sure that the only discharge path is from the high-voltage jaws to the valve spacer. However, since we are dealing with gas flow in a grounded metal chamber, it is critical to constantly monitor that the above conditions are present. Jaw voltage monitor signal, constantly monitored on an oscilloscope, is the voltage present at the output terminal of

[*] Ohmite TAP600, Ohmite Mfg. Co., Rolling Meadows, IL

the resistor box; a large drop in the jaw voltage indicates an arc. Two 20-Ohm 20-Watt current shunts[†] can also be used to monitor current flowing in and out of the power supply, if a discharge path to chamber ground is suspected. All monitor terminals in the resistor box are fitted with adjustable 2000:1 voltage dividers to prevent accidental damage to the measurement equipment.

[†] Ohmite TAH20, Ohmite Mfg. Co., Rolling Meadows, IL

5.2.2 Transition from glow to arc discharge

We measured the *I-V* curve of the discharge for typical operating conditions, as shown in Figure 24. The results confirm that the discharge is operated at the desired maximum-current normal-glow point of the *I-V* curve; for currents above 120 mA we observe a transition to abnormal glow followed by an abrupt transition to arc mode.

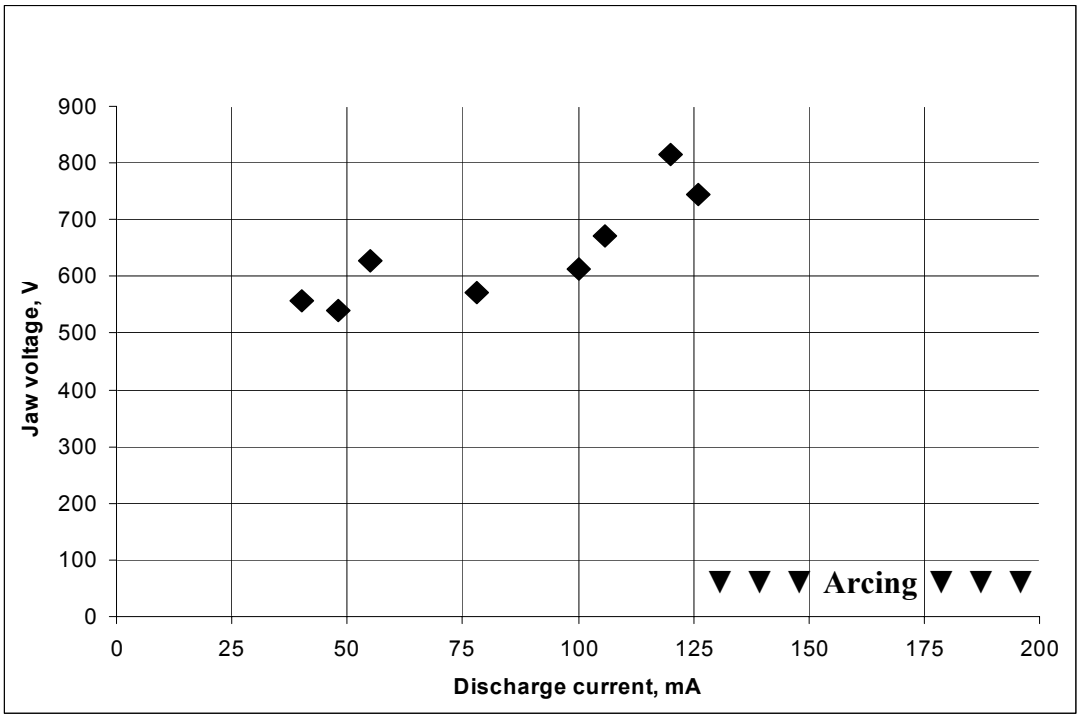

Figure 24: Measured discharge *I-V* curve.

Even though the discharge parameters are set to produce normal glow discharge, occasionally the discharge becomes unstable, producing arcs; we attribute this to contamination of the electrodes. Signs of instability show up in jaw voltage monitor signal, as shown in Figure 25. The instability can usually be removed by stopping the

measurement in progress, lowering the power supply voltage, then starting process gas flow and slowly raising the voltage while monitoring for arcs. As contaminants are burned away, the discharge returns to its stable mode. It is critical to never operate the discharge in the unstable (arcing) mode for extended periods of time: any data acquired in the unstable mode is suspect, as radical yield is changing unpredictably and irreproducibly; fluorescence background fluctuates due to bright flashes of light coming from the arcing, making background subtraction difficult; in extreme cases the valve overheats and poppet burnout occurs.

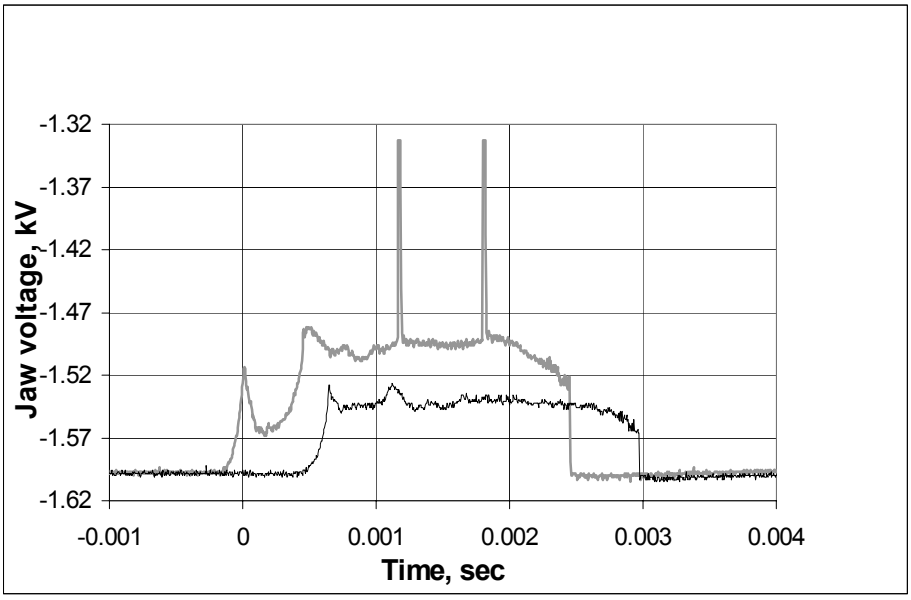

Figure 25: Onset of discharge instability.
Here process gas pressure was increased at a fixed voltage until arcs appeared.
Dark trace: stable discharge; light trace: occasional arcing.

5.2.3 High voltage switch

The profile of discharge current during a gas pulse exhibits a gradual ramp-up and gradual ramp-down, most likely due to a finite valve poppet opening/closing time. In addition, the profile exhibits a pattern of after-pulses likely attributed to bouncing of the valve poppet[*], as shown in Figure 26; the pattern of after-pulses is not reproducible exactly between different measurements. For certain types of measurements, the after-pulses represent a substantial source of background noise; the slow ramp-down of the discharge current is also not desirable, as the glow of the discharge interferes with fluorescence collection. For these types of measurements, a high-speed high-voltage switch in the circuit is activated to provide a rapid turn-off of the discharge current and a suppression of the after-pulses.

Switching is performed by a TTL-controlled MOSFET device[†]. The device is capable of switching currents up to 200 mA and voltages up to 3 kV in a sub-microsecond time. The switch unit includes a low-speed mechanical relay that functions as a safety interlock in case of MOSFET malfunction. Figure 27 gives an example of discharge current profile with the high-voltage switch in operation. Even though the supply voltage is reduced on a sub-μs timescale, the glow of the discharge, perhaps due to decaying metastables, is present for longer times. We find that the discharge glow

[*] The after-pulsing pattern changed dramatically when the poppet was replaced and when the valve spacer was added to the system. The poppet bounce effect appears to be a common problem of all Series 9 valves [140].

[†] HTS-31, Behlke Electronic GmbH., Kronberg, Germany

disappears within ~100 μs after the switch interrupts the high voltage supply; the exact delay depends on process gas pressure, and must be found experimentally for each measurement setting.

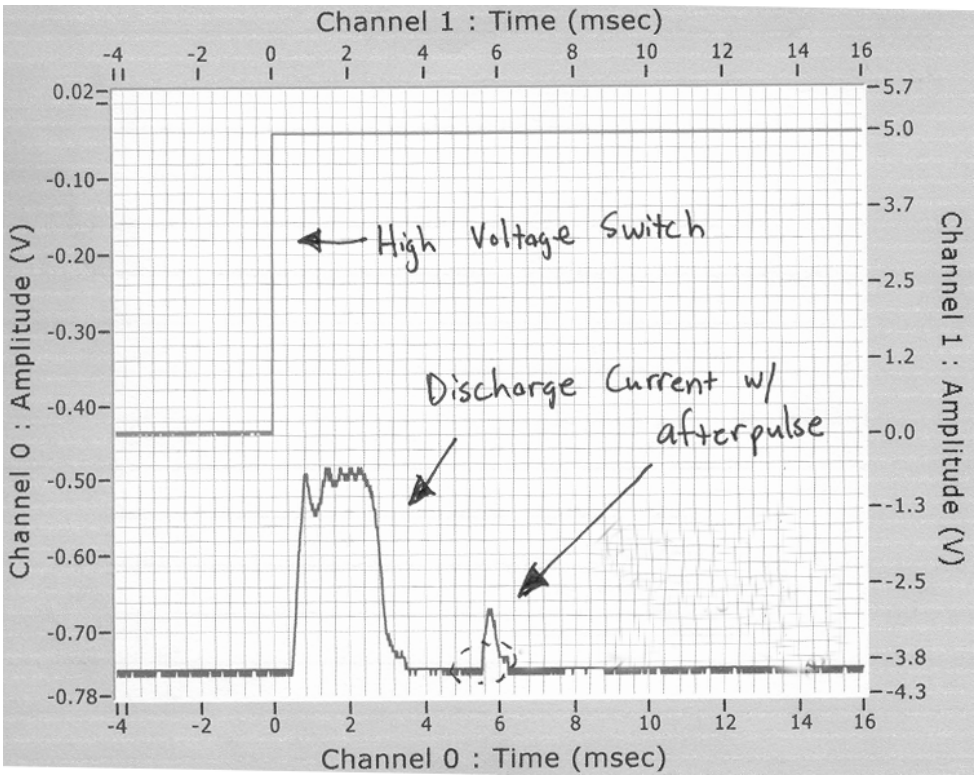

Figure 26: After-pulsing current profile.

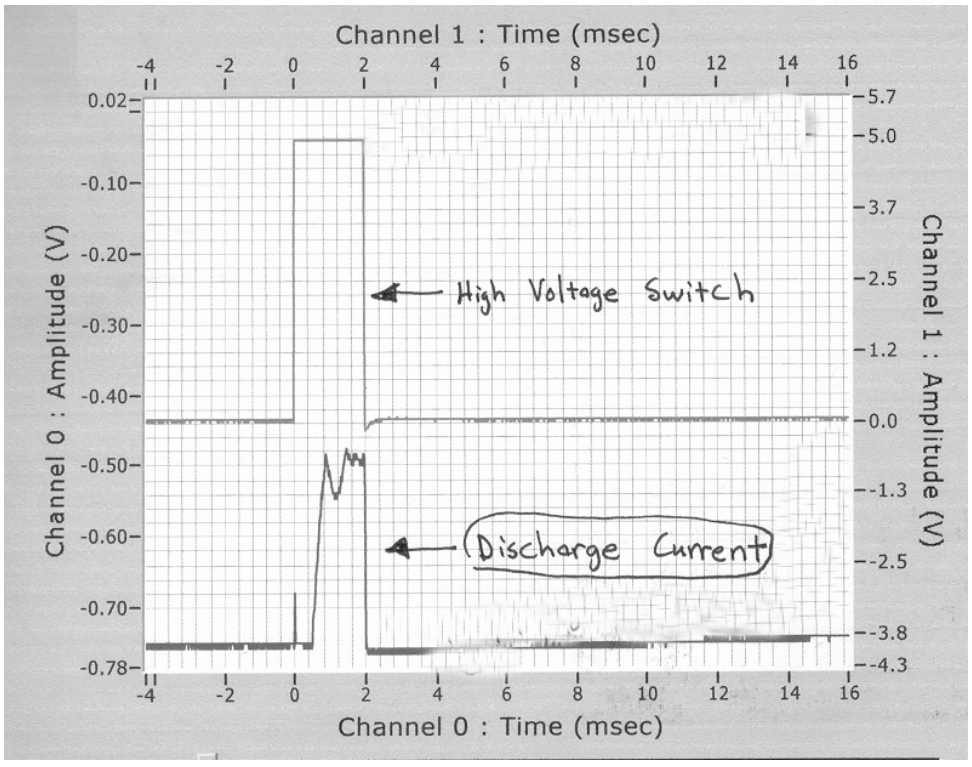

Figure 27: Discharge current profile with high voltage switch activated.

5.3 Gas handling system

The gas handling system schematic is shown in Figure 28 and Figure 29. It is not practical to describe its details here; instead, this section outlines design considerations that were important in setting up the system.

5.3.1 Process gas mixture preparation

The kinetics of radical production in glow discharge is extremely complex, as outlined in section 4.2.2. A number of processes, such as carrier gas ionization, avalanche multiplication, molecule fragmentation, radical recombination, electronic and vibrational excitation and quenching, background gas scattering etc. influence the radical yield. To provide sufficient flexibility for future radical production needs, the gas handling system is large and scalable. It takes mixture components from up to six different inputs, mixes them in a high-pressure vessel, and supplies process gas mixture at a given pressure via a vacuum regulator[‡]. The key component of the mixture is anhydrous ammonia[§] (99.999% purity); other inputs in the system presently are: argon[**] (99.999% purity), helium[**] (99.999%), neon[**] (99.999%), xenon[††] (99.995%), krypton[††] (99.995%). The system is

[‡] Tescom 64-5040KRU08, Tescom Corp. High Purity Controls Division, Elk River, MN

[§] Matheson Tri-gas, Montgomeryville, PA

[**] Airgas Inc., Radnor, PA

[††] Spectra Gases Inc., Branchburg, NJ

automated in order to make it possible to quickly scan through a variety of mixtures and identify the one most suitable for the particular measurement.

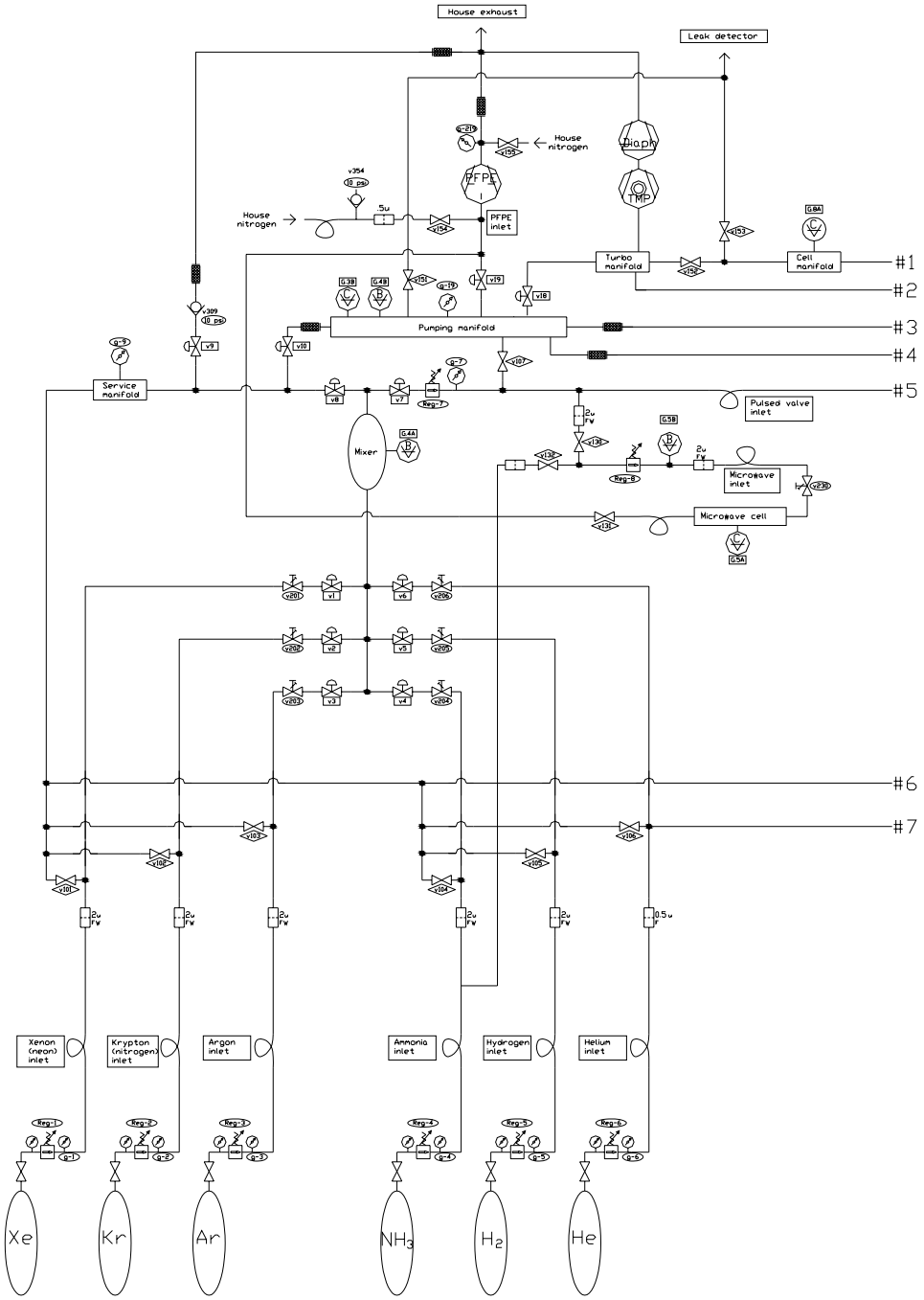

Figure 28: Gas handling system, part I

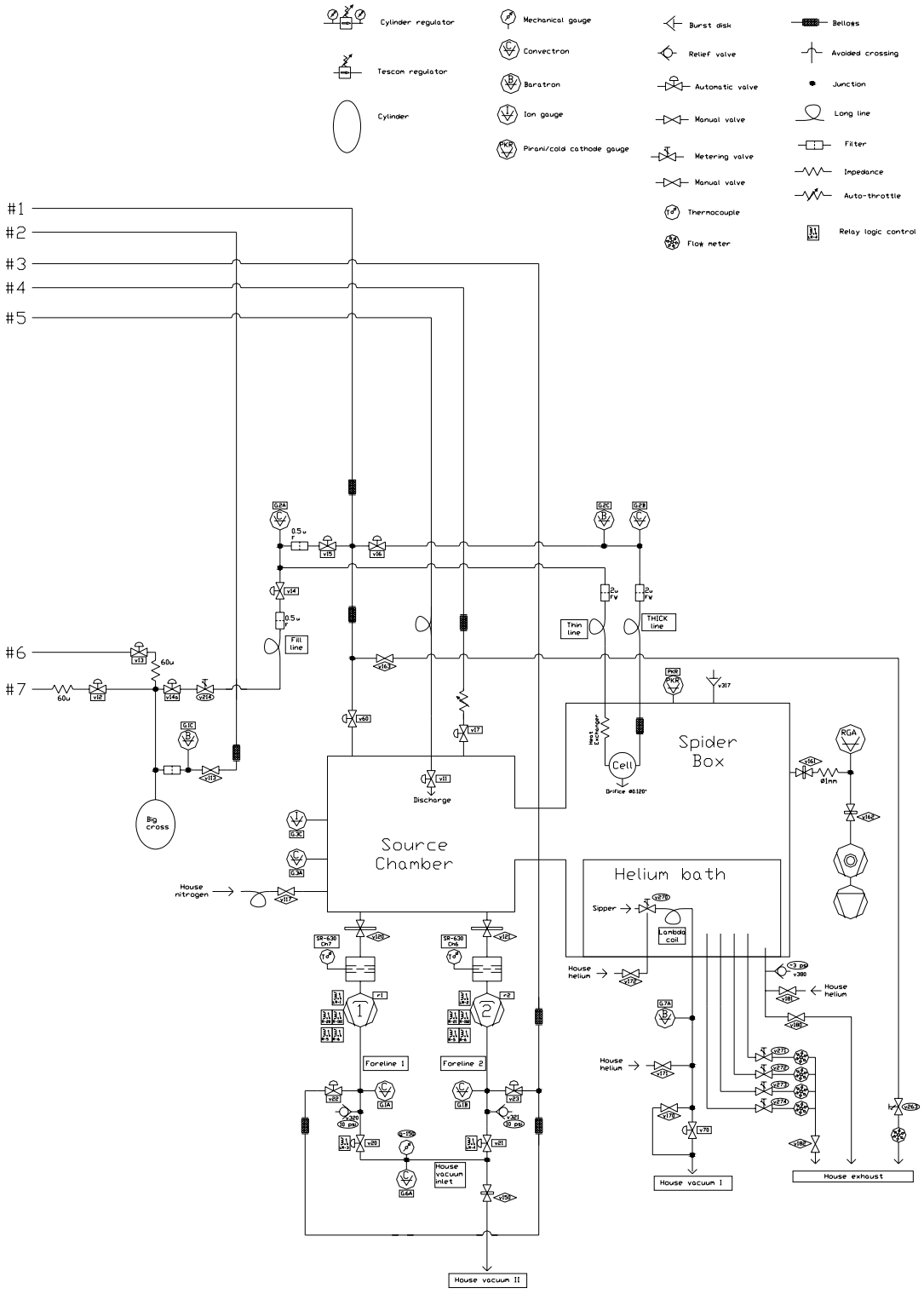

Figure 29: Gas handling system, part II

The gases from various inputs are placed into a vessel ("mixer") to create the process gas mixture; proper mixing of components is critical for repeatable production yields. We used a residual gas analyzer to test the mixing performance, and discovered that diffusive mixing is too slow for practical timescales. If components are placed into the mixer in an arbitrary order, mixing is not complete, as shown in Figure 30. This is easily seen from a calculation of inter-diffusion time for gases in the mixer: it is ~10^3 seconds; thus diffusion alone is not sufficient for mixing. Convective motion, however, is sufficient: when components are placed through the top of the mixer in order of increasing molar masses, we observe proper mixing on sub-minute timescale.

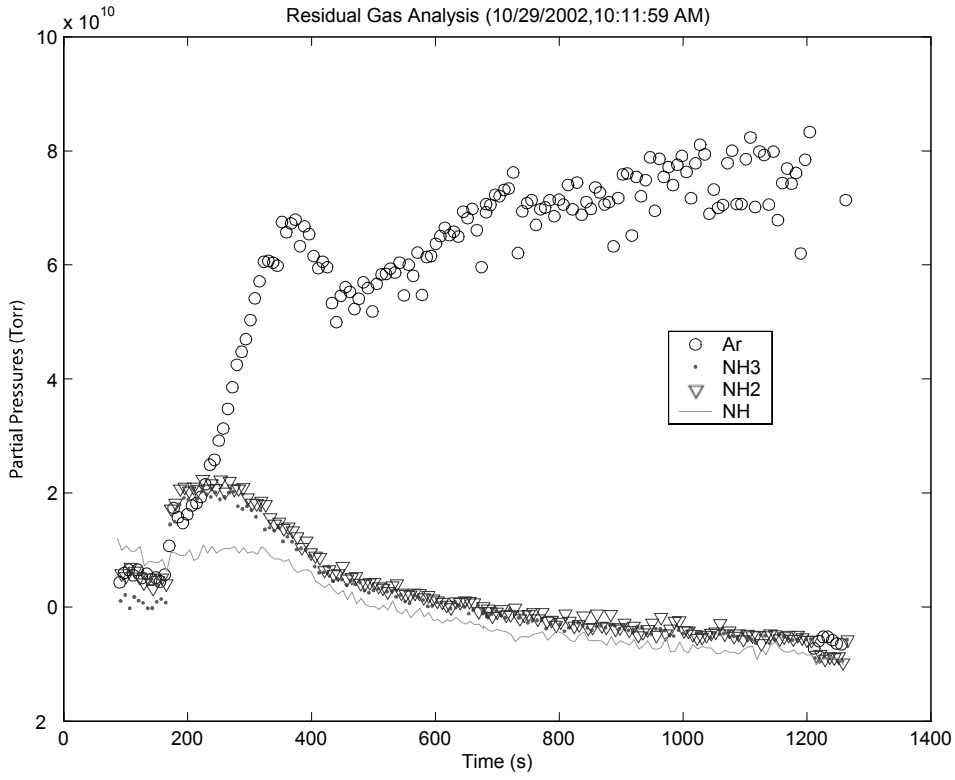

Figure 30: Evidence of poor non-convective mixing.
Here ammonia (mass 17) was placed into mixer above argon (mass 40).

Empirical evidence suggests that discharge cleanliness may have a substantial effect on radical production and on stability with respect to arcing. To maintain purity of the process gas mixture, only electropolished stainless steel tubing and specially cleaned fittings were used in construction of the system. To avoid corrosion by ammonia, no Viton o-rings or silver-plated gaskets were used anywhere in the gas handling or vacuum systems. Copper and brass, also known to have poor ammonia resistance, were avoided whenever possible[‡‡]. To avoid pump oil breakdown, all significant quantities of ammonia are pumped out of the system via a PFPE-filled rotary pump[§§].

[‡‡] We experimented with gold-plated copper ConFlat gaskets and discovered that their sealing is not reliable, so regular copper ConFlat gaskets were used throughout the system. We have observed corrosion on gaskets that were taken off vacuum chamber ports, so in the long run regular inspections and replacements may be required. Of course, cryostat and cell have numerous copper and brass parts that are not practical to replace with other materials, and we have to accept their limited lifetime.

[§§] Other common materials that are severely attacked by ammonia are plastics like Vespel, Acrylic, and Delrin. If corrosion resistance wasn't a concern, Vespel would be an ideal material for high-voltage component isolation.

5.3.2 Buffer gas supply

The buffer gas handling circuit is designed to provide a stable density of cold helium buffer gas in the cell. Buffer gas density and temperature is monitored with room-temperature pressure gauges and temperature sensors* on the outside of the cell. A "thick" (1/4" nominal diameter) line connects the cell with a high-precision capacitance manometer† at room temperature. The line is sufficiently large to avoid any thermomolecular effects [98]; we also verified the absolute accuracy of pressure measurement to be within 30% using a fixed-volume rise-of-pressure method. Relative accuracy of density measurement is within a few percent, limited by temperature differentials in the buffer gas cell.

Any flow of buffer gas through the thick line would affect the pressure measurement, so helium is flowing into the cell through a separate, "thin" line. The thin line (1/16" nominal diameter) connects the cell with the gas handling system helium supply. The line passes through a heat exchanger attached to the helium bath to ensure that incoming helium is cooled to the cell temperature.

The helium supply is a 10-liter volume filled to a pressure between 1 and 1000 Torr. A variable impedance separates the volume from the thin line; for a given setting of the impedance the pressure in the cell is linearly related to the supply pressure, which allows us to accurately set the required buffer gas densities.

---

* Uncalibrated silicon diodes DT-470-SD-13 and calibrated Cernox sensors CX-1030-SD-1.4B from Lakeshore Cryotronics Inc.

† Baratron 627B-U5TBD2B, 50 mTorr full scale; MKS Instruments Inc.

5.4 Vacuum chamber and pumping

The vacuum chamber is composed of two parts: source chamber, which houses the radical source and provides high vacuum pumping, and main chamber (colloquially referred to as "spider box"), which houses the cryogenic apparatus. Two vacuum spaces are joined with a 9" nominal diameter bellows and held together with a rigid mechanical structure designed to prevent the parts from moving as the chamber is evacuated. Figure 31 shows the overall layout of the vacuum system.

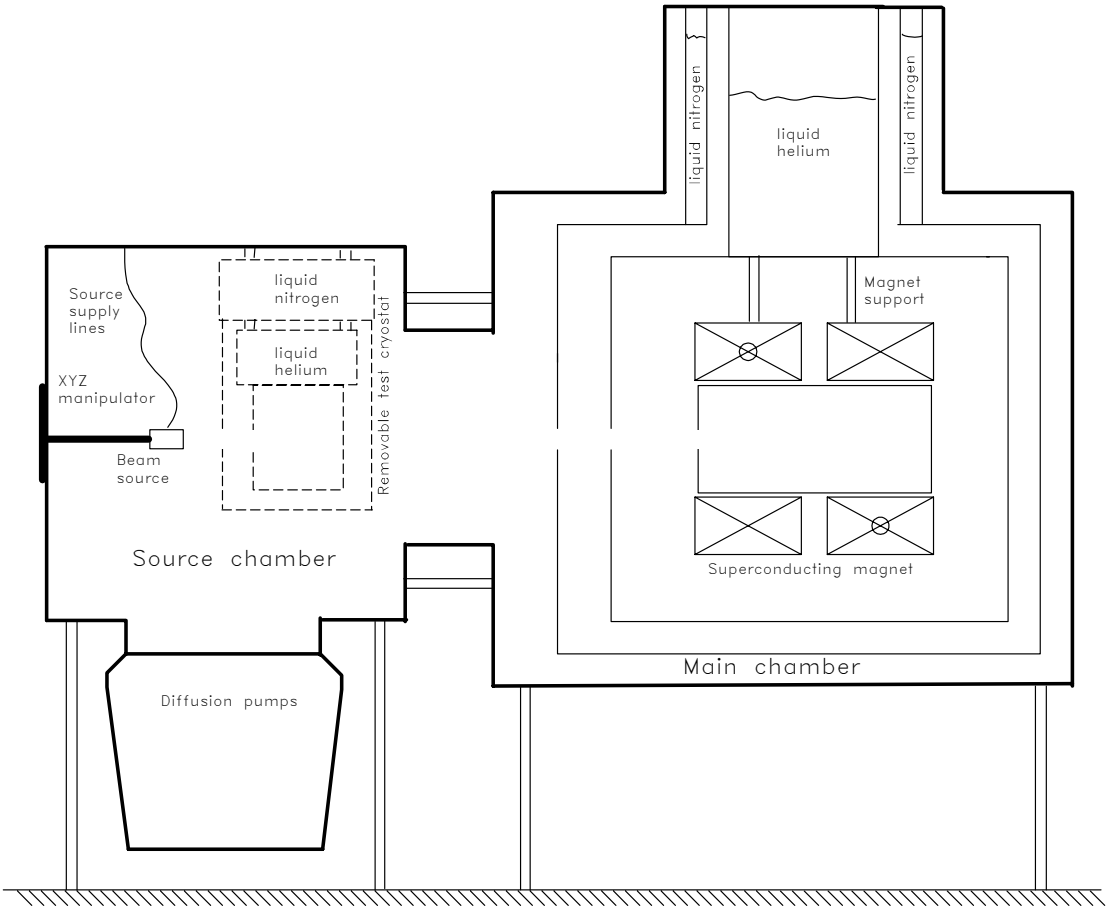

Figure 31: Layout of the vacuum system.

5.4.1 Source chamber

The source chamber houses the pulsed valve and provides electrical, gas, and other feedthroughs. Two diffusion high-vacuum pumps[‡] with liquid nitrogen cold traps provide ~2000 liter/s pumping speed at inlet pressures up to 10^{-3} torr. The pumps are filled with light-fraction (non-fluorinated) diffusion pump oil; in order to prevent oil breakdown by ammonia, the liquid nitrogen cold traps, which condense ammonia in them, are allowed to warm up above 85 K only with the diffusion pumps cold; released ammonia is then diverted into a fluorinated-oil pump[§]. Figure 33 shows the dependence of chamber pressure on total gas load from the pulsed valve and the dependence of beam flux into the cell (measured with a mass-spectrometer, see 6.1.2) on the chamber pressure. Measurements shown in Figure 32 and Figure 33 confirm that the pumps are adequate for nominal gas loads[**] up to 10 Torr·s·Hz[††], which corresponds to ~10^{-4} mTorr background gas pressure, and that no adverse effects on forward beam flux due to background gas appear for this gas load.

The test cryostat, described in section 3.1, can be installed inside the source chamber to perform tests of radical production and spectroscopy of cold NH, as described in section 6.2.

[‡] VHS-6, Varian Vacuum Inc.

[§] Leybold D8B, filled with PFPE oil

[**] Nominal gas load is defined here as product of process gas stagnation pressure times nominal pulsed valve open time times pulse repetition rate.

[††] = 13 atm·msec·Hz

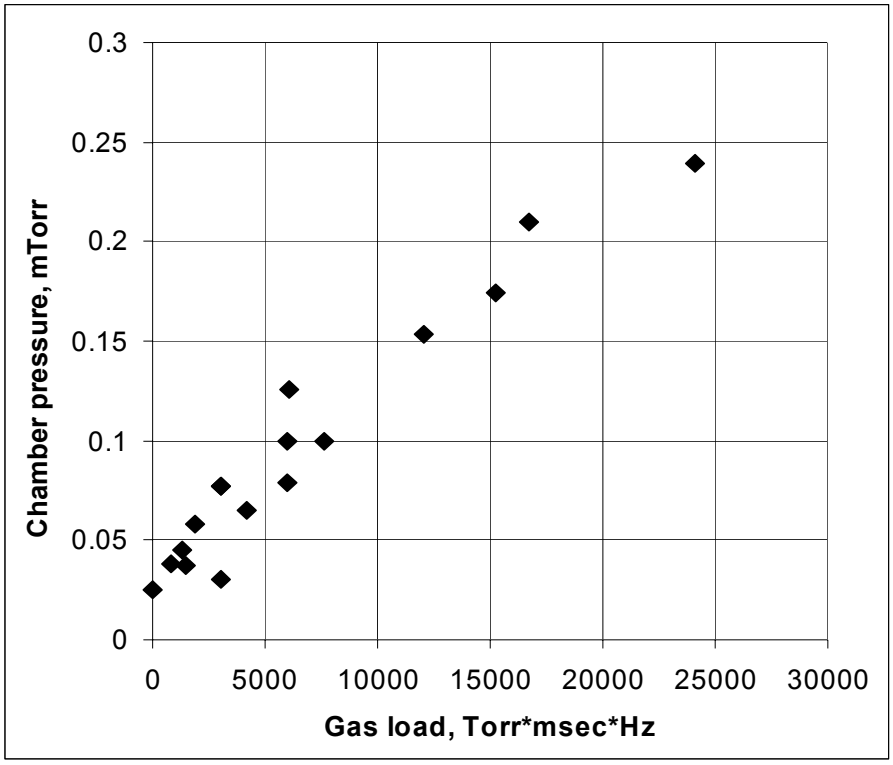

Figure 32: Performance of source chamber diffusion pumps under gas loads.

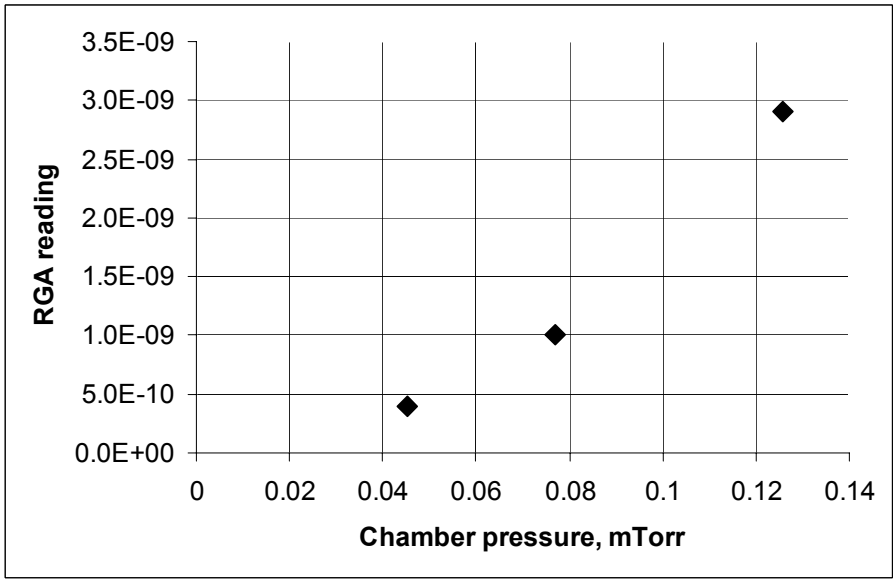

Figure 33: Correlation of chamber pressure and centerline beam flux.

5.4.2 Main chamber

The main chamber is shown in Figure 34. The chamber houses the main cryostat, radiation shields, and superconducting magnet. Side ports provide 5 axes of optical access to the center of the cryocell, spaced at 30^{o} in the plane perpendicular to the molecular beam axis. Additional ports are available for off-axis optical access, fluorescence collection through the back of the cell, and feedthroughs.

The chamber is constructed of 0.75" thickness stainless steel 304; while SS 304 is known to become magnetic after being subjected to mechanical stress[‡‡], we calculate the worst-case scenario force on the energized magnet to be under 1 N[§§]. Another function of the thick stainless steel plates of the main chamber is personnel protection in the unlikely event of catastrophic failure of the magnet: in anti-Helmholtz configuration at operating current the magnet stores 32 kJ of energy[***].

[‡‡] see Fig. 9 on p.20-4 of Metals Handbook: Desk Edition, ASM, 1985.

[§§] A bigger problem is presented by strongly-magnetic objects outside the vacuum space, e.g. fastening hardware, gas cylinders, etc. A soft-iron object 25 mm in diameter at the outer surface of the main chamber will experience ~10 N force when the magnet is at full operating current; 40 cm away the force is still as much as ~0.5 N for Helmholtz configuration and ~0.1 N in anti-Helmholtz configuration.

[***] which is approximately the kinetic energy of a WWII anti-tank round; a 10-kg projectile ejected from a failed magnet would have 80 m/s velocity.

Figure 34: Main vacuum chamber, scale drawing.

Approximate dimensions are 28"x28"x30". On the left is molecular beam entrance port (“South side”); on top is cryostat mounting port.

5.5 Main cryostat and radiation shields

The main cryostat* and radiation shields attached to it are shown in Figure 35 and Figure 36. The cryostat is a common liquid-nitrogen shielded helium bath; it is designed to accommodate magnet leads and a ^{3}He refrigerator.

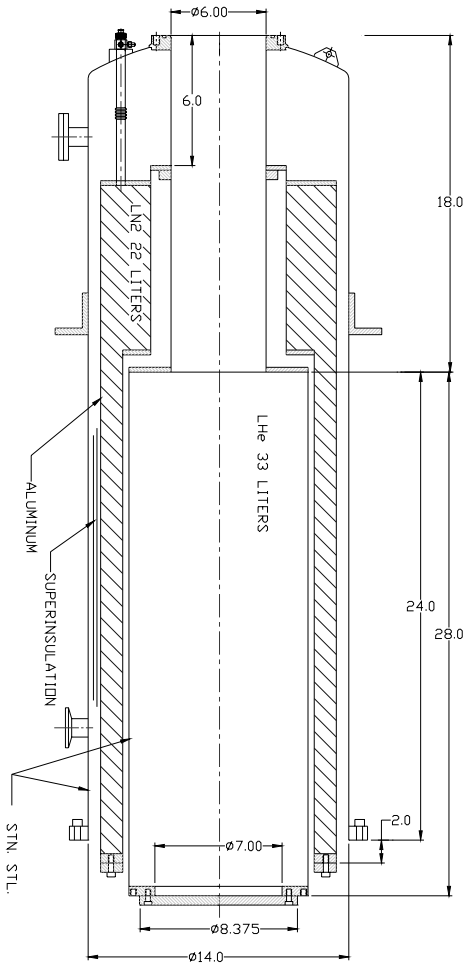

Figure 35: Main cryostat, schematic view.

* Precision Cryogenic Systems Inc., Indianapolis, IN

Radiation shields are a critical item in our effort to combine an in-vacuum superconducting magnet with a room-temperature molecular beam. In the past, buffer-gas cooling experiments relied on helium surrounding the magnet to generate stable 4-K temperatures throughout the magnet. For the in-vacuum magnet configuration, we have to rely on thermal conductivity of solid materials, and thermal radiation reaching the magnet or its current-supply leads may produce "hot spots" that can cause a quench; sufficient performance of the radiation shields is therefore crucial. The shields are constructed of 0.125" thickness OFE copper and gold-plated with 50 μm gold to increase their IR reflectivity. To verify the shield performance, we placed electric heaters in various locations and measured steady-state temperatures when heaters were turned on. We conclude that the 77-K shield temperatures remain within 10 K of the nitrogen bath temperature, 4-K shield temperatures within 1 K of the helium bath temperatures, and that up to 1 Watt of additional power can be deposited into the 4-K shield while maintaining its temperature within 1K of that of helium bath.

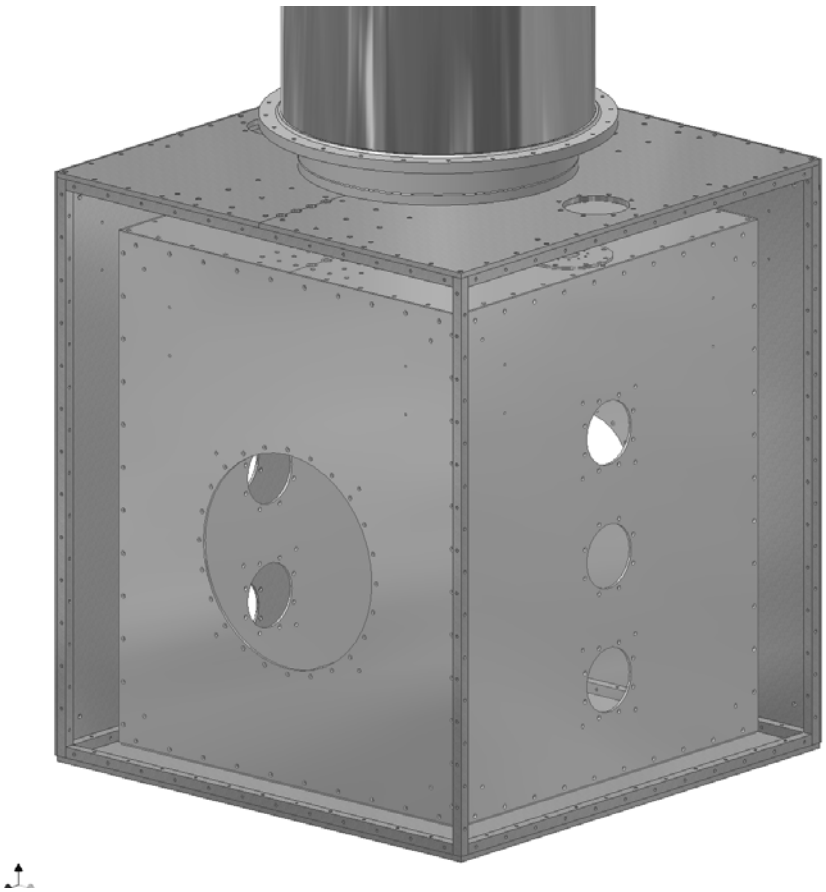

Figure 36: Radiation shields, scale drawing.

Parts removed to show hidden detail.

5.5.1 Lambda coil refrigerator

Sensitivity of Zeeman relaxation measurement depends on the thermodynamic equilibrium ratio of populations of high-field seekers to low-field seekers

$$f_{Zeem} = \exp[\frac{2\mu B_{Zeem}}{k_B T}] \tag{22}$$

and the success of trapping depends similarly on the population of molecules at the trap edge

$$f_{trap}^{-1} = \exp[-\frac{\mu B_{trap}}{k_B T}] \tag{23}$$

Since maximum values of Zeeman and trapping fields B_{Zeem} and B_{trap}, and the value of molecule magnetic moment μ, are fixed, varying temperature T is the only approach to enhance these factors. The effect of lower cell temperatures on sensitivity of Zeeman relaxation measurements and on success of trapping is shown in Figure 37.

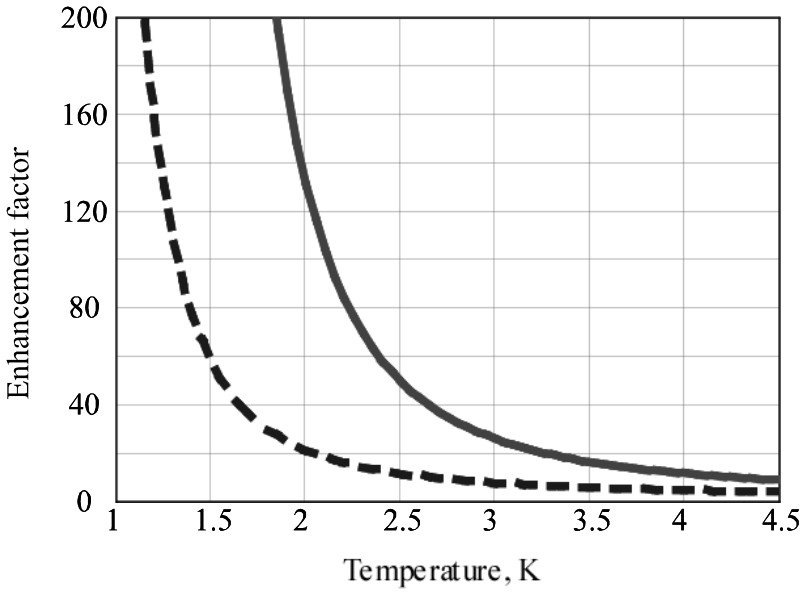

Figure 37: Temperature-dependent enhancement factors.
Solid curve: f_{Zeem}; dashed curve: f_{trap}; assume $2\mu_B$ molecules and magnet running at corresponding operating currents.

In order to achieve temperatures below 4.2 K, some type of refrigerator must be added to the cryostat. In the future generations of the apparatus we plan to add a ^{3}He refrigerator to lower the cell temperature to ~500 mK, similar to the apparatus described in section 7.3. At the current stage, in order to avoid technical complications associated with thermal isolation of a cryocell from the magnet bore, we chose to cool the entire 4-K part of the apparatus, i.e. the 4-K shield, the magnet support structure, and the magnet, to a lower temperature. Large radiative heat loads would not permit the use of a ^{3}He refrigerator to provide cooling of such a massive object, so a lambda-coil refrigerator was installed to provide cooling down to as low as 2.5 K. As can be seen from Figure 37, this

temperature decrease already provides a substantial benefit for the Zeeman relaxation measurement[†].

Figure 38 shows a schematic of the lambda-coil refrigerator[‡]. The refrigerator achieves cooling by simply pumping on liquid ^{4}He; the main difference between using a lambda coil and pumping on the entire bath is that a significantly longer run time can be obtained. Heat capacity of liquid helium in the bath is much greater than heat capacity of the parts the apparatus to be cooled[§]; for the lambda coil, only liquid helium at the very bottom of the bath needs to be cooled, while pumping on the bath requires cooling of all of helium in the bath. Additional benefits of a lambda coil are simplified operation of vapor-cooled magnet leads and the possibility of adding liquid helium to the bath while the apparatus is below 4 K.

[†] If, however, the radiative loads are contained by separating the magnet thermally from the copper radiation shields, cooling the entire magnet with a ^{3}He refrigerator becomes practical. We calculate that only ~0.5 J of energy is released when the entire magnet is cooled from 1.2 K to 0.3 K, which corresponds to latent heat of ~170 ml of liquid ^{3}He, much less than a typical refrigerator charge.

[‡] The design was modeled after an unidentified Oxford Instruments Inc. product; sipper needle valve supplied by Janis Research Company Inc., Wilmington, MA.

[§] E.g. specific heat at 2.5K of 4He is ~3 J/g·K and of Cu is ~30 μJ/g·K [141]

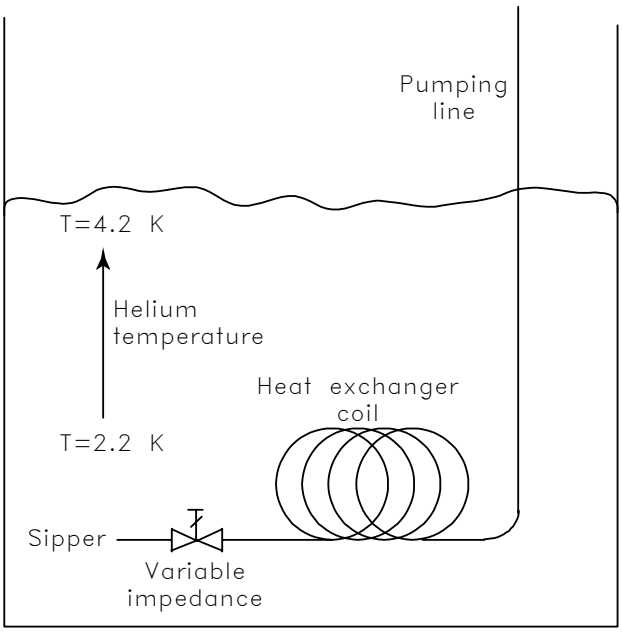

Figure 38: Lambda coil schematic.

5.6 Charcoal cryopumping

Presence of helium gas immediately outside the cell opening causes scattering of the incoming molecular beam, and helium entering the region outside 4-K space will generate enormous heat loads. Thermal radiation shields surrounding the cell must be optically opaque, so two options exist to prevent helium buildup between the cell and the radiation shields: operating a pump inside the cryogenic region to capture helium leaving the cryocell, or constructing gas-conducting radiation shields (e.g. chevron baffles, see 3.1 and [102; 142]). Our experience indicates that both methods have to be implemented for different locations in the apparatus, as described below.

5.6.1 Charcoal sorbs

The only type of pump for helium gas capable of operating at 4 K is a cryosorbtion pump; among various sorb materials available, coconut charcoal has the best pumping properties for 4-K pumping of helium [99; 100]. Figure 39 gives a schematic of charcoal cryopumping in the NH trapping setup. There are four key elements:

(1) charcoal tube, designed to capture helium atoms in the region immediately in front of the cell orifice;

(2) 4-K plate, designed to prevent helium from entering the space between 4-K shield and 77-K shield;

(3) supersorb, designed to capture helium that escaped from charcoal tube and 4-K hole and to absorb helium generated in the regeneration process;

(4) 77-K optically-opaque gas-conductive baffles, that allow helium that entered the 4K-77K shield space to be pumped by the source chamber diffusion pumps.

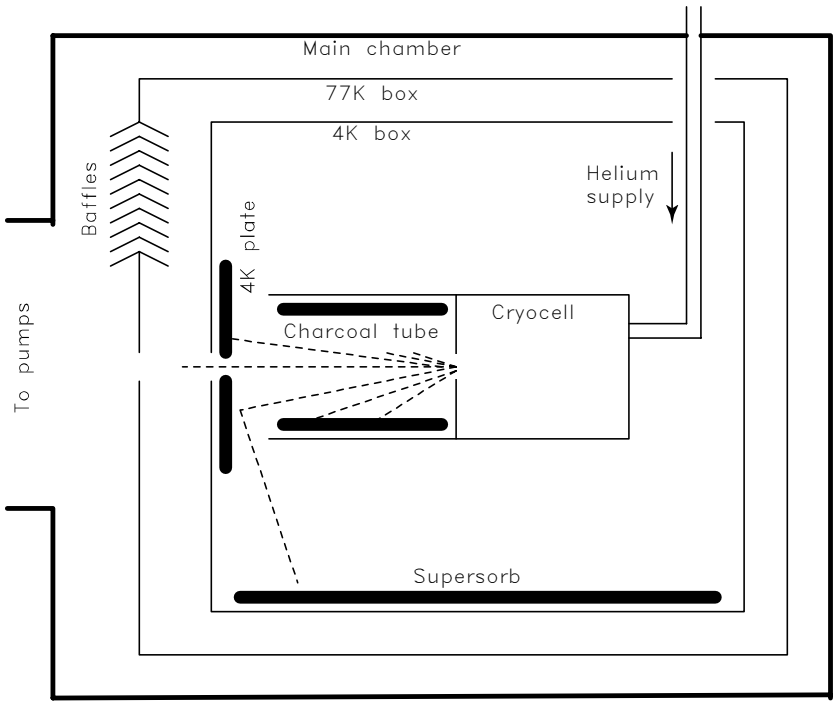

Figure 39: Cryopumping diagram.

5.6.2 Regeneration

The pumping speed of a layer of 20/40 mesh coconut charcoal attached to a cooled metal surface at 4 K is typically* equal to 3-4 liter/s·cm^2 † for 4-K helium gas and

* The typical value is supported by our experience and by published data; water vapor contamination and variations in charcoal-to-copper attachment method may significantly alter this value.

gradually decreases as helium accumulates on it [99]; the pumping speed drops rapidly below levels acceptable in our apparatus at accumulations of $\sim 1\times10^{20}$ cm^{-2} [101]. It is therefore necessary to regularly desorb helium from cryopumping surfaces for which high pumping speeds are critical, i.e. from the charcoal tube and the 4-K hole. Calculations indicate that a typical run time which the charcoal tube can survive without significant decrease in pumping speed is ~100 seconds at $n = 2\times10^{16}$ cm^{-3} buffer gas density in the cell.

A chart of buffer gas flow and regeneration is shown in Figure 40. The regeneration heat pulse is produced with electric heaters mounted on the charcoal tube and the 4-K plate. The majority of desorbed helium gas remains in the 4-K space and is cryopumped by the supersorb. Due to the very large ratio of pumping speed of the supersorb to total conductance of openings in the 4-K box, very little helium enters into the 77K space, so the system does not suffer any significant loss of liquid helium bath during regeneration. Temperatures return to their equilibrium values within ~20 minutes, at which point the system is ready for another measurement.

The supersorb is designed to handle multiple hours of operation. Its pumping speed is not very critical, as long as it is much larger than the total conductance of openings in the 4-K shield, so large accumulations of helium can be tolerated. Nevertheless it eventually becomes necessary to regenerate the supersorb. In this process a very large amount of helium must pass through the 77K space into the diffusion pumps, and liquid helium bath empties rapidly from the resulting heat load; regeneration of the

---

† Here cm^2 refers to the area of the metal surface, not the total surface area of charcoal attached to it

supersorb is accompanied by an overall temperature increase of the apparatus to tens of Kelvin. At the end of the supersorb regeneration process new liquid helium must be transferred into the helium bath and the system must be cooled back down to 4 K before operation can continue.

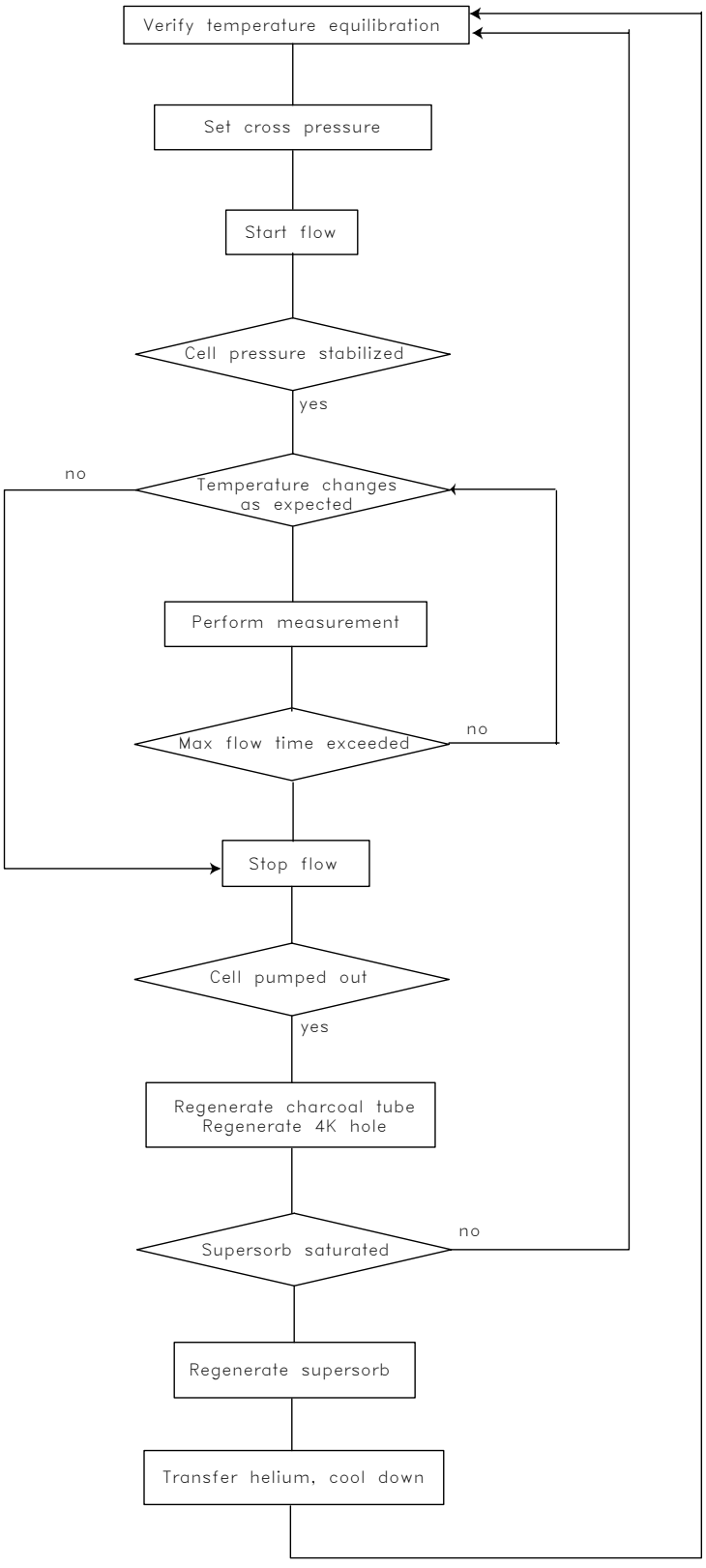

Figure 40: Buffer gas handling and charcoal regeneration diagram.

5.7 Superconducting magnet and magnet support

Ref. [143] provides a detailed description of the design and manufacturing process of superconducting magnets used in our group, including the magnet used in the setup described in this work. This section provides only basic information on the magnet, and [143] should be consulted for further details.

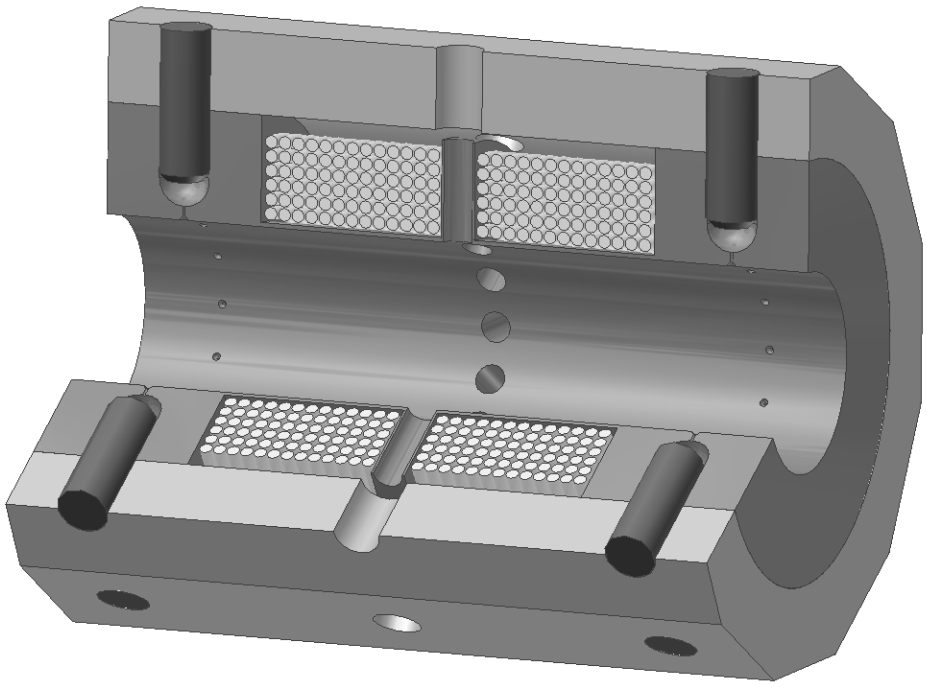

Figure 41: Internal construction of trapping magnet, scale drawing.
Current supply leads, G-10 annuli between bobbin and coils, and heat-transfer copper strips not shown; coil windings not to scale.

5.7.1 Mark V magnet

The magnet consists of two superconducting coils held together by a multi-part titanium structure, as shown in Figure 41. The coils can be operated in two configurations: Helmholtz, where currents in the coils are equal and parallel, and anti-Helmholtz, where currents in the coils are equal and anti-parallel (see Figure 42). As shown in Figure 43, the Helmholtz configuration produces a nearly uniform field inside the magnet bore, which is used for Zeeman relaxation measurements; the anti-Helmholtz configuration produces a spherical quadrupole field used in magnetic trapping. Field non-uniformity has an effect on cell volume that can be addressed by a probe laser set to a given frequency; for reader's convenience, we provide calculations of addressable volumes in Figure 44 without further explanation.

The coils are wound on a Grade 6 (5% Al, 2.5% Sn) titanium bobbin. In the anti-Helmholtz configuration a 27-ton force pushes the coils apart; a Grade 6 titanium cask, held on the bobbin with Grade 6 titanium pegs, prevents the coils from moving. Copper strips attached along the coils ensure that the windings are in thermal equilibrium with the titanium parts.

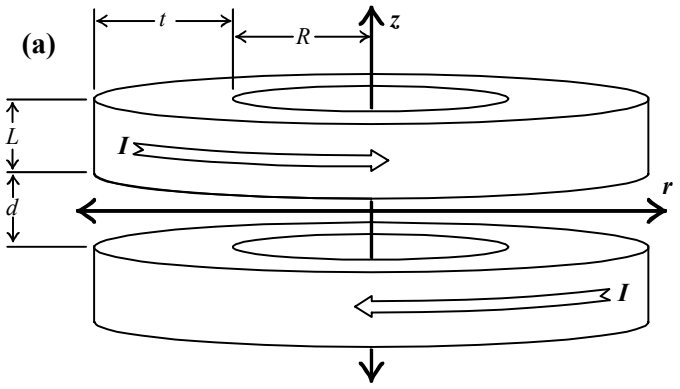

Figure 42: Magnet coils in anti-Helmholtz configuration.

Coil dimensions: L = 63.5 mm, d = 15.24 mm, t = 33.59 mm, R = 41.21 mm ; each coil contains 4745 windings of Cu:NbTi 2:1 superconducting wire.

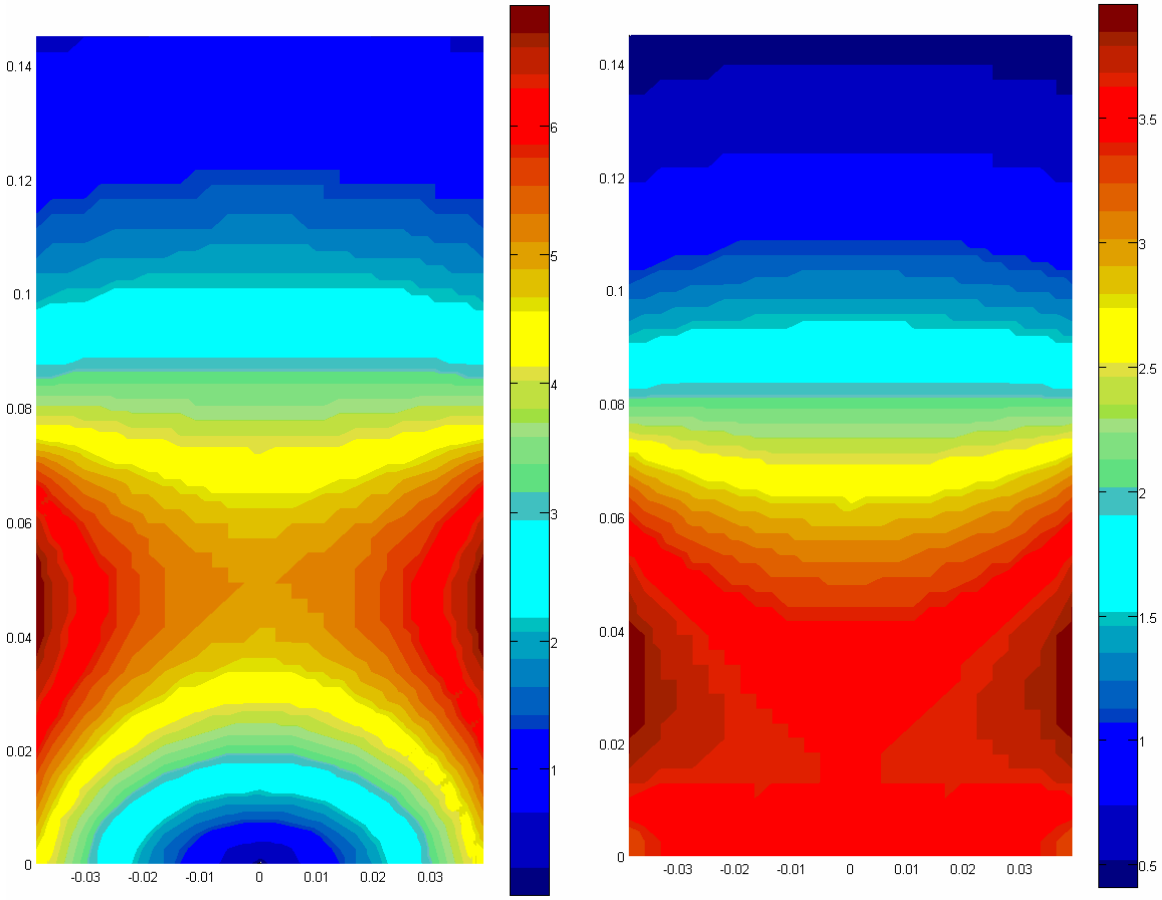

Figure 43: Field profiles inside magnet bore.

Left: anti-Helmholtz configuration at 145 A; right: Helmholtz configuration at 60 A.

Distances in meters, field in Tesla.

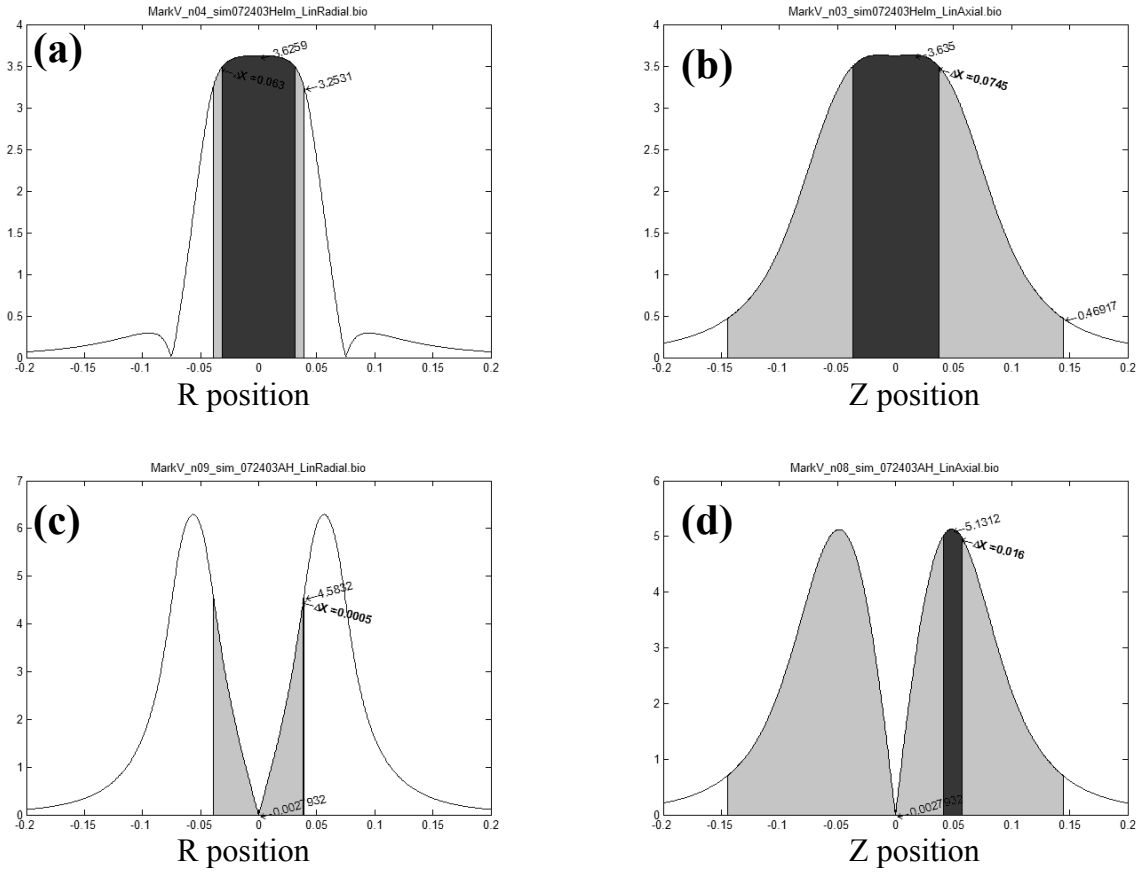

Figure 44: Spectroscopic addressing of NH molecules at different points inside magnet bore.

(a) Helmholtz field, probe beam propagating radially through midplane Z=0;

(b) Helmholtz field, probe beam propagating axially along magnet centerline R=0;

(c) anti-Helmholtz field, probe beam propagating radially through midplane Z=0;

(d) anti-Helmholtz field, probe beam propagating axially along centerline R=0;

Distances in meters, field (vertical axis) in Tesla. Helmholtz field at 60 Amp magnet current, anti-Helmholtz field at 145 Amp. Light shading: area inside magnet bore; dark shading: areas addressable by a single laser frequency assuming transition linewidth of 1 GHz (approximately corresponding to 4 K Doppler-broadened hyperfine). Thin arrows indicate field values at boundaries; boldface arrows indicate spatial extent of the addressable regions. Spatial resolution 0. 5 mm.

5.7.2 In-vacuum operation

Unlike previous designs of high-threshold anti-Helmholtz traps [143], our magnet is designed to operate in vacuum. Cooling of the coils is accomplished by thermally connecting magnet bobbin and cask to the helium bath with copper heat links, as shown in Figure 47. The links also provide stable mechanical support of the magnet. Magnet supply current leads are routed through the helium bath, via a superconducting vacuum feedthrough at the bottom of the bath, and in vacuum to the magnet. To reduce the possibility of a quench in the in-vacuum leads the leads are thermally anchored to the magnet support structure with G10-insulated copper strips.

Grade 6 titanium does not become superconducting at 4.2 K, which means that the magnet bobbin and cask have no effect on the magnetic field profile. As described in section 5.5.1, temperature of the bottom of the helium bath can be lowered to ~2.5 K with a lambda-coil refrigerator; this would also lower the temperature of the entire magnet assembly. Our measurements of Grade 6 titanium alloy indicate that it superconducts below T_c = 3.0 K, as shown in Figure 45. A superconducting cask would alter the magnetic field profile dramatically, so successful operation of the magnet below 3 K is only possible at fields high enough to drive the titanium normal. For low fields, like those involved in evaporating cooling experiments, the refrigerator arrangement has to be modified to cool a cryocell separately from the magnet, as shown in Figure 46.

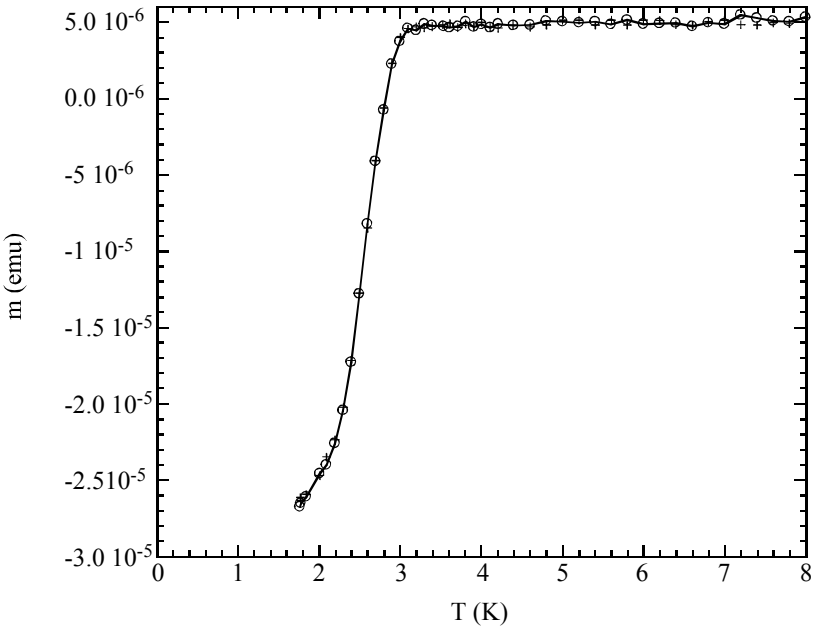

Figure 45: Superconducting transition in Grade 6 titanium.
Magnetic moment *m* as a function of temperature of a 15.1 mm^3 sample of Grade 6 titanium alloy in an applied field of 1 mT. The onset of superconductivity can be seen at ~ 3 Kelvin. Open symbols: zero field cooled data. Crosses: field cooled data.

At the current stage of the experiment only high-field operation is planned, and cell temperature of 2.5-4.2 K is sufficient; to simplify the experimental setup we use the magnet bore as the cryocell. Two ends of the magnet bore are capped with indium-sealed flanges; one side has a recessed copper plate with a 3-mm opening that serves as the cell entrance, the other has a fused silica window for fluorescence collection.

Access ports in the midplane of the magnet bobbin provide optical access and buffer gas supply. Sealing of the side ports is accomplished with concentric grease seals. For this type of seal, a tight-fitting tube is greased with silicon vacuum grease* and inserted in the side port. The resulting seal has been tested to withstand pressure

* Dow Corning 976V High Vacuum grease

differentials of a few Torr at leak rates below 10^{-6} mbar·liter/s. Such sealing quality is fully adequate for a system where a 3-mm opening is always present between the cell and vacuum space.

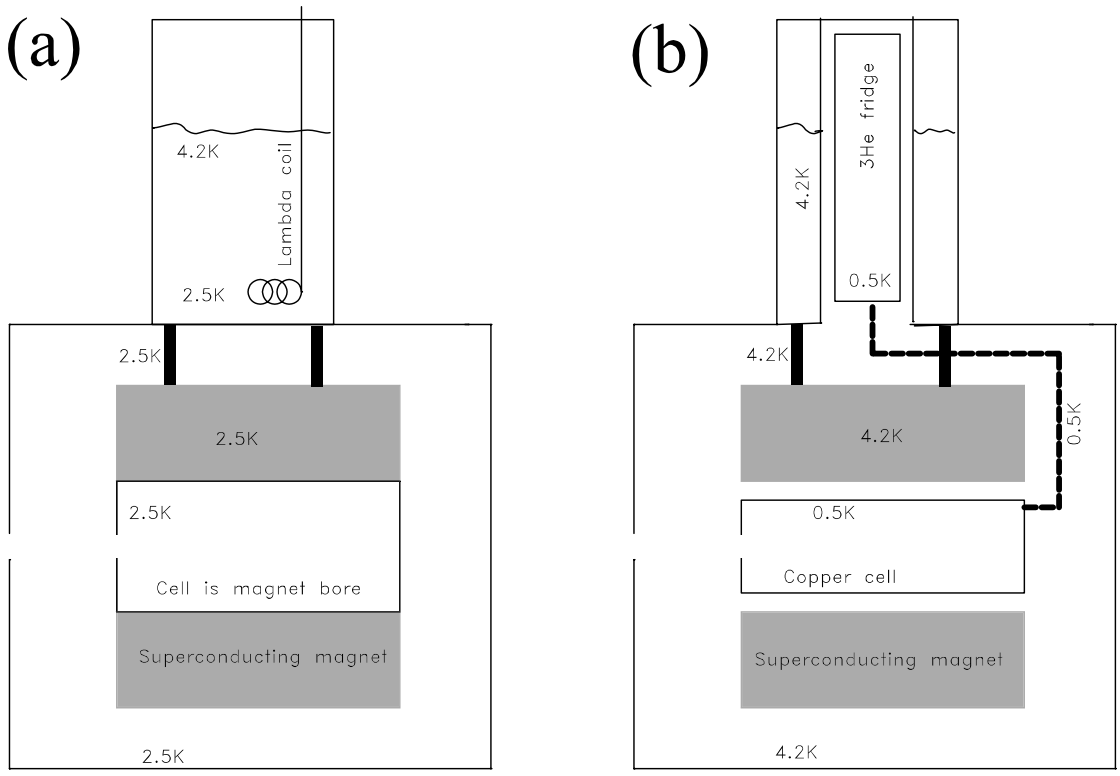

Figure 46: Possible cryocell configurations: (a) Magnet bore serves as the cell; (b) Separate cryocell in the magnet bore.

5.7.3 Quench tests

A series of quench tests was conducted on the magnet to verify proper operation in both Helmholtz and anti-Helmholtz configuration, in liquid and in vacuum. The test results are shown in Table 11. The magnet did not reach design current in Helmholtz configuration; the operating current, however, is sufficient for the types of measurements

we plan to conduct. The surprising quench behavior of the magnet in anti-Helmholtz configuration does not fit the usual training pattern [144]. We are not able to verify the source of this behavior; it is known that another magnet of a similar design exhibited the same initial quench pattern, but never reached currents anywhere near the design current [145].

	Helium bath, Anti-Helmholtz	Vacuum test rig, Anti-Helmholtz	Vacuum test rig, Helmholtz	Main chamber, Helmholtz
Design current	***145 A***	***145 A***	***105 A***	***105 A***
Test 1	60 A quench	60 A quench	54.5 A quench	60 A – **passed**
Test 2	62 A quench	62.6 A quench	56.5 A quench	-
Test 3	62.8 A quench	63.3 A quench	58.3 A quench	-
Test 4	143 A – **passed**	143 A – **passed**	61.0 A ultra-slow ramp quench[†]	-
Test 5	140 A fast-ramp – **passed**	80 A fast-ramp – **passed**	-	-
Operating current	**143 A**	**143 A**	**60 A**	**60 A**

Table 11: Mark V quench test results

[†] ramp rate 400 sec/Amp

5.7.4 Magnet support structure

The magnet support structure, shown in Figure 47, provides cooling of titanium of the magnet. The structure is made entirely of OFE copper. A transition plate is attached to the bottom of the helium bath; a horizontal plate is suspended from it on four vertical posts. The magnet cask is attached to 4 cask end pieces; the joints are greased[‡] to improve thermal contact[§]. To prevent any mechanical stress in the magnet due to differential contraction, the cask end pieces are attached to the horizontal plate via thin sheets of copper that serve as stress-relief; as thin sheets may allow some movement of the magnet along the Z axis, the magnet is held at its midplane with a stabilizer structure. The structure holds the magnet mechanically and provides a good thermal connection from the magnet cask to the helium bath. Although the bobbin is rigidly connected to the cask, it is not clear how good the thermal contact between the cask and the bobbin, and consequently between the helium bath and the coils, is. To provide a known-good thermal path directly from the bobbin to the helium bath, thin strips of copper (thin enough to remove any possibility of mechanical stress due to thermal contraction or movement of bobbin with respect to cask) are installed between the bobbin and the cask end pieces.

[‡] Apiezon N Cryogenic High Vacuum Grease, M&I Materials Ltd, Manchester, UK

[§] see [146], Ref. [147], and references therein for the justification of use of Apiezon N in improving metal-to-metal thermal contact

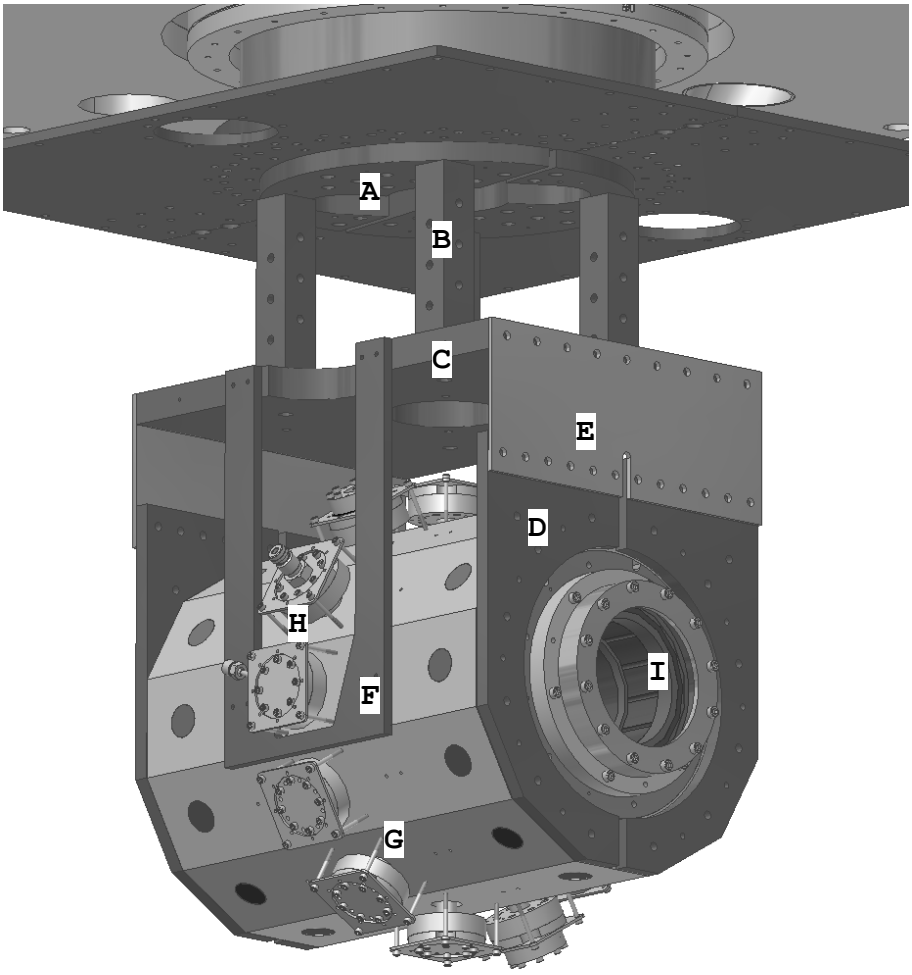

Figure 47: Magnet support structure, scale drawing.

A: Transition plate, B: Vertical posts, C: Horizontal plate, D: Cask end pieces, E: Stress-relief, F: Z-stabilizer, G: blank side port, H: fill line connection port, I: fluorescence collection window. Bobbin heat links not shown.

5.8 Laser system

The optical detection system is schematically shown in Figure 48. Its main element is a reference-cavity-stabilized dye laser[*]. The dye is pumped with 9 Watts of doubled Nd:YVO laser light[†]. The dye laser light is frequency-doubled in a resonant doubling cavity[‡], which prodices ~1 mW of 336 nm light with a sub-MHz line width. The light is then free-space coupled into either a microwave reference cell or the cryocell, where it is used to perform absorption or fluorescence measurements as described in Figure 49.

Coupling the light into the apparatus via a fiber would simplify many aspects of daily experiment operation. We attempted delivering the light via a quartz single-mode fiber[§]; however, the losses in the fiber turned out to be orders of magnitude larger than initially projected, and we were not able to use it[**].

---

[*] Coherent 699-21, running DCM dye in DMSO solvent

[†] Coherent Verdi V-10

[‡] Spectra-Physics LAS, Delta concept

[§] Fiber: QSMJ-A3A,A3A-320-2/125-3-12 high power patchcord, adjustable Angle FC/PC connectors each end, 2/125um singlemode 320nm fiber, 3mm OD PVC jacketed, 12 meters long;

Collimators: HPUCO-2,A3A-442-S-5BQ Non-Contact style SM fiber collimator for 442nm with an adjustable angle FC compatible receptacle and a f=5mm boconvex fused silica lens;

Supplier: OZ Optics Ltd., Nepian, Canada

[**] At this time we are not able to locate an alternative source of single-mode fibers capable of 336 nm operation.

A multimode fiber[††] transmitted a substantial amount of light, but the speckle output pattern (common to all multimode fibers), which fluctuated due to mechanical vibrations of the fiber and shifted as laser frequency changed, produced unacceptable background noise. Attempts to stabilize the pattern with a mode scrambler[‡‡] did not succeed.

[††] F-MCB-T multimode fiber, high OH content, NA 0.22, 100 μm core; Newport Corp.

[‡‡] FM-1, Newport Corp., Irvine, CA

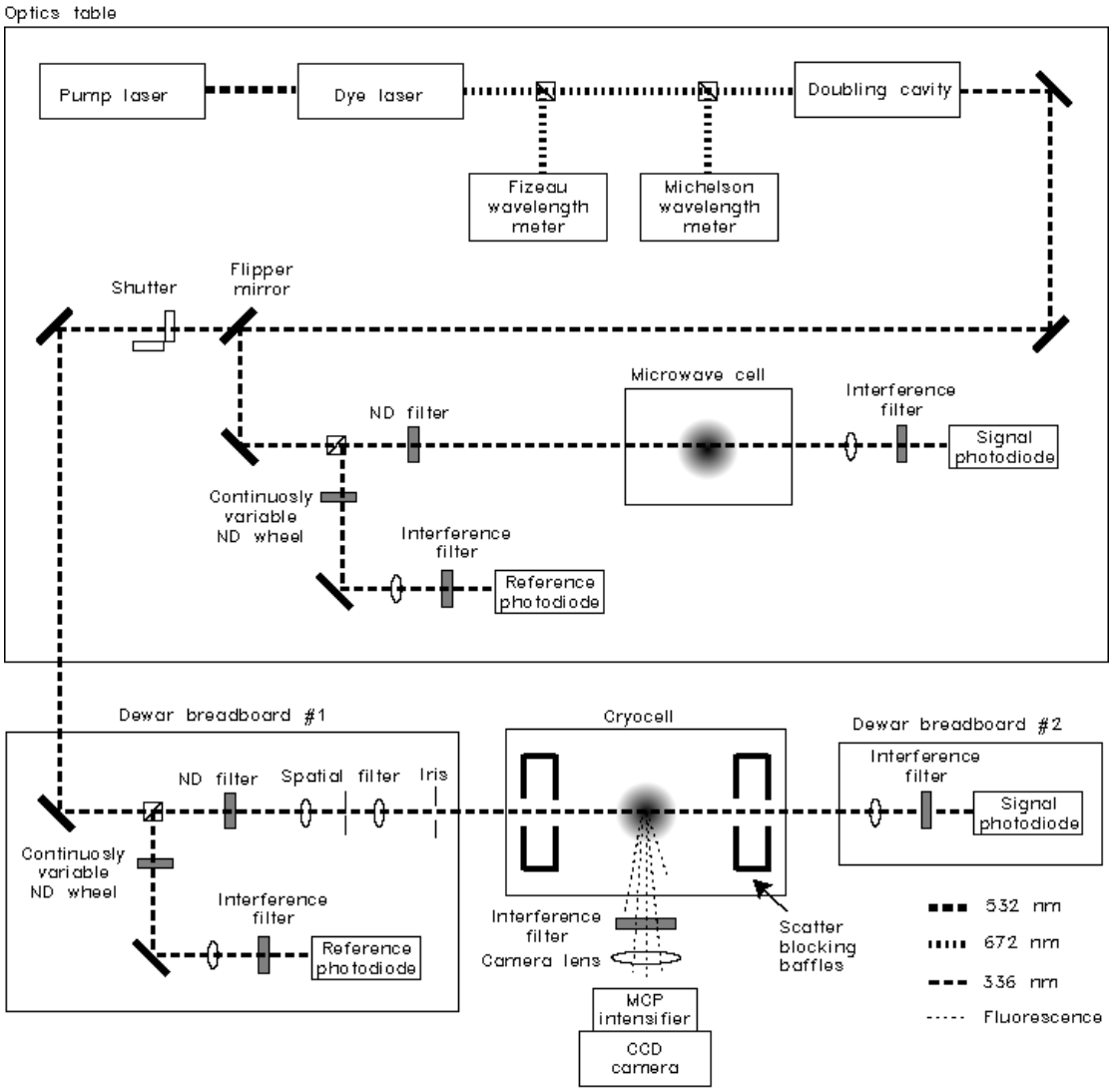

Figure 48: NH optics setup.

5.8.1 Laser wavelength measurement

Accurate laser frequency control is somewhat challenging in our setup, in part because the majority of measurements are done at a single frequency fixed for extended periods of time, as opposed to rapid frequency scans common in other experiments, so frequency references commonly used with dye lasers, e.g. etalon cavities or absorption cells, can not be easily used. Dye laser frequency is controlled coarsely by etalon mode adjustment, and finely by an external voltage source. The frequency is continuously monitored by a scanning Michelson interferometer[§§] ("WA-1500") and a Fizeau interferometer[***] ("Wavemaster"). Dye laser has microsecond-timescale dropouts in intensity due to unavoidable presence of bubbles in the dye solution. These dropouts do not affect fluorescence or absorption data collection, since our integration times are typically in the millisecond range; however, it is often impossible to obtain a stable reading from the WA-1500. Wavemaster readings are not affected by the dropouts, but the accuracy of the Wavemaster is insufficient to precisely locate the spectral features. We typically wait to acquire a few stable readings from WA-1500 at a fixed external voltage to determine the absolute frequency position, then use the change in external voltage to determine relative frequency changes. Wavemaster readings are constantly monitored to prevent unnoticed mode-hops which would change the absolute frequency position.

[§§] Burleigh WA-1500, 0.001 cm^{-1} resolution, 0.003 cm^{-1} absolute accuracy

[***] Coherent Wavemaster, 0.01 cm^{-1} resolution, 0.11 cm^{-1} absolute accuracy

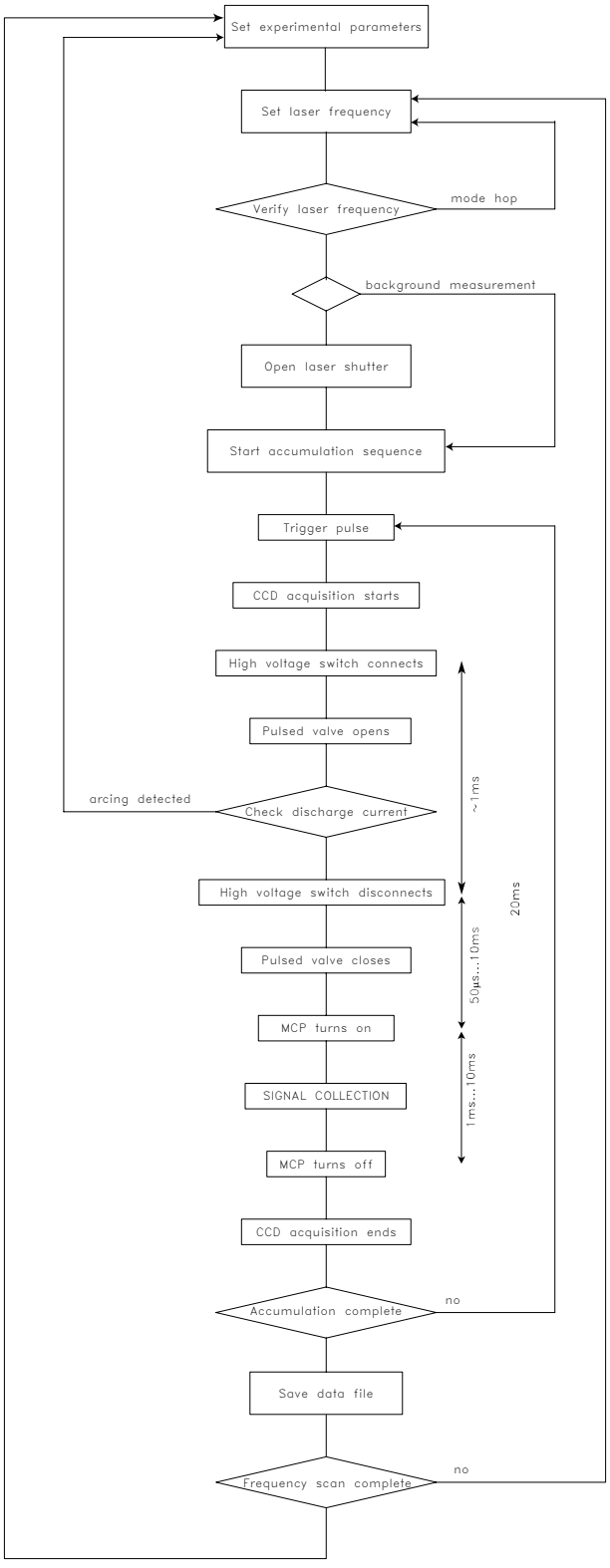

Figure 49: Diagram of a typical fluorescence measurement.

5.8.2 Fluorescence collection

The molecules are excited on the

$$R_{11}(0): X^3\Sigma^-(v''=0,N''=0,J''=1) \rightarrow A^2\Pi_0(v'=0,J'=2)$$

line at 29770.60 cm^{-1}. The excited state decays as described in section 4.1.2; fluorescence from all decay paths is collected by an MCP-intensified CCD camera[†††].

The camera is fitted with a 78mm f#/3.8 lens[‡‡‡] and an interference filter[§§§] that blocks room lights entirely and light from discharge glow partially. As both excitation and fluorescence occur at the same wavelength, it is impossible to filter out scattered light from the excitation laser using spectral methods; technical limitations of camera readout electronics do not allow us to use temporal filtering either[****]. As a result, special measures have to be taken to minimize scatter intensity in the signal region of the camera image. In the test cryostat described below, windows were fitted with light-adsorbing baffles[††††]. In the main cryostat such baffles are not practical due to geometrical

[†††] Princeton Instruments ITE/CCD

[‡‡‡] Electrophysics LQ78F3.8; transmission at 336 nm is 90%

[§§§] Optosigma 079-0450; 337 nm center wavelength, 10 nm FWHM, 25% transmission, 0.01% blocking

[****] As the experiment is switching to photomultiplier tubes for fluorescence collection, we note that temporal filtering, which involves modulating the laser intensity at ~1 MHz and turning on the PMT during laser-off part of the modulation cycle, becomes an attractive option.

[††††] Black Ebanol coating on brass parts; Aotco Metal Finishing Co., Billerica, MA

constraints, and alignment of the excitation beam with feedback on scatter intensity is used instead to minimize laser scatter.

The camera collects only ~10^{-4} of the total fluorescence signal; the signal is typically spread over ~10^3 pixels; as a result, photon shot noise is a significant source of noise. To overcome this, we integrate camera signal for 60 to 1000 discharge pulses; the integration also averages out any pulse-to-pulse fluctuations of discharge yield. The principal trade-off in this approach is that only a few data points can be acquired before the sorbs must be regenerated.

5.8.3 Absorption measurement

Fluorescence measurements are quite difficult to calibrate if one wants to obtain an absolute number of molecules in the cell. We use absorption measurements to obtain the calibration for strong signals, and then scale the numbers with the observed fluorescence signal for weak signals.

The absorption measurement is done using a balanced detector scheme. Laser beam is split with a 50/50 non-polarizing beamsplitter; one of the beams is sent to a "reference" photodiode[‡‡‡‡] through a continuously variable neutral density filter, the other is sent through the cell into an identical "signal" photodiode. Outputs of two photodiodes are individually amplified and then sent into a differential amplifier[§§§§]. Laser frequency is first set to a known off-resonance value, and the continuous neutral density filter is adjusted to produce a zero voltage output at the differential amplifier. Laser is then

[‡‡‡‡] New Focus 2001-FS

[§§§§] Stanford Research Systems SR560

scanned across the spectral line, and amplifier output as function of frequency scan voltage is recorded. The method allows detection of fractional absorption below 10^{-4}, limited primarily by photon shot noise of the laser beam, which can not be reduced due to concerns of possible transition saturation and spectral hole burning.

6 NH Experiment:

Production and Cooling

In this chapter we describe experiments on production of NH radicals using a microwave and a DC glow discharge, detection of NH using a quadrupole mass-spectrometer and a laser detection system, and results of buffer gas cooling of NH in the test cryocell. We also describe the ongoing effort to buffer-gas cool and trap NH in the next-generation cryocell, and discuss possible reasons for the inability to detect NH in the next-generation setup so far.

6.1 Production of NH

6.1.1 Microwave discharge cell

The microwave discharge setup, schematically shown in Figure 50, provided two functions. At the early stage of the project, it was used to verify the possibility of breaking down NH_3 in a discharge to produce NH. It was also used to locate the spectral lines and to test absorption detection setup.

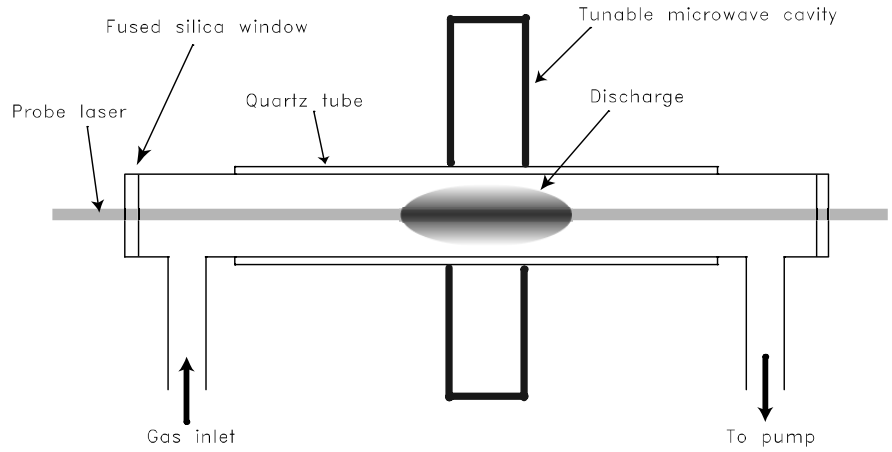

Figure 50: Microwave discharge cell schematic.
Gas inlet is fitted with a needle valve to regulate process gas flow.

The microwave discharge setup consists of a quartz flow tube surrounded by an air-cooled tunable microwave cavity*. A process gas of 100% NH_3 is flown through the flow tube at pressures of ~300 mTorr. A microwave power generator† supplies 25 W of

* Custom-made; Anderson group, Harvard University Department of Chemistry and Chemical Biology

† HV15A; Scintillonics Inc., Fort Collins, CO

power into the cavity, which is tuned to minimize the reflected power. A discharge is ignited, either spontaneously or with a handheld ionizer. Microwave discharge produces NH radicals which are detected in absorption as described in section 5.8.3.

Figure 51 shows a typical absorption line observed in the discharge. The linewidth is not consistent with a room-temperature Doppler-broadened line, indicating that NH radicals do not survive multiple collisions with other molecules in the discharge. We were also not able to make firm conclusions on rotational state distribution, further supporting the assumption that the radicals do not reach thermal equilibrium with the process gas and tube walls.

For the purpose of calculating the yield of the discharge, we assume that the rotational state distribution is close to a room-temperature equilibrium. This gives the average density of NH $X^3\Sigma^-(v''=0)$ in the discharge of $n_{NH} = 10^{11}$ cm^{-3}. The yield of NH in the cell is then $\kappa_{NH} = 10^{-5}$ NH $X^3\Sigma^-(v''=0)$ molecules produced per NH_3 molecule entering the flow tube; this is consistent with our initial expectations based on Ref. [148]. We observed many of the lines of the $X^3\Sigma^-(v''=0) \rightarrow A^2\Pi_0(v'=0)$ band listed in Ref. [114], and identified the frequency position of the $R_{11}(0)$ line that was later used for fluorescence detection of buffer-gas cooled NH.

We found that the microwave source is a very simple way to produce NH radicals. However, the rather low yields, most likely associated with recombination in high-density process gas, and the difficulty in converting a microwave discharge cell into a molecular beam source limit the uses of the source to a tabletop frequency reference.

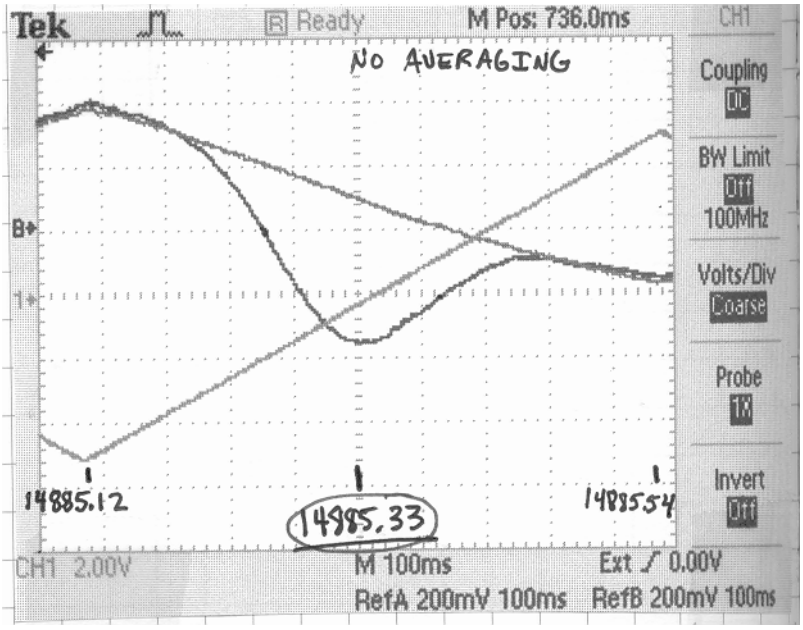

Figure 51: Typical microwave absorption signal.
Light-gray trace: laser scan voltage; frequency markers are in cm^{-1} of dye laser (i.e. undoubled) frequency.
Dark-gray traces: absorption differential amplifier output with the microwave discharge on (curved trace) and off (straight trace). Slope of the straight baseline trace is due to etalon effects in various optical elements.

6.1.2 Mass-spectrometer detection

While the laser system was successfully used to detect NH radicals in the microwave setup, laser detection of un-cooled products of a glow discharge beam source faces a significant difficulty: as we learned from the microwave discharge, translational and rotational distribution of produced radicals may remain far away from thermodynamic equilibrium; the exact state distribution may also change with changing discharge parameters. Since laser detection is sensitive to a specific electronic,

vibrational, and rotational state of the molecules, it is impractical to use it for investigation of total production yields from the beam source.

In order to verify the successful operation of the glow discharge source we used a residual gas analyzer (RGA) setup schematically shown in Figure 52. The setup consists of a quadrupole mass spectrometer[‡] (QMS) in a differentially pumped vacuum region. Molecules from the discharge source located in the source chamber enter the QMS region, where they are ionized, separated in the quadrupole field according to their mass and degree of ionization, and detected with a Faraday cup detector.

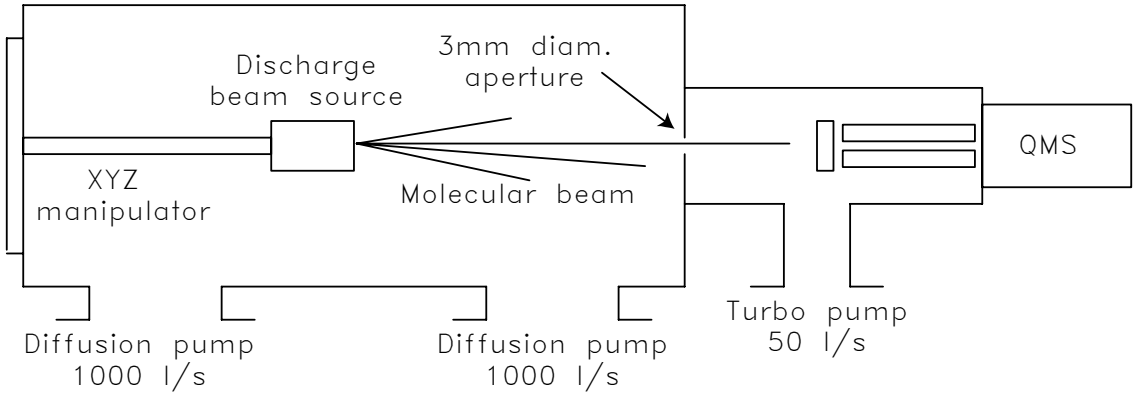

Figure 52: Mass-spectrometer setup schematic.

An example measurement is shown in Figure 53. Uncertainties in conversion of mass spectrometer signal into absolute radical flux prevents extracting absolute numbers of radicals from this measurement; however, using typical conversion factors for common molecules would indicate that the yield of NH is ~10%. The high value of the yield compared to the microwave cell is most likely due to a very small length of the

[‡] Prisma 80; Pfeiffer Vacuum

high-density region that the radicals must traverse between their creation and the no-collision free-flight zone; recombination losses are thus greatly reduced. The measurements confirm that the yield is increasing with increased jaw voltage up to the arcing transition, as expected from normal glow discharge theory given in section 4.2.2.

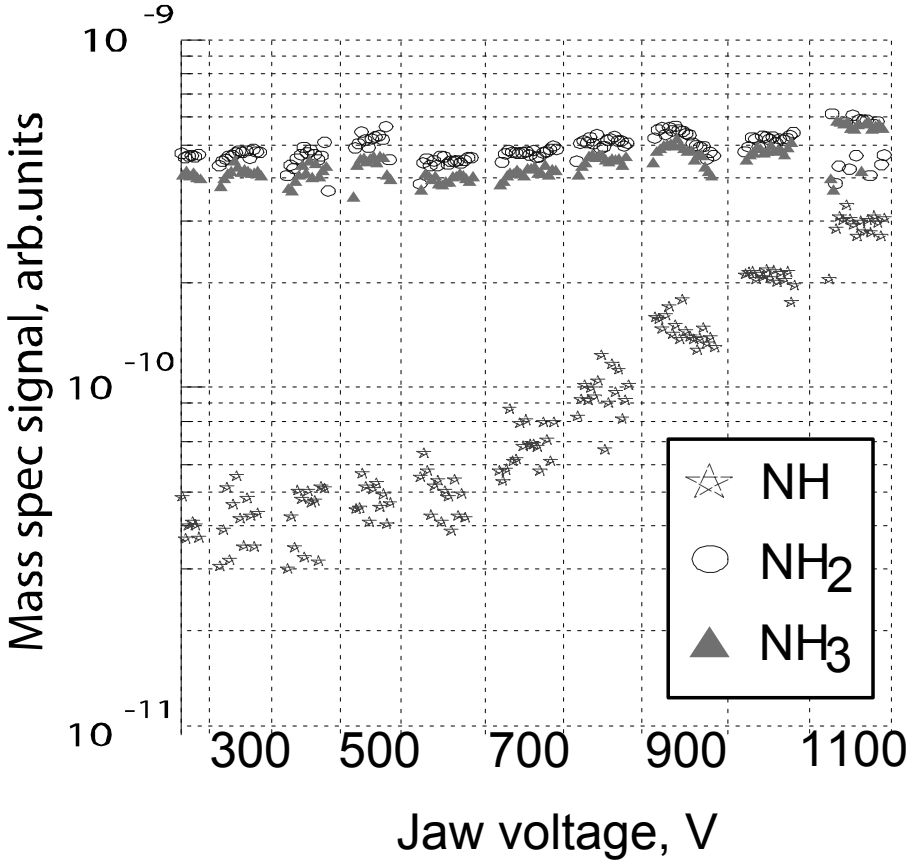

Figure 53: Mass-spectrometer signal dependence on jaw voltage.

6.2 Buffer-gas cooling of NH

Once production of NH radicals in the glow discharge beam source was confirmed in the mass-spectrometer tests, and laser detection was optimized using a microwave cell, we attempted to buffer-gas cool NH. A test cryostat, described in section 3.1, was installed into the source chamber in the beam path, see Figure 54 and Figure 31.

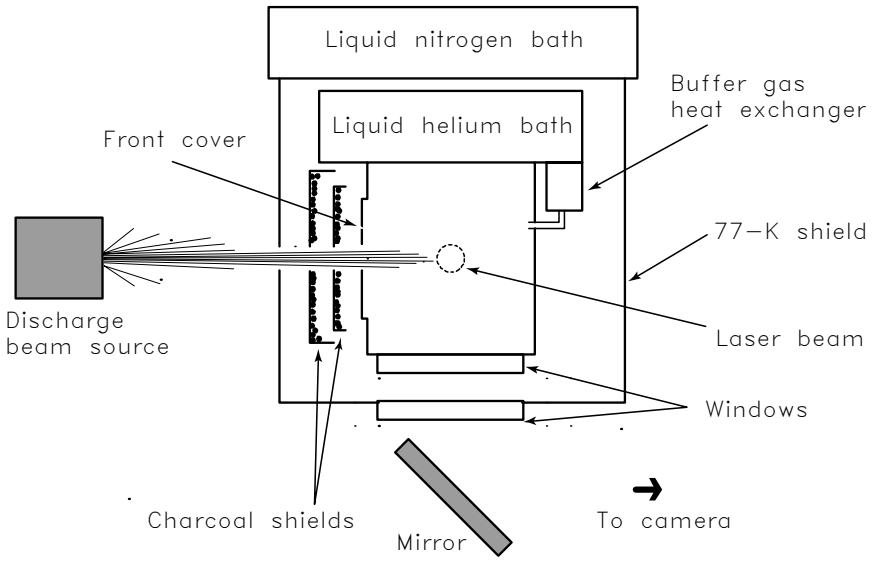

Figure 54: NH cooling in test cryostat, schematic.

6.2.1 Loading performance

The measurement was done using laser-induced fluorescence (see section 5.8.2), with absorption measurement used for absolute calibration (see section 5.8.3). A typical

fluorescence image of cold NH radicals in the buffer gas is shown in Figure 56, and a typical absorption profile is shown in

Figure 57. We varied the buffer gas pressure in the cell to determine the optimal buffer gas density. The results of this measurement are shown in Figure 55; the maximum loading numbers are achieved at 3×10^{16} cm^{-3} buffer gas density in the cell. The value is somewhat different from the peak point from section 3.2.1; the explanation for this is that small modifications to the charcoal shield arrangement changed some of parameters in the loading model from section 3.2, producing a shift in the peak-loading value of buffer gas density.

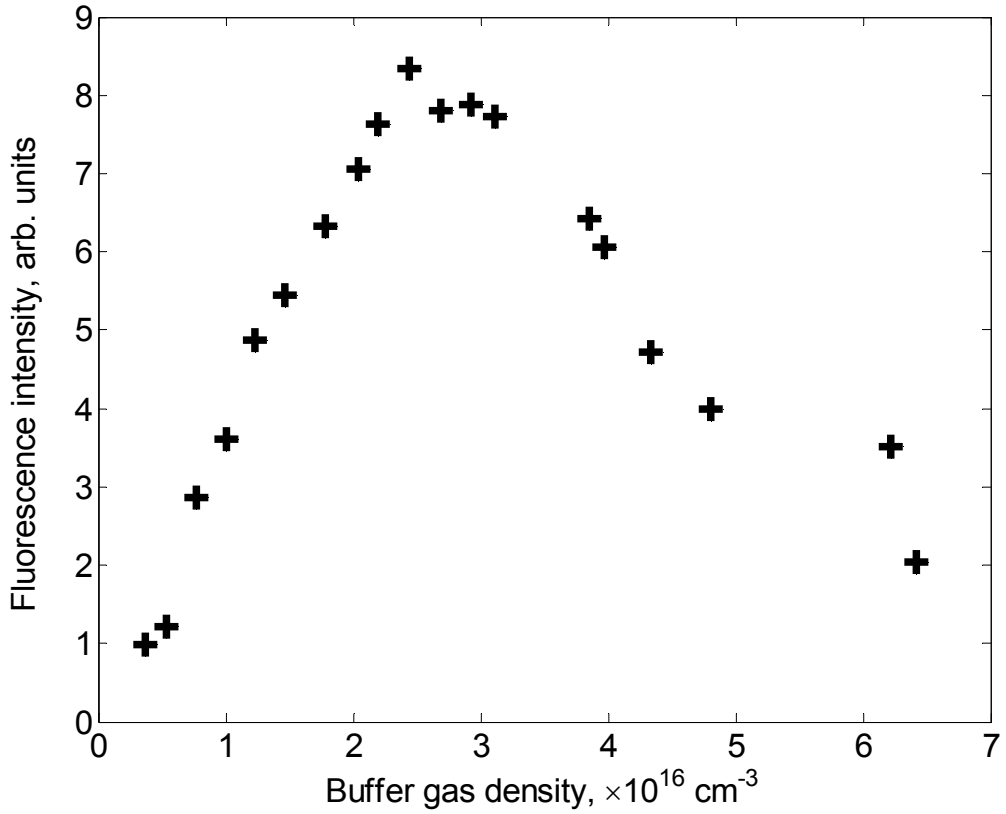

Figure 55: Buffer gas density effect.

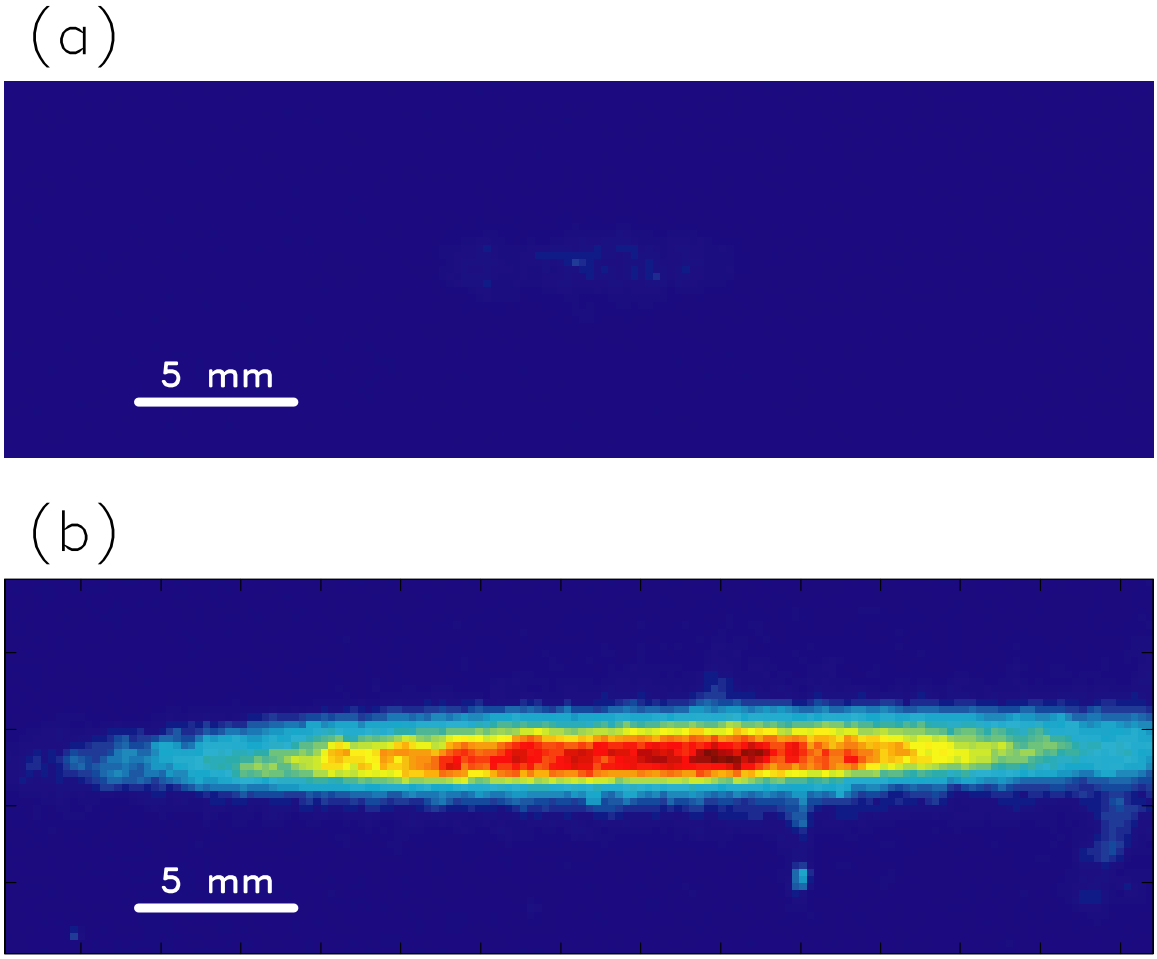

Figure 56: Typical fluorescence images of NH in cryocell.

(a) No buffer gas; some free-flight laser-induced fluorescence seen;

(b) Buffer gas density 4×10^{16} cm^{-3}; fluorescence distributed along laser beam path.

Molecular beam enters the image from the top; probe laser traverses the image left to right. Fluorescence feature dimensions correspond to laser beam width (vertical) and cell size (horizontal). Distance from image center to cell orifice is 32 mm, to valve nozzle – 80mm.

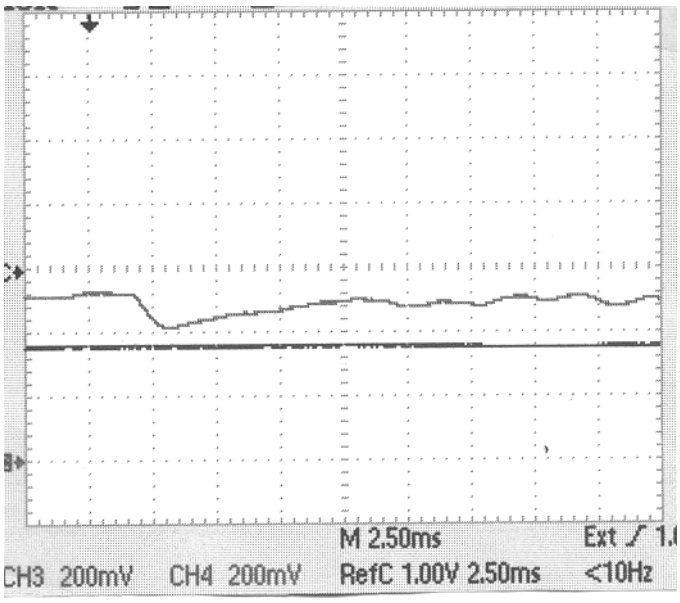

Figure 57: Typical time-resolved on-resonance NH absorption signal.
Light trace is differential amplifier output at gain 1000; dark traces are individual photodiode outputs. Laser frequency is kept constant at the peak on-resonance value. Pulse valve opens at the trigger marked with a vertical arrow. Fixed offset of amplifier output is due to photodiode balance drifts. Signal shown corresponds to maximum absorption of ~10^{-3}.

The maximum number of NH $X^3\Sigma^-$(v"=0,N"=0) molecules loaded into the buffer gas cell was measured to be

$N_{NH} = 10^{11} \ldots 10^{12}$.

The uncertainty is mainly due to lack of knowledge of precise spatial distribution of the molecules. Lacking the ability to perform absolute-number state-insensitive detection of NH in free flight, we can not extract the loading efficiency as it was done in Chapter 3. However, a large (~10^{12}) number of NH loaded into the cell suggests that there are no adverse effects causing radical loss prior to entering the cell.

6.2.2 Diffusion lifetime

Time-resolved fixed-frequency absorption signals for NH in the buffer gas cell, like that shown in

Figure 57, provide an idea of the time dependence of NH density on time. However, the noise level in absorption signal due to etalon effects makes it difficult to fit these time profiles. We configured fluorescence detection camera to acquire data in a 500 μs window, and delayed the camera trigger with respect to the discharge trigger by a variable time delay. The result of this measurement is shown in Figure 58. The time profile of the signal fits to a single exponential with a time constant of τ_{diff} = 3.1±0.5 ms. This loss rate is consistent with diffusion to the walls. This is an important result, as it confirms that no unexpected recombination or quenching processes have an effect on the observed NH $X^3\Sigma^-$(v"=0,N"=0) population. Due to technical limitations, we are unable to determine the spatial distribution of NH in the cell with accuracy necessary to convert this loss time profile into an exact measurement of NH-He elastic cross-section. We can, however, fit the signal time profile to a single-exponential form

$$I(t) = I_0 \exp[-t/\tau_{diff}] \tag{24}$$

and assume that the loss is dominated by the (1,1) diffusion mode*, and that the loss process is approximated by a solution to a constant-coefficient diffusion equation in a cylindrical geometry. From the fitted value τ_{diff} = 3.1±0.5 ms at buffer gas density of 3×10^{16} cm^{-3}, we can then extract the NH-He elastic cross-section. Given the assumptions above, the extracted value a lower limit on the cross-section:

* see section 0 for a detailed explanation

$\sigma_{NH-He}^{el.\min} = 1.5 \times 10^{-15}$ cm^2.

From the observed fluorescence intensity distribution along the laser beam we conclude that the actual value of the cross-section is likely to be an order-unity factor above the lower-limit value.

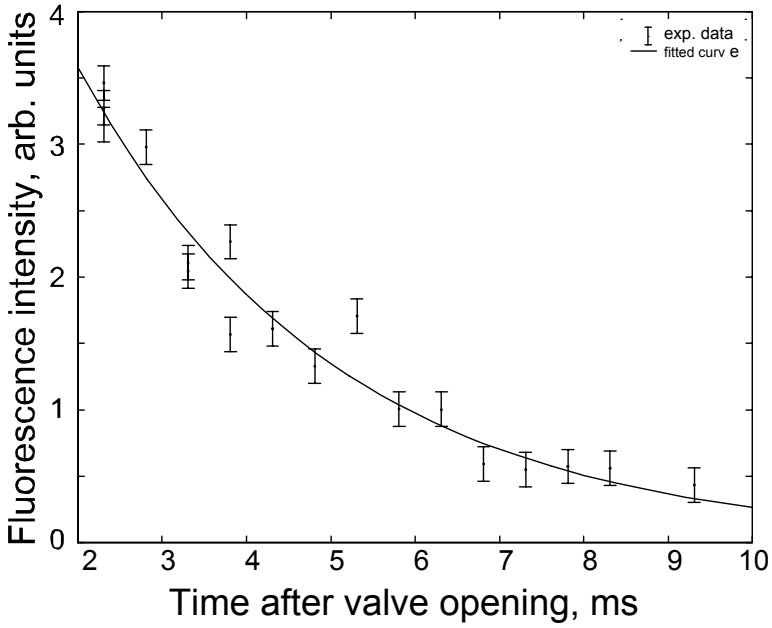

Figure 58: Fluorescence signal time decay.
Markers show integrated fluorescence intensity for $R_{11}(0)$ line on-resonance laser frequency; line is fit to Eq. (24). Buffer gas density is 3×10^{16} cm^{-3}.

6.2.3 Translational and rotational thermalization

Translational temperature of the molecules was determined by scanning laser frequency over the $R_{11}(0)$ line and fitting the spectrum to a Doppler-broadened lineshape, as shown in Figure 59. The line profile is composed of five hyperfine lines spaced over ~1 GHz [115]; since Doppler broadening of NH at 4.2 K is 338 MHz FWHM [79], the fit

is very sensitive to the exact positions of the hyperfine lines. Published measurements of NH hyperfine structure allow us to put an upper limit for translational temperature of

$T_{trans} < 6$ K.

This limit indicates efficient translational thermalization of NH with helium gas. Once lower cryocell temperatures are achieved in the next-generation apparatus, we will be able to resolve individual hyperfine lines in the profile, dramatically improve the fit quality, and produce a more precise value for translational temperature.

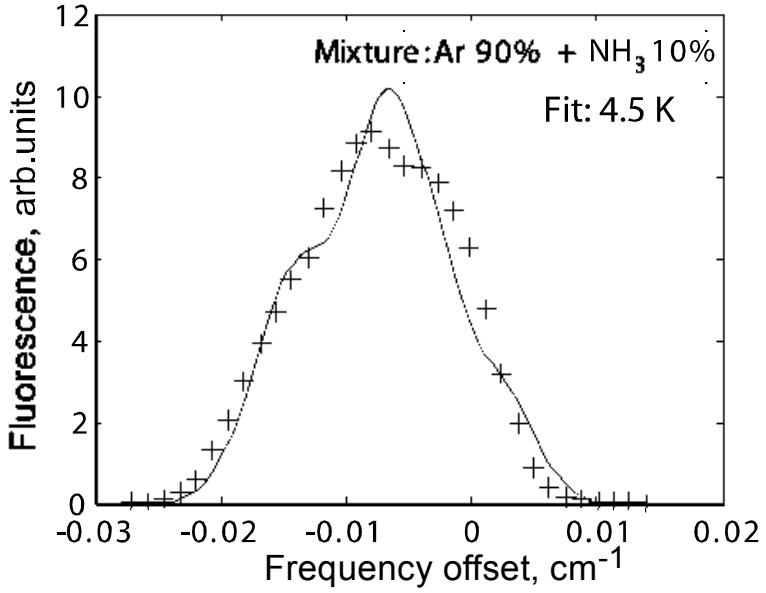

Figure 59: Translational temperature measurement.
Crosses are integrated fluorescence intensity, line is a Voigt profile fit using hyperfine line positions from Ref. [115].

Rotational temperature was determined by comparing the on-resonance fluorescence signal of $R_{11}(0)$ line with that of $R_{11}(1)$ line and assuming a Boltzmann

distribution of molecules between rotational states. The upper limit for the rotational temperature is

$T_{rot} < 8$ K;

as expected, rotational distribution rapidly comes into equilibrium with helium temperature. The uncertainty in the rotational temperature comes from poor signal-to-noise ratio for measurements on $R_{11}(1)$ line, the signal of which is over 100 times weaker than that for $R_{11}(0)$.

6.2.4 Process gas mixture optimization

The gas handling system is designed to automatically produce process gas mixtures so that the mixture can be quickly optimized for a specific parameter set. At this point we have not attempted automatic operation of the system, so only a few mixtures could be investigated to find a high NH yield recipe.

We compared number of NH $X^3\Sigma^-$(v"=0,N"=0) loaded into the test cryostat cell from mixtures of NH_3 with Ar, Xe, and Kr. The result of the measurement is shown in Figure 60 and Table 12. We conclude that 10% NH_3 in 90% Ar provides highest loading numbers among the mixtures investigated; this measurement is consistent with observations of yields in the mass-spectrometer setup. We also note that the mixture composition has no effect on the Doppler linewidth.

Mixture	Peak discharge current, mA	Relative peak fluorescence	Relative radical-per-mA ratio
100% NH_3	40	100%	2.50%
10% NH_3 in Ar	**50**	**200%**	**4.00%**
10% NH_3 in Xe	25	55%	2.20%
10% NH_3 in Kr	30	125%	4.17%

Table 12: Relative performance of various process gas mixtures.

Stagnation pressure at +15 psig, high voltage supply at -1500 V, resistor box at 4 kOhm; buffer gas density 2.5×10^{16} cm^{-3}.

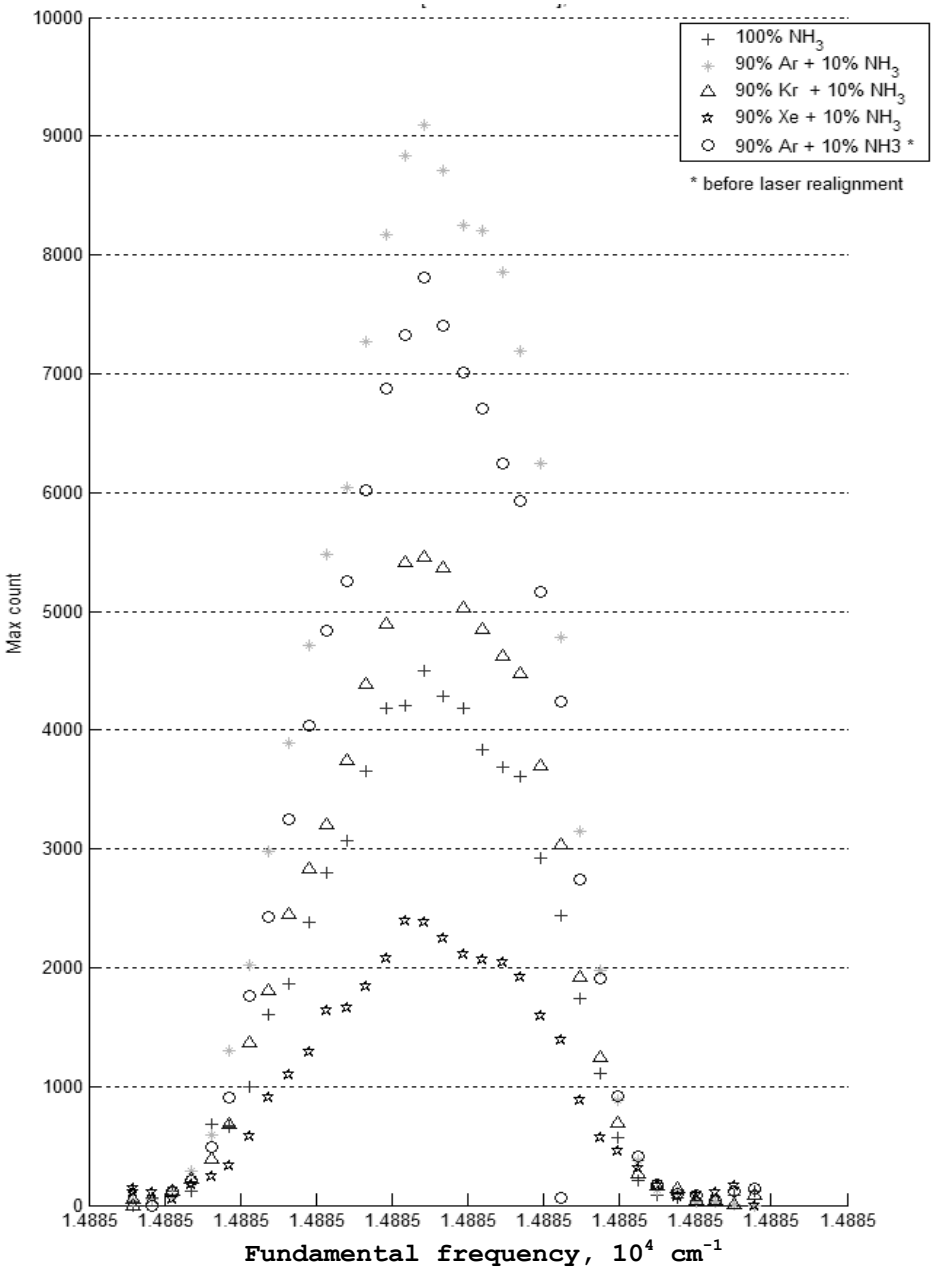

Figure 60: Process gas mixture optimization, see Table 12.

6.3 NH in the next-generation setup

Following the successful production of NH radicals and their cooling in the test cryostat we attempted detection of cold NH in the next-generation setup. However, we did not succeed in detecting NH in the buffer gas. This section outlines the issues that came to light during our attempts.

(1) Minimum detectable number of NH radicals in the next-generation setup turned out to be significantly higher than was initially expected. The signal-to-noise ratio of our camera-based fluorescence detection system is primarily limited by scatter of the probe laser, which can not be filtered spectrally or temporarily. In the test cryostat, blackened baffles placed near cell windows suppressed a significant portion of the laser scatter; unsuppressed scatter was concentrated in a few spots, where it was possible to use spatial filtering. In the next-generation setup we did not implement baffles, hoping to use active alignment to minimize scatter. The actual level of scattered light turned out to be significantly above our expectations, and its spatial distribution turned out to be highly uniform, preventing spatial filtering.

(2) We were not able to "lock onto" a free-flight signal of NH radicals in the cell without buffer gas in order to optimize fluorescence collection and production prior to attempts at acquiring buffer gas data. This inability was due to the fact that in the next-generation setup the camera looks along the magnet centerline directly into the discharge, while in the test cryostat we utilized a 3-axis geometry with molecular beam, laser beam, and camera axes perpendicular to each other. Anticipating problems with this geometry,

we planned to use the high voltage switch to rapidly cut off the discharge flash and turn the camera on after the flash has disappeared, but before NH molecules traversed the cell region. The discharge flash, however, lasts long enough after the switch cutoff time, and our noise level is poor enough, that we were not successful in implementing the initial plan.

(3) Scattering of the molecular beam by helium gas streaming from the cell orifice is a much larger problem in the next-generation setup than it was in the test cryostat. First, the molecules have to traverse a scattering region that is an order of magnitude longer than the one in the test cryostat. Second, while in the test cryostat helium coming out of the cell orifice that wasn't immediately cryopumped by charcoal would bounce away from the molecular beam path into the vacuum space, in the next-generation setup helium atoms that do not stick to the charcoal tube bounce back into the molecular beam path. This makes the next-generation setup much more sensitive to the exact value of helium-charcoal sticking probability, which is beyond our ability to measure or control. This discussion is continued in more detail in Appendix A.

(4) During our search for signal we tried to maximize the signal-to-noise ratio by making fluorescence collection time window as narrow as possible. In doing that we assumed that the peak of the signal would occur within at most a few ms following the discharge. Subsequent simulations of diffusion of NH in buffer gas showed that this assumption was not correct. Figure 61 shows the result of a simulation of diffusion in a realistic cell geometry. The signal peaks at ~12 ms after the molecular beam pulse. Before that time the molecules did not have enough time to diffuse into the probe region.

Further details on the molecules' time-dependent spatial distribution are presented in Appendix B.

(5) In designing the apparatus we assumed that placing cell entrance orifice one cell radius away from the probe region does not introduce any substantial signal losses due to cell wall absorption. This assumption was not correct, as can be seen in simulations presented in Figure 62. The cloud of molecules thermalizes within a few mm of the entrance orifice and begins to diffuse into the cell. The center of the cloud reaches depth of ~20 mm, or one half of cell radius, in ~15 ms. This is the time when the signal in the probe beam at 40 mm depth position reaches the peak seen in Figure 61. After that the molecules are rapidly lost to the walls of the cell; even though the center of the cloud slowly moves deeper into the cell towards the probe beam, the total number of molecules in the cloud is rapidly depleted by wall loss.

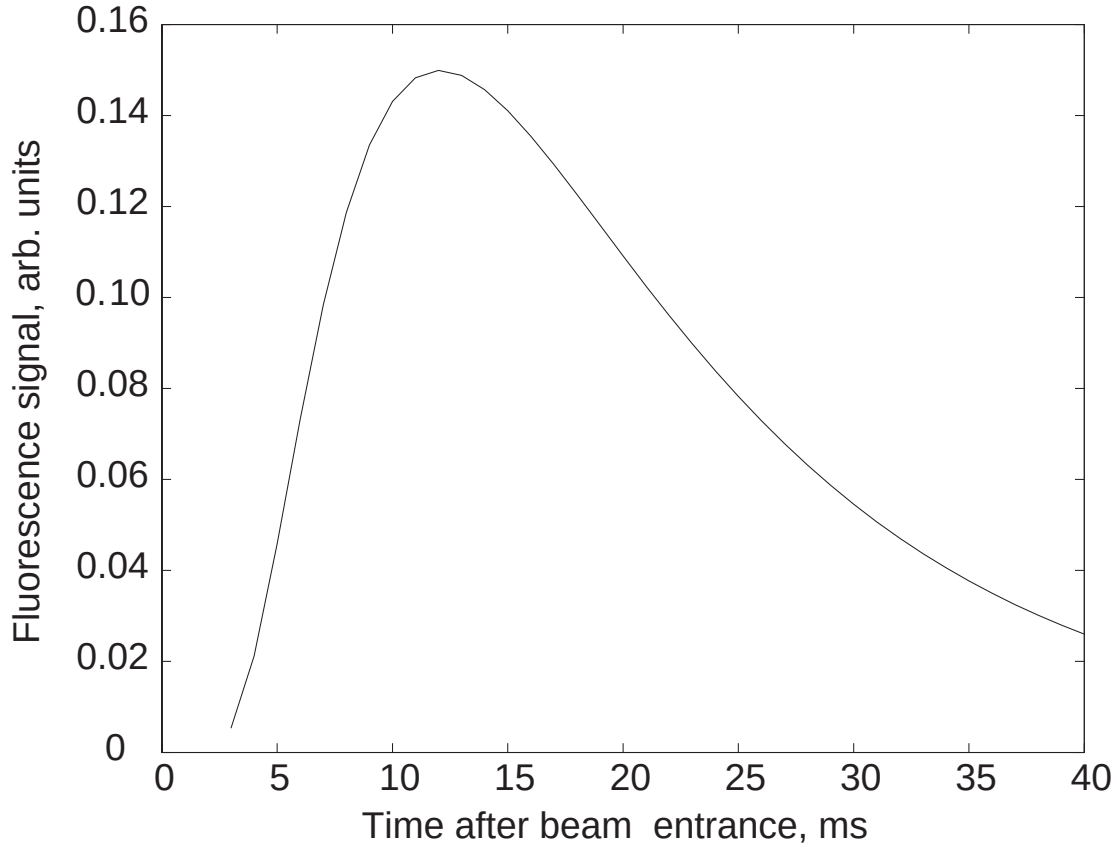

Figure 61: Simulation of integrated fluorescence signal of NH in buffer gas. Simulation parameters are: cell length 200 mm, cell radius 40 mm, entrance-to-probe laser distance 40mm, buffer gas pressure 10 mTorr, cell temperature 4.2 K, molecule-helium diffusion cross-section 1.5×10^{-15} cm^2. The parameters correspond to diffusion 1/*e* time of the (1,1) mode $\tau_{1,1} = 17.3$ ms. See also Figure 62.

The issues listed above are likely responsible for us not seeing NH signal in the buffer gas. We are currently in the process of addressing detection-related issues are currently addressed. NH molecules in free flight have been detected and their numbers optimized using a mass spectrometer connected to the magnet bore. A PMT has been installed to collect fluorescence perpendicular to the molecular and laser axes, and high-speed time-resolved fluorescence collection has been implemented with it. Absorbing

baffles were installed in the cell to suppress laser scatter. It is likely that the resulting reduction of detection noise level will allow us to observe NH in buffer gas in the nearest future. Resolving the issues related to helium scattering and diffusion would improve the signal even further, but would require significant cell design changes.

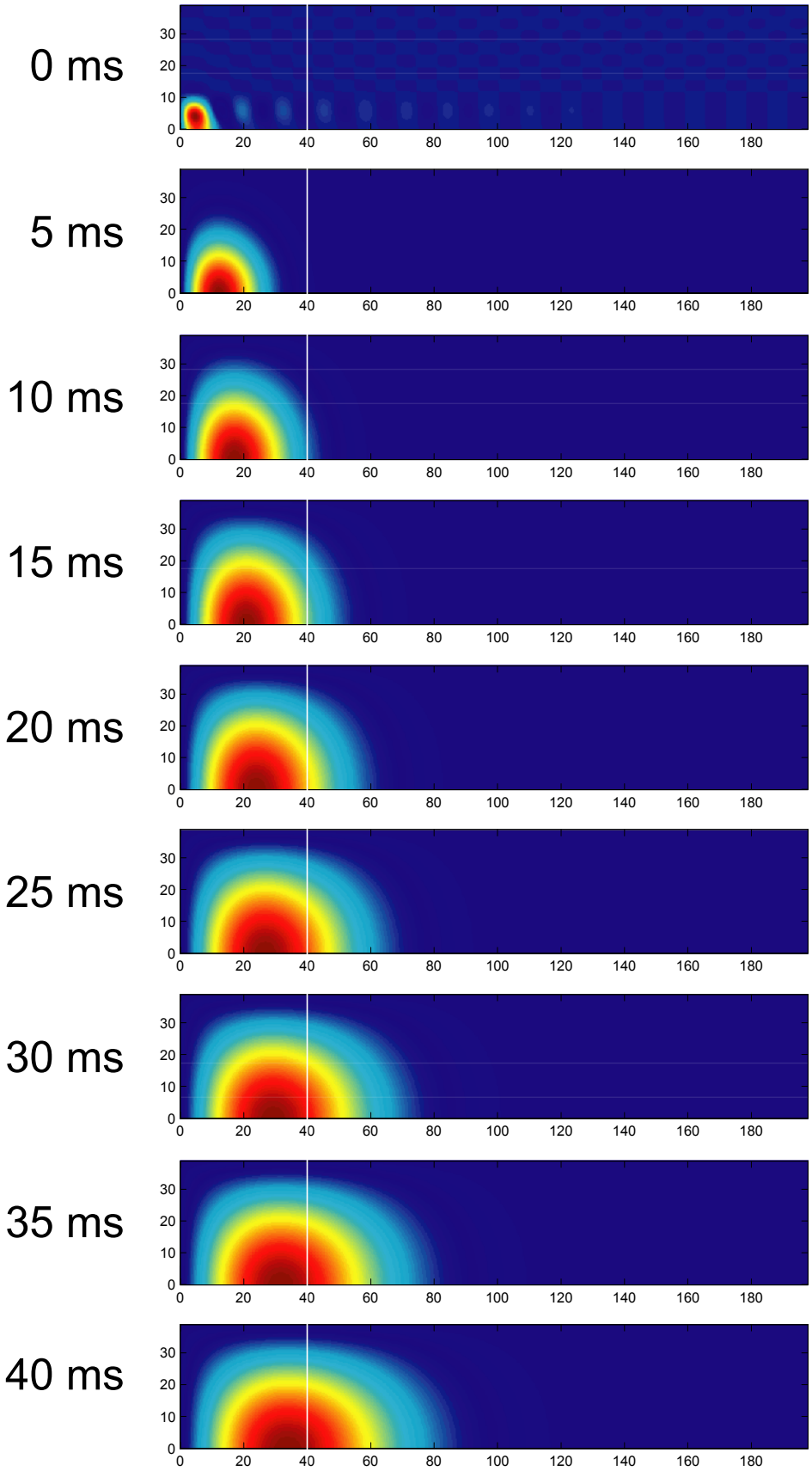
0 ms
5 ms
10 ms
15 ms
20 ms
25 ms
30 ms
35 ms
40 ms
0 20 40 60 80 100 120 140 160 180
0 10 20 30

Figure 62 (prev.page): Spatial distribution of molecules from diffusion simulations. Simulation parameters: see Figure 61. White line: position of probe beam. Color scale is rescaled for each image for clarity; consult Figure 61 for absolute signal magnitude.

7 Zeeman relaxation in CaF

The rate of Zeeman relaxation in cold collisions of molecules with helium is a critical parameter in deciding whether a particular molecule can be used for buffer-gas cooling and trapping. Prior to this work, a single measurement of the parameter existed [66], for CaH-^{3}He collisions at 400 mK. In this chapter we describe a measurement of Zeeman relaxation rate for CaF-^{3}He collisions at 2 K. The new measurement allows us to establish a trend in the dependence of Zeeman relaxation rates on molecular constants. The observed dependence is in agreement with theoretical predictions by Krems et al. [23], which confirms that the theory can be used to guide future buffer-gas cooling experiments.

7.1 Theory of Zeeman relaxation in $^2\Sigma$ molecules

Consider $^2\Sigma$(N"=0) molecules in a magnetic field surrounded by ^{3}He gas. Of the two electronic spin projection states, M_S=+1/2 (low-field seeking state, LFS) is trappable and is higher in energy, while M_S =-1/2 (high-field seeking state, HFS) is not trappable and is lower in energy. Transitions from M_S =+1/2 to M_S =-1/2 are referred to Zeeman relaxation. Zeeman relaxation is a trap loss process: once a molecule falls into a non-trappable state, it is ejected from the trap. The transition can not occur spontaneously; it can also be shown [24] that the electrostatic part $V(\mathbf{R},\mathbf{r})$ of the molecule-helium Hamiltonian

$$\begin{aligned} H &= -\frac{1}{2\mu} R^{-2} \frac{\partial}{\partial R} R^2 \frac{\partial}{\partial R} + \frac{\ell^2}{2\mu R^2} + H_{as} + V(R,r) - V_m(r) \\ H_{as} &= -\frac{1}{2\mu_m} r^{-2} \frac{\partial}{\partial r} r^2 \frac{\partial}{\partial r} + \frac{\mathbf{N}^2}{2\mu_m r^2} + \gamma \mathbf{N}\cdot\mathbf{S} + V_m(r) + 2\mu_0 \mathbf{B}\cdot\mathbf{S} \end{aligned} \tag{25}$$

is diagonal in M_S, and thus can not induce the Zeeman transitions[*]. The only M_S-changing component of Eq. (25) is then the spin-rotation interaction[†] $V_{SR}=\gamma\mathbf{N}\cdot\mathbf{S}$. Thus we expect the Zeeman relaxation rate to depend on the molecule's spin-rotation constant γ. Larger γ's would result in larger Zeeman rates. As the molecules are assumed to be prepared in the lowest rotational state N"=0, we would expect the effect of spin-rotation interaction to

[*] We refer the reader to Ref. [24] for a detailed explanation of (25) and for expressions for matrix elements of its components.

[†] Following Ref. [23], we ignore the interaction between the molecular spin and the nuclear spin of ^{3}He. While the interaction is M_S-changing, it is extremely small and does not influence this discussion

vanish. However, collisions can induce a "second-order" process shown in Figure 63, where the spin-flip occurs through the N"=1 state, where $\gamma\mathbf{N}\cdot\mathbf{S}$ no longer vanishes. Therefore we expect the Zeeman rate to decrease with increasing rotational constant B_v. Detailed analysis in Ref. [149] indicates that γ^2/B_v^4 is the scaling parameter for Zeeman relaxation rates in collisions of $^2\Sigma$ molecules with atoms‡.

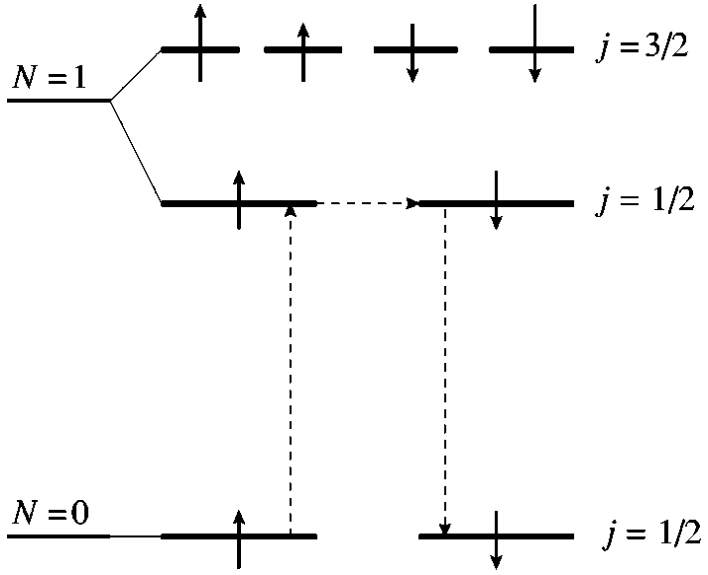

Figure 63: Spin-flipping mechanism in $^2\Sigma$ molecules; from Ref. [23].

‡ As described in Ref. [22], this discussion applies only to $^2\Sigma$ molecules. For $^3\Sigma$ molecules such as NH, the Hamiltonian of the form (25) contains an additional spin-spin coupling term (see [24]) $V_{SS} = \frac{2}{3}\lambda_{SS}\left[\frac{4\pi}{5}\right]^{1/2}\sqrt{6}\sum_q (-1)^q Y_{2-q}(r)[\mathbf{S}\otimes\mathbf{S}]_q^{(2)}$, which mixes N"=0 and N"=2 states, which results in M_S-changing transitions. The scaling parameter for this channel is λ_{SS}^2/B_v^2. The spin-rotation spin-flip channel is still present in $^3\Sigma$ molecules, but it is typically much weaker than the spin-spin channel, and so can be ignored.

So far we have avoided any discussion of collisional energy dependence of the Zeeman relaxation rate. The above scaling law is derived for the inelastic cross-section, which must be velocity-averaged to calculate the Zeeman relaxation rate at a given temperature. In general, the exact dependence of both elastic and inelastic cross-sections on collision energy must be calculated for each particular system. At low (<1 mK) temperatures the Zeeman cross-section is predicted [150] to scale as $\sqrt{T}$, while elastic cross-section is expected to be energy-independent. At intermediate energies (~100 mK) the dependence may be rather complex due to collisional resonances. At higher (~1 K) energies both elastic and inelastic cross-sections are expected to become energy-independent. In this work we assume that for all measurements (CaH at 400 mK, CaF at 2 K) the cross-sections may be assumed to be energy-independent, and we write the expected scaling law for Zeeman relaxation cross-section of $^2\Sigma$ molecules around 1 K as:

$$\sigma_{Zeem} \propto \frac{\gamma^2}{B_v^4} \qquad (26)$$

The Zeeman rate is then given by a product of the inelastic cross-section and the average molecule-helium velocity[§].

[§] Conveniently, for most molecules X the reduced mass for a ^{3}He-X system is close to the mass of ^{3}He, so the average velocity for different molecules is a constant times $\sqrt{T}$.

7.2 Properties of CaF

A number of features make calcium monofluoride CaF an attractive system for investigation of cold collisions. One is its simple structure: alkali-earth fluorides are the molecular-physics equivalents of alkali atoms in atomic physics. The molecule is composed of closed-shell ions Ca^{2+} and F^- with one free electron orbiting them [151]. Another reason is that from a spectroscopy standpoint, CaF is a very convenient molecule. Its naturally-occurring isotope content is 97% $^{40}Ca^{19}F$, its electronic ground state $X^2\Sigma^+$ has no orbital angular momentum, no spin-spin coupling, small spin-rotation coupling, and only two hyperfine sublevels due to fluorine's nuclear spin $^1/_2$. CaF can be produced in very large numbers in laser ablation of CaF_2 [152], and can be easily detected on a well-studied [153]* strong X↔A transition. Finally, the expected difference in Zeeman rates of CaH and CaF is such that we expect the CaF Zeeman rate to be large enough to be unambiguously different from that of CaH, yet small enough for an accurate measurement to be performed in our apparatus†. Table 13 summarizes the relevant parameters of CaF and CaH.

* complete list of observed transitions is available from the authors of [153]

† CaF is also strongly polar, with the dipole moment of 3.07 Debye [154], which may make it an attractive candidate for future molecular trapping experiments

	CaF $X^2\Sigma^+(v=0)$	CaH $X^2\Sigma^+(v=0)$
Mass, amu	59	41
Reduced mass, amu	2.85	2.80
Vibrational splitting v=0 to v=1, K	837	1813
Rotational splitting N=0 to N=1, K	0.9855	12.17
Spin-rotation constant γ, mK	1.895	59.71
Translational temperature, K	**2**	*0.4*
Cross-section scaling parameter γ^2/B_v^4, cm^2	1.26×10^{-4}	3.45×10^{-6}
Relative rate scaling parameter $T^{1/2}\gamma^2/B_v^4$	×82	×1
Elastic cross-section‡, cm^2	$\mathbf{(0.8+0.6/-0.2)\times10^{-14}}$	$\mathit{(1.5\pm0.6)\times10^{-14}}$
Rotational relaxation rate, cm^3s^{-1}	$\mathbf{> 2.1\times10^{-15}}$	$\mathit{> 10^{-15}}$
Vibrational relaxation rate, cm^3s^{-1}	**-**	$\mathit{< 10^{-16}}$
Zeeman relaxation rate, cm^3s^{-1}	$\mathbf{(7.7+5.4/-2.5)\times10^{-15}}$	$\mathit{10^{(-17\pm1)}}$
Ratio of elastic to inelastic cross-section	$\mathbf{10^4}$	$\mathit{> 10^5}$

Table 13: Comparison of CaF and CaH.

Data from: [153]; [72] (italics) and references therein; this work (boldface).

‡ see remarks in Appendix B of this work and in Appendix B of [71]

7.3 Experimental setup

The experimental setup is described in Refs. [71; 155]. A cryocell is schematically shown in Figure 64. The cell is cooled to ~500 mK with a ^{3}He refrigerator. A split-coil Helmholtz magnet creates a near-uniform field of up to 4 Tesla in the cell.

A precursor sample, vacuum hot-pressed calcium fluoride CaF_2 powder pellet, is mounted on the top end-cap of the cell. The sample is ablated with a doubled Nd:YAG laser to produce CaF molecules. A lump of manganese ^{55}Mn is mounted next to the CaF sample to generate Mn atoms used as a buffer gas density reference, as described below.

Ablation laser pulses result in rapid local heating of the inside of the cell. The heat is transmitted to outside walls of the cell and into the refrigerator on a timescale much longer than a timescale of a single measurement. The temperature inside the buffer gas immediately following the YAG pulse is therefore higher than the baseline temperature indicated by a ruthenium oxide thermometer on the outside of the cell. As it is not practical to place thermometers inside the buffer gas, we rely on Doppler broadening of spectral lines of atoms or molecules in the cell to infer the actual temperature of the buffer gas. This approach, of course, relies on the assumption that translational thermalization of laser-ablated atoms occurs much faster than any changes in temperature of the buffer gas. Multiple past experiences [77; 155] support this assumption.

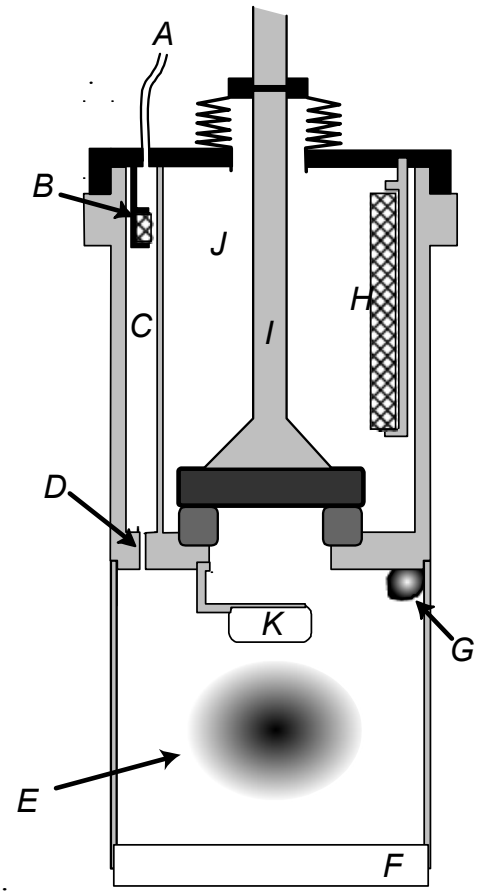

Figure 64: CaF cell schematic; from [71].
A: Fill line; B: Fill line sorb; C: "Waiting Room"; D: High-impedance pin-hole; E: Cooled sample; F:Window; G: Ablation Target (CaF or Mn); H: Large sorb; I: Valve shaft; J: "Pumping Chamber".

7.3.1 Spectroscopy

Optical detection system used in this experiment is shown in Figure 68. Note that the probe laser enters the cell through the bottom window, propagates along the cell centerline, reflects off a mirror, and then exits the cell through the bottom window.

Taking advantage of very large production yields of CaF (>10^{13} per pulse) and Mn (>10^{12} per pulse) and short radiative lifetimes of their transitions (21.9 ns, 58 ns), we use laser absorption, as opposed to LIF, to detect both CaF and Mn. The probe beam is split between two PMT detectors, "Signal" and "Reference". Typical optical densities are 1…3, so there is no need for a balanced-detector method described in section 5.8.3. Laser intensity fluctuations are removed by digitally dividing the output of the Reference PMT by that of the Signal PMT. A typical divided output is shown in Figure 66.

Two different lasers are used for probing CaF and Mn transitions, a dye[§] and a diode[**] correspondingly. Frequency of the lasers is continuously scanned in a sinusoidal pattern at 125 Hz[††] to obtain frequency- and time-resolved absorption spectra. Laser frequency is monitored with both WA-1500 and Wavemaster wavelength meters.

Manganese atoms are detected on a $^6S_{5/2} \rightarrow {}^6P_{7/2}$ transition at 24802.25 cm^{-1}. Spectra are fitted to a Voigt profile; the effect of pressure broadening is confirmed to be negligible by comparing spectral fits at different buffer gas densities. CaF is detected on $X^2\Sigma^+(v''=0) \rightarrow A^2\Pi_i(v'=0)$ transitions at 603 nm. Level structure of the two states and the designation of rotational lines are shown in Figure 67. We use two different rotational branches,

$R_{21}(N'')$: $X^2\Sigma^+(v''=0,J''=N''+1/2) \rightarrow A^2\Pi_{3/2}(v'=0,J'=N''+3/2)$ and

---

[§] Coherent 899-21

[**] External-cavity DL100, Toptica GmbH.

[††] Maximum scan rate of 125 Hz is actually too slow for our measurements. Whenever possible, the phase difference between the scan waveform and the YAG trigger is varied in 60^o increments for each data point to produce an effective scan rate of 3×125 Hz

$Q_{11}(N'')$: $X^2\Sigma^+(v''=0,J''=N''+1/2) \rightarrow A^2\Pi_{1/2}(v'=0,J'=N''+1/2)$

for our measurement, as shown in Table 14. The choice of the lines for a particular measurement is dictated by technical limitation of the dye laser: the width of a thick-etalon mode of the laser is ~1 cm^{-1}, so tuning between frequencies separated by more than ~0.5 cm^{-1} presents a significant inconvenience. We therefore use closely-spaced Q_{11} lines to perform measurements in zero magnetic field. In magnetic field, however, the Q_{11} branch has a large (~1 cm^{-1}/Tesla) Zeeman shift, so we use the R_{21} lines, which have a shift of ~0.2 cm^{-1}/Tesla, to perform in-field measurements.

Magnetic field along the probe beam is somewhat non-uniform, as shown in Figure 65. This results in magnetic broadening of transitions, which complicates spectrum analysis somewhat. We use calculated a field profile[‡‡] to model the broadened line profiles, then perform least-squares fits to adjust for any deviation of actual line profile from the calculated one caused by lack of precise knowledge of the molecules' spatial distribution.

The magnetic field defines the spin quantization axis to be along the cell centerline, with the direction set by polarity of magnet current. In order to avoid any uncertainties in comparing the signal from M_S=+1/2 and M_S=-1/2 spectral components, for in-field measurements we place a linear polarizer directly in front of the cell window. Several data points were acquired twice at opposite magnet current polarities to verify absence of errors due to the probe beam propagating off-axis.

[‡‡] BiotSavart program, Ripplon Inc., Burnaby BC, Canada

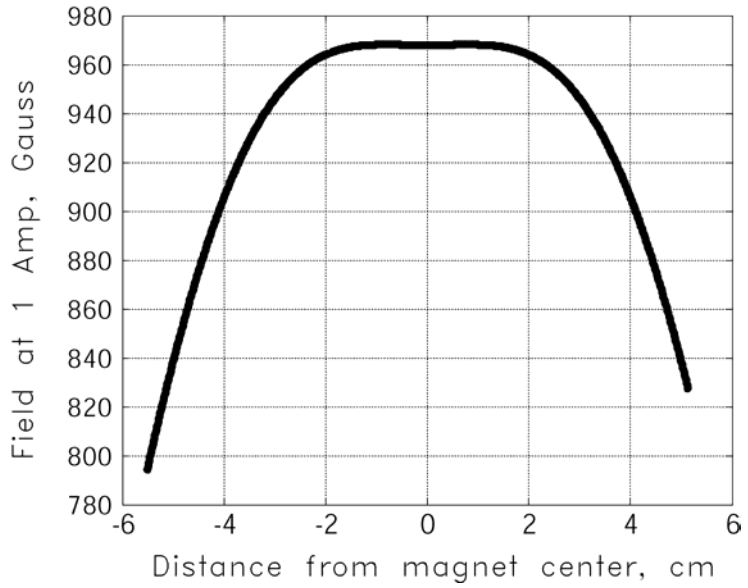

Figure 65: Calculated magnetic field profile along probe laser path.

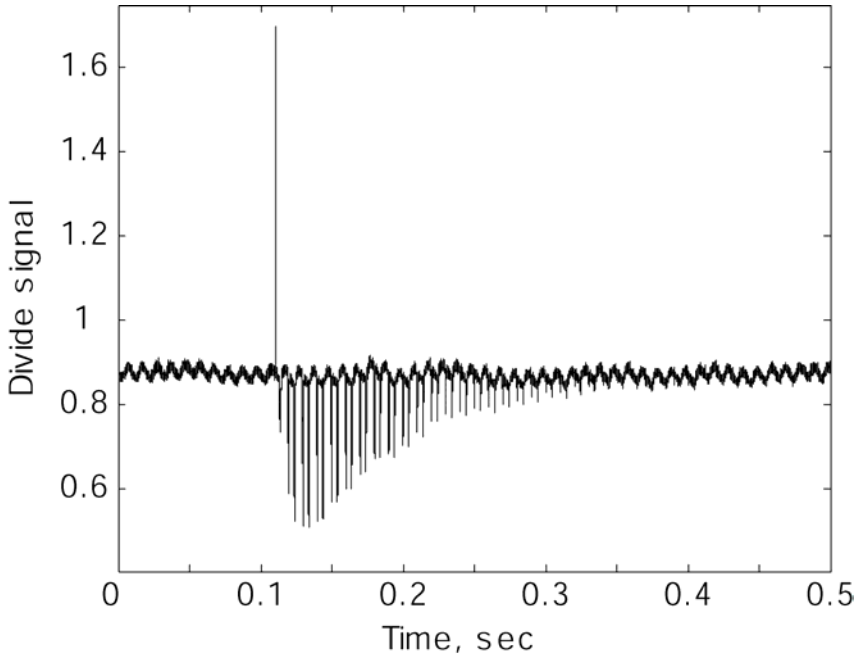

Figure 66: Typical CaF absorption signal.

Tall peak is ablation flash. Baseline modulation is due to etalon effects.

N"	R_{21}(N")	Q_{11}(N")
0	16566.10	16493.10
1	16567.17	16493.45
2	16568.24	16493.77
3	16569.31	16494.14

Table 14: Selected rotational lines of CaF, in cm^{-1}.

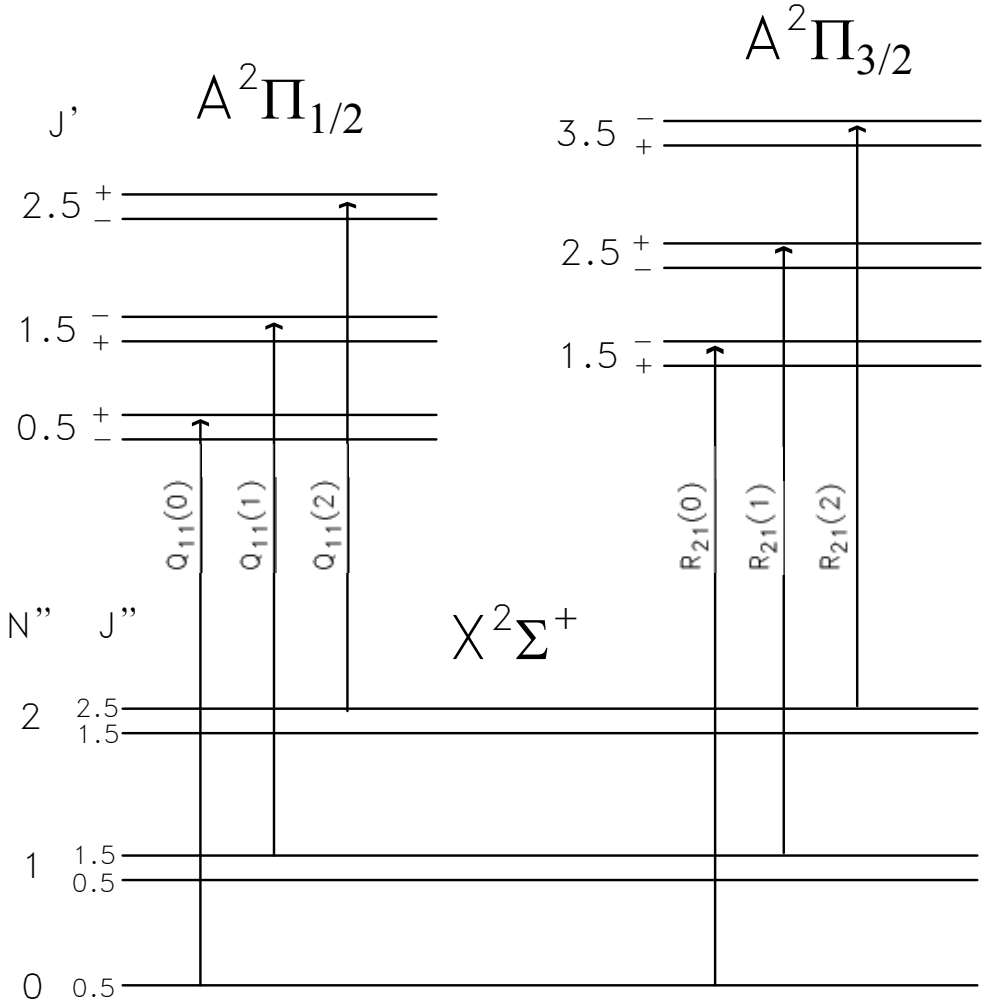

Figure 67: Rotational lines used in the experiment.

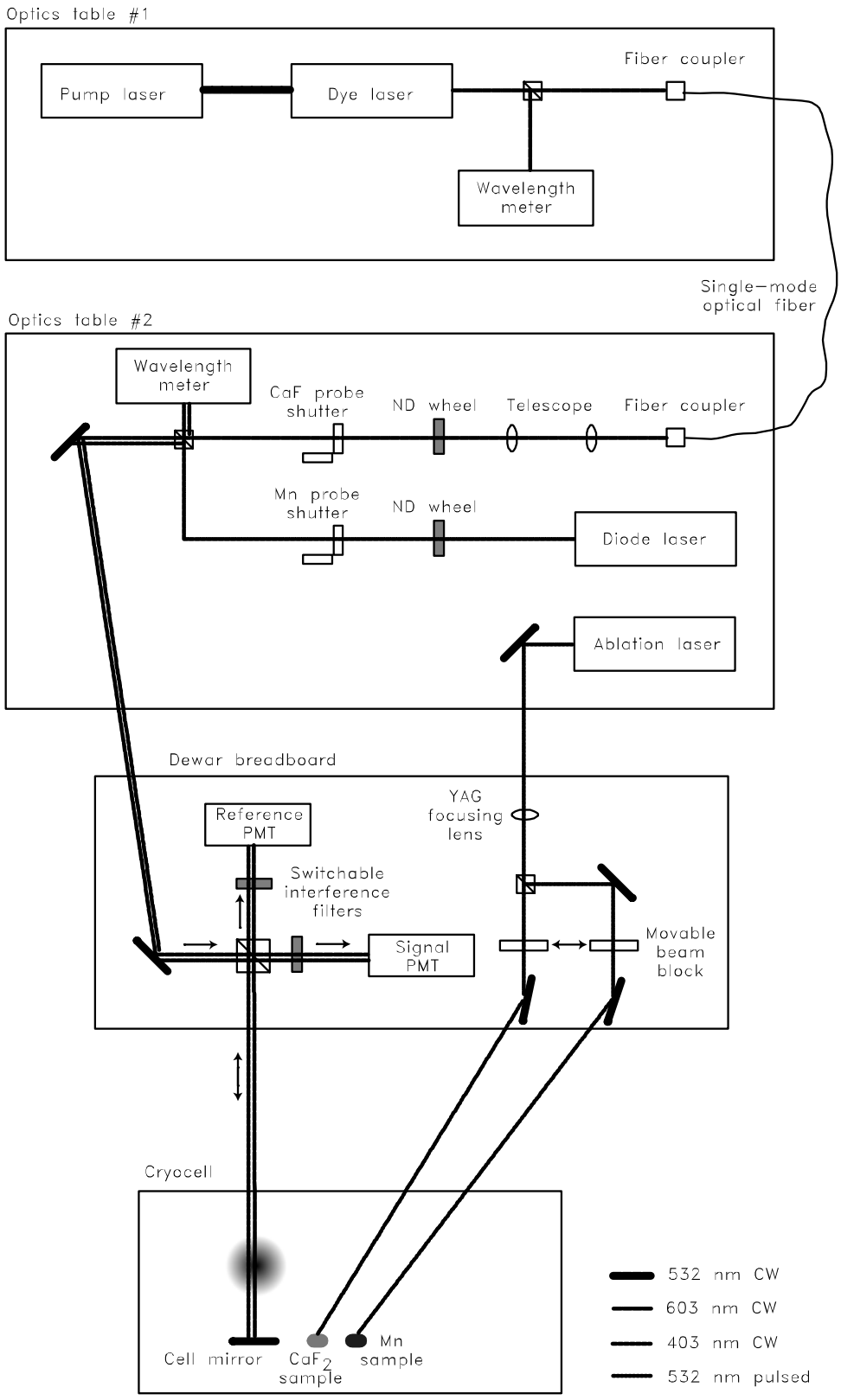

Figure 68: CaF optics setup.

7.3.2 Buffer gas density

Buffer gas handling in the CaF experiment is substantially different from the schemes described in previous chapters. Helium buffer gas is supplied into the cell by means of a cryogenic charcoal sorb, which contains a large quantity of helium and is connected to the cell via a high-impedance tube. Buffer gas density is set to an initial high value (~3×10^{16} cm^{-3}) by heating the charcoal sorb and letting helium into the cell through the impedance. The sorb is then quickly cooled down, which interrupts helium supply. Helium slowly leaves the cell through the inlet impedance and through leaks in the cell valve. Buffer gas density decreases exponentially with a 1/*e* timescale of ~30 minutes. Helium can also be removed rapidly by opening the cell valve.

Cell pressure can not be monitored directly in the CaF apparatus, so we must use other means to determine buffer gas density for each measurement. We take advantage of a significant difference between a typical measurement time (~1 s) and the 1/*e* time of buffer gas density decay (~30 min). CaF measurements are interspersed with measurements of diffusion lifetime of Mn, from which we extract the helium density using a previously-measured Mn-He diffusion cross-section [156]. Helium density dependence on time is then interpolated between the measured points to obtain values of helium density for all CaF measurements.

For very low buffer gas densities (~10^{15} cm^{-3}), the approach can no longer be used, as amounts of helium evaporated by the heat of the ablation laser become comparable to the amount of helium present in the cell prior to the ablation pulse. This

effect is referred to as “cold loading” [72]. As the amount of evaporated helium is constant from pulse to pulse, but different from sample to sample, we can use diffusion loss time of CaF as a buffer gas density indicator for the low helium densities.

7.3.3 Effect of YAG pulse energy

Changing the energy of the ablation laser pulses has two effects on the production of CaF. The total number of CaF increases with increased pulse energy, as shown in Table 15. From [72] we expect a turning point, above which the numbers start to decrease with increased energy. We do not reach that point for the range of pulse energies used in the experiment. The other effect is heating of the buffer gas, and the resulting increase in translational temperature of the molecules, see Table 15. For all measurements described in this chapter we assumed that the pulse energy of 8.5 mJ offers the optimal balance between the molecule yield, and thus signal strength, and the translational temperature.

Q-delay, μs	Pulse energy, mJ	Peak OD	Translational temperature, K	Yield per mJ, relative
320	8.5	1.3	2.04	100%
340	5.2	1.0	1.23	125%
360	2.5	0.26	1.09	68%

Table 15: Effect of pulse energy on CaF production.
Steady-state cell temperature: 500 mK, buffer gas density: 1.5×10^{16} cm^{-3}.

7.4 Signal time profile

Peak optical density of CaF, which is proportional to molecule number once thermalization has occurred, decays with time as shown in Figure 69. The time decay fits to a single exponential

$$OD(t) = OD_0 \exp(-t/\tau_{loss})$$

indicating a single-body loss process, such as diffusion. The same single-exponential behavior, with a different time constant, is observed for the Mn signal, and for all other atomic species (Cr, Eu, Na, …) for which this apparatus has been used in the past.

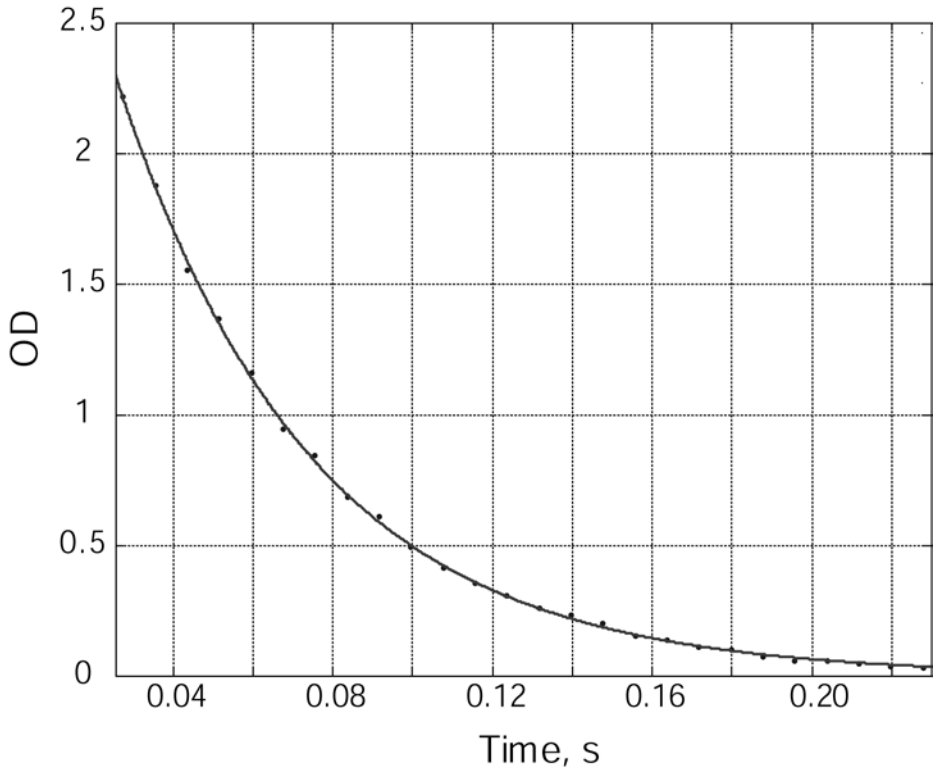

Figure 69: Typical CaF signal time profile.
Dots: measured optical density; line: fit to a single exponential. Time zero on this plot is at the start of data acquisition.

From previous experience it is known [156] that time decay of the total number of Mn atoms in the cell is well-described by[§§] a rate equation of the form:

$$\frac{dN_{Mn}}{dt} = -N_{Mn} \frac{f_{geom}}{n_{He}\sigma_{Mn-He}} \sqrt{\frac{T_{Mn}}{\mu_{Mn}}} \tag{27}$$

where n_{He} is helium density, T_{Mn} is translational temperature of Mn atoms, $\sigma_{Mn\text{-}He}$ is diffusion cross-section, f_{geom} is a factor dependent on cell geometry, and μ_{Mn} is the reduced mass of Mn-He system. We assume that translational thermalization occurs much faster than the diffusion loss, and that T_{Mn} does not depend on n_{He}. Both assumptions are consistent with observations.

We initially expected CaF loss to be described by the a similar equation:

$$\frac{dN_{CaF}}{dt} = -N_{CaF} \frac{f_{geom}}{n_{He}\sigma_{CaF-He}} \sqrt{\frac{T_{CaF}}{\mu_{CaF}}} \tag{28}$$

where all factors except $\sigma_{CaF\text{-}He}$ are nearly-identical to those for Mn. Since both Mn and CaF thermalize to similar translational temperatures, their reduced masses are nearly identical, and the geometrical factor is the same for both of them. To verify this assumption, we fitted Mn and CaF signals at several buffer gas densities to:

$$OD_{Mn}(n_{He}, t) = OD^{0}{}_{Mn}(n_{He}) \times \exp(-\frac{t}{\tau_{Mn}(n_{He})})$$

$$OD_{CaF}(n_{He}, t) = OD^{0}{}_{CaF}(n_{He}) \times \exp(-\frac{t}{\tau_{CaF}(n_{He})})$$

where we expect from (27) and (28):

[§§] Here we assume that the (1,1) approximation, further described in Appendix B, holds for both Mn and CaF

$$\frac{\tau_{CaF}}{\tau_{Mn}} = K\frac{\sigma_{CaF-He}}{\sigma_{Mn-He}} = const \tag{29}$$

The results of the fit are shown in Figure 70.

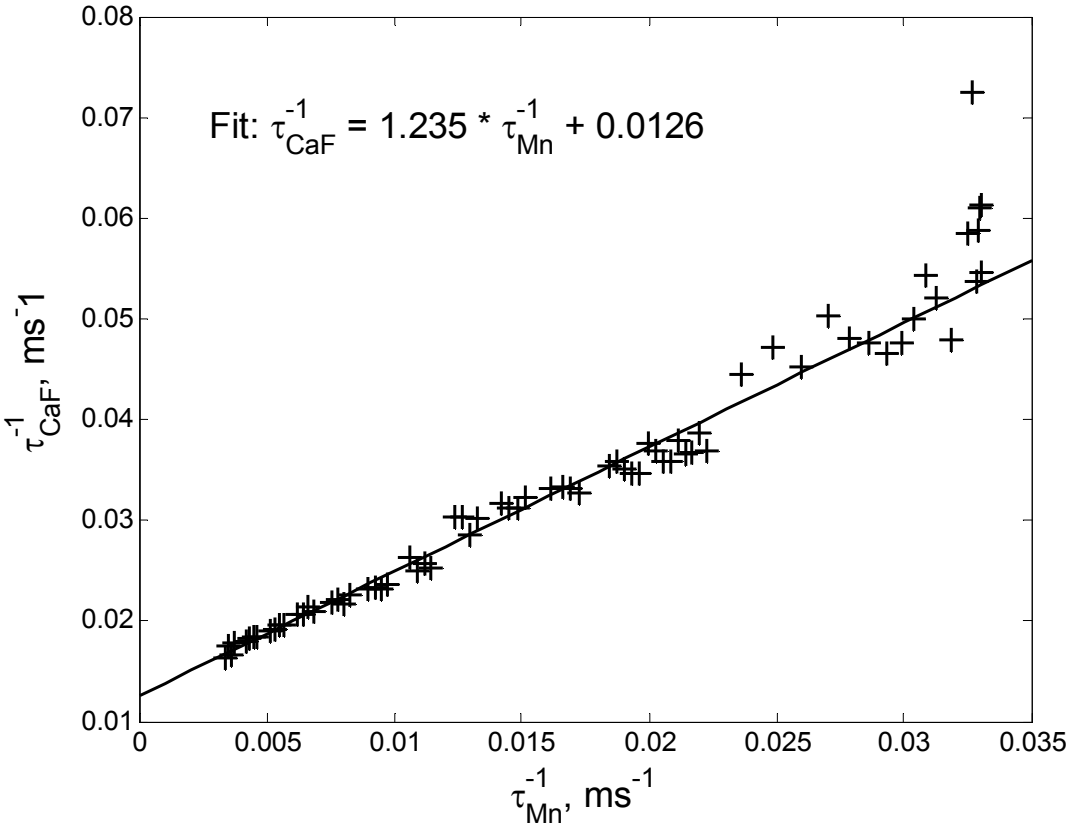

Figure 70: Loss timescales of CaF and Mn.
Crosses correspond to data at different values of buffer gas densities; line is linear fit. At low helium densities (far right side of the graph) Mn diffusion loss is not a good indicator of buffer gas density due to cold loading, and, as expected, data deviates from the linear fit.

The data fits to a linear relation that differs from (29) in that it has a fixed offset:

$$[\tau_{CaF}]^{-1} = 1.235 \times [\tau_{Mn}]^{-1} + 0.0126 \tag{30}$$

This indicates that an extra, buffer-gas independent single-body loss term has to be added to Eq.(28). CaF loss is then described by:

$$\frac{dN_{CaF}}{dt} = -N_{CaF}\frac{f_{geom}\sqrt{T/\mu}}{n_{He}\sigma_{CaF-He}} - \frac{N_{CaF}}{\tau_{extra}} \tag{31}$$

where $\sigma_{CaF-He} = 0.809 \times \sigma_{Mn-He}$ and $\tau_{extra} = 79.4$ ms.

The existence of an extra buffer-gas density independent loss term is somewhat surprising. Processes such as recombination or molecular-state changes are not expected to be buffer-gas density independent. A possible explanation for this loss term is dust created during ablation pulse that sweeps CaF molecules out of the buffer gas. If dust particles are large enough so that their motion is not affected by the presence of helium, they will travel ballistically through the cell in approximately $\tau_{dust} \simeq \sqrt{2L_{cell}/g} \approx 200$ ms. At times shorter than τ_{dust} we expect a roughly constant density of dust particles in the cell, independent of buffer gas density. To verify this explanation, we simultaneously ablated CaF and Mn. The loss of Mn was still described by a single exponential, but the loss timescale was shorter compared to not ablating CaF simultaneously. This measurement confirms that dust particles, or similar ballistic-traveling condensation centers, are likely responsible for the extra loss term in CaF.

It is important to note that a buffer-gas independent single-body loss mechanism was observed in another molecular cooling experiment, where vanadium monoxide was ablated [78]. In the VO experiment the extra loss mechanism was much stronger than diffusion loss, preventing trapping or Zeeman relaxation measurements. Fortunately, the extra loss term in CaF turned out to be comparable to diffusion loss at the relevant buffer gas densities, so the measurement in CaF could proceed.

7.5 Translational thermalization

We determine translational temperature of CaF molecules by fitting observed absorption spectra to a Voigt profile, as shown in Figure 71. Appendix C provides details on calculating hyperfine line positions in CaF spectra. Hyperfine structure at zero magnetic field is clearly resolved and was previously measured to a high degree of precision. We are therefore able use hyperfine line positions to calibrate voltage-to-frequency conversion of our laser, which is then used to extract frequency information from measured spectra.

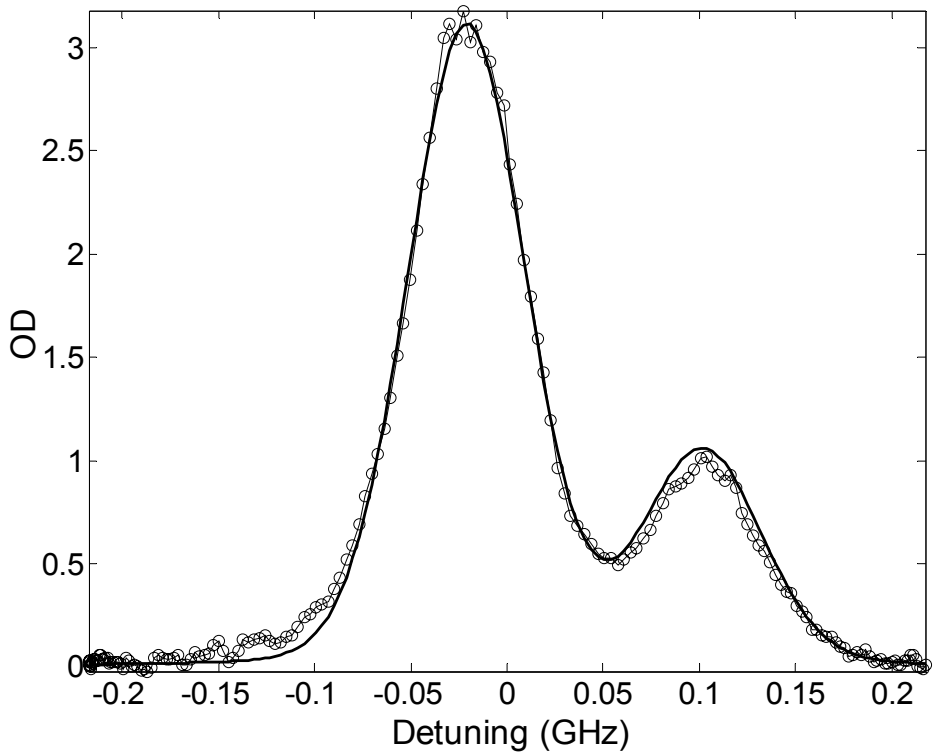

Figure 71: Typical zero-field spectrum of CaF $R_{21}(0)$.

Circles: data; line: fit to Voigt profile. Here T_{fit} = 2.194 K.

The dependence of translational temperature on time after ablation pulse is shown in Figure 72. The molecules thermalize to T_{trans}^{final} = 2.0±0.3 K within ~5 ms after the ablation pulse for typical buffer gas densities of ~1×10^{16} cm^{-3}. We attribute the difference between the final translational temperature of the molecules and the steady-state cell temperature to heating by ablation laser. The same difference is also present in thermalization of Mn atoms. The 1/*e* time of thermalization is shorter than 5 ms and exhibits a weak dependence on buffer gas density. However, since laser frequency scan rate is limited to 125 Hz, we are not able to extract more precise information about early-time thermalization dynamics. The observed thermalization time is consistent with a model in section 3.2.3.

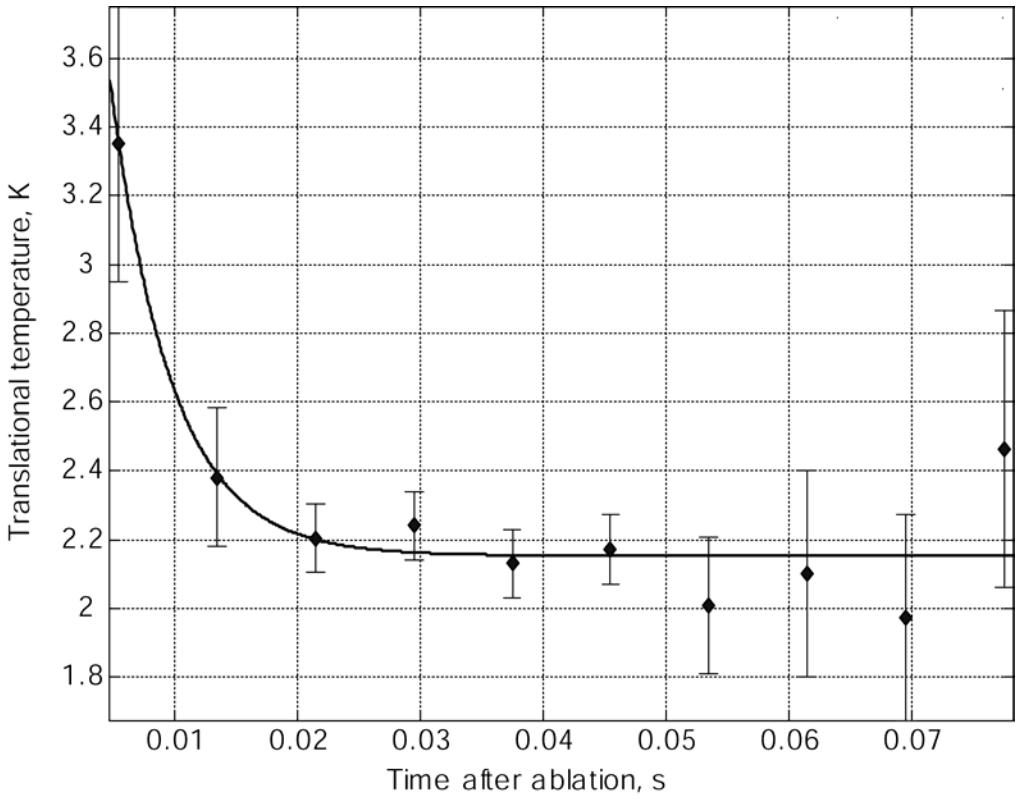

Figure 72: Translational thermalization of CaF.
Diamonds: translational temperature from Voigt profile fits, bars: fit uncertainty; line: single-exponential fit.

7.6 Rotational thermalization

Rotational temperature is determined by measuring the populations of N"=0 and N"=1 rotational states of CaF $X^2\Sigma^+$(v"=0) and assuming an equilibrium Boltzmann distribution among all rotational states. To verify applicability of the equilibrium distribution, we also measure the population of N"=2 state, which found to be consistent with a Bolzmann distribution for the temperature extracted from the N"=0 and N"=1 populations. In order to avoid tuning the laser between thick etalon modes, we use closely-spaced Q_{11}(N") lines for this measurement, and extract populations from OD of the signal by fitting to a Voigt profile, as shown in Figure 71. We observe that the rotational temperature settles to a final value in under 15 ms, consistent with full rotational thermalization with the buffer gas[***].

By observing time dependence of rotational state populations one may expect to measure the rotational thermalization rate for CaF-^{3}He collisions. As the spacing between $Q_{11}(0)$ and $Q_{11}(1)$ is ~10 GHz, which is much larger than the maximum laser scan width of 400 MHz, we can not observe populations of N"=0 and N"=1 states simultaneously. This limits our ability to extract rotational thermalization dynamics from the measured

[***] The final rotational temperature of 0.65 K differs from 2 K measured for final translational and spin temperatures, which is most likely due to incorrect use of Honl-London factors [157] to convert population ratios into temperature. Since we don't expect any surprises in rotational thermalization of diatomic molecules [158], and since the ratio clearly comes to its final value, we did not investigate this discrepancy further.

line intensities. We are able to measure only a lower limit on the rotational thermalization rate:

$$\Gamma_{rot} > 2.1\times10^{-15}\ cm^3\cdot s^{-1}$$

With the assumption that the rotational thermalization cross-section is energy-independent in the ~1 cm^{-1} collision energy range, this gives the lower limit on the rotational-state-changing inelastic cross-section in collisions of CaF $X^2\Sigma^+(v''=0)$-^{3}He:

$$\sigma_{rot} > 1.7\times10^{-19}\ cm^2$$

This measurement is consistent with theoretical predictions [158] [14], and with the previous measurements on CaH [66].

We also attempted measuring the rate for collision-induced vibrational relaxation $X^2\Sigma^+(v''=1)\rightarrow X^2\Sigma^+(v''=0)$ by measuring absorption on the $X(v''=1)\rightarrow A(v'=1)$ $R_{21}(N''=0)$ line. However, low signal levels prevented us from extracting any information from the measurement. We do not expect any vibrational relaxation on the timescales relevant for this experiment, as typical cross-sections for vibrational relaxation in collisions with He are in the $<10^{-20}$ cm^2 range [10; 13; 159-162].

7.7 Zeeman relaxation

Measurement of collision-induced Zeeman relaxation rate proceeds as follows. Molecules are first prepared at a known translational and rotational temperature in a uniform constant magnetic field which splits energies of low- and high-field seeking states. The initial ratio of population of the two states is a non-equilibrium value, e.g. 1:1. Collisions with helium gradually bring the populations into thermodynamic equilibrium, where the ratio of populations is given by the appropriate Boltzmann factor. By observing the dynamics of this equilibration process we extract the Zeeman relaxation rate.

Several issues must be addressed before a measurement can proceed:

(1) Any other relaxation processes, i.e. electronic, vibrational, and rotational relaxation, have to occur at known rates. From section 7.4 we conclude that the population of $X^2\Sigma$ electronic state does not change due to any metastable-state relaxation processes, so we may assume the electronic state relaxation rate to be zero. We also expect the vibrational relaxation rate to be much smaller than other rates in the experiment, as described in section 7.6. Rotational relaxation, on the other hand, is expected to be extremely fast. While we are able to place a lower bound on the rate ($\Gamma_{rot} > 2.1\times10^{-15}$ $cm^3\cdot s^{-1}$), we do not have reasons to believe that the actual rotational relaxation rate is comparable to the observed Zeeman relaxation rate ($\Gamma_{Zeem} = 7.7\times10^{-15}$ $cm^3\cdot s^{-1}$), and we assume the rotational relaxation rate to be infinite.

(2) Energy splitting between the Zeeman levels has to be large compared to the translational energy of the molecules, so that the equilibrium LFS-HFS population ratio

$$\left.\frac{n_{LFS}}{n_{HFS}}\right|_{eq.} = \exp\left(-\frac{\Delta E(B)}{k\,T_{trans}}\right) \equiv \chi \tag{32}$$

is measurably different from the initial non-equilibrium ratio of 1:1. Details of Zeeman effect in CaF $X^2\Sigma^+$ are provided in Appendix D; from that calculation we see that, to a large degree of accuracy, the splitting between low- and high-field seekers at Tesla-range fields is given by

$$[\Delta E, \mathrm{cm}^{-1}] = 0.935 \cdot [B, \mathrm{Tesla}]\,. \tag{33}$$

Since kinetic energy of 1 cm^{-1} corresponds to translational temperature of 1.44 K, we see that a few Tesla are necessary to obtain χ substantially different from 1. For our experimental parameters of T_{trans} = 2 K and B = 3.4 T we have χ^{-1} = 9.9, which is easily detectable with the levels of noise present in our apparatus.

(3) Translational temperature has to be equal or close to its final value during the measurement in order for meaningful results to be extracted. This is fulfilled in our measurements, as translational thermalization takes <5 ms, while Zeeman equilibration takes tens of ms. A detailed comparison of the measured translational and spin temperatures is shown in Figure 76.

(4) As described in section 7.3.1, tuning the laser between different etalon modes introduces substantial delays and uncertainties in comparing spectral line intensities. Therefore, the two spectral lines used to extract populations of low- and high-field seekers must be no more than ~15 GHz apart. However, as we learned from the rotational relaxation measurement, this is not sufficient if we want to compare the dynamics of line intensities at short times after the ablation pulse. In order to reliably extract the time dependence of intensity ratios, both lines have to be within a single laser scan, i.e. the

lines have to be no more than ~300 MHz apart. Fortunately, as shown in Figure 73, Zeeman shifts in transitions $X^2\Sigma^+(v''=0,N''=0)\rightarrow A^2\Pi_{3/2}(v'=0,J'=3/2)$ are such that there exists a field (~3.5 Tesla) at which the shifts for low- and high-field seekers are exactly equal, but their slopes are substantially different. This means that by tuning the magnetic field around 3.5 Tesla we can position the lines for low- and high-field seekers on the same laser scan and minimize any overlap between them, as shown in Figure 74.

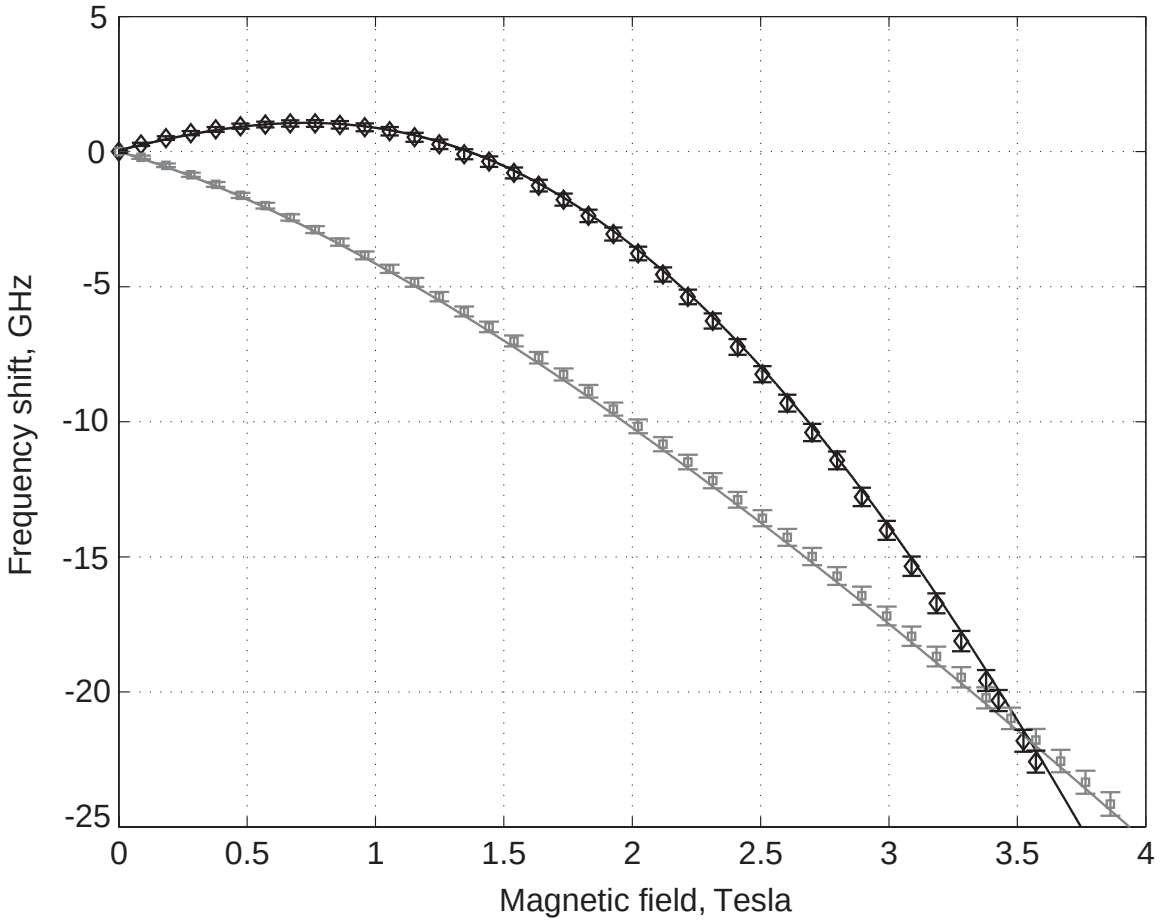

Figure 73: Zeeman shift in CaF $X^2\Sigma^+(v''=0,N''=0)\leftrightarrow A^2\Pi_{3/2}(v'=0,J'=^3/_2)$ transition. Diamonds (black): low-field seekers; squares (gray): high-field seekers.

Lines: Zeeman shift calculated from published molecular constants, see Ref. [163].

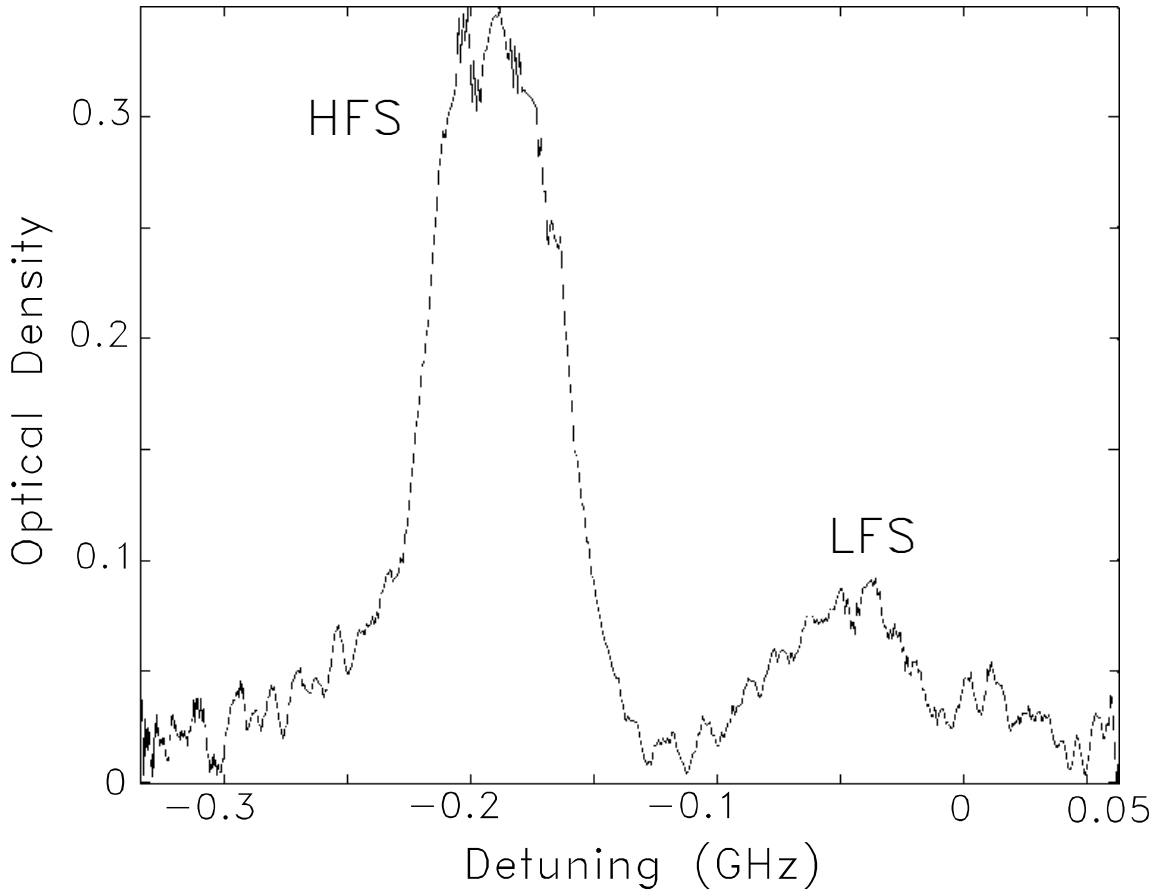

Figure 74: Typical spectrum of CaF at 34 kGauss.
The field is set so that the two lines are well-separated, but close enough to fit in the same laser frequency scan.

Once the time-resolved spectra are acquired, the optical densities can be converted into state populations using Voigt profiles that include Doppler and magnetic broadening. Some difficulty in performing the conversion comes from the facts that the magnetic field along the probe laser path is non-uniform (see Figure 65), the slopes of Zeeman shifts at 3.4 Tesla for the two states are different (see Figure 73), and the distribution of molecules in the cell is not known accurately. The two lines will thus have

substantially different magnetic broadening which is dependent on the spatial distribution of the molecules. In order to eliminate this uncertainty, we calculate the expected OD-to-population conversion factors assuming a (1,1) spatial distribution (see Appendix B), then introduce an adjustable parameter α which describes the deviation of expected conversion factors from the actual ones. From fitting the measured spectra we determine α=0.89±0.05. The dominant source of error in our measurement of Zeeman relaxation rate Γ_{Zeem} is then the error in $\sigma_{Mn-He} = 1.0^{+0.7}_{-0.3} \times 10^{-14}\,\text{cm}^2$ measured in Ref. [156].

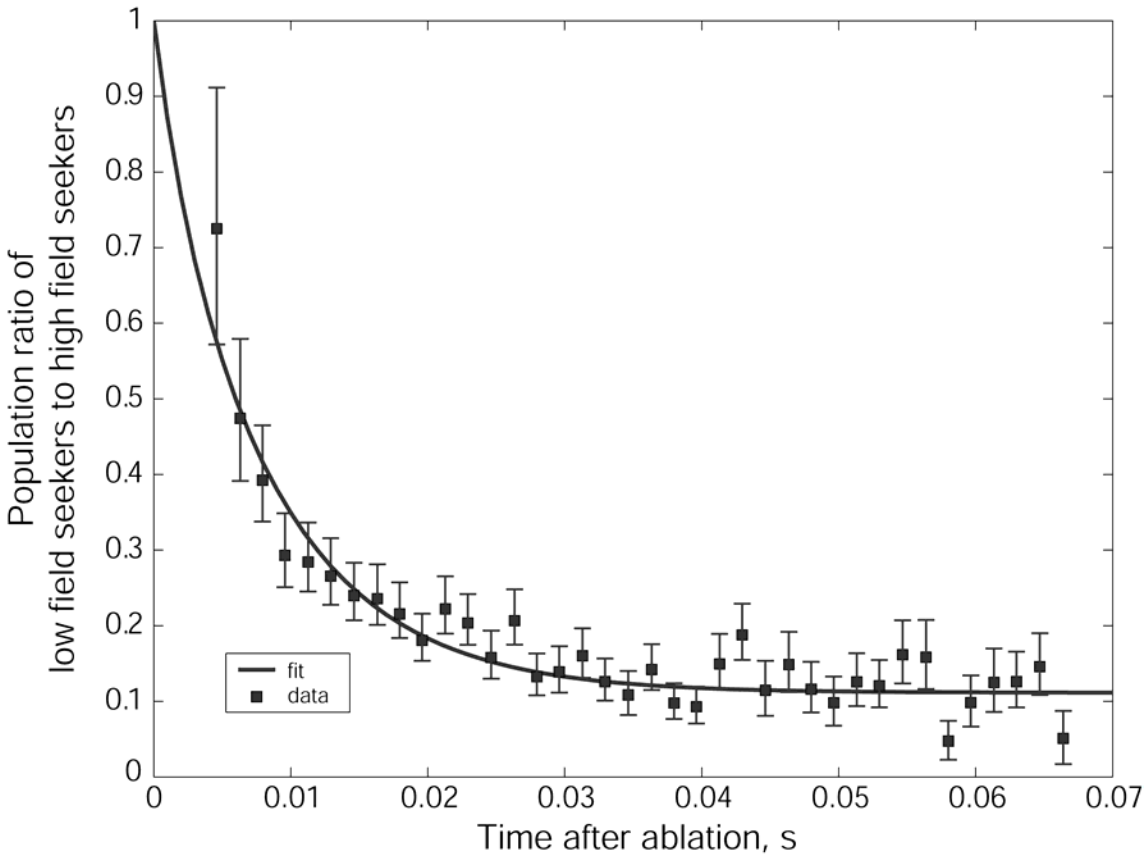

Figure 75: Ratio of populations of M_S=+$^1/_2$ and M_S=-$^1/_2$ states vs. time at 3.4 Tesla. Squares: populations extracted from spectral fits, bars: systematic errors. Line: Zeeman relaxation model fit, see text.

Figure 75 shows the measured time dependence of the population ratio of low- and high-field seekers. Figure 76 shows the same data converted into spin temperature $T_{spin} = -(\Delta E/k_B)\times\log(n_{LFS}/n_{HFS})$. As expected, the population ratio asymptotes to a final value; the final value is equal to χ (see Eq. (32)), i.e. the final value of spin temperature is equal to that of the translational temperature.

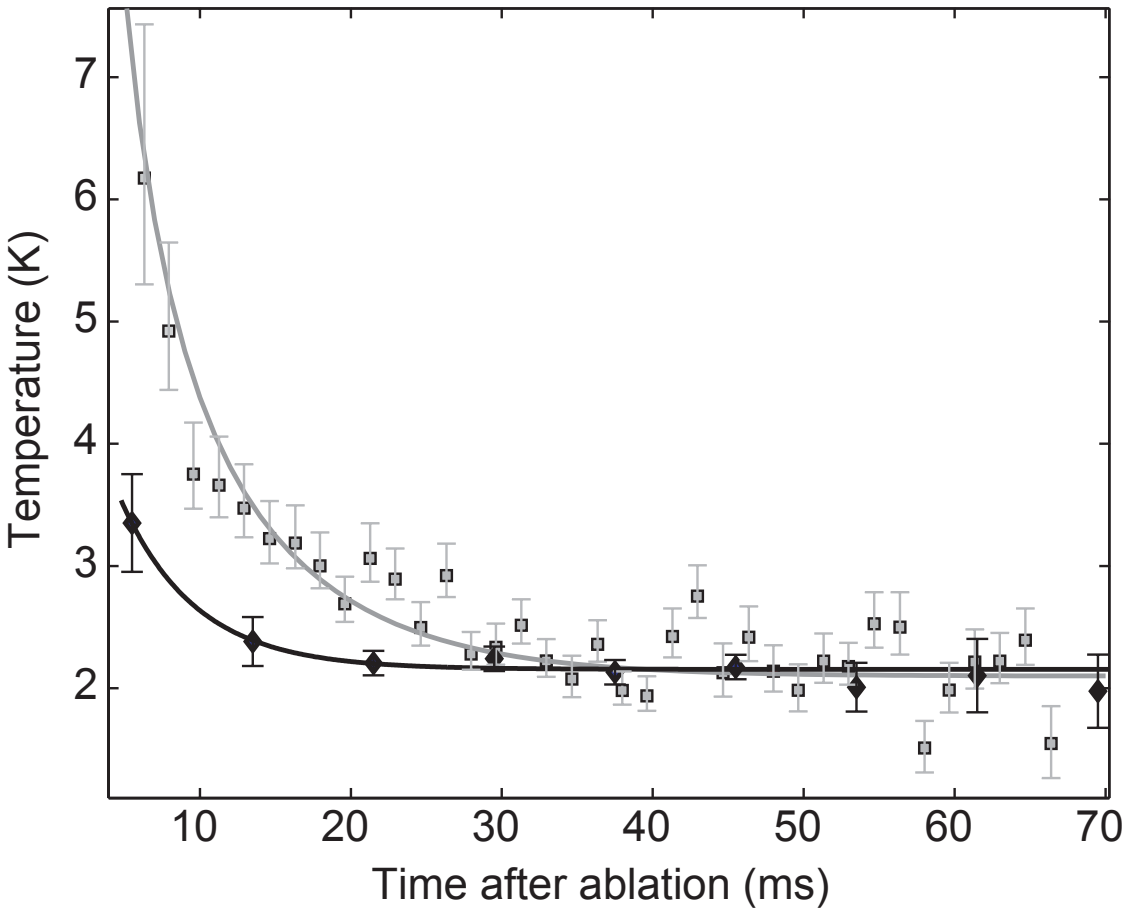

Figure 76: Spin and translational thermalization.
Diamonds (black): translational temperature, line: single-exponential fit.
Squares (gray): spin temperature, line: model fit, see text.

In order to extract the Zeeman relaxation rate from the time dependence of the population ratio, we make several simplifying assumptions. We assume that the ablation pulse creates equal populations of low- and high-field seekers n_{LFS} and n_{HFS}. After the pulse the populations are lost due to diffusion with timescales τ_{LFS}^{diff} and τ_{HFS}^{diff} correspondingly, and inter-converted due to Zeeman relaxation (LFS→HFS) and thermal excitation (HFS→LFS). We then have the following rate equations:

$$\begin{aligned}\frac{dn_{HFS}}{dt} &= -\frac{1}{\tau_{HFS}^{diff}} n_{HFS} + g_{down} n_{He} n_{LFS} - g_{up} n_{He} n_{HFS} \\ \frac{dn_{LFS}}{dt} &= -\frac{1}{\tau_{LFS}^{diff}} n_{LFS} - g_{down} n_{He} n_{LFS} + g_{up} n_{He} n_{HFS}\end{aligned} \tag{34}$$

where n_{He} is helium density, g_{down} is the LFS→HFS transition rate, and g_{up} is the HFS→LFS thermal excitation rate. From thermodynamic detailed balance considerations we see that

$$g_{up} = g_{down} \exp\left(-\frac{\Delta E}{kT_{trans}}\right) \tag{35}$$

since in equilibrium we must have $n_{LFS} = n_{HFS} \exp(-\Delta E / kT_{trans})$. Numerical simulations of diffusion in buffer gas with a realistic magnetic field profile indicate that, given the degree of magnetic field non-uniformity present in our cell, we can assume $\tau_{LFS}^{diff} \simeq \tau_{HFS}^{diff} \simeq \tau_{diff}$, i.e. the magnetic field has no effect on diffusion loss rates of HFS and LFS. Finally, we make an approximation that the Zeeman relaxation rate remains

constant at all times after ablation[†††], and write $g_{down} = \Gamma_{Zeem}$. Collecting all of the above, we obtain the following equation defining time dependence of the population ratio:

$$\frac{d}{dt}\left(\frac{n_{LFS}}{n_{HFS}}\right) = \Gamma_{Zeem}\, n_{He}\left[\left[1+\left(\frac{n_{LFS}}{n_{HFS}}\right)\right]\cdot\exp\left(\frac{\Delta E}{k_B\, T_{trans}(t)}\right)-\left(\frac{n_{LFS}}{n_{HFS}}\right)-\left(\frac{n_{LFS}}{n_{HFS}}\right)^2\right] \quad (36)$$

with an initial condition:

$$\left.\left(\frac{n_{LFS}}{n_{HFS}}\right)\right|_{t=0} = 1 \quad (37)$$

Eqs.(36), (37) can be numerically integrated for a given value of Γ_{Zeem} to produce the dependence of the population ratio on time. This dependence is then used as a fit function for the data, as shown in Figure 75. From these fits we then extract the value of Γ_{Zeem}:

$$\Gamma_{Zeem} = 7.7^{+5.4}_{-2.5}\times 10^{-15}\,\mathrm{cm}^3/\mathrm{s} \quad (38)$$

To put this rate in perspective we will convert it into a cross-section. We assume that the cross-section, which is generally energy-dependent, is nearly constant for collisional energies ~1 cm^{-1}. The assumption is consistent with theoretical calculations of CaH-He cross-sections [14; 15]. Using $\sigma_{Zeem} = \Gamma_{Zeem} / v$, where v is mean collision velocity, we obtain

$$\sigma_{Zeem}^{CaF-He} = 6.3^{+4.4}_{-2.1}\times 10^{-19}\,\mathrm{cm}^2 \quad (39)$$

[†††] the rate actually depends on $(T_{trans})^{1/2}$, which has a weak time dependence

The success of buffer-gas based trapping depends on the ratio of elastic and Zeeman-relaxation cross-sections. Using the relative elastic cross-section of CaF obtained in section 7.4:

$$\sigma_{el}^{CaF-He} = 0.809\,\sigma_{el}^{Mn-He} \tag{40}$$

and the value of Mn-^{3}He elastic cross-section[‡‡‡] from [156]:

$$\sigma_{el}^{Mn-He} = 1.0^{+0.7}_{-0.3} \times 10^{-14}\ \text{cm}^2 \tag{41}$$

we obtain

$$\frac{\sigma_{el}^{CaF-He}}{\sigma_{Zeem}^{CaF-He}} = 1.3^{+1.3}_{-0.5} \times 10^4 \tag{42}$$

This ratio indicates that spin depolarization in CaF takes ~10^4 collisions with He. This is a rather good ratio, as translational thermalization requires only ~10^2 collisions (see section 3.2.3), and we conclude that CaF can potentially be trapped using the buffer gas method. As techniques to trap and thermally isolate 1-μ_B species are advancing [155], it is likely that this ratio will be sufficient to produce a thermally-isolated trapped sample of CaF.

[‡‡‡] In this work we use elastic and diffusion cross-sections interchangeably. The difference is not material in the context of this discussion. For further details, see [71].

7.8 Discussion

While the value of Zeeman relaxation rate of CaF in collisions with ^{3}He is an important parameter for possible trapping of CaF, this work has much broader implications for the buffer-gas based trapping method. When buffer gas cooling and trapping is undertaken for a molecule, a substantial effort must be undertaken in researching of available spectroscopic information, setting up molecule-specific production, laser excitation, fluorescence detection, etc. If the molecule is subsequently found to be unsuitable for trapping due to a high Zeeman relaxation rate, switching to another molecule will require repeating a large portion of this effort.

Prior to this work, a single order-of-magnitude measurement existed for Zeeman relaxation of a molecule (CaH $X^2\Sigma^+$) in cold collisions with helium [66]. Theoretical calculations produced a calculated rate which was consistent with the measurement [14; 15]. However, the complexity of such calculations prevents us from using them to evaluate a range of interesting molecules for their Zeeman relaxation "fitness". A new approach to this problem was proposed in Ref. [23]: scaling parameters were introduced which may be used to determine relative suitability of $^2\Sigma$ and $^3\Sigma$ molecules for buffer-gas based trapping (see section 8.3). However, in order to verify the applicability of the scaling parameter theory to predict trends in Zeeman relaxation rates of $^2\Sigma$ molecules, at least two measurements of such rates must exist.

By comparing the measured rate for CaF, $(7.7+5.4-2.5)\times10^{-15}$ cm^{3}s^{-1} at 2 K, with the previously measured rate for CaH, $10^{-17\pm1}$ cm^{3}s^{-1} at 0.4 K, we see that their ratio (×800

with an order-of-magnitude accuracy) is consistent with what is expected from the theory (×82, see Table 13). Our measurement thus confirms that the theory of Krems et al. [23] may be used to select molecules for future buffer-gas trapping experiments[§§§].

[§§§] The order-of-magnitude discrepancy is not surprising. First, the accuracy of the CaH measurement is only order-of-magnitude. Second, the simple theory neglects any effects due to anisotropic molecular potentials of molecules in question.

8 Future directions

8.1 Other molecules of interest

Buffer gas cooling and magnetic trapping are general techniques, applicable to any paramagnetic molecule. While the present experiment is focused on NH, switching to other species can be accomplished by making small modifications to the apparatus. This chapter focuses primarily on 2-μ_B Σ-state molecules; the discussion will be expanded section 8.3.

8.1.1 Group V monohydrides

Monohydrides of group V elements, namely PH, AsH, SbH[****], are very similar to NH in their structure. They have 2-μ_B $X^3\Sigma$ ground states, and optical transitions $X^3\Sigma \leftrightarrow A^3\Pi_i$ at 340 nm, 330 nm, and 380 nm correspondingly. Most importantly, all of them can be produced by simply substituting a corresponding process gas (PH_3, AsH_3, SbH_3) for ammonia in the discharge source [164]. Handling of these precursor gases is somewhat challenging due to their toxicity, however, all technical challenges related to their use are routinely resolved in the semiconductor industry. As collisional properties of NH are understood better, it may be interesting to compare them to molecules of similar structure to establish common trends.

8.1.2 Group V monofluorides

Theoretical calculations predict that there is a strong dependence of Zeeman relaxation rate on the value of the rotational constant of the molecule. The ability to reliably predict Zeeman relaxation rates is critical for future work on buffer-gas cooling of molecules; by comparing Zeeman relaxation rates of monohydrides to those of monofluorides for a range of species we may expect to verify these predictions (see Table 16).

[****] while not quite fitting the pattern, BiH also has a ground state designated X 0^+ ($^3\Sigma^-$) and a studied transition to an excited B 0^+ state at 470 nm

A \ *B*	H	D	F
N	16.699	8.782	1.205
P	8.537	4.363	0.567
As	7.199	3.670	0.364

Table 16: Rotational constants (in cm^{-1}) of selected AB molecules that have $X^3\Sigma^-$ ground state, a gaseous AB_3 precursor, and have been produced in a glow discharge beam source[††††].

Measurement with group V monofluorides appears particularly easy in our apparatus, as their ground state has a 2 μ_B magnetic moment, and they can be produced by substituting the corresponding process gas (NF_3, PF_3, AsF_3) for ammonia in the discharge source. With the exception of NF, which does not have a convenient strong one-photon transition, spectroscopic detection can be accomplished on strong $X^3\Sigma \leftrightarrow A^3\Pi_i$ transitions in the 300-400 nm range.

8.1.3 Group V halides

In addition to monofluorides, other group V halides, e.g. NCl, NI, PCl, etc., have a 2-μ_B Σ ground state ($X^3\Sigma^-$). They can be produced either in a beam (e.g discharge in PH_3+CF_4 mixture produces PF [165] or discharge in N_2+Cl_2 produces NCl [166]) or

[††††] references are too numerous to list, but the reader may, e.g., search for "E.Hirota" or "Y.Endo" in INSPEC or SCI

using laser ablation. It is likely that ablation of, e.g., solid ammonium fluoride NH_4F will yield substantial numbers of NH $X^3\Sigma^-$ and NF $X^3\Sigma^-$; ablating NH_4Cl may yield NH $X^3\Sigma^-$ and NCl $X^3\Sigma^-$, etc. Similarly to monohydrides, most Group V halides have easily accessible strong X-A transitions.

8.1.4 Molecules without a common process gas

A wide range of interesting molecules can be loaded into the system if one is willing to invest into development of less-common sources and detection schemes. Of high interest are molecules with a high magnetic moment, e.g. CrH ($X^6\Sigma$), MnH ($X^7\Sigma$), MnF ($X^7\Sigma$). High magnetic moment makes the trap threshold higher, relaxing requirements for superconducting magnet technology and cryogenics. A possible method of production for beams of refractory-metal-monohydride or refractory-metal-monofluoride molecules is nozzle ablation in a reactive gas. A refractory metal target (e.g. a lump of Mn) is positioned in the nozzle of a beam containing e.g. H_2, F_2, or SF_6. An ablation laser hits the target in sync with a gas pulse; the energy of the laser evaporates the metal, and dissociates the gas; reactivity of H and F ensures formation of the required radicals.

If a clean beam source is not required, a range of interesting molecules can be produced via in-cell laser ablation. For refractory metal-monohydrides or -monofluorides, one could ablate a compressed mixture of fine powders of the metal and another solid material with high hydrogen or fluorine content; a wide range of organic materials fit the requirement.

Another class of molecules that would be of significant interest is rare earth monohydrides. Recent experiments on Zeeman relaxation in rare earth atoms point to a

dramatic suppression of Zeeman relaxation by the outer *s*-shell electrons; it is possible that rare earth monohydrides also offer extremely low Zeeman relaxation rates. These molecules should be rather simple to produce via either the methods described above for refractory metals, or by laser-ablating rare earth hydrides: rare earth metals readily absorb large quantities of hydrogen to form MH_2 and MH_3 compounds at room temperature [167].

8.2 Stern-Gerlach filtering

In section 4.2.3 we described potential issues associated with unwanted products of glow discharge, and mentioned Stern-Gerlach filtering as a possible solution to most of them. This section presents further insights into design of a Stern-Gerlach filtering stage.

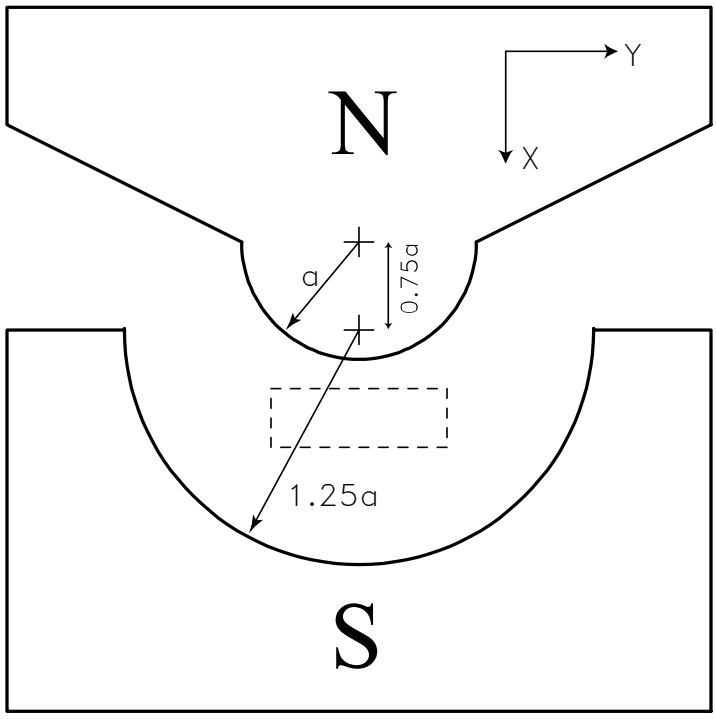

Figure 77: Cross-section of a "two-wire" Stern-Gerlach filter.

An example of a Stern-Gerlach-type filter in a so-called two-wire configuration [168] is shown in Figure 77. The setup consists of two semi-circular magnet poles with radii *a* and *1.25a* and centers at (*x=0, y=0*) and (*x=0.75a, y=0*); the length of the poles in Z direction is *L>>a.* This setup creates a near-uniform magnetic field gradient within a

rectangular zone ("sweet zone") with boundaries (*1.1a<x<1.3a, -0.7a<y<0.7a*). The value of the gradient is

$$\frac{dH}{dx} = -0.984\frac{H_0}{a} \tag{43}$$

where H_0 is the field in the middle of the "sweet zone". A molecular beam coming through the "sweet zone" and entering a detector positioned at distance Z_0 after the filter will be deflected by

$$\Delta X = 0.984\frac{H_0}{a}\frac{L(L+2Z_0)}{2mv^2}\mu \tag{44}$$

where μ is the magnetic moment of the particles, m is their mass, and v is beam velocity. In a supersonic beam all particles, regardless of their individual masses, are traveling at the same forward velocity

$$v_{beam} = \sqrt{\frac{C_P^{eff}}{M^{eff}}T_0} \tag{45}$$

where C_P^{eff} and M^{eff} are heat capacity and molar mass of the gas mixture, and T_0 is source temperature. Therefore, the deflection of individual mixture components will be determined only by their respective ratios of μ/m, which vary significantly between different discharge byproducts. Introducing a Stern-Gerlach filtering stage can thus produce a beam composed solely of molecules of interest.

As high beam fluxes are critical for our experiments, we need to evaluate whether a large "sweet zone" and significant deflection can be produced with common magnetic technologies. Consider a room-temperature molecular beam of NH seeded in Ar; Eq. (45) then gives beam velocity v_{beam} = 550 m/s. To deflect NH molecules by 5 mm, which is significant given the typical cell entrance aperture diameter of 3 mm, we can use a 10-cm

long filter positioned 20 cm before the aperture with a = 1.5 cm. The required magnetic field is H_0 = 7.7 kGauss can be achieved with common permanent-magnet and soft-iron materials; the "sweet zone" dimensions are 3 mm by 21 mm, which can pass a beam which is at least an order of magnitude higher in flux than what is currently available in our apparatus.

If Stern-Gerlach filtering is implemented, the discharge source can be converted to a true slit geometry [169-172] by modifying the pulsed valve and valve spacer described in Chapter 5. This way the capacities of the molecular beam and the Stern-Gerlach filter can be matched and fully utilized; converting the cell entrance to a slit geometry is also a trivial modification.

8.3 Systematic investigation of diatomic molecules

In this section we propose a systematic way for further investigation of diatomic molecules for buffer-gas loaded magnetic trapping. As in previous chapters, we do not consider non-zero angular momentum molecules, those in ground states $X^2\Pi$ (OH, CH, NO, SF, …), $X^3\Pi$ (C_2, I_2, Cl_2, F_2, SiO, …), $X^3\Delta$ (ZrO, …), etc. or those in long-lived metastable states (CO $d^3\Delta$, …). These molecules can easily be trapped with a magnetic field; Ch. 6.3 of ref. [173] provides details on calculating Zeeman energy shifts in non-Σ molecules. New evidence from buffer-gas cooling of rare-earth atoms indicates that certain non-S atoms (e.g. Dy $^5I_8$) have surprisingly low Zeeman relaxation rates [76]; similar physics may perhaps occur in high-Λ molecules, making them stable with respect to spin-flipping collisions. While in this work we ignore non-Σ molecules to simplify the discussion, we recommend that they be investigated in the near future.

In this chapter we consider three separate categories of molecules: 1-μ_B $^2\Sigma$ (see Table 17), 2-μ_B $^3\Sigma$ (see Table 18), and many-μ_B $^{(2S+1>3)}\Sigma$ (see Table 19). For this discussion we assume that the theoretical predictions [22; 23; 149] of the scaling of Zeeman relaxation rates with molecular constants hold for all $^2\Sigma$ and $^3\Sigma$ molecules, and that elastic cross-sections in molecule-helium collisions are approximately constant for all diatomics.

Table 17 lists values of rotational constant B and spin-rotation constant γ for selected $^2\Sigma$ molecules; values of γ^2/B^4 are plotted in Figure 78. We see that the parameter

values span at least 4 orders of magnitude; adding measurements of Zeeman relaxation on BaF and PdH to existing data on CaH and CaF would cover the range with a datapoint approximately once every decade. Assuming that elastic-to-inelastic rate ratio of 10^4 is the cut-off point for trapping of a 1-μ_B molecule in a dilution refrigerator-based apparatus, trapping of the following spectroscopically well-studied $^2\Sigma$ molecules can be attempted: BO, CN, ZnH, CaF, ZnD. Note that Figure 78 does not include every known $^2\Sigma$ molecule, so this list may be significantly longer.

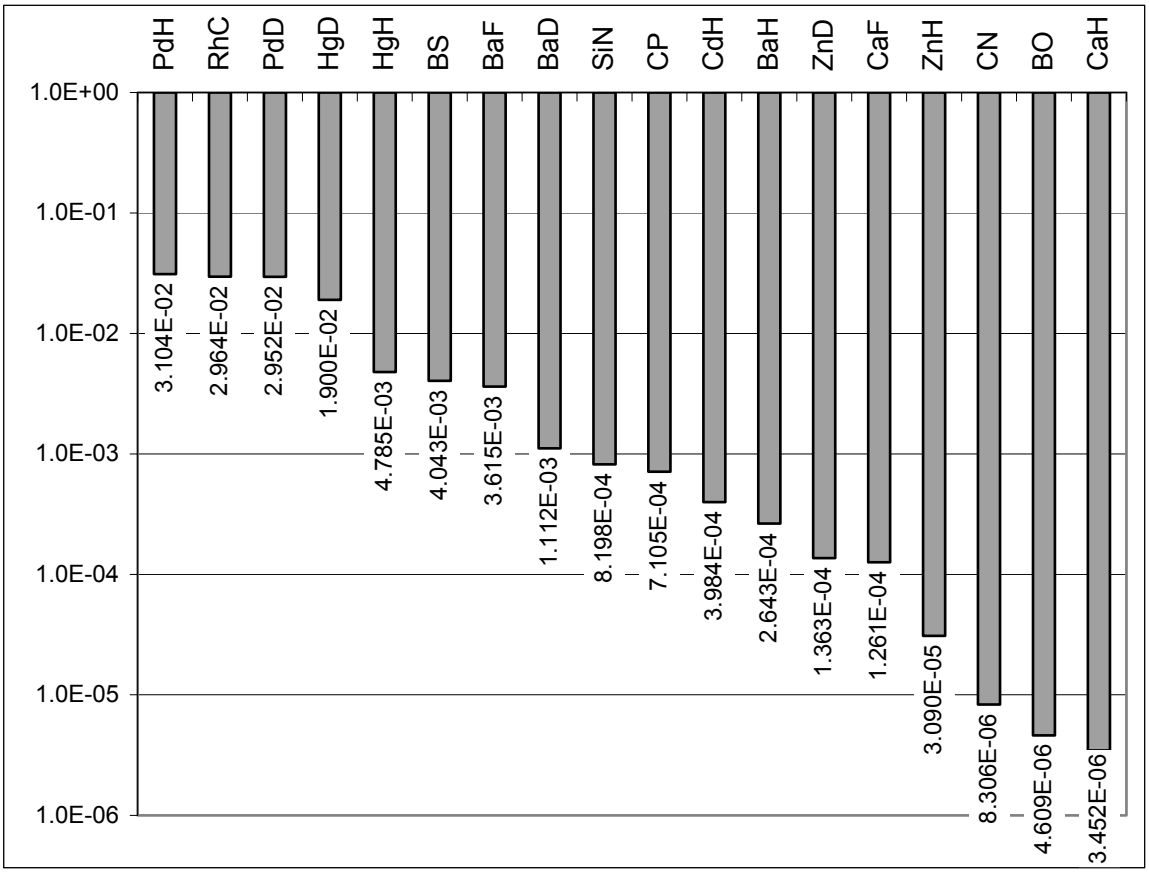

Figure 78: Zeeman relaxation parameter γ^2/B_v^4 in cm^2 for selected $X^2\Sigma(v''=0)$ molecules.

Smaller value indicates better buffer-gas loading properties. Most molecules may be produced by both glow discharge‡‡‡‡ and ablation of solid precursor.

‡‡‡‡ for details, search in an abstract database for works of E. Hirota or Y. Endo

	γ, cm^{-1}	B_v, cm^{-1}	γ^2/B_v^4, cm^2
PdH	-2.300E+00	3.6130	3.104E-02
RhC	-6.210E-02	0.6006	2.964E-02
PdD	-2.288E+00	3.6489	2.952E-02
HgD	1.080E+00	2.7990	1.900E-02
HgH	2.130E+00	5.5490	4.785E-03
BS	2.660E-02	0.6468	4.043E-03
BaF	2.800E-03	0.2158	3.615E-03
BaD	9.720E-02	1.7072	1.112E-03
SiN	1.530E-02	0.7310	8.198E-04
CP	-1.700E-02	0.7986	7.105E-04
CdH	5.900E-01	5.4370	3.984E-04
BaH	1.860E-01	3.3823	2.643E-04
ZnD	1.310E-01	3.3497	1.363E-04
CaF	1.317E-03	0.3425	1.261E-04
ZnH	2.480E-01	6.6794	3.090E-05
CN	1.040E-02	1.8996	8.306E-06
BO	6.500E-03	1.7400	4.609E-06
CaH	3.400E-02	4.2778	3.452E-06
SrH			
RbO			
NeH			
MgF			
CsO			
ClO			
BeH			
BeF			

Table 17: Constants of selected $X^2\Sigma(v''=0)$ molecules.

Data from [173] and various articles in J.Chem.Phys.

Table 18 lists values of rotational constant B, spin-rotation constant γ, and spin-spin coupling constant λ_{SS} for selected $^3\Sigma$ molecules; values of $\lambda_{SS}\,{}^2/B^2$ are plotted in Figure 79. Measurements of Zeeman relaxation on NH, PH[§§§§] and PF[*****] should be within immediate reach of both the ablation and the beam apparatus; NF[†††††], NCl[‡‡‡‡‡] and PCl can also be detected using a pulsed dye laser system. The resulting Zeeman relaxation data would cover 6 orders of magnitude in the parameter range, and can be used for both refinement of cold collision theory and for decision-making on which $^3\Sigma$ molecules are good trapping candidates.

[§§§§] detection on $X^3\Sigma$-$A^3\Pi$ at 340 nm

[*****] detection on $X^3\Sigma$-$A^3\Pi$ at 340 nm (τ = 2 μs)

[†††††] detection on forbidden transition $X^3\Sigma$-$b^1\Sigma$ at 560 nm (τ=200 ms)

[‡‡‡‡‡] detection on forbidden transition $X^3\Sigma$-$b^1\Sigma$ at 665 nm

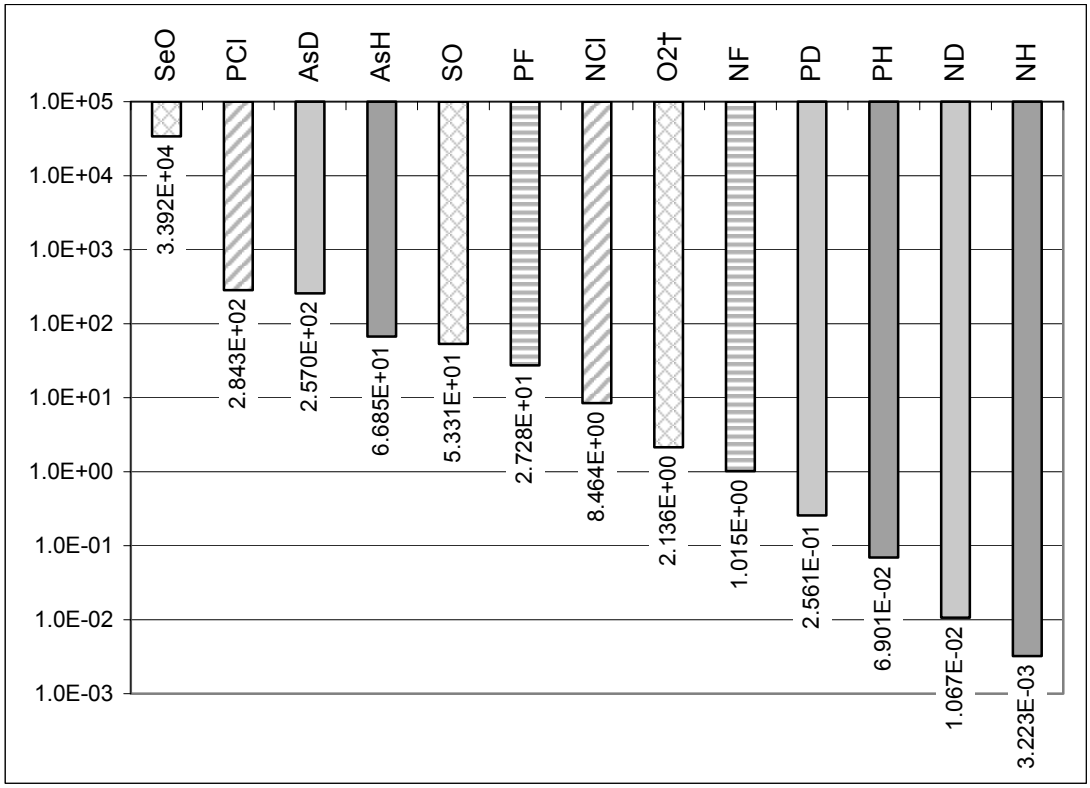

Figure 79: Zeeman relaxation parameter λ_{SS}^2/B_v^2 for selected $X^3\Sigma^-(v''=0)$ molecules. Smaller value indicates better buffer-gas loading properties. All listed molecules can be produced in a glow discharge, and many in laser ablation.

Shading: dark solid: hydride, light solid: deuterated hydride, horizontal hatch: fluoride, diagonal hatch: chloride, cross-hatch: oxide.

† $^{16}O^{18}O$.

	λ_{SS}, cm^{-1}	γ, cm^{-1}	B_v, cm^{-1}	λ_{SS}^2/B_v^2
SeO	86.565	-3.000E-02	0.470	3.392E+04
S_2	11.860	-6.660E-03	0.295	1.621E+03
PCl	4.264	-3.070E-03	0.253	2.843E+02
AsD	58.828	-1.470E-01	3.670	2.570E+02
AsH	58.868	-2.810E-01	7.200	6.685E+01
SO	5.263	-5.567E-03	0.721	5.331E+01
PF	2.948	1.500E-03	0.564	2.728E+01
NCl	1.881	6.959E-03	0.647	8.464E+00
$^{18}O^{18}O$	1.985	-7.487E-03	1.278	2.412E+00
$^{16}O^{18}O$	1.985	-7.959E-03	1.358	2.136E+00
$^{16}O^{16}O$	1.985	-8.423E-03	1.438	1.906E+00
NF	1.215	-4.800E-03	1.206	1.015E+00
PD	2.208	-3.990E-02	4.363	2.561E-01
PH	2.210	-7.690E-02	8.413	6.901E-02
ND	0.907	-3.030E-02	8.782	1.067E-02
NH	0.928	-5.300E-02	16.345	3.223E-03

Table 18: Constants of selected $X^3\Sigma^-$(v"=0) molecules.

Data from [173] and various articles in J.Chem.Phys.

Many-μ_B molecules are attractive trapping candidates, as the technical requirements for the cryogenic apparatus are significantly lower for high-μ_B species. Table 19 lists some of the previously-studied $^{[2S+1>3]}\Sigma$ molecules; production ideas can be found in section 8.1.4. Of particular interest are 6-μ_B molecules of MnF and MnCl, which can be produced by laser-ablating solid MnF_2 and $MnCl_2$, and can be rather easily detected on $X^7\Sigma$-$A^7\Pi$ transitions around 400 nm.

MnH	MnF	MnCl	MnBr	FeH	CrH	MnO	FeO	CrO	BCl	GeH	ScO	LaO
$^7\Sigma^+$	$^7\Sigma$	$^7\Sigma$	$^7\Sigma$	$^6\Sigma^+$	$^6\Sigma$	$^6\Sigma$	$^5\Sigma^+$	$^5\Sigma$	$^4\Sigma^-$	$^4\Sigma$	$^4\Sigma$	$^4\Sigma$

Table 19: Selected high-μ_B molecules with a known Σ ground state.

Finally, there is growing evidence [76; 77] that outer filled *s*-shells in heavy atoms in the lanthanide group of the periodic table may "shield" such atoms from spin-flipping collisions with helium. Ref. [112] lists several diatomic compounds of the lanthanides with a known ground state as shown in Table 20. It would be very interesting to measure Zeeman relaxation on these molecules, as surprising collisional physics may be uncovered.

	X state	Lowest allowed transition	Transition bandhead, cm-1
LaS	$^2\Sigma^+$	B ↔ X	13766.86
YbCl	$^2\Sigma$	$A_1 \rightarrow X$	17892.1
YbH	$^2\Sigma$	D ↔ X	15375.58
YbF	$^2\Sigma$	$A_1 \leftrightarrow X$	18106.28
CeO	$^3\Pi_2$	$A_3 \leftrightarrow X_3$	12162.2

Table 20: Diatomic compounds of lanthanides for which a known term of the ground state is listed in ref. [112]§§§§§.

§§§§§ Refs. [112], [31], [113], while convenient, represent the state of molecular spectroscopy in 1970s, and many exotic diatomics have been studied since the time these references were published. Some examples are studies of LnH (Ln=Ce, Tb, Nd) [174], LnO (Ln=Ce, Pr, Nd, Sm, Eu, Gd,) [175], LnN (Ln = Ce, Pr, Nd, Sm, Eu) [176] molecules produced by laser-ablating Ln metals in the corresponding gases, etc. Visible-spectrum spectroscopic studies have been done for a range of rare earth diatomics, as can be seen in Table 21.

	H	F	O
La	Bernard A, Chevillard J, *J. Mol. Spec.* **208**, 150 (2001)	Kaledin LA, Kaledin AL, Heaven MC, *J. Mol. Spec.* **182**, 50 (1997)	A Bernard and C Effantin, *Can. J. Phys.* **64**, 246 (1986)
Ce			C. Linton et al., *J. Mol. Spec.* **102**, 441 (1983)
Pr			M Dulick and RW Field. *J. Mol. Spec.* **113**, 105 (1985)
Nd			Linton C et al., *J. Mol. Spec.* **225**, 132 (2004)
Pm			
Sm			G. Bugin and C. Linton. *J. Mol. Spec.* **137**, 114 (1989)
Eu			L.A. Kaledin and E.A. Shenyavskaya. *J. Mol. Spec.*. **133**, 469 (1989)
Gd		Kaledin LA et al., *J. Mol. Spec.* **176**, 148 (1996)	L.A. Kaledin et al., *J. Mol. Spec.* **165**, 323 (1994)
Tb		Kaledin LA et al., *Mol. Phys.* **83**, 881 (1994)	L.A. Kaledin and E.A. Shenyavskaya. *J. Mol. Spec.*. **90**, 590 (1981)
Dy		McCarthy MC et al. *J. Mol. Spec.* **179**, 253 (1996)	L.A. Kaledin and E.A. Shenyavskaya. *J. Mol. Spec.*. **90**, 590 (1981)
Ho		L.A. Kaledin et al.. *J. Mol. Spec.*. **154**, 417 (1992)	L.A. Kaledin and E.A. Shenyavskaya. *J. Mol. Spec.*. **90** (1981), p. 590.
Er			
Tm			
Yb	Vanzee RJ, Seely ML, Weltner W, *J. Chem. Phys.* **67**, 861 (1977)	K.L. Dunfield et al., *J. Mol. Spec.* **174**, 433 (1995)	Linton S et al., *J. Mol. Spec.* **101**, 332 (1983)

Table 21 (prev. page): Selected visible-range spectroscopic studies of rare-earth diatomics[******].

[******] YbX are by far the best-studied rare-earth diatomics. Visible-range spectra are also available for:

YbBr [Dickinson CS, Coxon JA, *J. Mol. Spec.* **224**, 27 (2004)],

YbCl [Linton C, Adam AG*, J. Mol. Spec.* **206**, 161 (2001)],

YbS [Melville TC, Coxon JA, Linton C, *J. Chem. Phys.* **113**, 1771 (2000)].

Appendix A: Expanded model of beam loading

Initial tests of the next-generation setup indicated that, while individual components of it perform as expected, the NH signal in the cryocell was not detected. This appendix expands the model for beam loading of buffer gas cell, outlined in chapter 3, in order to better understand the trade-offs associated with various sets of experimental parameters in the next-generation setup.

The expanded loading model provides a framework for determining the optimal length of the charcoal tube depending on other parameters of the experiment. The model takes into the effects of ballistic expansion of the molecular beam, scattering of the beam by background gas and by buffer gas outside the cell, and diffusion of radicals in the cell. We divide the beam path into three regions, as shown in Figure 80:

- cell region filled with a high density of buffer gas, where NH moves diffusively and where it is absorbed on walls;
- tube region, where buffer gas density is determined by the rate of helium streaming out of the cell region and the rate at which it is cryopumped by the charcoal on the

charcoal tube and 4K plate, and where the molecular beam travels ballistically; we consider the length of the tube region as a variable;

- chamber region, similar to tube region, but helium pumping speed is fixed.

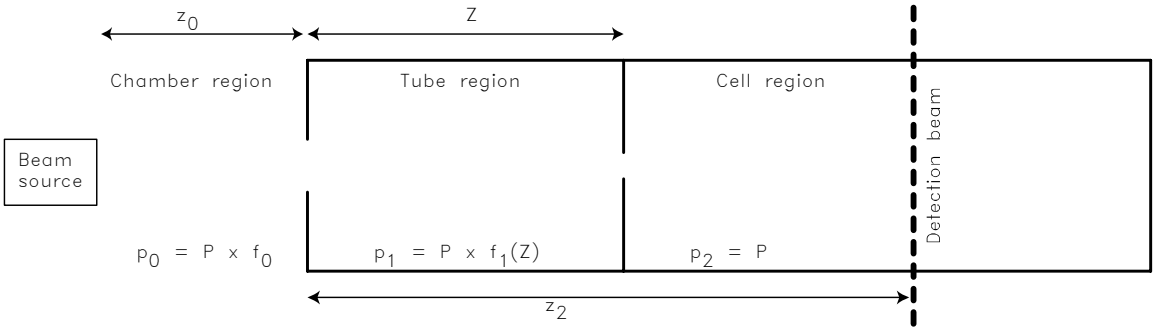

Figure 80: Diagram of expanded loading model assumptions.

The model contains two variables: P – pressure of helium inside the cryocell, (typically in the 1..10 mTorr range), and Z – length of the tube region, in the range of 0..100 mm. Below we estimate the reduction in molecular signal in the probe beam due to each of the effects above.

We assume that the expansion has a free-flight nature, i.e. phenomena like shock waves have no effect on the beam intensity. Ballistic expansion is then expected to produce an inverse-quadratic dependence of signal on distance between valve and cell, due to solid angle considerations:

$$I_1^{z_0}(Z) = \left[\frac{z_0}{Z + z_0}\right]^2$$

where z_0 – minimum distance between valve nozzle and 4 K plate, currently 50 mm.

To determine the effect of background gas scattering, we assume that a single collision of a molecule in the beam with the background gas is sufficient to remove the

molecule from the beam. The signal dependence is described by Beer-Lambert law; in the chamber region, the loss is given by

$$I_2^{f_0}(P) = \exp[-P \cdot \frac{f_0\ z_0\ \sigma}{k_B T_{room}}] \tag{46}$$

where σ is NH-He elastic cross-section, assumed to be 1.5×10^{-15} cm^2; f_0 – ratio of chamber pressure to cell pressure, assumed to be 10^{-3}; and T_{room} is room temperature, 300 K. In the tube region, the ratio of pressures depends on the length of the charcoal tube as follows:

$$f_1(Z) = \frac{\alpha \cdot R_c^{\ 2}}{\beta \cdot R_t^{\ 2} + \gamma \cdot 2R_t \cdot Z} \tag{47}$$

where R_c is cell orifice radius, 1.5 mm; α is the ratio of actual cell orifice conductance to that calculated for effusive flow, assumed to be 5; R_t is charcoal tube radius, 25 mm; β is ratio of tube end pumping speed to that of a perfect pump, assumed to be 0.5; γ is same of tube sides, assumed 0.2. The tube attenuation factor is then

$$I_3(P,Z) = \exp[-P \cdot f_1(Z) \cdot Z \cdot \frac{\sigma}{k_B T}] \tag{48}$$

where T is cell temperature, 4.2 K.

Once the beam enters the cryocell, the molecules thermalize with the buffer gas in ~100 collisions, see Eq. (19). During thermalization the molecules travel a distance of

$$z_{therm}(P) = \frac{\sqrt{100}\ k_B T}{P \cdot \sigma \sqrt{1 + \frac{M_{NH}}{M_{He}}}} \tag{49}$$

after which they begin to diffuse in the buffer gas. As z_2, the distance between 4-K plate and probe laser beam, is presumed fixed at 150 mm, and the cell radius is fixed at 38 mm,

there is a strong dependence of the number of molecules that get to the probe beam on *Z*. As *Z* is increased, the molecules have a smaller distance to cover, so they are less likely to be absorbed on cell walls before getting to the probe beam. The expression below was obtained from numerical solutions of the diffusion equation described in Appendix B; we will not derive the analytical expression for it here. The empirical formula for the diffusion

$$I_4(P,Z) = 10^{\frac{Z - z_{therm}(P)}{L_{diff}}} \tag{50}$$

where L_{diff} is a geometry-related factor calculated to be 30 mm.

The overall dependence of molecule signal on P and Z is given by[††††††]

$$I(P,Z) = I_1 \cdot I_2 \cdot I_3 \cdot I_4 \tag{51}$$

Figure 81 shows the dependence of predicted signal on the length of the charcoal tube. We observe that shortening the tube from its maximum length of 100 mm results in a decrease of signal, and that the exact dependence of *I* on *Z* is very sensitive to assumptions of the model.

[††††††] The signal-to-noise ratio of our measurements is typically set by the photon shot noise. Diffusion time directly affects the maximum camera integration time per frame. Here we assume that the number of acquisition frames per data set is adjusted to compensate for any changes in integration time to keep the measurement signal-to-noise ratio fixed. Otherwise, an additional factor of the form $I_5(P) = \sqrt{P/\text{torr}}$ needs to be introduced into the expression.

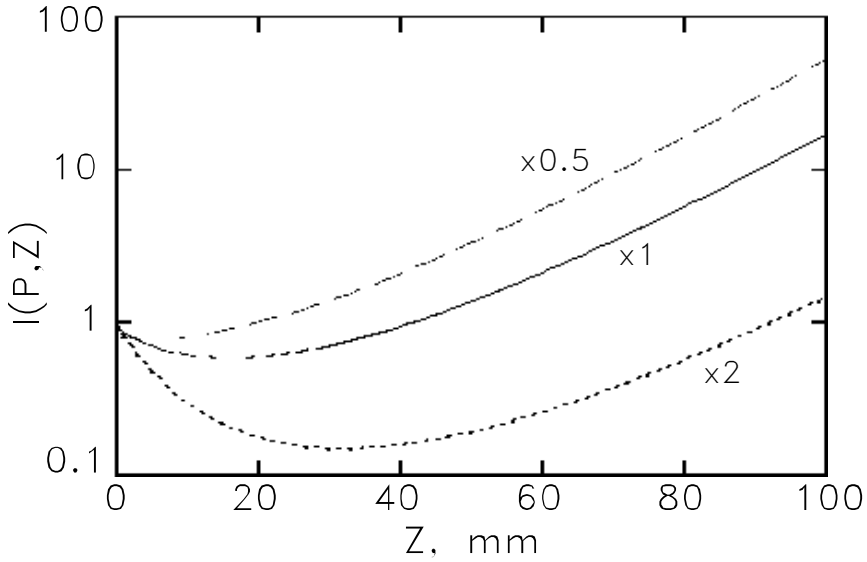

Figure 81: Loading model predictions for optimal tube length at fixed pressure. Different curves correspond to different assumptions about the exact value of σ.

Appendix B: Diffusion equation

In the course of this work it was realized that our "intuitive" understanding of diffusion processes in buffer gas cell is often inadequate. This section provides a brief overview of important features of diffusion equation solutions that are relevant to buffer gas cooling.

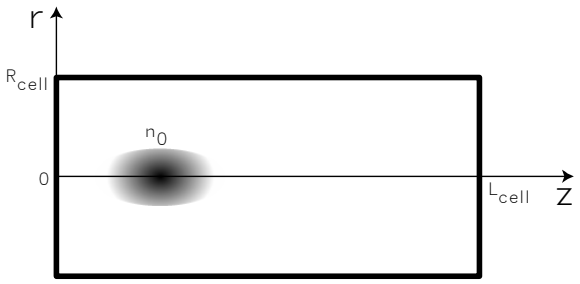

Figure 82: Diffusion equation: initial distribution and boundary conditions.

Analytical solutions

Consider the following model for molecules in the buffer gas. A cylindrical cell, as shown in Figure 82, is filled with a constant uniform density of helium gas n_{He}. Molecules are loaded into the cell, either using beam loading or laser ablation in a cylindrically-symmetric manner (e.g. ablation sample is mounted on the cell end-cap and

ablated axially). Within a very small period of time the molecules completely thermalize with buffer gas to a translational temperature T; at this moment (t=0) there exists a known distribution of molecular density $n(r,z,t=0)=n_0(r,z)$. The molecules then diffuse through the helium according to a diffusion equation

$$\frac{\partial n}{\partial t} = D_{NHHe}\Delta n \tag{52}$$

with a diffusion coefficient given by

$$D_{NHHe} = \frac{3}{16}\sqrt{\frac{2\pi k_B T}{\mu_{NHHe}}}\frac{1}{\sigma_{NHHe} n_{He}} \tag{53}$$

where μ_{NHHe} is the reduced mass of NH-He system and σ_{NHHe} is the diffusion cross-section. We assume that NH is absorbed by the walls, so the diffusion equation boundary condition is:

$$n(r = R_{cell}, z, t) = n(r, z = 0, t) = n(r, z = L_{cell}, t) = 0 \tag{54}$$

Solutions to this equation are well-known [177]:

$$n(r,z,t) = \sum_{m=1}^{\infty}\sum_{n=1}^{\infty} n_{m,n}(r,z,t) \tag{55}$$

$$n_{m,n}(r,z,t) = B_{m,n}\cdot J_0[\mathrm{R_{m\text{-}1}}\frac{r}{R_{cell}}]\cdot\sin[n\pi\frac{z}{L_{cell}}]\cdot\exp[-\frac{t}{\tau_{m,n}}] \tag{56}$$

$$B_{m,n} = \frac{4}{R_{cell}^2 L_{cell}\cdot(J_1[\mathrm{R_{m\text{-}1}}])^2}\int_0^{R_{cell}} r\,dr\int_0^{L_{cell}} dz\, n_0(r,z)\cdot J_0[\mathrm{R_{m\text{-}1}}\frac{r}{R_{cell}}]\cdot\sin[n\pi\frac{z}{L_{cell}}] \tag{57}$$

$$\tau_{m,n} = \left[D_{NHHe}\left(\left(\mathrm{R_{m\text{-}1}}\frac{1}{R_{cell}}\right)^2 + \left(n\pi\frac{1}{L_{cell}}\right)^2\right)\right]^{-1} \tag{58}$$

where $J_0(x)$ is a zeroth-order Bessel function of the first kind and R_{k-1} is its k-th root[‡‡‡‡‡‡].

We refer to each of $n_{m,n}(r,z,t)$ as the (m,n) mode of the diffusion equation; the distribution between modes is given by coefficients $B_{m,n}$ which depend only on the initial distribution $n_0(r,z)$. We refer to $\tau_{m,n}$ as diffusion lifetime of the (m,n) mode – the mode decays exponentially with a $1/e$ time of $\tau_{m,n}$. We immediately notice that $\tau_{m,n}$ decreases for increasing m and n; this means that higher-order modes will decay more rapidly than the low-order ones.

The (1,1) approximation

A buffer-gas experiment always has a certain early-time cutoff (e.g. time for discharge glow, ablation flash, etc. to subside) before which no measurement is done; it is therefore possible to terminate the sums in (55) at some m_{max}, n_{max} without any change in accuracy of predictions. It is frequently assumed (e.g. in [72]) that the timescales of interest in the experiments are sufficiently long so that $m_{max} = n_{max} = 1$, i.e. the distribution is completely described by the (1,1) mode. Another justification for only considering the (1,1) mode is that the initial distribution in most experiments is such that $B_{1,1} >> B_{m,n}$, i.e. the non-(1,1) modes are very sparsely populated and don't need to be considered. As described below, such assumptions are not always acceptable.

Time decay profile of the distribution is used for most buffer gas experiments to extract the elastic molecule-helium cross-section, so it is important to understand the

[‡‡‡‡‡‡] First few roots of J_0 are: 2.405, 5.520, 8.654, 11.792, 14.931, 18.071, 21.212, 24.347, 27.489, 30.630, …

limitations of the (1,1) approximation. The departure from the (1,1) approximation may also have a significant impact on the experiment design, as described below.

Diffusion in test cryostat

We will use the test cryostat as an illustration for this discussion. The test cryocell is not cylindrically symmetric, and simple analytical solutions do not exist for an arbitrary shape; we will have to approximate the cell as a cylinder. The cylinder parameters are radius R_{cell} = 19 mm and length L_{cell} = 51 mm.

For n_{He} = 10 mTorr, T = 4.2 K, σ_{NHHe} = 1.5×10^{-15} cm^2 (see section 6.2.2) the values of $\tau_{m,n}$ are shown in Figure 83.

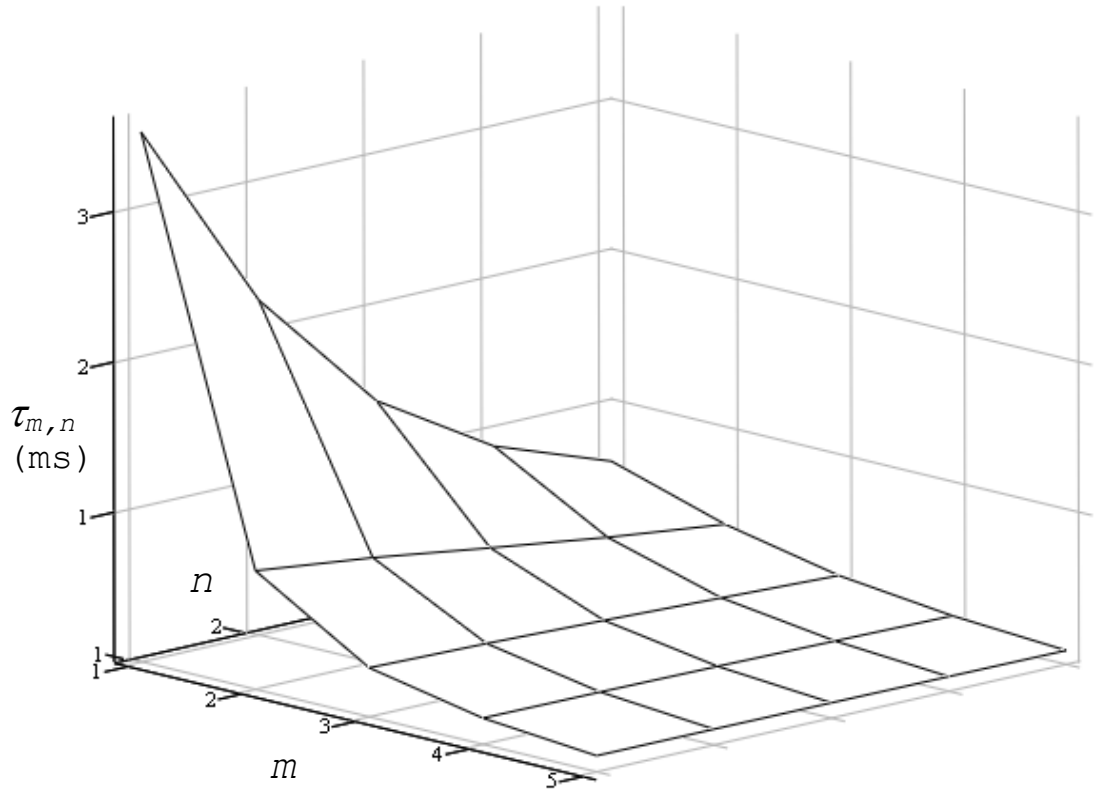

Figure 83: Calculated diffusion mode lifetimes for model test-cryostat cell.

As seen in Figure 83, the difference between the lifetime of the (1,1) mode is not substantially different from the nearby non-(1,1) modes: compare $\tau_{1,1}$ =3.53 ms with $\tau_{1,2}$ = 2.23 ms. This means that, for arbitrary $B_{m,n}$ distribution, for the (1,1) mode to become dominant in the time decay of the signal one needs to acquire signal for multiple 1/*e* times[§§§§§§]. In many buffer gas experiments the measurements are not done for times this long due to signal-to-noise or dynamic range limitations of the measurement equipment.

Figure 84 gives the distribution of $B_{m,n}$ for the initial distribution filling a 10-mm radius volume at the cell end[*******]. This is a distribution typical for beam loading experiments. We see that the assumption that $B_{1,1} >> B_{m,n}$ does not hold. Even after t=3.5 ms has elapsed, the peak of the distribution does not correspond to the (1,1) mode.

We conclude that in analyzing time decay profiles for buffer gas loading experiments loaded with a beam source it is incorrect to assume that the decay is

---

[§§§§§§] If $B_{1,1}=B_{1,2}$, then the (1,1) mode will be an order of magnitude stronger than the (1,2) mode only at t_{x10}=14 ms; note that before that time the signal will appear to decay with a timescale faster than $\tau_{1,1}$, so t_{x10} corresponds to many more observed "diffusion lifetimes" than the value of $t_{x10}/\tau_{1,1}$

[*******] The fact the initial distribution of molecules in the beam-loaded buffer gas cell fills only a small volume of a few mm in diameter leads to a possible simplification of the trapping apparatus: the trapping magnet can be made very small, e.g. with a 10-mm bore radius. Such magnet, while having the same trapping field as the larger one described in section 5.7, will have significantly smaller forces pushing the coils apart, and therefore can be made much lighter and cheaper.

dominated by the (1,1) mode. In order to extract precise values of elastic cross-sections (as opposed to lower limits) it is necessary either to have sufficient dynamic range to observe the signal for tens of decay times, or have sufficient signal-to-noise ratio and point-to-point repeatability to distinguish a single-exponent fit from two- or multiple-exponent fits, or have spatial distribution information to determine time dependence of $B_{m,n}$'s.

Another potential pitfall in assuming the immediate formation of the (1,1) distribution is that there may be a time delay between the injection of molecules into the buffer gas and the appearance of signal, as molecules slowly diffuse towards the probe beam. If such time delay is taken into account, incorrect conclusions on signal strength can be made.

It remains an open question whether laser ablation produces spatial distributions that have $B_{1,1} >> B_{m,n}$. There is some evidence that, at least in some cases, it does not. In the CaF experiment the in-field spectral lines did not correspond to a (1,1) mode distribution in the magnetic field shown in Figure 65. It is unlikely that the calculated field profile has more than percent-level errors in it, so we conclude that the mode population was spread over, at least, several (1,n) modes. In other experiments a time-delayed arrival of atoms to a trapping saddle point was observed, which is a strong indication that the dominant (1,1) mode is not formed. Studies are currently being done to determine the dependence of mode distribution on laser ablation parameters.

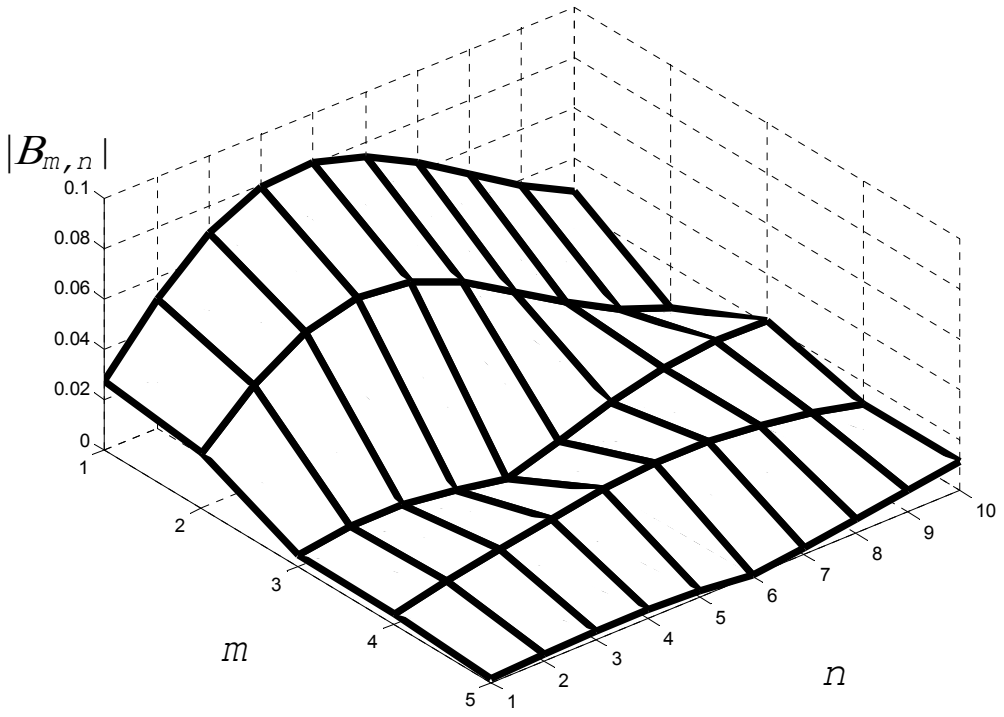

Figure 84: Mode distribution for a 10-mm thermalization radius.

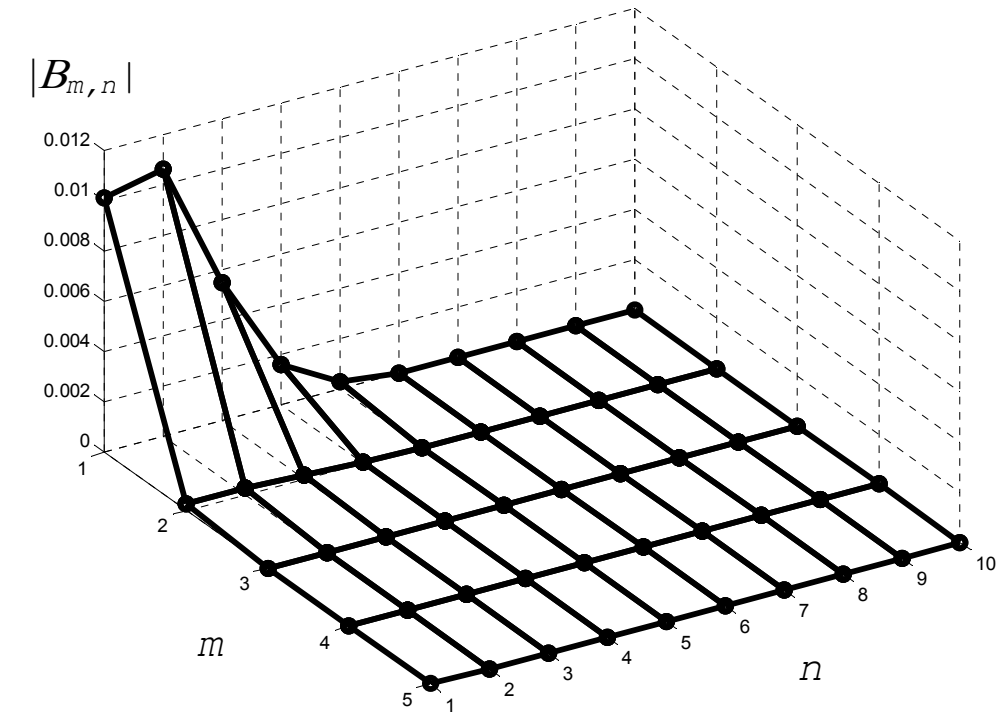

Figure 85: Mode distribution at t =3.52 ms = $\tau_{1,1}$.

Appendix C : Zero-field spectrum of CaF

This appendix provides a brief reference on calculating fine and hyperfine line positions in CaF spectrum at zero external magnetic field. In the $X^2\Sigma^+ \rightarrow A^2\Pi_i$ transitions of CaF the hyperfine structure is completely dominated by the X-state. For our spectrum simulations we use a model Hamiltonian and constants from Ref. [178]. We define the following MathCAD functions:

$$HR(n) := B_{00}\cdot n\cdot(n+1)$$

$$HA(n) := \frac{-\left(\gamma_{00} + b_{00} + C_{I00}\right)}{4}$$

$$HB(n) := \sqrt{(2n+1)^2\left(\gamma_{00} - C_{I00}\right)^2 + \left(2b_{00} + c_{00} - 2C_{I00}\right)\left(2b_{00} + c_{00} - 2\gamma_{00}\right)}$$

$$HC(n) := \frac{\left(b_{00} - \gamma_{00} - C_{I00}\right)}{4}$$

$$HD(n,f) := (2\cdot n+1)\cdot\left(\gamma_{00} + C_{I00}\right) + \frac{c_{00}}{2\cdot f+1} - \frac{\left(c_{00}\right)^2\cdot f\cdot(f+1)}{2B_{00}\cdot(2f+1)^3}$$

$$H1(n,j,f) := \frac{-\left(3\cdot b_{00} + c_{00}\right)}{4}$$

$$H2(n,j,f) := 2B_{00} - \gamma_{00} + \frac{\left(b_{00} - c_{00}\right)}{4} - C_{I00}$$

$$H3(n,j,f) := HR(n) + HA(n) + \frac{(j-n)}{2}HB(n)$$

$$H4(n,j,f) := HR(n) + HC(n) + \left(\frac{f-n}{4}\right)\cdot HD(n,f)$$

where

$B_{00} := 10303.988\,\text{MHz}$

$C_{I00} := 2.876\,10^{-2}\,\text{MHz}$

$\gamma_{00} := 39.659\,\text{MHz}$

$b_{00} := 109.1839\,\text{MHz}$

$c_{00} := 40.1190\,\text{MHz}$

We calculate line positions according to the following table:

N"	J"	F"	Line position
0	1/2	0	*H1 (0, 1/2, 0)*
		1	*H4 (0, 1/2, 1)*
1	1/2	0	*H2 (1, 1/2, 0)*
	1/2	1	*H3 (1, 1/2, 1)*
	3/2	1	*H3 (1, 3/2, 1)*
	3/2	2	*H4 (1, 3/2, 2)*
X>2	X-1/2	X-1	*H4 (X, X-1/2, X-1)*
	X-1/2	X	*H3 (X, X-1/2, X)*
	X+1/2	X	*H3 (X, X+1/2, X)*
	X+1/2	X+1	*H4 (X, X+1/2, X+1)*

Table 22: Model Hamiltonian for calculation of zero-field line positions.

The calculated line positions are then used to simulate the observed spectra and to calibrate the voltage-to-frequency conversion of the dye laser.

Appendix D : Zeeman effect in CaF $X^2\Sigma^+$

When an external magnetic field is applied, both $X^2\Sigma^+$ and $A^2\Pi_i$ states experience a Zeeman shift. Model Hamiltonians, like that in Appendix C, are typically not available for arbitrary magnetic fields, so the energy levels must be calculated by diagonalizing appropriate realistic Hamiltonians.

The Zeeman shift of $X^2\Sigma^+$ determines the potential energy difference between low- and high-field seekers, and must be known well in order to interpret the Zeeman relaxation measurements. In the case of highly non-uniform fields, a question of avoided crossings also becomes critical, as will be discussed later in this appendix. Finally, the difference in Zeeman effects of X- and A-states determines the Zeeman shift of the observed optical transition. Calculation of Zeeman shifts in Hund's case (a) $A^2\Pi_i$ states is not trivial, and the reader is referred to Ref. [163]. On the other hand, the calculation for Hund's case (b) $X^2\Sigma^+$ state is simple, and the approach can be readily applied to other $X^2\Sigma^+$ molecules of interest.

The Hamiltonian for $X^2\Sigma^+$ state of a molecule in a magnetic field can be written as:

$$H = H_{rot} + H_{spin-rot} + H_{spin-iso} + H_{spin-nuc-aniso} + H_{nuc-rot} + H_{Zeeman} + H_{nuc.Zeeman} \quad (59)$$

where

$$H_{rot} = B_{v"N"} \mathbf{N}^2 \quad (60)$$

$$H_{spin-rot} = \gamma_{v"N"} \mathbf{N} \cdot \mathbf{S} \quad (61)$$

$$H_{spin-nuc-iso} = b_{v"N"} \mathbf{S} \cdot \mathbf{I} \quad (62)$$

$$H_{spin-nuc-aniso} = c_{v"N"} I_z S_z \quad (63)$$

$$H_{nuc-rot} = C^I_{v"N"} \mathbf{N} \cdot \mathbf{I} \quad (64)$$

$$H_{Zeeman} = \mu S_Z B \quad (65)$$

$$H_{nuc.Zeeman} = \mu_N I_Z B \quad (66)$$

are rotational, electron spin – rotation, electron spin – nuclear spin isotropic, electron spin – nuclear spin anisotropic, nuclear spin – rotation, electron spin – magnetic field, and nuclear spin – magnetic field interaction Hamiltonian components correspondingly. The constants in (60)-(64) are named after their corresponding interactions and are in general dependent on v" and N". Once the appropriate constants are located (for CaF, we used constants in [153], [178], and [179]), a computer program can be used to diagonalize the Hamiltonian for arbitrary values of external magnetic field.

The code is especially simple if we ignore the spin-nuclear spin anisotropic coupling term and later introduce its effect manually[†††††††]. We use the Hund's case (b) basis:

$|N,M_N\rangle\,|S,M_S\rangle\,|I,M_I\rangle$

In this basis write the matrix elements of (59) (excluding (63); for matrix elements, consult, e.g. [24]) and diagonalize the matrix. The output of the diagonalization code is provided in Figure 86.

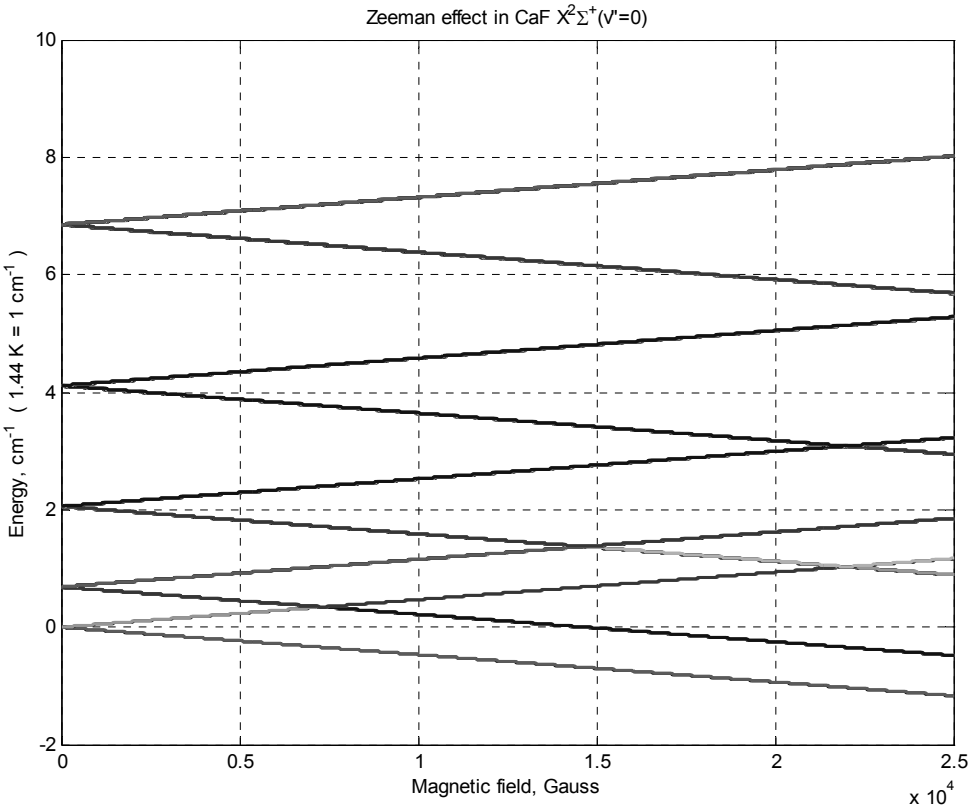

Figure 86: Calculated Zeeman effect in CaF $X^2\Sigma^+$(v"=0,N"=0…4) up to 25 kGauss.

[†††††††] this is due to the fact that (65) and (66) contain projections of the electronic and nuclear spins S_Z, I_Z onto the magnetic field axis, while (63) contains projections onto the internuclear axis S_z, I_z

We observe that at large fields the effect is essentially linear, i.e.

$$H_{Zeeman} \rightarrow \quad \pm \mu_B B \quad \text{for} \quad \mu_B B >> \gamma(N + \tfrac{1}{2}) \tag{67}$$

At small fields, however, the spin-orbit interaction couples states with different $|N,M_N>$ and the energy shift is not linear, as seen in Figure 87.

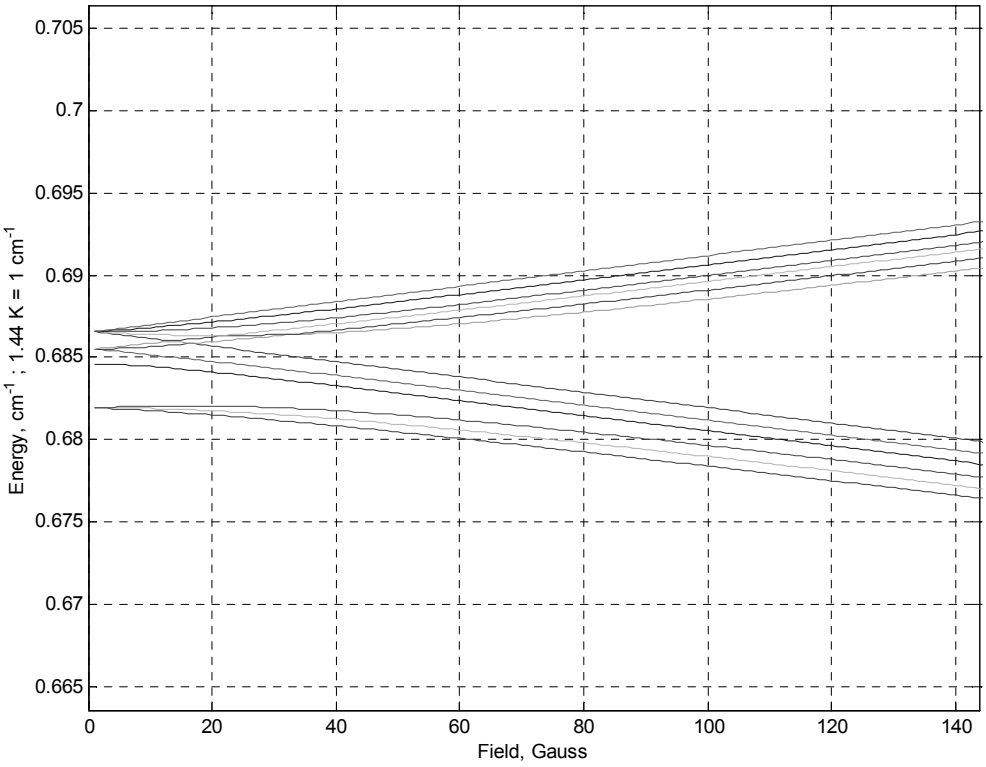

Figure 87: Calculated Zeeman effect in CaF $X^2\Sigma^+$(v"=0,N"=0…1) up to 150 Gauss.

In the absence of the anisotropic term (63), all level crossings seen in Figure 86 are allowed. The anisotropic interaction, however, couples state pairs (N,N+2), e.g. (N"=0,J"=1/2,F"=1) and (N"=2,J"=3/2,F"=1), which have the same parity and the same quantum number F". This means that the crossings between these states become avoided crossings, with the size of the gap between levels given by the anisotropic constant

$C^I_{0,0} = 9.59\times10^{-7}$ cm^{-1}.

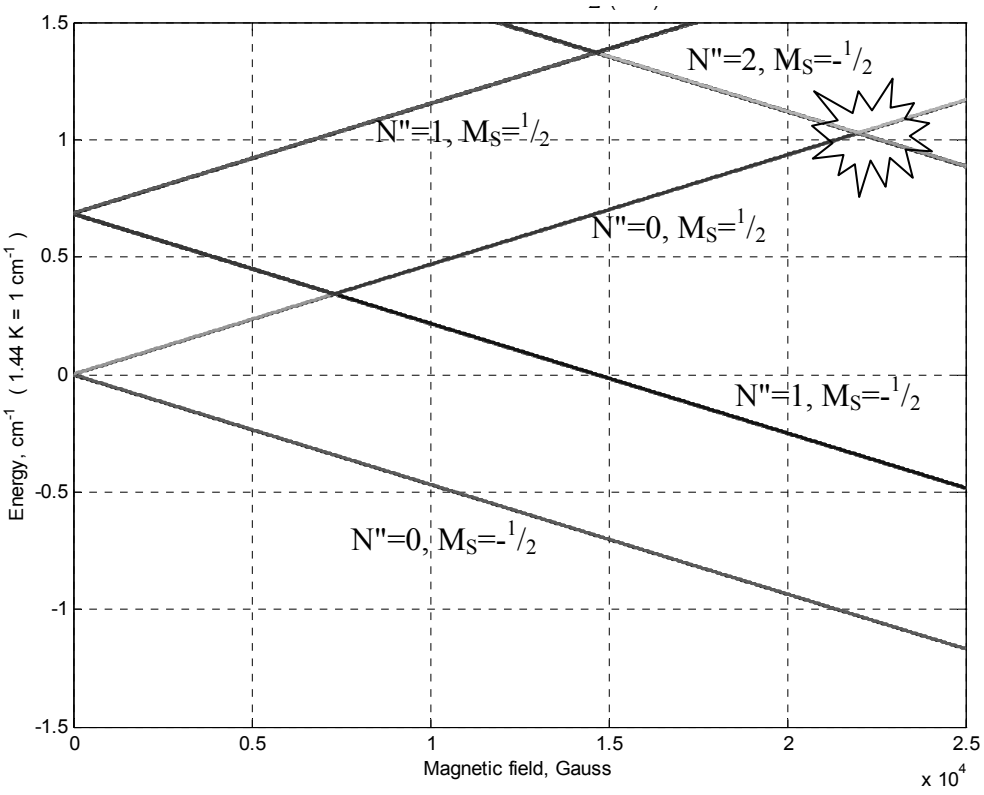

Figure 88: Location of an avoided crossing between N"=0 and N"=2 levels due to the anisotropic spin-nuclear spin interaction.

The avoided crossing is not a concern in our experiment, since the molecules are subjected to a near-uniform magnetic field, and since away from the immediate vicinity the levels preserve their low-field or high-field seeking nature. The situation is very different in a strongly non-uniform trapping field. The molecule in a low-field seeking state (N"=0,J"=1/2,F"=1, M_S=1/2) moving into a high-field region near a trap edge may approach the avoided crossing and continue along the high-field seeking N"=2,J"=3/2,F"=1, M_S=-1/2) level, which will result in the molecule being ejected from the trap by the field gradient. Detailed simulations of the trapping dynamics including

these Landau-Zener effect transitions are necessary to determine whether the molecules are trappable in a given field configuration for a given temperature. We note that in the case of CaF, the crossing is located at a substantial field value (~22 kGauss) and the gap between the levels is very small, so we still expect CaF to be a good trapping candidate.

Bibliography

1. M. Anderson, J. Ensher, M. Matthews, C. Wieman and E. Cornell. *Science* **269**, 198 (1995).

2. B. d. Marco and D. Jin. *Science* **285**, 1703 (1999).

3. R. Onofrio, C. Raman, J. M. Vogels, J. R. Abo-Shaeer, A. P. Chikkatur and W. Ketterle. "Observation of superfluid flow in a Bose-Einstein condensed gas." *Physical Review Letters* **85**, 2228 (2000).

4. M. O. Mewes, M. R. Andrews, D. M. Kurn, D. S. Durfee, C. G. Townsend and W. Ketterle. "Output coupler for Bose-Einstein condensed atoms." *Physical Review Letters* **78**, 582 (1997).

5. H. Stapelfeldt, H. Sakai, E. Constant and P. B. Corkum. "Deflection of neutral molecules using the nonresonant dipole force." *Physical Review Letters* **79**, 2787 (1997).

6. D. DeMille. "Quantum Computation with Trapped Polar Molecules." *Physical Review Letters* **88**, 067901 (2002).

7. M. A. Baranov, M. S. Mar'enko, V. S. Rychkov and G. V. Shlyapnikov. "Superfluid pairing in a polarized dipolar Fermi gas." *Physical Review A* **66**, 013606 (2002).

8. L. D. Carr, G. V. Shlyapnikov and Y. Castin. "Achieving a BCS transition in an atomic Fermi gas." *Physical Review Letters* **92** (2004).

9. L. Santos, G. V. Shlyapnikov, P. Soller and M. Lewenstein. "Bose-Einstein condensation in trapped dipolar gases." *Physical Review Letters* **85**, 1791 (2000).

10. C. Zhu, N. Balakrishnan and A. Dalgarno. "Vibrational relaxation of CO in ultracold He-3 collisions." *Journal of Chemical Physics* **115**, 1335 (2001).

11. A. V. Avdeenkov and J. L. Bohn. "Ultracold collisions of oxygen molecules." *Physical Review A* **64**, 052703 (2001).

12. N. Balakrishnan, R. C. Forrey and A. Dalgarno. "Threshold phenomena in ultracold atom-molecule collisions." *Chemical Physics Letters* **280**, 1 (1997).

13. N. Balakrishnan, A. Dalgarno and R. C. Forrey. "Vibrational relaxation of CO by collisions with He-4 at ultracold temperatures." *Journal of Chemical Physics* **113**, 621 (2000).

14. N. Balakrishnan, G. C. Groenenboom, R. V. Krems and A. Dalgarno. "The He-CaH((2)Sigma(+)) interaction. II. Collisions at cold and ultracold temperatures." *Journal of Chemical Physics* **118**, 7386 (2003).

15. N. Balakrishnan, G. C. Groenenboom, R. V. Krems and A. Dalgarno. "The He-CaH((2)Sigma(+)) interaction. I. Three-dimensional ab initio potential energy surface." *Journal of Chemical Physics* **118**, 7380 (2003).

16. J. L. Bohn. "Cold collisions of O-2 with helium." *Physical Review A* **62**, 032701 (2000).

17. J. L. Bohn. "Molecular spin relaxation in cold atom-molecule scattering." *Physical Review A* **61**, 040702 (2000).

18. J. L. Bohn. "Inelastic collisions of ultracold polar molecules." *Physical Review A* **63**, 052714 (2001).

19. J. L. Bohn, A. V. Avdeenkov and M. P. Deskevich. "Rotational Feshbach resonances in ultracold molecular collisions." *Physical Review Letters* **89**, 203202 (2002).

20. R. C. Forrey, V. Kharchenko, N. Balakrishnan and A. Dalgarno. "Vibrational relaxation of trapped molecules." *Physical Review A* **59**, 2146 (1999).

21. R. V. Krems and A. A. Buchachenko. "Ultracold inelastic atomic collisions: Threshold relaxation of O(P-3(0)) by He." *Physical Review A* **6402** (2001).

22. R. V. Krems, H. R. Sadeghpour, A. Dalgarno, D. Zgid, J. Klos and G. Chalasinski. "Low-temperature collisions of NH(X3 Sigma(-)) molecules with He atoms in a magnetic field: An ab initio study." *Physical Review A* **68**, 051401 (2003).

23. R. V. Krems, A. Dalgarno, N. Balakrishnan and G. C. Groenenboom. "Spin-flipping transitions in (2)Sigma molecules induced by collisions with structureless atoms." *Physical Review A* **67**, 060703 (2003).

24. R. V. Krems and A. Dalgarno. "Quantum-mechanical theory of atom-molecule and molecular collisions in a magnetic field: Spin depolarization." *Journal of Chemical Physics* **120**, 2296 (2004).

25. A. Volpi and J. L. Bohn. "Molecular vibration in cold-collision theory." *Physical Review A* **65** (2002).

26. A. Volpi and J. L. Bohn. "Magnetic-field effects in ultracold molecular collisions." *Physical Review A* **65**, 052712 (2002).

27. A. Volpi and J. L. Bohn. "Fine-structure effects in vibrational relaxation at ultralow temperatures." *Journal of Chemical Physics* **119**, 866 (2003).

28. A. Hatakeyama, K. Oe, K. Ota, S. Hara, J. Arai, T. Yabuzaki and A. R. Young. "Slow spin relaxation of Rb atoms confined in glass cells filled with dense He-4 gas at 1.85 K." *Physical Review Letters* **84**, 1407 (2000).

29. I. B. Khriplovich and S. K. Lamoreaux. *CP Violation without Strangeness, Electric Dipole Moments of Particles, Atoms, and Molecules.*, Springer, New York (1997)

30. J. T. Bahns, W. C. Stwalley and P. L. Gould. "Laser cooling of molecules: A sequential scheme for rotation, translation, and vibration." *Journal of Chemical Physics* **104**, 9689 (1996).

31. G. Herzberg. *Molecular Spectra and Molecular Structure*, 2nd edition, reprint w/corrections. Krieger, Malabar (1989)

32. M. D. Di Rosa, private communication.

33. V. Vuletic and S. Chu. "Laser cooling of atoms, ions, or molecules by coherent scattering." *Physical Review Letters* **84**, 3787 (2000).

34. J. T. Bahns, P. L. Gould and W. C. Stwalley, Formation of cold (T<1 K) molecules. Advances in Atomic, Molecular, and Optical Physics. B. Bederson and H.Walther, Academic Press. **42:** 171. (2000)

35. D. J. Heinzen, R. Wynar, P. D. Drummond and K. V. Kheruntsyan. "Superchemistry: Dynamics of coupled atomic and molecular Bose- Einstein condensates." *Physical Review Letters* **84**, 5029 (2000).

36. W. C. Stwalley and H. Wang. "Photoassociation of ultracold atoms: a new spectroscopic technique." *Journal of Molecular Spectroscopy* **195**, 194 (1999).

37. J. Weiner, V. S. Bagnato, S. Zilio and P.S. Julienne. "Experiments and theory in cold and ultracoled collisions." *Reviews of Modern Physics* **71**, 1 (1999).

38. D. Comparat, C. Drag, A. Fioretti, O. Dulieu and P. Pillet. "Photoassociative Spectroscopy and Formation of Cold Molecules in Cold Cesium Vapor: Trap-Loss Spectrum versus Ion Spectrum." *Journal of Molecular Spectroscopy* **195**, 229 (1999).

39. C. M. Dion, C. Drag, O. Dulieu, B. L. Tolra, F. Masnou-Seeuws and P. Pillet. "Resonant coupling in the formation of ultracold ground state molecules via photoassociation." *Physical Review Letters* **86**, 2253 (2001).

40. A. Fioretti, D. Comparat, A. Crubellier, O. Dulieu, F. Masnou-Seeuws and P. Pillet. "Formation of Cold Cs2 Molecules through Photoassociation." *Physical Review Letters* **80**, 4402 (1998).

41. C. Gabbanini, A. Fioretti, A. Lucchesini, S. Gozzini and M. Mazzoni. "Cold rubidium molecules formed in a magneto-optical trap." *Physical Review Letters* **84**, 2814 (2000).

42. A. N. Nikolov, J. R. Ensher, E. E. Eyler, H. Wang, W. C. Stwalley and P. L. Gould. "Efficient production of ground-state potassium molecules at sub-mK temperatures by two-step photoassociation." *Physical Review Letters* **84**, 246 (2000).

43. J. P. Shaffer, W. Chalupczak and N. P. Bigelow. "Highly excited states of ultracold molecules: Photoassociative spectroscopy of Na2." *Physical Review Letters* **83**, 3621 (1999).

44. T. Takekoshi, B. Patterson and R. J. Knize. "Optical trapping of ultracold molecules." *Abstracts of Papers of the American Chemical Society* **220**, 299 (2000).

45. C. A. Regal, M. Greiner and D. S. Jin. "Lifetime of molecule-atom mixtures near a Feshbach resonance in 40K." *Physical Review Letters* **92** (2004).

46. S. Durr, T. Volz, A. Marte and G. Rempe. "Observation of molecules produced from a Bose-Einstein condensate." *Physical Review Letters* **92** (2004).

47. K. Xu, T. Mukaiyama, J. R. Abo-Shaeer, J. K. Chin, D. E. Miller and W. Ketterle. "Formation of quantum-degenerate sodium molecules." *Physical Review Letters* **91** (2003).

48. K. E. Strecker, G. B. Partridge and R. G. Hulet. "Conversion of an atomic Fermi gas to a long-lived molecular Bose gas." *Physical Review Letters* **91** (2003).

49. M. W. Zwierlein, C. A. Stan, C. H. Schunck, S. M. F. Raupach, S. Gupta, Z. Hadzibabic and W. Ketterle. "Observation of Bose-Einstein condensation of molecules." *Physical Review Letters* **91** (2003).

50. L. Radzihovsky, J. Park and P. B. Weichman. "Superfluid transitions in bosonic atom-molecule mixtures near a feshbach resonance." *Physical Review Letters* **92** (2004).

51. S. Y. T. van de Meerakker, R. T. Jongma, H. L. Bethlem and G. Meijer. "Accumulating NH radicals in a magnetic trap." *Physical Review A* **6404** (2001).

52. H. L. Bethlem, G. Berden and G. Meijer. "Decelerating neutral dipolar molecules." *Physical Review Letters* **83**, 1558 (1999).

53. E. Nikitin, E. Dashevskaya, J. Alnis, M. Auzinsh, E. R. I. Abraham, B. R. Furneaux, M. Keil, C. McRaven, N. Shafer-Ray and R. Waskowsky. "Measurement and prediction of the speed-dependent throughput of a magnetic octupole velocity filter including nonadiabatic effects." *Physical Review A* **68** (2003).

54. S. A. Rangwala, T. Junglen, T. Rieger, P. W. H. Pinkse and G. Rempe. "Continuous source of translationally cold dipolar molecules." *Physical Review A* **67** (2003).

55. M. Gupta and D. Herschbach. "Slowing and speeding molecular beams by means of a rapidly rotating source." *Journal of Physical Chemistry A* **105**, 1626 (2001).

56. B. Friedrich. "Slowing of supersonically cooled atoms and molecules by time-varying nonresonant induced dipole forces - art. no. 025403." *Physical Review A* **6102**, 5403 (2000).

57. M. S. Elioff, J. J. Valentini and D. W. Chandler. "Subkelvin cooling NO molecules via "billiard-like" collisions with argon." *Science* **302**, 1940 (2003).

58. R. deCarvalho, J. M. Doyle, B. Friedrich, T. Guillet, J. Kim, D. Patterson and J. D. Weinstein. "Buffer-gas loaded magnetic traps for atoms and molecules: A primer." *European Physical Journal D* **7**, 289 (1999).

59. J. K. Messer and F. C. Delucia. "Measurement of Pressure-Broadening Parameters for the Co-He System at 4-K." *Physical Review Letters* **53**, 2555 (1984).

60. H. L. Bethlem, F. M. H. Crompvoets, R. T. Jongma, S. Y. T. van de Meerakker and G. Meijer. "Deceleration and trapping of ammonia using time-varying electric fields." *Physical Review A* **65** (2002).

61. M. R. Tarbutt, H. L. Bethlem, J. J. Hudson, V. L. Ryabov, V. A. Ryzhov, B. E. Sauer, G. Meijer and E. A. Hinds. "Slowing heavy, ground-state molecules using an alternating gradient decelerator." *Physical Review Letters* **92**, 173002 (2004).

62. H. L. Bethlem, A. J. A. van Roij, R. T. Jongma and G. Meijer. "Alternate gradient focusing and deceleration of a molecular beam." *Physical Review Letters* **88** (2002).

63. R. Wynar, R. S. Freeland, D. J. Han, C. Ryu and D. J. Heinzen. "Molecules in a Bose-Einstein condensate." *Science* **287**, 1016 (2000).

64. A. J. Kerman, J. M. Sage, S. Sainis, T. Bergeman and D. DeMille. "Production and state-selective detection of ultracold RbCs molecules." *Physical Review Letters* **92**, 153001 (2004).

65. C. A. Regal, C. Ticknor, J. L. Bohn and D. S. Jin. "Creation of ultracold molecules from a Fermi gas of atoms." *Nature* **424**, 47 (2003).

66. J. D. Weinstein, R. deCarvalho, T. Guillet, B. Friedrich and J. M. Doyle. "Magnetic trapping of calcium monohydride molecules at millikelvin temperatures." *Nature* **395**, 148 (1998).

67. D. Egorov, J. D. Weinstein, D. Patterson, B. Friedrich and J. M. Doyle. "Spectroscopy of laser-ablated buffer-gas-cooled PbO at 4 K and the prospects for measuring the electric dipole moment of the electron - art. no. 030501." *Physical Review A* **63**, 030501(R) (2001).

68. H. J. Metcalf and P. V. D. Straten. *Laser Cooling and Trapping*, Springer-Verlag(1999)

69. J. Doyle, private communication.

70. R. deCarvalho. *Inelastic Scattering of Magnetically Trapped Atomic Chromium.* Ph.D. thesis, Harvard University, 2003.

71. R. Michniak. *Enhanced Buffer Gas Loading: Cooling and Trapping of Atoms with Low Effective Magnetic Moments.* Ph.D. thesis, Harvard University, 2004.

72. J. D. Weinstein. *Magnetic Trapping of Atomic Chromium and Molecular Calcium Monohydride.* Ph.D. thesis, Harvard University, 2002.

73. H. L. Bethlem, G. Berden, F. M. H. Crompvoets, R. T. Jongma, A. J. A. van Roij and G. Meijer. "Electrostatic trapping of ammonia molecules." *Nature* **406**, 491 (2000).

74. T. Takekoshi, B. M. Patterson and R. J. Knize. "Observation of optically trapped cold cesium molecules." *Physical Review Letters* **81**, 5105 (1998).

75. J. D. Weinstein, R. deCarvalho, J. Kim, D. Patterson, B. Friedrich and J. M. Doyle. "Magnetic trapping of atomic chromium." *Physical Review A* **57**, R3173 (1998).

76. C. I. Hancox, private communication.

77. C. I. Hancox, S. C. Doret, M. T. Hummon, R. V. Krems and J. M. Doyle. "S-state suppression of cold inelastic collisions in non-S-state atoms." *submitted to Physical Review Letters*

78. J. D. Weinstein, R. deCarvalho, K. Amar, A. Boca, B. C. Odom, B. Friedrich and J. M. Doyle. "Spectroscopy of buffer-gas cooled vanadium monoxide in a magnetic trapping field." *Journal of Chemical Physics* **109**, 2656 (1998).

79. W. Demtroder. *Laser spectroscopy: basic concepts and instrumentation*, 2nd enl. Springer, Berlin; New York (1996)

80. S. Svanberg. *Atomic and Molecular Spectroscopy: Basic Aspects and Practical Applications*, 3rd ed. Springer-Verlag(2001)

81. G. Berden, R. Engeln, P. C. M. Christianen, J. C. Maan and G. Meijer. "Cavity-ring-down spectroscopy on the oxygen A band in magnetic fields up to 20 T." *Physical Review A* **58**, 3114 (1998).

82. M. M. Beaky, T. M. Goyette and F. C. DeLucia. "Pressure broadening and line shift measurements of carbon monoxide in collision with helium from 1 to 600 K." *Journal of Chemical Physics* **105**, 3994 (1996).

83. D. R. Willey, R. L. Crownover, D. N. Bittner and F. O. Delucia. "Very Low-Temperature Spectroscopy - the Pressure Broadening Coefficients for Co-He between 4.3-K and 1.7-K." *Journal of Chemical Physics* **89**, 1923 (1988).

84. B. C. Regan, E. D. Commins, C. J. Schmidt and D. DeMille. "New limit on the electron electric dipole moment." *Physical Review Letters* **88** (2002).

85. E. Commins, S. Ross, D. DeMille and B. Regan. *Physical Review A* **50**, 2960 (1994).

86. L. R. Hunter. *Science* **252**, 73 (1991).

87. E. A. Hinds and B. E. Sauer. *Physics World* **04**, 37 (1997).

88. B. E. Sauer, S. B. Cahn, M. G. Kozlov, G. D. Redgrave and E. A. Hinds. *Journal of Chemical Physics* **110**, 8424 (1999).

89. D. DeMille, F. Bay, S. Bickman, D. Kawall, D. Krause, S. E. Maxwell and L. R. Hunter. "Investigation of PbO as a system for measuring the electric dipole moment of the electron." *Physical Review A* **6105** (2000).

90. P. G. H. Sandars. *Physical Review Letters* **19**, 1396 (1967).

91. M. G. Kozlov and V. F. Ezhov. *Physical Review A* **49**, 4502 (1994).

92. J. D. Cobine. *Gaseous Conductors.*, McGraw-Hill, New York (1941)

93. F. Martin, R. Bacis, J. Verges, J. Bachar and S. Rosenwaks. *Spectrochimica Acta Part a-Molecular and Biomolecular Spectroscopy* **44A**, 889 (1988).

94. C. H. Townes and A. L. Schawlow. *Microwave Spectroscopy*, Dover, New York (1975)

95. B. Friedrich, private communication.

96. G. Scoles. *Atomic and molecular beam methods*, Oxford University Press, New York (1988)

97. H. Pauly. *Atom, molecule, and cluster beams*, Springer, Berlin; New York (2000)

98. T. R. Roberts and S. G. Sydoriak. "Thermomolecular Pressure Ratios for He-3 and He-4." *Physical Review* **102**, 304 (1956).

99. D. W. Sedgley, A. G. Tobin, T. H. Batzer and W. R. Call. "Characterization of Charcoals for Helium Cryopumping in Fusion Devices." *Journal of Vacuum Science & Technology a-Vacuum Surfaces and Films* **5**, 2572 (1987).

100. A. G. Tobin, D. W. Sedgley, T. H. Batzer and W. R. Call. "Evaluation of Charcoal Sorbents for Helium Cryopumping in Fusion-Reactors." *Journal of Vacuum Science & Technology a-Vacuum Surfaces and Films* **5**, 101 (1987).

101. J.-C. Boissin (2003). Achievement of UHV conditions with cryocondensation helped by cryosorption on argon frost. International Workshop on Extreme High Vacuum Application and Technology.

102. J. M. Lafferty, Ed. Foundations of Vacuum Science and Technology. John Wiley and Sons Inc. New York (1998).

103. http://masterweb.jpl.nasa.gov/reference/paints.htm.

104. http://cua.harvard.edu/~nh/BlackPaint.htm.

105. M. R. Walkiewicz, P. J. Fox and R. E. Scholten. "Candlestick rubidium beam source." *Review of Scientific Instruments* **71**, 3342 (2000).

106. E. Arimondo, M. Inguscio and P. Violino. "Experimental Determinations of Hyperfine-Structure in Alkali Atoms." *Reviews of Modern Physics* **49**, 31 (1977).

107. G. P. Barwood, P. Gill and W. R. C. Rowley. "Frequency measurements on optically narrowed Rb-stabilised laser diodes at 780 nm and 795 nm." *Applied Physics B (Photophysics and Laser Chemistry)* **B53**, 142 (1991).

108. D. R. Lide. *CRC Handbook of Chemistry and Physics*, 79th. CRC Press, Boca Raton (1998)

109. M. V. Romalis, E. Miron and G. D. Cates. "Pressure broadening of Rb D-1 and D-2 lines by He-3, He-4, N-2, and Xe: Line cores and near wings." *Physical Review A* **56**, 4569 (1997).

110. R. Campargue. *Atomic and Molecular Beams: The State of the Art 2000*, Springer-Verlag Telos(2001)

111. T. Klaus, S. Takano and G. Winnewisser. "Laboratory measurement of the N=1 from 0 rotational transition of NH at 1 THz." *Astronomy and Astrophysics* **322**, L1 (1997).

112. *NIST Chemistry Webbook*, http://webbook.nist.gov

113. S. N. Suchard and J. E. Melzer. *Spectroscopic data*, IFI/Plenum, New York (1975)

114. R. N. Dixon. "The 0-0 and 1-0 Bands of the A(3)Pi-X(3)Sigma- System of NH." *Canadian Journal of Physics* **37**, 1171 (1959).

115. W. Ubachs, J. J. Ter Meulen and A. Dymanus. "High-resolution laser spectroscopy on the A(3)Pi from X(3)Sigma- transition of NH." *Canadian Journal of Physics* **62**, 1374 (1984).

116. A. Schadee. "HONL-LONDON FACTORS FOR PI-3-SIGMA-3 AND SIGMA-3-PI-3 TRANSITIONS WITH INTERMEDIATE COUPLING." *ASTRONOMY AND ASTROPHYSICS* **41**, 213 (1975).

117. S. E. Maxwell, private communication.

118. W. Schoellkopf (2001). Internal memo, unpublished., Harvard University.

119. D. R. Herrick, M. B. Robin and A. Gedanken. "Spin-Rotation Effects in the Stern-Gerlach Deflection Spectra of 3-Sigma- Molecules and Their Complexes with Argon." *Journal of Molecular Spectroscopy* **133**, 61 (1989).

120. D. W. Kohn, H. Clauberg and P. Chen. "Flash pyrolysis nozzle for generation of radicals in a supersonic jet expansion." *Review of Scientific Instruments* **63**, 4003 (1992).

121. G. Schonnenbeck, H. Biehl, F. Stuhl, U. Meier and V. Staemmler. "Vuv photolysis of hydrazoic acid: Absorption and fluorescence excitation spectra." *Journal of Chemical Physics* **109**, 2210 (1998).

122. H. Biehl and F. Stuhl. "Vacuum-ultraviolet photolysis of N/sub 2/H/sub 2/: generation of NH fragments." *Journal of Chemical Physics* **100**, 141 (1994).

123. F. Rohrer and F. Stuhl. "The 193 (and 248) nm photolysis of HN/sub 3/: formation and internal energy distributions of the NH (a/sup 1/ Delta, b/sup 1/ Sigma /sup +/, A/sup 3/ Pi, and c/sup 1/ Pi) states." *Journal of Chemical Physics* **88**, 4788 (1988).

124. R. D. Kenner, R. K. Browarzik and F. Stuhl. "Two-photon formation of NH/ND(A/sup 3/ Pi) in the 193 nm photolysis of ammonia. II. Photolysis of NH/sub 2/." *Chemical Physics* **121**, 457 (1988).

125. A. Hofzumahaus and F. Stuhl. "NH (A/sup 3/II) rotational population generated by ArF laser photolysis of NH/sub 3/." *Journal of Chemical Physics* **82**, 5519 (1985).

126. F. Rohrer and F. Stuhl. "NH(a/sup 1/ Delta to X/sup 3/ Sigma /sup -/) emission from the gas-phase photolysis of HN/sub 3/." *Chemical Physics Letters* **111**, 234 (1984).

127. H. K. Haak and F. Stuhl. "ArF (183 nm) laser photolysis of HN/sub 3/, CH/sub 3/NH/sub 2/, and N/sub 2/H/sub 4/: formation of excited NH radicals." *Journal of Physical Chemistry* **88**, 3627 (1984).

128. J. E. Nicholas, A. I. Spiers and N. A. Martin. "Kinetics and mechanism in the decomposition of NH/sub 3/ in a radio-frequency pulse discharge." *Plasma Chemistry and Plasma Processing* **6**, 39 (1986).

129. P. G. Carrick and P. C. Engelking. "Spin-orbit cooling and population inversion in nozzle expansions of NH." *Chemical Physics Letters* **108**, 505 (1984).

130. T. D. Hain, M. A. Weibel, K. M. Backstrand and T. J. Curtiss. "Rotational state selection and orientation of OH and OD radicals by electric hexapole beam-focusing." *Journal of Physical Chemistry A* **101**, 7674 (1997).

131. T. Amano, P. F. Bernath and A. R. W. McKellar. "Direct observation of the nu /sub 1/ and nu /sub 3/ fundamental bands of NH/sub 2/ by difference frequency laser spectroscopy." *Journal of Molecular Spectroscopy* **94**, 100 (1982).

132. R. D. Kenner, F. Rohrer and F. Stuhl. "Generation of NH(a/sup 1/ Delta) in the 193 nm photolysis of ammonia." *Journal of Chemical Physics* **86**, 2036 (1987).

133. Y. P. Raizer. *Gas discharge physics*, Springer-Verlag, Berlin (1997)

134. S. Davis, D. T. Anderson, G. Duxbury and D. J. Nesbitt. "Jet-cooled molecular radicals in slit supersonic discharges: sub-Doppler infrared studies of methyl radical." *Journal of Chemical Physics* **107**, 5661 (1997).

135. R. D. Kenner, F. Rohrer, R. K. Browarzik, A. Kaes and F. Stuhl. "Two-photon formation of NH/ND(A/sup 3/ Pi) in the 193 nm photolysis of ammonia. I. Mechanism and identification of the intermediate species." *Chemical Physics* **118**, 141 (1987).

136. S. Y. T. van de Meerakker, B. G. Sartakov, A. P. Mosk, R. T. Jongma and G. Meijer. "Optical pumping of metastable NH radicals into the paramagnetic ground state." *Physical Review A* **68** (2003).

137. H. H. Nelson, J. R. McDonald and M. H. Alexander. "Temperature-Dependence of the Collisional Quenching of Nh(a Delta-1) by N-2, O-2, Co, and Xe." *Journal of Physical Chemistry* **94**, 3291 (1990).

138. D. Patelmisra and P. J. Dagdigian. "State-Resolved Electronic Quenching of Nh(A1-Delta) by Xe and Co." *Journal of Chemical Physics* **97**, 4871 (1992).

139. W. Hack and K. Rathmann. "Collision-Induced Intersystem Crossing of Nh(A1-Delta,Upsilon"=0,1) by N2 and Xe - Temperature-Dependence (N2) and Product States (N2, Xe)." *Journal of Physical Chemistry* **96**, 47 (1992).

140. A. Peters'_group, private communication.

141. F. Pobell. *Matter and Methods at Low Temperatures*, Springer(1996)

142. A. Roth. *Vacuum Technology*, 3rd Ed. North-Holland(1990)

143. J. G. E. Harris, W. C. Campbell, D. Egorov, S. E. Maxwell, R. A. Michniak, S. V. Nguyen, L. D. v. Buuren and J. M. Doyle. "Deep superconducting magnetic traps for neutral atoms and molecules." *Review of Scientific Instruments* **75**, 17 (2004).

144. M. N. Wilson. *Superconducting Magnets*, Oxford Science Publications, Oxford (1997)

145. D. Weise, private communication.

146. http://irtek.arc.nasa.gov/ThermCont_page/ThermCont.html.

147. L. J. Salerno and P. Kittel, Thermal Contact Conductance. Cryogenic Handbook. J. Weisend, Taylor & Francis. (1998)

148. S. Davis. *High Resolution Infrared Spectroscopy of Slit-Jet Cooled Transient Molecules: From van der Waals Clusters, to Hydrogen Bound Dimers, to Small Organic Radicals.* Ph.D. thesis, University of Colorado, 1999.

149. H. Cybulski, R. V. Krems, H. R. Sadeghpour, A. Dalgarno, J. Klos, G. C. Groenenboom, A. v. d. Avoird, D. Zgid and G. Chalasinski. "Interaction of NH(X3Sigma-) with He: potential energy surface, bound states and collisional Zeeman relaxation." *to be submitted to Physical Review A*

150. R. V. Krems and A. Dalgarno. "Threshold laws for collisional reorientation of electronic angular momentum." *Physical Review A* **67**, 050704 (2003).

151. W. E. Ernst, S. Kindt, K. P. R. Nair and T. Toerring. *Physical Review A* **29**, 1158 (1984).

152. B. S. Zhao, M. Castillejo, D. S. Chung, B. Friedrich and D. Herschbach. "Cool pulsed molecular microbeam." *Review of Scientific Instruments* **75**, 146 (2004).

153. L. Kaledin, J. Bloch, M. McCarthy and R. Field. "Analysis and deperturbation of the A(2)Pi and B-2 Sigma(+) states of CaF." *Journal of Molecular Spectroscopy* **197**, 289 (1999).

154. W. J. Childs, L. S. Goodman, U. Nielsen and V. Pfeufer. "Electric-dipole moment of CaF (X 2 +) by molecular beam, laser-rf, double- resonance study of Stark splittings." *Journal of Chemical Physics* **80**, 2283 (1984).

155. J. G. E. Harris, R. A. Michniak, S. V. Nguyen, N. Brahms, W. Ketterle and J. M. Doyle. "Buffer gas cooling and trapping of atoms with small effective magnetic moments." *Europhysics Letters* **67**, 198 (2004).

156. S. V. Nguyen, S. C. Doret, J. S. Helton, K. Maussang, R. A. Michniak, J. G. E. Harris, W. Ketterle and J. M. Doyle. "Magnetic trapping and cold collisions of manganese." *manuscript in preparation*

157. L. T. Earls. "Intensities in 2 Pi -2 Sigma Transitions in Diatomic Molecules." *Physical Review* **48**, 423 (1935).

158. R. Krems, private communication.

159. N. Balakrishnan, M. Vieira, J. F. Babb, A. Dalgarno, R. C. Forrey and S. Lepp. "Rate coefficients for ro-vibrational transitions in H-2 due to collisions with He." *Astrophysical Journal* **524**, 1122 (1999).

160. N. Balakrishnan, R. C. Forrey and A. Dalgarno. "Quantum-mechanical study of ro-vibrational transitions in H-2 induced by He atoms." *Astrophysical Journal* **514**, 520 (1999).

161. N. Balakrishnan and A. Dalgarno. "On the quenching of rovibrationally excited molecular oxygen at ultracold temperatures." *Journal of Physical Chemistry A* **105**, 2348 (2001).

162. R. V. Krems. "Vibrational relaxation of vibrationally and rotationally excited CO molecules by He atoms." *Journal of Chemical Physics* **116**, 4517 (2002).

163. R. Krems, D. Egorov, J. S. Helton, K. Maussang, S. V. Nguyen and J. M. Doyle. "Zeeman effect in CaF(A2Pi_3/2)." *manuscript in preparation*

164. L. Neitsch, F. Stuhl, P. J. Dagdigian and M. H. Alexander. "Inelastic collisions of fine structure and Lambda -doublet resolved rotational states of PH(A/sup 3/ Pi, nu =0) with helium." *Journal of Chemical Physics* **106**, 7642 (1997).

165. C. Yamada, M. C. Chang and E. Hirota. "Infrared diode laser spectroscopy of the PF radical." *Journal of Chemical Physics* **86**, 3804 (1987).

166. C. Yamada, Y. Endo and E. Hirota. "The microwave spectrum of the N [sup 35]Cl radical in the X [sup 3] Sigma [sup -] state." *Journal of Chemical Physics* **79**, 4159 (1983).

167. Rare-earth Element. Encyclopaedia Britannica. (2004)

168. N. A. Kuebler, M. B. Robin, J. J. Yang, A. Gedanken and D. R. Herrick. "Fully Resolved Zeeman Pattern in the Stern-Gerlach Deflection Spectrum of O-2 (3-Sigma-G-, K = 1)." *Physical Review A* **38**, 737 (1988).

169. K. R. Comer and S. C. Foster. "Infrared-Spectroscopy of the Products of a Corona-Excited Supersonic Expansion." *Chemical Physics Letters* **202**, 216 (1993).

170. G. Hilpert, H. Linnartz, M. Havenith, J. J. ter Meulen and W. L. Meerts. "Tunable infrared and far-infrared direct absorption spectroscopy of molecular ions in a supersonic jet expansion." *Chemical Physics Letters* **219**, 384 (1994).

171. H. Linnartz, T. Motylewski, F. Maiwald, D. A. Roth, F. Lewen, I. Pak and G. Winnewisser. "Millimeter wave spectroscopy in a pulsed supersonic slit nozzle discharge." *Chemical Physics Letters* **292**, 188 (1998).

172. T. Motylewski and H. Linnartz. "Cavity ring down spectroscopy on radicals in a supersonic slit nozzle discharge." *Review of Scientific Instruments* **70**, 1305 (1999).

173. M. Mizushima. *The theory of rotating diatomic molecules.*, John Wiley & Sons, New York (1975)

174. S. Willson and L. Andrews. "Characterization of the reaction products of laser-ablated early lanthanide metal atoms with molecular oxygen. Infrared spectra of LnO, LnO(+), LnO(-), LnO(2), LnO(2)(+), LnO(2)(-), and LnO(3)(-), and (LnO)(2) in solid argon." *Journal of Physical Chemistry A* **103**, 3171 (1999).

175. S. Willson and L. Andrews. "Characterization of the reaction products of laser-ablated lanthanide metal atoms with molecular hydrogen. Infrared spectra of LnH, LnH(2), LnH(3), and LnH(4) molecules in solid argon." *JOURNAL OF PHYSICAL CHEMISTRY A* **104**, 1640 (2000).

176. S. Willson and L. Andrews. "Characterization of the reaction products of laser-ablated early lanthanide metal atoms with dinitrogen. Infrared spectra of LnN, LnN(2), (LnN)(2), and Ln(NN)(x) molecules." *JOURNAL OF PHYSICAL CHEMISTRY A* **102**, 10238 (1998).

177. J. B. Hasted. *Physics of atomic collisions*, Butterworths, London (1964)

178. W. J. Childs, G. L. Goodman and L. S. Goodman. "Precise determination of the v and N dependence of the spin-rotation and hyperfine interactions in the CaF X21/2 ground state." *Journal of Molecular Spectroscopy* **86**, 365 (1981).

179. M. A. Anderson, M. D. Allen and L. M. Ziurys. "The Millimeter-Wave Spectrum of the CaF Radical (X2S+)." *Astrophysical Journal* **424**, 503 (1994).